Études des corrélations de spin dans un système d'atomes dipolaires piégés dans un réseau optique

Youssef Aziz Alaoui

To cite this version:

Youssef Aziz Alaoui. Études des corrélations de spin dans un système d'atomes dipolaires piégés dans un réseau optique. Supraconductivité [cond-mat.supr-con]. Université Paris-Nord - Paris XIII, 2022. Français. NNT : 2022PA131078 . tel-04028326

HAL Id: tel-04028326
https://theses.hal.science/tel-04028326

Submitted on 14 Mar 2023

UNIVERSITÉ PARIS XIII - SORBONNE PARIS NORD
ÉCOLE DOCTORALE SCIENCES, TECHNOLOGIES, SANTÉ GALILÉE

DOCTORAL DISSERTATION

Études des corrélations de spin dans un ensemble d'atomes dipolaires piégés dans un réseau optique

Studies of spin correlations in an ensemble of lattice trapped dipolar atoms

---

Thèse de doctorat menée au laboratoire de physique des lasers et présentée par

Youssef AZIZ ALAOUI

Pour l'obtention du grade de Docteur en Physique

Soutenue le 30 Septembre 2022 devant le jury d'examen composé de

Brune Michel, LKB	Examinateur
Lahaye Thierry, LCF	Rapporteur
Nascimbène Sylvain, LKB	Rapporteur
Perrin Hélène, LPL	Examinatrice
Westbrook Christopher, LCF	Président du Jury
Laburthe Tolra Bruno, LPL	Directeur de thèse
Vernac Laurent, LPL	Co-directeur de thèse

“ *Le but de cette thèse est de munir son auteur du titre de Docteur …*”

Adrien Douady

Remerciements

Cela fait maintenant quelques mois que je suis docteur et à l'heure où j'écris ces remerciements, c'est d'abord à vous deux, Bruno et Laurent, que je pense. Merci de m'avoir accueilli dans ce groupe qui est maintenant le mien et dont j'ai pu, ces dernières années, apprécier la convivialité et le dynamisme. Je n'oublierai pas ce petit périple expérimental qui fut le nôtre et que vous m'avez offert de vivre dans cette sombre salle mystérieusement nommée *Nanochrome*. J'espère n'en n'oublier ni les joies, ni les frustrations et je vous remercie encore une fois de m'avoir accompagné, tard parfois, dans cette aventure. Merci à vous.
Ma reconnaissance va aussi aux joyeux lurons de la mezzanine : Lucas, Pierre, Andréa, Charles, Hussein, Julien, qui eurent la bonté de supporter mes innombrables pauses café.
Je n'oublie pas bien sûr les autres membres de l'équipe Kaci, Ziad, Benjamin, Martin, Etienne, Paolo, Olivier, et enfin Thomas aux mains duquel je laisse cette belle manip' et à qui je souhaite beaucoup de réussite. Ces vœux de réussite, je les adresse aussi à tous les autres doctorant(e)s du laboratoire, et tous ceux avec qui il m'a été donné, au détour d'un couloir, d'échanger quelques mots.
Je souhaite remercier aussi les membres des ateliers électronique et mécanique sans lesquels rien de tout ceci n'aurait été possible, je pense en particulier à Fabrice et Haniffe qui firent montre d'une grande réactivité tout au long de ma thèse.
Je remercie aussi les petites mains et les grands cœurs du service administratif : Maryse Médina, Carole Grangier, Alexandre Sourie et Sylvie Spielmann. Merci pour votre disponibilité et votre patience.
À mon père, à ma mère, à ma famille petite et grande, mes pensées les plus chaudes, cette thèse est vôtre autant qu'elle est mienne. Je vous aime.
À Alice.
…

Contents

List of Figures

Physical Constants

Speed of Light	$c = 2.998\,\mathrm{m\,s^{-1}}$
Bohr radius	$a_0 = 5.292 \times 10^{-11}\,\mathrm{m}$
Reduced Planck constant	$\hbar = 1.055 \times 10^{-34}\,\mathrm{J\,s}$
Electronic Landé factor	$g_s = 2.002$
Bohr Magneton	$\mu_B = 9.274 \times 10^{-24}\,\mathrm{J\,T^{-1}}$
Vacuum permeability	$\mu_0 = 4\pi 10^{-7}\,\mathrm{kg\,m\,s^{-2}\,A^{-2}}$
Fine structure constant	$\alpha = 1/137$
Elementary charge	$\mathrm{e} = 1.602 \times 10^{-19}\,\mathrm{C}$
Vacuum permittivity	$\epsilon_0 = 8.854 \times 10^{-12}\,\mathrm{F\,m^{-1}}$

Introduction

Never mind, it's only a small obstacle

– Rohinton Mistry (A fine balance)

Chromium, dipole dipole interactions and Bose Einstein condensation

The dipole dipole interactions

Most quantum gases' characteristics (shape, density, excitations, stability, collisional properties...) are dictated by the nature and strength of interparticle interactions. These interactions take numerous forms: contact interactions for example are short ranged and isotropic, **dipole dipole interactions** (DDI) on the contrary are considered[1] to be **long ranged**, **anisotropic** and can be either **attractive** or **repulsive**.

$$V_{\mathrm{dd}}^{12} = \frac{\gamma_d}{4\pi r^3}\left(\mathbf{d_1}.\mathbf{d_2} - 3\frac{(\mathbf{d_1}.\mathbf{r})(\mathbf{d_2}.\mathbf{r})}{r^3}\right) \tag{1}$$

Equation 1: The general form of the dipole dipole interaction between two dipole moments $\mathbf{d_1}$ and $\mathbf{d_2}$ separated by $\mathbf{r}$. The γ_d constant depends on the precise nature of the interaction at hand [1].

These peculiarities give rise to a plethora of interesting phenomena that have been studied in different quantum simulation platforms [2][3][4]. These platforms can be broadly categorized into **dipolar electric** and **dipolar magnetic** platforms.
Rydberg atoms, Rydberg molecules and heteronuclear molecules pertain to the former whereas alkali atoms, **highly magnetic** atoms and magnetic molecules belong to the latter.

$$\frac{\mu_0 \mu_b^2}{(ea_0)^2/\epsilon_0} \simeq \frac{\alpha^2}{4} \tag{2}$$

Equation 2: Typical ratio between magnetic ($\simeq \mu_B$, the Bohr magneton) and electric dipole moments ($\simeq ea_0$). $\alpha \simeq \frac{1}{137}$ is the fine structure constant. Magnetic dipole moments are in general orders of magnitude smaller than electric dipole moments

Chromium falls into the highly magnetic atoms category, hence called because their magnetic dipole moments are relatively high. For example erbium and dysprosium sport dipole moments of 7 μ_b and 10 μ_B respectively whereas chromium has a 6 μ_B dipole moment, which makes for dipole dipole interactions that are 36 times stronger than those at play in alkali atoms such as cesium or rubidium ($d = 1\mu_b$). The strength of these dipolar interactions can be otherwise gauged using ϵ_{dd}, **the dipolar parameter**

---

[1] Depending on the point of view and dimensionality of the problem DDI can be seen as short or long ranged, see [1]

$$\epsilon_{\mathrm{dd}}^{Cr} = \frac{a_{\mathrm{dd}}}{a} = 0.16 \tag{3}$$

Where

- $a_{\mathrm{dd}} = \frac{\gamma_d m}{12\pi\hbar^2}$ is the so called **dipolar length**, it measures the *absolute strength* of the dipole dipole interaction [5]
- a is the s-wave scattering length

Equation 3: The dipolar parameter ϵ_{dd} characterizes the relative strength of dipole dipole and contact interactions and therefore, the behavior of the system when both kinds of interactions are contributing. For example Bose Einstein condensates with $\epsilon_{\mathrm{dd}} > 1$ are *unstable against 3D collapse* in spherical traps [5]. In the case of chromium, dipole dipole interactions are dominated by contact interactions. For comparison $\epsilon_{\mathrm{dd}}^{Rb} = 0.007$ while $\epsilon_{\mathrm{dd}}^{HCn} = 240$.

Still and as suggested by Eq. 2, when compared to other dipolar entities the interactions between magnetic atoms remain relatively weak with typical coupling strengths ranging from 10 and 10^3 Hz, whereas they reach values as high as 10^4 and 10^6 Hz for polar molecules and Rydberg atoms respectively. This is however at the expanse of smaller coherence times[2]: 1 μs for Rydberg atoms, 10 ms for polar molecules and 100 ms for magnetic atoms. Moreover magnetic atoms experiments generally involve a greater number of constituents ($N \approx 10^4 - 10^5$) than other platforms, this *natural* scalability is complemented by great collisional stability features which most molecule experiments for example still lack. All of these characteristics represent important assets as far as quantum simulation (of itinerant magnetism notably) and quantum computing are concerned. Details on these numbers and more can be found in [8].

Bose Einstein condensation

The main isotope of the chromium atom is bosonic, it was first condensed in 2004 [9]. Bose Einstein condensates (BECs) are peculiar states of matter characterized by the saturation of excited bosonic particles' spatial density within the thermodynamic limit ($V \to \infty, \frac{N}{V} = cste$ where V is the system size and N the number of particles). **For spatial densities greater than a certain threshold n_{max}^{ex}, all particles added to the system will condense into its ground state**.
The existence of the n_{max}^{ex} quantity is not systematic and depends on the particulars of the Hamiltonian spectrum and the dimensionality of the problem at hand. When it exists however, n_{max}^{ex} is in general an increasing function of the temperature, which is to say that even though it would be increasingly hard to observe, the Bose Einstein condensation phenomenon can, a priori, happen at any temperature and is **not to be confused with the more trivial accumulation of particles in the system's lowest energy state which can occur in the framework of Boltzmann's statistics** when $k_B T$ is smaller than the system's typical energy spacing between Hamiltonian eigenstates. This condensation criterion can also be expressed in terms of phase space density:

---

[2] The numbers given for Rydberg atoms and molecules should be seen as lower bounds as much greater coherence times have been demonstrated in recent experiments [6] [7]

$$\phi(\mathbf{0}) = n(\mathbf{0})\lambda_T^3 > \phi_C = 2.6 \tag{4}$$

Where

- $\phi(\mathbf{0})$ is the phase space density at the minimum of the potential landscape
- $n(\mathbf{0})$ is the spatial density at the minimum of the potential landscape
- $\lambda_T = \sqrt{\frac{2\pi\hbar^2}{mk_BT}}$ is the de Broglie wavelength
- ϕ_c is the critical phase space density $\phi_c = \zeta(3/2)$ where ζ is Riemann's zeta function

Equation 4: Condensation criterion for a general 3D potential/trap $V(\mathbf{r})$ in the so called semi-classical approximation ($k_BT >> \hbar\omega$ where ω is the trap's typical oscillation frequency) [10]. The higher the phase space density, the higher the condensed particle fraction. The condensation phenomenon exhibits other universal traits, for example, at transition, particles in the gas phase all share the same entropy per particle $s = \frac{\zeta(5/2)}{\zeta(3/2)}\frac{5}{2}k$ [11] p.293

The procedure leading to the condensation of the chromium atoms will be briefly described in Chap. 1.

The chromium BEC physics [12] is however not the focus of the present work wherein we will mainly study the interactions between chromium atoms trapped in ***optical lattices****, that is between chromium atoms which ultimately end up interacting through dipole dipole interactions alone. This is the subject of the following section.*

Chromium atoms in optical lattices and previous experimental observations

Chromium atoms in optical lattices

Chromium atoms trapped in optical lattices are a very rich physical system whose workings - involving transport, contact and dipolar phenomena - make it a platform ideal for the study of quantum magnetism. **A most general description** of this system is given by the following Hamiltonian

$$\hat{H} = \hat{H}_{\mathrm{t}} + \hat{H}_{\mathrm{int}} \tag{5}$$

Where

- $\hat{H}_{\mathrm{t}} = -t \sum_{\langle i,j\rangle,m} (a^i_m)^\dagger a^j_m$ describes spin dependent tunneling in the lattice's Wannier basis. Here, a^x_y (resp. $(a^x_y)^\dagger$) is the annihilation (resp. creation) operator of a particle in site x in the spin state y.
- $\hat{H}_{\mathrm{int}} = \frac{1}{2} \sum_{\substack{k,l,m,n \\ g,h,i,j}} U^{g,h,i,j}_{k,l,m,n} (a^i_l)^\dagger (a^j_n)^\dagger a^g_m a^h_k$, describes interaction between spin particles located at sites g and h initially ending up at sites i and j. The strength of these interactions are given by the $U^{g,h,i,j}_{k,l,m,n}$ parameters. Contact and dipole dipole interactions alike are both captured by $\hat{H}_{\mathrm{int}}$

Equation 5: The Hamiltonian governing the evolution of an assembly of chromium atoms trapped in an optical lattice

In the **deep lattice limit**, **tunneling and superexchange-like processes can be neglected** [1], the $\hat{H}$ Hamiltonian then **reduces to the dipole dipole interaction** between all particles in the lattice $\hat{H}_{\mathrm{dd}}$[3]. The complexities of this remaining term are better understood when written in its operatorial form

$$\hat{H}_{\mathrm{dd}} = \sum_{i<j} \hat{H}^{ij}_{\mathrm{dd}} = \sum_{i<j} \frac{d^2}{r^3_{ij}} \left[\hat{S}^z_i \hat{S}^z_j + \frac{1}{2}\left(\hat{S}^+_i.\hat{S}^-_j + \hat{S}^-_i \hat{S}^+_j\right) - \frac{3}{4}\left(2z\hat{S}^z_i + r^-\hat{S}^+_i + r^+\hat{S}^-_i\right)\left(2z\hat{S}^z_j + r^-\hat{S}^+_j + r^+\hat{S}^-_j\right)\right] \tag{6}$$

Where

- $d^2 = \frac{\mu_0 (g_s \mu_B)^2}{4\pi}$
- r_{ij} is the distance between the (i,j) pair
- (x,y,z) are the component of the unit $\mathbf{r}_{ij}$ vector joining the two dipoles
- $r^\pm = x \pm iy$
- $\hat{S}^\pm = \hat{S}^x \pm i\hat{S}^y$

It can be seen from this equation that the dipole dipole interaction between two atoms is the combination of three distinct physical processes

1. The **elastic dipole dipole interaction** or **Ising term** which does not change the internal states (the spin projections on the quantization axis) of the atoms

$$\hat{H}^{\mathrm{el}}_{\mathrm{dd}} = \frac{d^2}{r^3}\left(1 - 3z^2\right)\hat{S}^z_1 \hat{S}^z_2 \tag{7}$$

2. The **exchange term** where the involved atoms exchange one unit of spin while conserving the total magnetization of the pair

$$\hat{H}^{\mathrm{ex}}_{\mathrm{dd}} = -\frac{d^2}{4r^3}\left(1 - 3z^2\right)\left(\hat{S}^+_1 \hat{S}^-_2 + \hat{S}^-_1 \hat{S}^+_2\right) \tag{8}$$

---

[3] And contact interactions for particles sharing the same lattice site!

3. The **relaxation terms** which lead to exchange between spin and orbital angular momenta, while concomitantly converting magnetic energy into kinetic energy.

$$\begin{aligned}\hat{H}_{\rm dd}^{\rm rel_1} &= -\frac{3d^2}{4r^3}(r^+)^2\hat{S}_1^-\hat{S}_2^- + h.c.\\ \hat{H}_{\rm dd}^{\rm rel_2} &= -\frac{3d^2}{2r^3} z r^+\left(\hat{S}_1^z\hat{S}_2^- + \hat{S}_2^z\hat{S}_1^-\right) + h.c\end{aligned} \tag{9}$$

Relaxation terms are somewhat **troublesome**, in that they are not conserving of the sample's total magnetization (see appendix D). These terms however can be controlled and even suppressed. In particular, **off-site dipolar relaxation** is inhibited by simply cranking up the external magnetic field: as a matter of fact and despite the apparent $\frac{1}{r^3}$ scaling, **dipolar relaxation is a localized interaction** whose effective range is inversely proportional to the square root of the external magnetic field [13]. In practice, given typical lattice spacings, off-site dipolar relaxation is greatly reduced for magnetic fields above 10 mG.

On-site dipolar relaxation on the other hand can be suppressed by getting rid of any *doublons*, that is, by getting rid of any pairs of particles that happen to have been loaded in the same lattice site[4], this can be done by promoting all the atoms in the most excited state $m_s = \pm 3$ and forcing all on-site dipolar relaxation events to happen before the dynamics is triggered for example.

This is exactly what was achieved by our team in previous experiments [15], wherein all of tunneling, super exchange and dipolar relaxation could be neglected, the remaining Hamiltonian terms shaping together into what is known as the RMN or secular dipolar Hamiltonian $\hat{H}_{\rm sec}$, an effective actualization of the XXZ Heisenberg model which is of particular interest to the condensed matter and AMO communities.

$$\begin{aligned}\hat{H}_{\rm sec} &= \frac{1}{2}\sum_{i,j}\frac{d^2}{r_{ij}^3}\left(1-3\frac{z^2}{r_{ij}^2}\right)\left[\hat{S}_i^z\hat{S}_j^z - \frac{1}{4}\left(\hat{S}_i^+.\hat{S}_j^- + \hat{S}_i^-\hat{S}_j^+\right)\right]\\ &= \frac{1}{2}\sum_{i,j}\frac{d^2}{r_{ij}^3}\left(1-3\cos^2(\theta_{ij})\right)\left[\hat{S}_i^z\hat{S}_j^z - \frac{1}{4}\left(\hat{S}_i^+.\hat{S}_j^- + \hat{S}_i^-\hat{S}_j^+\right)\right]\end{aligned} \tag{10}$$

Where θ_{ij} is the angle between the polarizing magnetic field and the $\mathbf{r}_{ij}$ vector.

Previous experimental observations

These endeavors have uncovered spin dynamics brought about by non local dipole dipole interactions between atoms pinned to the nodes of a 3D anisotropic lattice initially prepared in an excited coherent (or not [16]) spin state.

The dynamics in question was studied by monitoring the various spin populations of the system. This evolution can be simulated using **mean field** methods. In the case at hand, these theories predict that the evolution of any given spin in the lattice is dictated by its interaction with the mean magnetic field B_{MF} created by neighboring entities ??.

As it turns out, **this kind of mean field expansions could not explain the experimental observations** (for lattice experiments), which, on the other hand, were adequately described by more involved **GDTWA** based algorithms which account for the **inherently fluctuating**[5] **nature of the spin** vector.

---

[4] Contrary to *fermionic statistics which allow for the preparation of dense band insulators with at most one atom per lattice site* [14], bosonic statistics allow for the presence of more than one particle within the same lattice site, even in the polarized case.

[5] A feature that is intimately linked to quantum correlations as will be seen later

$$\hat{H}^{MF}_{\mathrm{sec}} = \sum_{i}^{N} \mathbf{B}_i^{MF} . \hat{\mathbf{S}}_i \tag{11}$$

Equation 11: Mean field secular Hamiltonian. In this mean field paradigm, all kinds of **spin fluctuations** $\delta\mathbf{S} = \mathbf{S} - \langle\mathbf{S}\rangle$ are neglected, as such each spin interacts with a mean magnetic field which is generated by the mean orientation of the spins $\mathbf{B}_i^{MF} = -\sum_{j\neq i} \frac{1}{2}\frac{d^2}{r_{ij}^3}\left(1-3\cos^2(\theta_{ij})\right)\left\{\langle S_j^x\rangle, \langle S_j^y\rangle, -2\langle S_j^z\rangle\right\}$[15]

For example, mean field simulations predicted a relatively pronounced and *sustained* oscillatory behavior of the spin populations (see Fig.1), a feature which was not observed neither experimentally nor in the GDTWA simulations wherein the steady state was reached relatively quickly.
These findings strongly hinted at the **instrumental role played by quantum fluctuations in our platform** and their contribution to the **thermalization** process of the system that was then studied, a system which could be considered to be mostly isolated.

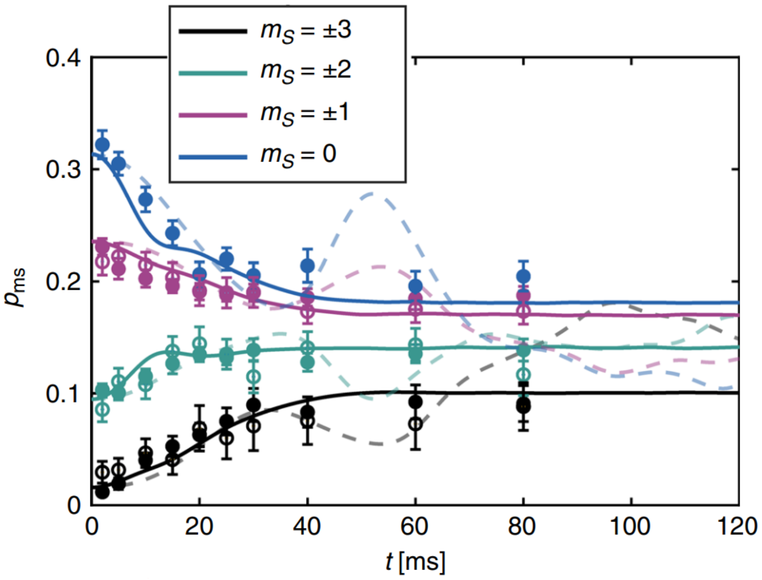

Figure 1: *Long-time evolution of state populations for* [an initial tilt angle of the spins] $\theta = \frac{\pi}{2}$*: Data points are compared with corresponding best fitting GDTWA (solid lines...) and mean field (thin dashed lines...) simulations.* Image caption from [15]

Commonly accepted thermalization scenarios however generally emphasize the role of quantum correlations and more specifically the role of entanglement rather than fluctuations per se. The question arises then as to the precise relationship between quantum fluctuations and quantum correlations. A question which we try to answer in the following section.

From quantum fluctuations to thermalization

Thermalization of pure isolated systems

In the case of isolated pure systems thermalization[6], by which we mean their evolution towards some kind of **steady state**, can be understood in the sense of the **eigenstate thermalization hypothesis** which provides a set of mathematical conditions [17] under which some

---

[6] Pure systems undergoing unitary evolution remain pure

quantum observables'[7] expectation values (notably) evolve towards their micro-canonically ascribed values, values which are seemingly independent of the **exact** initial state particulars, despite the possibly unitary character of the system's evolution [17]. Of course, the observed evolution is still conditioned by the initial state's energy, and other conserved quantities.

Microscopically, **this thermalization-like phenomenon supposedly stems from the ability of quantum systems to act as their own reservoir**: by coupling to the remainder of the system that is considered, any given subsystem can thermalize through processes reminiscent of the classical picture which involves coupling to external (particle, energy...) pools. More general considerations [19] indicate however that these self-reservoirs are not limited to the role of energy or particle sinks, their essential function is to provide *any kind* of quantum degrees of freedom for their many components *to get so entangled*- See Table 1 - *with that no information about the initial state of the subsystem remains locally observable*, put otherwise, the spreading of quantum entanglement, or equivalently the individual decoherence of the system's subsystems, moves information about so that it becomes locally inaccessible, leading, in time, to thermalization, in the sense described above.

Separable pure states	Separable mixed states[8]
$\lvert\Psi\rangle = \lvert\psi^1\rangle \otimes \lvert\psi^2\rangle ... \otimes \lvert\psi^N\rangle$	$\rho = \sum_i^{N'} w_i \left[\otimes_j^N \rho_j^i\right]$

Table 1: Quantum states are either pure or mixed. A quantum state is either factorable or non-factorable. Both pure and mixed states can be factorable (or separable). We provide above the mathematical expression for separable states of both natures. N is the number of subsystems which are considered. N' is an arbitrary integer. $|\psi^j\rangle$ (resp. ρ_j^i) is a pure state (resp. a mixed state) describing the j^{th} subsystem. The w_i are positively valued probabilities. **Entangled states are all states which are not separable**, this definition being agreed upon for distinguishable particles at least[9]. Subsystems pertaining to a system that is in a entangled state cannot be described independently of other subsystems, as such these subsystems can be said to be strongly correlated.

As is explained above, the thermalization of isolated systems seems to stem from entanglement which refers to a **specific kind** [10] of **quantum correlations**. In the following sections we will try to draw a **clearer picture between quantum fluctuations and quantum correlations**, but before that a **brief preamble on classical and classical quantum states.**

---

[7] For a more detailed account on the systems and observables to which ETH applies, please refer to [18]. Integrable systems for example, that is those with too many conserved quantities and similarly those with strong disorder in which many body localization is predicted to happen generally fail to thermalize.

[9] $\sum^N w_i = 1$ otherwise this definition would be trivially true for all states as the definition of the tensor product

[9] When it comes to **indistinguishable particles**, one might argue that the traditional separability criterion does not adequately characterize entanglement. And it is true enough that the entangled character of some bosonic symmetrized or fermionic antisymmetrized states is but an artifact of the "surplus structure" that comes with the symmetrization process. For example the state $|\uparrow\rangle_1 |\downarrow\rangle_2$ which describes two non entangled distinguishable particles becomes when transposed to, say the bosonic case, entangled after symmetrization: $\frac{|\uparrow\rangle_1|\downarrow\rangle_2+|\downarrow\rangle_1|\uparrow\rangle_2}{\sqrt{2}}$. This *surplus structure*, $|\downarrow\rangle_1 |\uparrow\rangle_2$, is specific to the Hilbert space formalism [20]. In [21] such states whose non-factorizability is induced by the (anti-)symmetrization process are termed *tangled states*. The authors of [22] call into question the entangled character of such states as they show that they *never give rise to correlations that violate Bell's inequalities and that they are fully compatible with local hidden-variable models* for example [23]. Other definitions of entanglement proposed for example in [24] also reject the entangled character of tangled states.

[10] Non separability

Classical quantum states

Imagine that Alice (resp. Bob) can generate **orthogonal** states $|a\rangle$ (resp. $|b\rangle$) with probability p_a (resp. p_b). The global state shared between Alice and Bob reads

$$\rho_{AB}^{C} = \sum_a \sum_b p_a p_b |a\rangle \langle a| \otimes |b\rangle \langle b| \tag{12}$$

Where the C superscript stands for **classical**. The ρ_{AB}^{C} state is said to be *classical* because it remains undisturbed under the action of local measurements of the form $\sum_a |a\rangle \langle a|$ or $\sum_b |b\rangle \langle b|$.

In the same manner we can devise states that are invariant under measurements solely affecting Alice's subspace. The scenario corresponding to these states is the following: imagine that Alice produces a certain state $|a\rangle$ with probability p_a (we assume that the various states produced by Alice are orthogonal) which she transmits to Bob via a **noisy communication** channel. In general for each state $|a\rangle$ generated by Alice, Bob will receive a state of the form σ_a^B where σ_a^B is an $|a\rangle$ dependent mixed state. The final state shared by Alice and bob can be written

$$\rho_{AB}^{CQ} = \sum_a p_a |a\rangle \langle a| \otimes \sigma_a^B \tag{13}$$

Where the CQ superscript stands for **classical quantum**. Notice that all classical states are classical quantum states and that all classical quantum states are separable. On the other hand not all separable states are classical quantum states [25], the difference boiling down to the fact that for CQ states the $|a\rangle$ states should be orthogonal, which is not required for separable states.

$$\text{Classical states} \subset \text{Classical quantum states} \subset \text{Separable states} \tag{14}$$

From quantum fluctuations of observables to quantum correlations: the quantum covariance

Quantum states are most generally described by statistical ensembles of the form $\rho = \sum_i p_i |\psi_i\rangle\langle\psi_i|$, where p_i is the probability of having prepared state $|\psi_i\rangle$. This preparation uncertainty induces **incoherent** fluctuations. In general however, measurements of a quantum observable $\hat{O}$ will still display a certain amount of **quantum** or coherent fluctuations even when the system is prepared in a pure state $|\psi_i\rangle$ unless $|\psi_i\rangle$ is an eingenstate of $\hat{O}$. When **thermal equilibrium is reached**, the amount of **quantum** fluctuations[11] among all other incoherent fluctuations can be quantified by the so called **quantum variance**. This quantum variance can be defined mathematically in many ways one of which is given in [26]

---

[11] The zero point motion, which in the case of ^{4}He prevents it from solidifying at atmospheric pressure even at very low temperature, is a striking example of such quantum fluctuations

$$\Delta^2_Q \hat{O} = \Delta^2 \hat{O} - k_B T \chi_{\hat{O}} \tag{15}$$

where

- $\Delta^2_Q \hat{O}$ is the quantum variance of observable $\hat{O}$
- $\Delta^2 \hat{O}$ is the total variance of observable $\hat{O}$
- T is the temperature of the system
- $\chi_{\hat{O}}$ is the static susceptibility of $\langle \hat{O} \rangle$ with respect to a small perturbative field coupling to observable $\hat{O}$

Equation 15: The quantum variance quantifies the amount of coherent (or quantum) fluctuations of the $\hat{O}$ observable. The proportionality between the temperature and the variance of the $\hat{O}$ observable $\Delta^2 \hat{O}$ cannot be extended to quantum systems for which measurements results will in general display a remnant variability event at zero temperature. As put in [26], *the quantum variance encapsulates the idea that two equivalent ways of looking at fluctuations in classical statistical mechanics (namely fluctuations at equilibrium, and linear response to a perturbation) give different results when generalized to quantum statistical mechanics, in violation of the classical fluctuation dissipation theorem valid for classical systems at equilibrium.*

For **pure states** the quantum variance coincides with the total variance as there are no incoherent fluctuations in this case.
In statistics, correlations are derived from variances through the concept of covariance. If X and Y are two random variables, we have

$$2\mathrm{cov}\,(X, Y) = \mathrm{Var}\,(X+Y) - \mathrm{Var}\,(X) - \mathrm{Var}\,(Y)\,. \tag{16}$$

In the same fashion, the quantum variance concept calls for a most intuitive definition of **quantum correlations** as given by the **quantum covariance**:

$$\begin{aligned} 2\mathrm{cov}_Q\left(\hat{O}_A, \hat{O}_B\right) &= \Delta^2_Q\left(\hat{O}_A + \hat{O}_B\right) - \Delta^2_Q\left(\hat{O}_A\right) - \Delta^2_Q\left(\hat{O}_B\right) \\ &= 2\left[\mathrm{cov}\left(\hat{O}_A, \hat{O}_B\right) - k_B T \chi_{\hat{O}_A, \hat{O}_B}\right] \end{aligned} \tag{17}$$

Where

- A and B form a bipartition of the whole system S that is considered.
- $\chi_{\hat{O}_A, \hat{O}_B}$ is the cross-susceptibility of the system

Equation 17: The quantum covariance quantifies the **correlations between the coherent fluctuations** of observables $\hat{O}_A$ and $\hat{O}_B$ at thermal equilibrium [26]. Notice that much like the quantum variance, and contrary to the quantum discord which will be presented shortly, the quantum covariance is also an observable dependent quantity.

Strictly speaking the quantum covariance quantifies the correlations between the coherent fluctuations of observables, however it **also provides some degree of information as to the nature of the state** that is studied and as can be expected of such quantum correlations measures, **a non zero quantum covariance excludes classicality** [26]:

$$\rho_{AB}^{CQ} \implies \mathrm{cov}_Q\left(\hat{O}_A, \hat{O}_B\right) = 0 \ \forall (\hat{O}_A, \hat{O}_B) \tag{18}$$

Equation 18: A non zero quantum covariance proves that the state is not classical quantum. This is also the kind of state that is excluded by a non zero quantum discord as will be seen shortly.

Naturally, **the bigger the quantum covariance the further the ρ_{AB} state is from classicality**, and it can be shown that for thermal equilibrium states the quantum covariance cannot exceed a certain threshold without the presence of entanglement [26].

$$\rho \text{ is separable} \implies \mathrm{cov}_Q\left(\hat{O}_A, \hat{O}_B\right) \leq \frac{1}{8}(o_{max} - o_{min})^2 \tag{19}$$

where the spectra of $\hat{O}_A$ and $\hat{O}_B$ are bounded by o_{max} and o_{min}

Equation 19: To prove entanglement the cross-susceptibility of the system must be measured. Note however that $\hat{O}_A$ and $\hat{O}_B$ do commute as they are defined on two disjoint subsystems.

As it turns out, this quite natural definition of quantum correlations -the quantum covariance- is, a priori, independent of the generic **information theoretic** term associated to all those kinds of **correlations which are neither classical nor captured by entanglement**. These information theoretic quantum correlations were characterized by Zurek and Ollivier in their 2001 paper [27] through the quantum **discord quantity**.

Another definition of quantum correlations: the information theory point of view

The term quantum discord expresses the fact that two classically identical definitions of the **mutual information** (denoted in the following I and J) may differ when applied to quantum systems, this observation is reminiscent of the definition of quantum variance which denotes the invalidity of a classically valid thermodynamic identity (the classical fluctuation dissipation theorem) when generalized to the quantum world. The first definition of the mutual information between two random variables A and B reads:

$$I_C(A,B) = H(A) + H(B) - H(A,B) \tag{20}$$

Where :

- The C index indicates the classicality of the definition
- A and B are two random variables
- *H(A)* is the Shannon entropy : $H = -\sum_{a \in \mathscr{A}} p_a \log(p_a)$ with p_a the probability of getting outcome a amongst all possible outcomes forming space $\mathscr{A}$
- *H(A,B)* is the joint entropy of the pair (A,B) : $H = -\sum_{(a,b) \in (\mathscr{A},\mathscr{B})} p_{a,b} \log(p_{a,b})$ with $p_{a,b}$ the joint probability of getting outcome a, b . It accounts for the total *ignorance* on the pair (A,B)

Using the conditional entropy $H(A \mid B) = H(A,B) - H(B)$, one can also write:

$$J_C(A,B) = H(A) - H(A \mid B) = I_C(A,B) \tag{21}$$

The two forms of the mutual information coincide classically. For a bipartite system (A,B), one can therefore think of classical correlations (i.e. the mutual information) in two *equivalent* ways, either as the difference between the sum of local ignorances and the total

ignorance of the system, or the amount of information one can glean on one subsystem after measuring the other.
The first definition of the mutual information (20) can be extended to the quantum world by use of the von Neumann entropy

$$I_Q(A,B) = S(A) + S(B) - S(A,B) \tag{22}$$

Where

- The Q index indicates the quantum character of the definition
- $S(A) = -\mathrm{Tr}(\rho_A \log \rho_A)$ is the von Neumann entropy and ρ_A the reduced density matrix of subsystem A tracing out on B

The generalization of definition 21 on the other hand poses certain issues as *in quantum information theory, measurements can disturb quantum systems* [28], the $S(A\,|\,B)$ statement in particular is ambiguous until the *to be measured states of* B [27] are selected. In other words, adapting the definition of Eq. 21 to the quantum world first requires the choice of a set of local projective operators $\Pi_B^j = |j_B\rangle\langle j_B|$ corresponding to the measurement to be done. Upon measurement, the state of the system is given by:

$$\rho_{AB|j} = \frac{1}{p_j}\left(I_A \otimes \Pi_B^j\right)\rho_{AB}\left(I_A \otimes \Pi_B^j\right) \tag{23}$$

Where

- I_A is the identity matrix of subsystem A
- p_j is the probability of obtaining outcome j

The entropy of the whole system conditional to the measurement of B is then given by

$$S\left(AB\middle|\left\{\Pi_B^j\right\}\right) = \sum_j p_j S\left(\rho_{A|j}\right) \tag{24}$$

Where

- $\rho_{A|j} = \mathrm{Tr}_B(\rho_{AB|j})$ is the reduced density matrix of subsystem A after measurement

All in all, the second definition of the mutual information becomes

$$J_Q(A,B) = S(A) - S\left(AB\middle|\left\{\Pi_B^j\right\}\right) \tag{25}$$

In general both definitions of the *quantum mutual information* give out different results [27], a mismatch commonly known as the quantum discord. More specifically $J_Q(A,B) \le I_Q(A,B)$ for all measurements performed on B unless the state ρ_{AB} is **classical quantum** ($\rho_{AB} = \rho_{AB}^{CQ} = \sum_a p_a |a\rangle\langle a| \otimes \sigma_{i\,a}^{\,B}$). In this case choosing the appropriate measurement to perform on B gives maximum information on A so that $J_Q(A,B)$ reaches the upper bound $I_Q(A,B)$.
The minimal discrepancy that is otherwise found optimizing over the Π_B^j measurements is called quantum discord:

$$D(A,B) = I_Q(A,B) - \max_{\Pi_B^j} J_Q(A,B) \tag{26}$$

Equation 26: The computation of the quantum discord usually involves an optimization over the set of measurement to be performed, which is unsuitable to generic experimental endeavors.

Comparison between the quantum covariance and the quantum discord

- The **quantum covariance has not been generalized to out of equilibrium frameworks** yet: to measure the quantum covariance, one should define a temperature and measure susceptibilities which is not easily done for non stationary states. In this sense the quantum discord is a more general quantity.

- The **quantum covariance measures the degree of correlations between the coherent fluctuations of observables**. Ultimately the quantum **discord** - because of the optimization process involved in its definition- is an **observable independent quantity**.

- Classicality of a given state ρ_{AB} can be ruled out by proving that the quantum covariance of any two observables $\hat{O}_A$ and $\hat{O}_B$ is non zero. **It is harder to exclude classicality using quantum discord** as almost all measurements are discordant, even for a classical quantum state unless an optimal measurement is picked.

These two types of quantum correlations are not easily related to each other [26]. As for **entanglement** it can be related to both: on the one hand entangled states are a subset of the discordant set of states, which means that all entangled states are discordant. On the other hand, much like discord the quantum covariance can be used to exclude classicality and strong enough quantum covariances are also a proof of entanglement (see Eq. 19). Moreover and if nothing else this second point of view has the advantage to bridge in a clearer way the gap between quantum fluctuations and quantum correlations, comforting in some sense the theory according to which the thermalization observed in our system may be due, not simply to spin fluctuations neglected by the mean field treatment, but indeed to the development of quantum correlations within this system.

It would be of great experimental interest to confront these ideas to actual experimentation by monitoring and comparing the development of all these quantities (discord, spin quantum covariances, and entanglement) in relation to the thermalization of our system and go beyond theoretical speculations. This however cannot be done in our experiment because of several technical and physical limitations which we now discuss.

Technical constraints and experimental route

Technical constraints and entanglement

The development of entanglement is generally tracked using **entanglement witnesses**. These witnesses always involve the measurement of two **non commuting observables**. For spin particles, these observables are often taken to be orthogonal components of the collective spin. The class of entanglement witnesses that is adapted to our system requires that the collective spin be **squeezed** (see Fig. 2), or put otherwise that the variance of one of the spin components orthogonal to the collective spin be smaller than certain particular limits. **Witnesses based on spin squeezing are in general simpler for spin half systems** as compared to higher spin ensembles[12]. Moreover, recent numerical simulations[13] [30] indicate that the amount of squeezing generated in systems like ours might decrease as the number of interacting spins grows, which, given typical experimental uncertainties, would make it **hard purporting to any clear cut spin squeezing based proof of entanglement build-up**.

---

[12] It is of note in particular that squeezing is tantamount to entanglement in spin half systems, this is not true for higher spins $S > \frac{1}{2}$ for which, to put it shortly, only a *certain minimal amount of squeezing* is a proof of entanglement [29]

[13] Focused on 1D systems

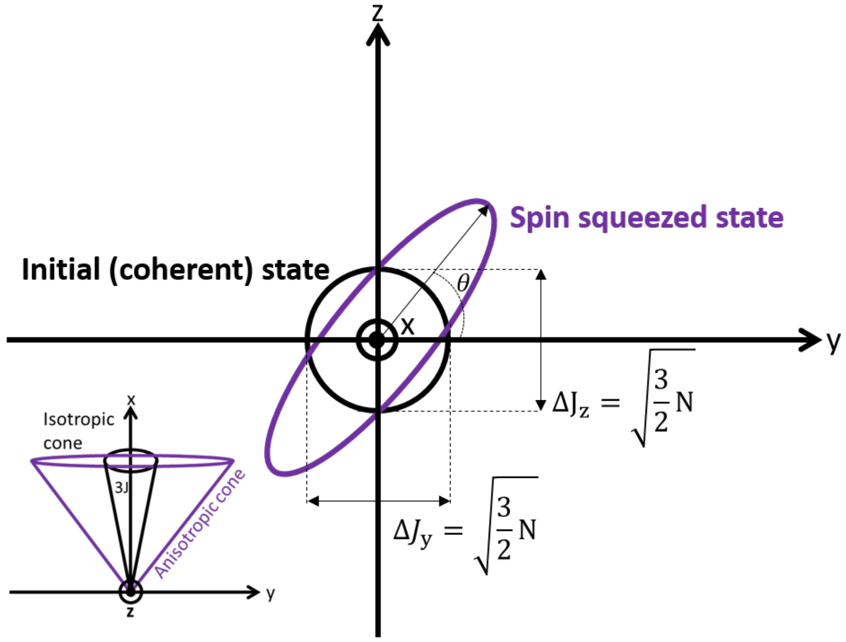

FIGURE 2: Schematic representation of both coherent and spin squeezed states. Coherent states [31] are states obtained after rotation of the $|J,-J\rangle_z$ ($|3,-3\rangle_z$) state, for many body samples such as ours they correspond to states of uncorrelated spins prepared in a certain identical stretched state. The initial state of the experiments reported on in this manuscript is such a state, it is obtained using a $\frac{\pi}{2}$ Rabi pulse of the $|3,-3\rangle_z$ state. The spin vector of such a state can be seen as an isotropic cone. When adequate correlations are established between the individual spins of the system, *it is possible to partly cancel out spin fluctuations in one direction at the expense of those enhanced in the other direction. This is the basic idea of spin squeezing.* [32]. The spin vector corresponding to these states with reduced variance along a certain direction ($\theta + \frac{\pi}{2}$ in the case at hand) can be seen as an anisotropic cone (if the state is still polarized, see [33] for a partial bestiary of spin squeezed states). A squeezed state does not need to saturate the Heisenberg uncertainty principle, for a spin state to be squeezed, it is only needed that the variance of the collective spin along at least one direction orthogonal to the mean collective spin be smaller than the standard quantum limit, that is the variance of the initial coherent spin state $\Delta^2 J_z$ (In our case, $||\langle\vec{J}\rangle|| = 3N$ and $\Delta^2 J_z = \frac{3}{2}N$. Squeezing generally requires nonlinear interactions [32]. Being quadratic, the Ising interaction between spins ($S^i_z.S^j_z$) can lead to the squeezing of the collective spin state. This supposition was numerically checked for small number (N=10) of spin 1 particles in a ring geometry [34].

In any cases these witnesses rely on the measurement of spin components lying in the plane orthogonal to the collective spin average direction. However, **such measurements were made practically impossible - in our experiment - by the so called *dephasing* phenomenon** as shown in Fig. 4 and Fig. 3

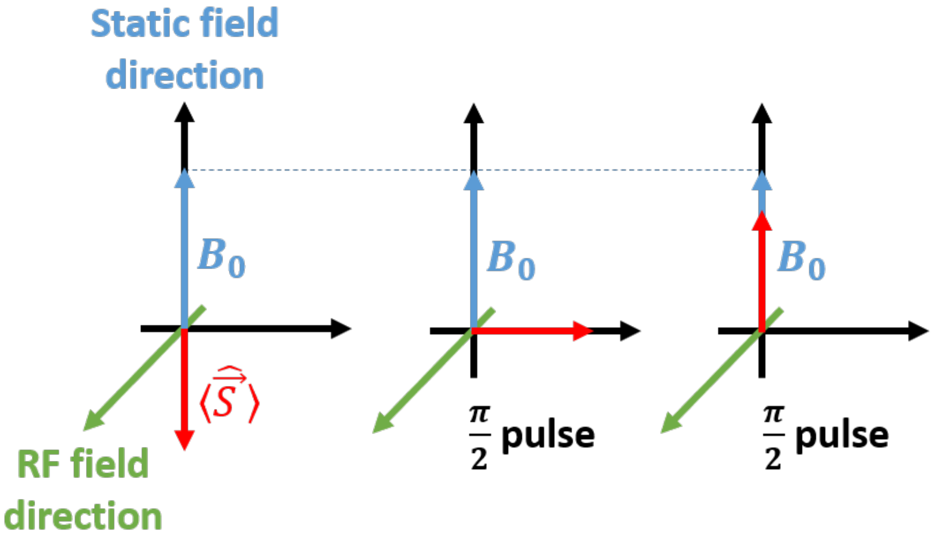

FIGURE 3: In a perfect world: the amplitude of the static quantization field is constant, in consequence the Larmor frequency and frequency of the the RF field are time independent. This means that **in the frame rotating at ω_{RF}, the spins' rotation is halted: applying two consecutive $\frac{\pi}{2}$ pulses is equivalent to the application of a single π pulse**.

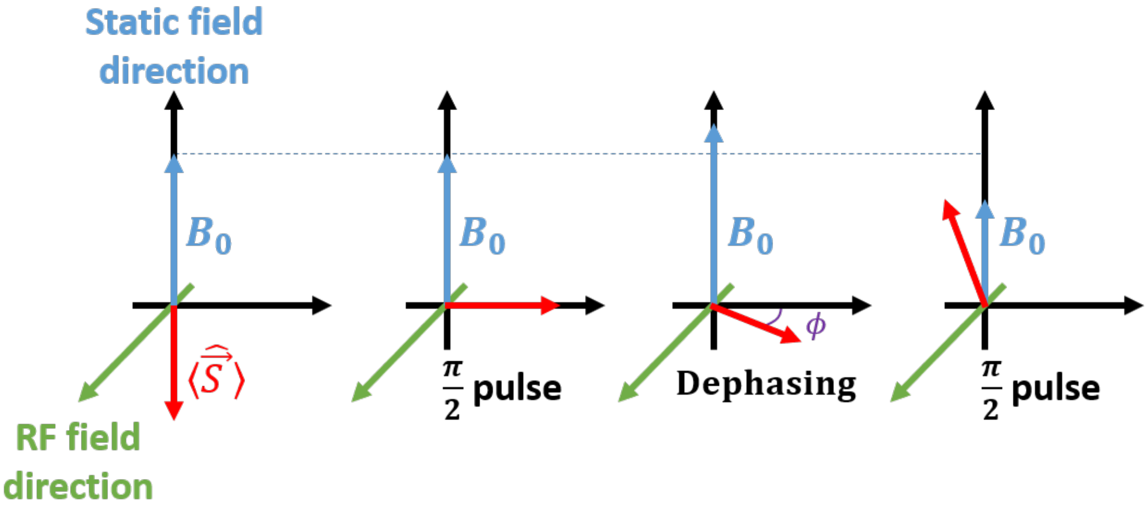

FIGURE 4: *Mais dans la vie en vrai* as put by Anne Sylvestre, the amplitude of the static field changes through time, in consequence **the spins do not remain still in the frame rotating at the RF frequency**. This uncontrolled rotation of the spins in between two consecutive Rabi pulses is what we call **dephasing**.

Dephasing prevents us from ever measuring the transverse components of the collective spin in a precise and reproducible manner. At most, one can measure a random component $\hat{S}_\phi = \cos(\phi)\,\hat{S}_x + \sin(\phi)\,\hat{S}_y$ of the spin, where ϕ, the dephasing angle, varies from shot to shot, in accordance with the erratic fluctuations of the external magnetic field. Typically, the dephasing is complete (i.e. the standard deviation of the dephasing angle $\Delta\phi = 2\pi$) in a few (≈ 10) milliseconds. This means that the **reproducible measurement of any transverse component of the spin would require one quite exquisite regulation of the external magnetic field on the order of the Hz**.

Technical constraints and other quantum correlations

As explained above the quantumness of correlations can be measured in at least two ways. The first one -**quantum discord**- involves quantities which are **not suited** to our experimental platform (the density matrix of the system) or any generic experimental endeavors for that matter, moreover **the optimization processes that it requires cannot be realistically carried out** for systems comprised of thousands of particles.
Quantum covariance on the other hand is only defined for systems which have reached thermal equilibrium, it is therefore **not suited for tracking the growth of correlations** as the dipolar dynamics unfurl, moreover it would be challenging to measure quantum covariances using our platform. One possible way of doing so, for perhaps spin 1 particles at most, is the following [35]:
Consider first that the system reaches a state of thermal equilibrium[14].
Consider the global spin populations operators $\hat{A}_m$ with $m \in [|-S, S|]$. To measure the quantum part of these observables' fluctuations we need to evaluate the susceptibilities (see Eq. 15):

$$\chi_{m,m'} = \frac{\partial \langle \hat{A}_m \rangle}{\partial \lambda_{m'}} \tag{27}$$

which quantifies the change of $\hat{A}_m$'s expectation value when a perturbation of the form $-\lambda_{m'}\hat{A}_{m'}$ is applied to the system.
Suppose that we can apply perturbations of the form $-\sum_m \lambda_m \hat{A}_m = -\mu_\alpha \sum_m m^\alpha \hat{A}_m$ where α =1 corresponds to the application of a magnetic field along the **z** axis (**first order Zeeman field**), $\alpha = 2$ corresponds to the application of a **quadratic Zeeman field**, $\alpha = 3$ corresponds to a **third order Zeeman field** and so on... Then we can measure the $\chi_{m\alpha}$ susceptibilities

$$\tilde{\chi}_{m\alpha} = \frac{\partial \langle \hat{A}_m \rangle}{\partial \mu_\alpha} \tag{28}$$

On the other hand, in the linear response regime we have

$$\begin{aligned} \langle \hat{A}_m \rangle &= \langle \hat{A}_m \rangle (0) + \sum_{m'} \chi_{m,m'} \lambda_{m'} \\ &= \langle \hat{A}_m \rangle (0) + \sum_{\alpha} \mu_\alpha \left[\sum_{m'} \chi_{m,m'} m'^\alpha \right] \end{aligned} \tag{29}$$

which implies that

$$\tilde{\chi}_{m\alpha} = \sum_{m'} \chi_{mm'} m'^\alpha \tag{30}$$

This equation can also be written

$$\tilde{\chi} = \chi M \tag{31}$$

Where

---

[14] This notion being, to me, a bit unclear as far as our experiment's system is concerned : it is not obvious that our system can ever be fully described by a thermal density matrix -even at long times when the systems reaches a steady state. This thermal description may make more sense for individual parts of the system which are expected to assume a thermal like behavior induced by entanglement

- $M = M_{m'\alpha} = m'^{\alpha}$ is a matrix with dimensions $2S+1 \times d$ where d is the number of generated Zeeman fields of order α (see below).
- χ is the matrix whose elements are given by the $\chi_{m,m'}$ susceptibilities
- $\tilde{\chi}$ is the matrix whose elements are given by the $\tilde{\chi}_{m,\alpha}$ susceptibilities

Inverting this relation shows that precise measurements of the $\tilde{\chi}_{m\alpha}$ susceptibilities can allow us to find the $\chi_{m,m'}$ population susceptibilities

$$\chi = \tilde{\chi} M^{-1} \tag{32}$$

Such an experiment is impossible for high spin particles, indeed accessing the full χ matrix requires the ability to generate and control Zeeman filed up to order 2S+1[15]... Note however that while we cannot in general, for higher spin particles, isolate every susceptibility $\chi_{m,m'}$ we can (through Eq. 29) **get to linear combinations of these susceptibilities** and therefore to **the quantum variance and covariance of some linear combinations of the populations** granted the system has reached thermal equilibrium.

Experimental route

Given the technical and physical particulars that we have discussed above our team has decided to focus on the growth, not of entanglement which is technically out of reach, nor quantum correlations which are unadapted to our experimental set-up, but simply **on the development of spin correlations in general** (see Fig. 5) in their relationship to thermalization. Investigating the growth of these correlations while retaining the many specificities (high number of atoms, and impossibility of local measurements) of our system has required the development of **new experimental methods**.

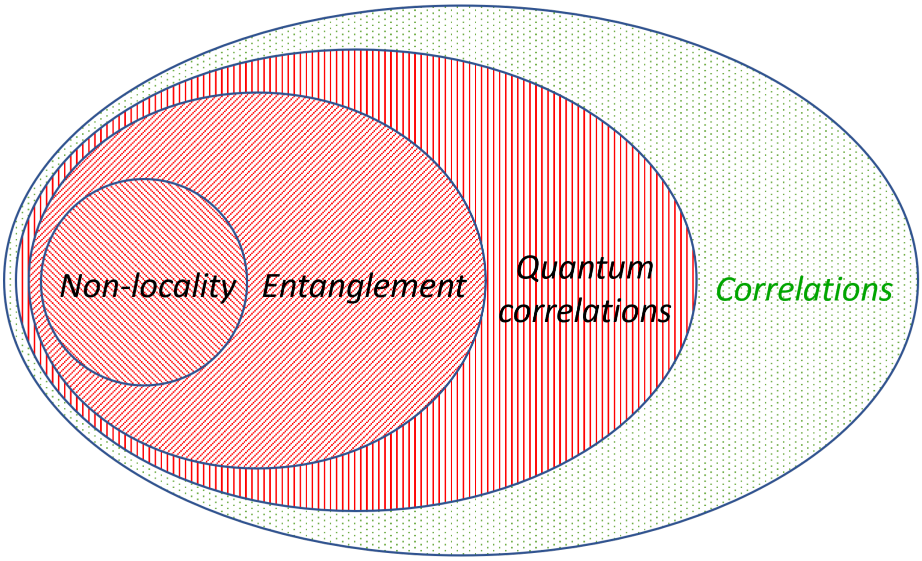

FIGURE 5: Correlations of varying *strengths* can emerge in any given system. The image above depicts the hierarchy between different *types* of correlations: a system exhibiting quantum correlations is correlated, for it to be entangled it must be quantum correlated (not a classical quantum state), and finally if it is to escape the grasp of local hidden variable theories [36], it must be entangled. Note that non local states can in turn be further categorized into EPR or Bell like states. In the chromium experiment we focus on global spin correlations (green).

---

[15] Put otherwise: a big enough perturbation variety should be applied to derive all of the individual susceptibilities

In this manuscript of mine I will discuss two of these methods, the first one is based on the measurement of the total **magnetization fluctuations** Chap. 3, while the second relies on the **sample's bipartition** Chap. 4.
The **principle** subtending both these methods being the same: to *infer the system's **atomic correlation** properties from readily accessible **global** observable statistics.*

Dissertation organization

In the **first chapter** of this manuscript we present **the building blocks of the experiments that were carried out** in the course of my PhD. The main experimental set up is presented and the condensation process is briefly described. The basic working principles of lattice physics as well as the actual geometry of the experiment's optical lattices are subsequently depicted, we focus in particular on the 1064 nm laser system which I have built. We then report on the triggering of the quench dynamics using resonant RF pulses. Finally, we lay out the principles of the two imaging systems used to collect experimental data, with a certain emphasis on the fluorescence one which I have also built.

The **second chapter** is quite technical. It focuses on data treatment: the observables with which we were concerned in the course of this PhD (expectation values, variances and covariances of spin populations) are sensitive to the many physical phenomena intervening either in the initialization, interaction or measurement stages of the experiment. These physical phenomena which are of inherently stochastic nature are such that these various statistical **moments** are not directly accessible. **Careful consideration of these noises' chronological hierarchy will let us extract the relevant correlation properties from our data**.

In **chapter three**, we present the first experiment which we have carried out in the course of this PhD. In this experiment, we monitor the quench dynamics of $N \sim 10000$ chromium atom pinned to an anisotropic 3D lattice. We focus on the time evolution of the statistical moments of the spin populations which we link to various global correlators gauging the development of correlations in our system. **We show that spin correlations indeed grow in our system as it thermalizes**.

The **fourth and last chapter** is dedicated to the experimental realization of a **new kind of bipartite measurement**. We show that this type of measurement reveals correlations that are inaccessible to the type of measurements performed in **chapter three** and **give an experimental proof of the development of these so called bipartite correlations in our system as it thermalizes**.

The **first appendix** focuses on the architecture of the 851-425 nm laser chain I have built during my PhD. The 425 nm laser is used for cooling and imaging purposes. The second one deals with the alignment of the bichromatic lattice. The **third addendum** reports on data treatment through the partial covariance technique. Finally, in **the fourth and last appendix**, I present the **exact** numerical simulation of the dissipative dynamics of a rectangular plaquette containing 8 singlons and 4 doublons.

1 The experiment

The intense atom glows. A moment, then is quenched in a most cold repose
– Percy Bysshe Shelley (Adonais)

In this first chapter, we briefly depict the steps leading to the production of the chromium Bose-Einstein condensate (BEC), in doing so we will be presenting the experimental set-up, focusing on the upgrades I have contributed. We will then describe other building blocks of the experiments, in particular, optical lattices, their basic working principles and geometries. A short section is then dedicated to the use of radio frequency fields in the triggering of the spin dynamics. Finally, we report on the imaging procedures used in the experiment. More detailed accounts of some aspects of the experimental setup can be found in [37, 38, 39, 40]

1.1 Bose-Einstein condensation

In this section we describe the main steps and apparatus used in the production of the chromium BEC.

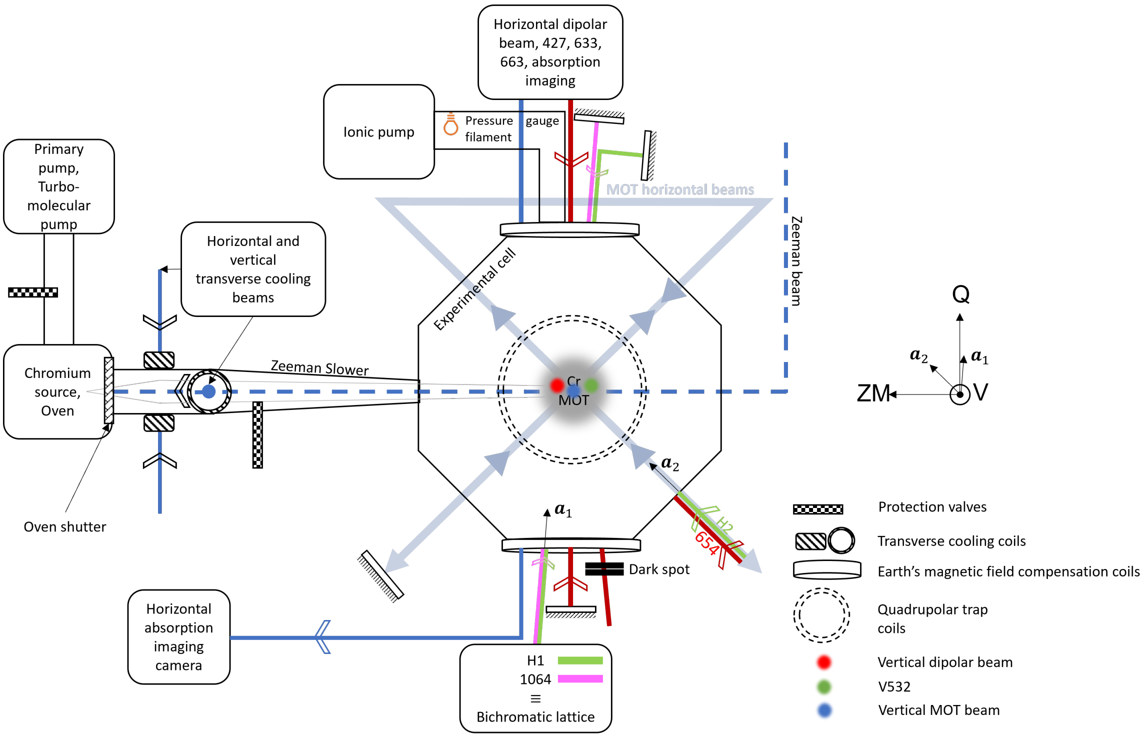

FIGURE 1.1: Schematic representation of the experimental set up. The H1, H2, V532 are the beams which together form the main optical lattice of the experiment. This basic architecture can be supplemented with an additional 1D lattice using the 1064 nm beam. The end result is a bichromatic lattice which allows for bipartite measurements, see Chap 4.

Cold atoms experiments require ultra-high vacuum conditions. These conditions are met in our set-up using three different pumps. The **primary pump** (backing pressure of 30 mBar) sets the stage for the **turbo-molecular**[1] one which governs the pressure within the oven[2]. The pressure within the oven enclosure varies between 2.10^{-10} mBar and 10^{-9} mBar depending on the oven's temperature. As for the **ionic pump** [3], it is dedicated to the experimental cell volume whose pressure is as low as 7.10^{-11} mBar, this pressure is of great importance as it dictates the collisional rate of the chromium atoms with the molecules of the background gas and ultimately the condensate's lifetime (12 s).

The effusive atomic beam that reaches this cell is generated by heating a 20 g, 99.7% pure chromium bar[4] up to $1400°C$. This temperature speaks of the compromise made between the lifetime of the chromium source and the need for an atomic influx strong enough to reach the quantum degeneracy regime [40].

The **transverse cooling** set-up greatly improves this influx by narrowing the transverse velocity distributions of the beam which in turn increases the number of atoms interacting with the Zeeman slower - factor 5 at least on the number of atoms captured by the magneto optical trap (MOT). The transverse cooling beams are σ^+ polarized and are red-detuned (by approximately Γ, see Fig. 1.2) with respect to the $|^7S_3, m_S = 3\rangle \rightarrow |^7P_4, m_S = 4\rangle$ cycling transition. This detuning is controlled (independent of other beams at 425 nm) by two pairs of quantization coils set in the Helmholtz configuration. These pairs of coils are set respectively along the **V** and **Q** directions, see Fig. 1.1.

The **Zeeman slower** (ZS) is a critical component of the experiment as it allows for a most effective deceleration of the atoms emitted by the oven: the maximum capture velocity of the ZS is 550 m.s^{-1}, the final velocity of the atoms is 40 m.s^{-1} [40]. This is achieved by immersing said atoms in a carefully engineered magnetic field, which, by inducing an inhomogeneous Zeeman effect along the traveling direction effectively compensates for the frequency detuning that is captured by the Doppler effect. The atoms are then readily caught in the **magneto-optical trap** (MOT) laid in the experimental chamber. In this kind of trap, spatially varying Zeeman shifts induced by magnetic gradients make for position dependent resonance conditions and ultimately for position dependent radiative forces which constantly push the atoms back to the center of the trap. These radiative forces are generated by 3 pairs of counter-propagating σ polarized 425 nm beams whose carefully chosen (red-)detuning also ensures additional cooling effects ($T \simeq 100 \pm 20\ \mu$K). The gradients on the other hand are those of a **quadrupolar magnetic field** which, in practice, is created by a pair of coils set in a anti-Helmholtz configuration.

The chromium MOT ($N = 5 \times 10^6$ [37]) does not contain as many atoms as alkali MOTs ($N \simeq 10^9$), this is mainly due to light assisted collisions whose rate is two to three orders of magnitude bigger for chromium than most alkali atoms [37]. It is of note however that chromium MOTs are also smaller which ensures high enough initial spatial densities for the atoms' successful Bose **condensation**.

---

[1] Spiral model SH-100, Varian. pumping capacity $110 L.s^{-1}$[39]

[2] HT12 model, ADDON company [39]

[3] VacIon Plus 75, Varian, pumping capacity 75 L.s^1 [39]

[4] Product of the GoodFellow Company[39]

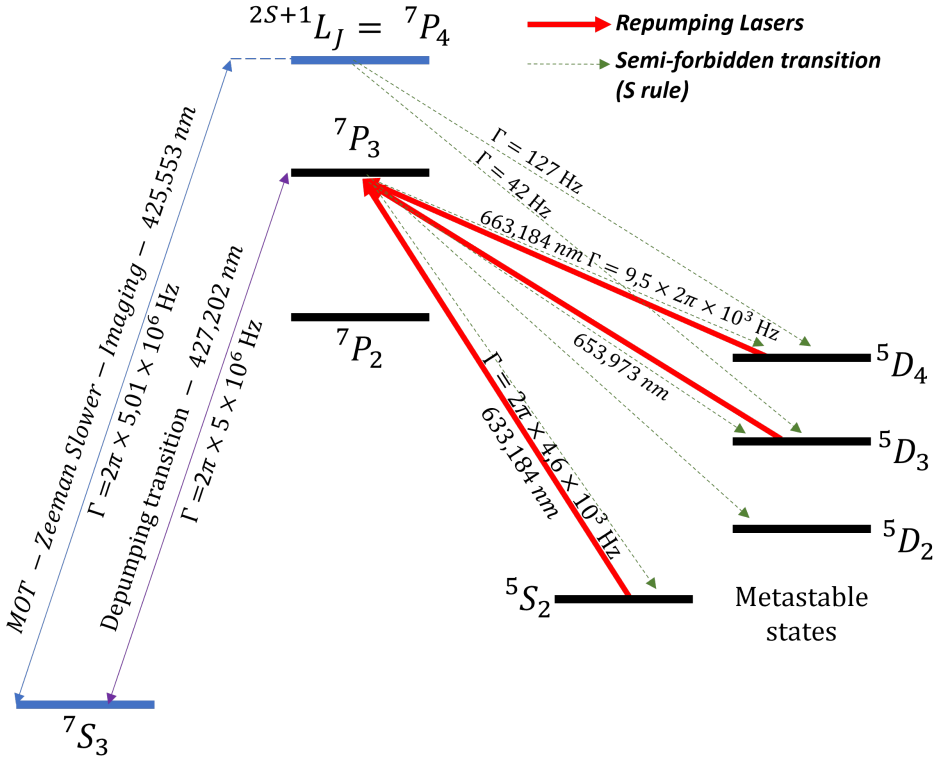

FIGURE 1.2: Transitions of interest for the Bose-Einstein condensation of Chromium. Γ is the decay rate from excited states to lower states relevant to the transition that is considered. The transition rates we show were taken from the NIST database except for the 127 and 42 Hz transition rates which were found in [41]

As mentioned in this manuscript's introduction, BECs are characterized by high phase space densities. Such densities are generally achieved through **forced evaporation** techniques which entail drastic atomic losses. For some atoms such as sodium and rubidium, it is possible to perform said evaporation directly in a magnetic trap, in the case of chromium however, **dipolar relaxation** rates prevent such simple approaches, indeed not only do these collisions heat up the atomic gas by converting magnetic energy into kinetic energy, they also induce a certain degree of spin depolarization. In particular atoms which end up with negative total spin projections $m_j \leq 0$ can escape the trap[5]. Alternatively, the evaporation can be carried out in an **optical dipolar trap**[6] (DT) which, being far detuned with respect to the trapping transition, is mostly insensitive to the atoms' spin degrees of freedom.

Loading this trap is a crucial step in the Bose-Einstein condensation process of chromium, it is however difficult to directly load atoms into such optical traps because of their relative shallowness (Trapping depth≤1 mK). In fact, it cannot be done by superimposing MOT and DT either, as is customary [42]. That is because, as mentioned before, light-assisted inelastic collisions constitute a great limitation to the number of atoms in the MOT, more so in the dipole trap wherein the atomic density is higher. Therefore even if MOT to DT atom transfer rates were excellent, it would still be insufficient to reach the quantum degeneracy regime [37]. Getting rid of light assisted collisions requires transferring atoms to internal states insensitive to the MOT beams. As it turns out both excited states $|{}^7P_4\rangle$ and $|{}^7P_3\rangle$

---

[5] The magnetic potential energy can be written $E_{p,mag} \simeq g\mu_B m_j B$, atoms with negative spin quantum number are driven away from the center of the quadrupolar trap where the magnetic field is at its lowest. They are called *high field seekers*.

[6] 1075 nm large band laser, waist at 40 μm, Rayleigh Length 4.7 mm, 100 W Ytterbium doped fiber laser, model: YLR-100-LP-AC

can decay towards such states, they are the $|{}^5D_4\rangle$,$|{}^5D_3\rangle$ and $|{}^5D_4\rangle$,$|{}^5D_3\rangle$,$|{}^5D_2\rangle$,$|{}^5S_2\rangle$ levels respectively, see Fig. 1.2. These are **metastable states**, their lifetimes, only considering radiative decay processes, reaching values greater than 50s [43]. The transition of the atoms to the $|{}^7P_4\rangle$ level is ensured by the MOT lasers (at 425.553 nm), whereas the transition to the $|{}^7P_3\rangle$ level is brought about by an additional low power **depumping laser** at 427 nm. Decays from the $|{}^7P_3\rangle$ level towards the metastable states occur at higher rates than those starting out from the $|{}^7P_4\rangle$ state, moreover the favorable $|{}^5S_2\rangle$ state which is specifically populated by this decay path has better collisional properties than the ${}^5D$ states [44].
All in all, these states accumulate within the magnetic trap without suffering from light assisted collisions, and are therefore efficiently transferred to the dipolar one, unless, as mentioned before, these atoms end up with negative total spin projections along the quantization axis. Tackling this particular issue, the atoms are subjected **radio frequency (RF) ramps** centered around the Larmor frequency. These rapid adiabatic passages (see 1.2.6), when executed at high enough frequency "cancel" [45] the effect of the magnetic forces. In particular negative m_s states are no longer ejected by the magnetic trap, their trajectories having been reduced to small oscillations around the center of the trap which greatly improves (60% typically) the number of atoms loaded in the horizontal dipolar trap (HDT).
Once the atoms have been loaded into the HDT, the magneto optical trap is switched off, and the atoms are repumped into the ground state using duly named **repumping lasers** (633.184 nm, 653.973 nm, 663.183 nm), whereupon atoms are polarized into the $|{}^7S_3, m_s = -3\rangle$ state using a 15 μs σ^- polarized 427 nm pulse, hence avoiding detrimental dipolar collisions whose rate would grow as the evaporation proceeds and the atomic density increases. More specifically, atoms in this fully stretched state can only incur spin changing dipolar *collisions* if their kinetic energy is close to the Zeeman induced energy difference between two consecutive substates i.e. $E_c = (2\times)g\mu_B B$: for strong enough magnetic fields, and low enough temperatures, this condition is rarely fulfilled for atoms in the $|{}^7S_3, m_s = -3\rangle$ state, and when it is, the collision only contributes to the increase of cloud's phase space density (after repumping) [46].

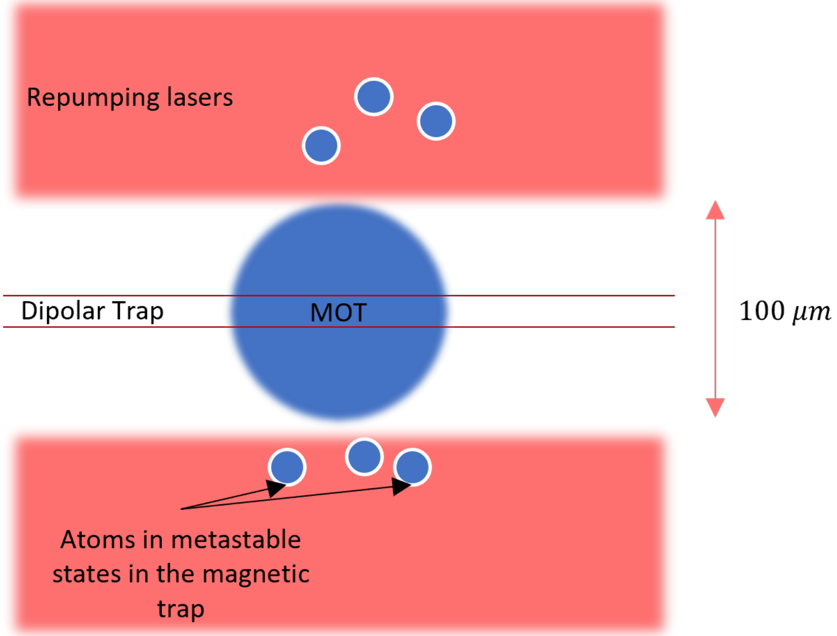

FIGURE 1.3: The repumping lasers take two distinct paths, the second of which we call *dark spot*, see Fig. 1.1. This path is active during the accumulation step. A metallic wire is used to obstruct the center part of the beams, in doing so the repumping lasers interact only with metastable atoms that are outside the reach of the horizontal dipolar laser but which are still magnetically trapped. By transferring them back to ground state, they once again interact with the MOT light, and have therefore a new chance of accumulating into the dipolar trap.

At this stage, there are about $[5\times10^5 - 3\times10^6]$ atoms in the HDT, their temperature is more or less one third ($T \simeq 90\mu$K) that corresponding to the trap's depth [7] and the evaporation process can finally begin. In practice, it starts by diverting part of the horizontal beam's power to an alternative route, that is the **vertical dipolar beam**, all the while decreasing the laser's overall power. Horizontal and vertical beams form into a cross shaped pattern, the point of intersection effectively corresponds to a *dimple* of potential in which atoms accumulate.
At this point, the depth of the dipolar trap is further decreased, by lowering the overall laser's power, this process takes approximately 15 s, the phase space density increases gradually until eventually leading to the formation of condensates with a number of atom N ranging from 10000 to 20000 with temperatures as low as 50 nK, Thomas-Fermi radii of 5 μm, and spatial density of approximately 2×10^{14} cm^{-3}. The optical trap's frequencies are approximately $(2\pi\times(245,298,210)$ Hz ± 10%)[12].

Final notes:

- Additional coils surround the experimental cell and compensate undesired magnetic gradients, such as the residual field of the ZS, that of the ionic pump and the earth's.
- All of the beams at 425 nm (the Zeeman slower beam, the transverse cooling beams, the imaging beams, the MOT beams) share a common origin: a Master Diode-Tapered Amplifier system which was set up at the very beginning of this doctoral work. This system, as well as other diodes and relevant frequency locks, are described in greater detail in App. A.

---

[7] To maximize the overlap between the HDT and the MOT, the HDT's transverse mode is adapted through the modulation of the RF frequency fed to the AOM controlling it, the reported temperature largely depends on the particulars of this frequency modulation

Once the chromium atoms have been condensed, they can be efficiently[8] *loaded into* ***optical lattices****, at which stage, they settle in the so-called Mott insulating phase, hence named because of the strong suppression of transport phenomena it displays. Dipolar dynamics can at last be triggered using strong resonant* ***radio frequency (RF) pulses****. These aspects are described in the following section.*

1.2 Optical lattices and triggering of spin dynamics

In this section we outline the basic working principles of optical lattices, we then describe the geometry of the actual experiment's lattices and the associated loading routines. We finally present the interaction of spin particles with radio frequency magnetic fields and explain how this interaction can be used to trigger spin dynamics

1.2.1 Basic principles

Placing a neutral two-level atom in a monochromatic electric field **E** oscillating at frequency ω_L will induce an electric dipole **D** whose interaction with said electric field can be written [47]

$$V_{dip} \propto -\mathbf{D}.\mathbf{E} \propto \alpha(\omega_L)I \tag{1.1}$$

Equation 1.1: Interaction potential between a neutral atom and an oscillating electric field of intensity I. Vectorial and tensorial components of the atomic polarisability α offer subtle experimental knobs that can be used for spin preparation, as was done by our team to initialize atoms in the $m_s = -2$ state [48]

For far detuned light, this *dipole potential energy* takes the following form

$$V_{dip} = \frac{\hbar\Omega^2}{4\delta} \tag{1.2}$$

Where

- $\Omega = \frac{d|E|}{\hbar}$ is the **Rabi frequency**, it depends on both the amplitude of the electric field $|E|$ and the strength of the transition under consideration. This strength is characterized by the dipole matrix element d
- $\delta = \omega_L - \omega_0$ is the **detuning**, that is the difference between the electric field's frequency of oscillation and the frequency of the transition under consideration

Far-off resonance light can therefore be used to trap atoms, in particular depending on the detuning's sign, atoms will either be attracted or repelled from intensity maxima. While chromium is in no way a two-level atom, the basic principles enclosed within Eq.1.2 still hold true, and chromium can indeed be trapped using far detuned light. This effect comes into play in the optical trapping (DT) of atoms described in the previous section.

The particularity of optical lattices however lies in their periodic structure, that is in the alternation between lows and highs of light intensity. Depending on the light's detuning, atoms can be loaded into either of these peaks and valleys, forming into more or less crystalline arrangements. Generally speaking such periodic light structures arise from the

---

[8] Optical lattices were experimentally available way before 1995, the advent of Bose Einstein condensation has nonetheless allowed for better loading of these lattices: momentum-wise, only low lying lattice bands are populated, spatially, unit filling is more easily achieved

interference of two or more coherent beams.

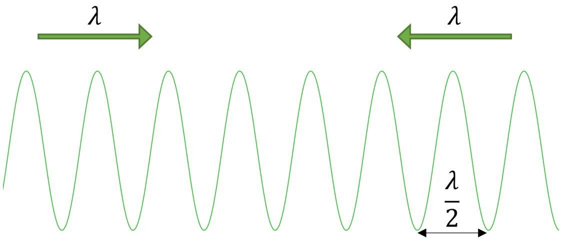

FIGURE 1.4: A 1D optical lattice is the result of interferences between two coherent beams, the spatial period i of this lattice depends on the angle θ between both beams: $i = \frac{\lambda}{2\sin(\theta/2)}$. For counterpropagating beams $i = \frac{\lambda}{2}$

All of the experiments that are to be presented in this manuscript were conducted in a 3D anisotropic 532 nm lattice. An additional 1D 1064 nm lattice was set up during my doctorate, and was used to carry out bipartite measurements, the details of these measurements will be discussed in Chap. 4. Let us for now review the **experimental set-up specific to this newly added laser**.

1.2.2 The 1064 nm laser's set-up

The 1064 nm laser[9] setup is presented in Fig. 1.5. It is of note that the 1064 and 532 nm beams are generated by two distinct apparatus, there is therefore no phase or frequency relationship between these beams.

In order to form a bichromatic lattice along the $\mathbf{a}_1$ direction, these beams are mixed together using a dichroïc mirror. After they have passed the atoms, the lasers are split apart using a second dichroïc mirror and reflected back using dedicated mirrors. Decoupling the reflected beams allows for simpler alignment procedures, this however increases the beams' optical paths' differential fluctuations, which ultimately modifies the intensity pattern at the vicinity of the the atomic cloud. The control and stability of this pattern will be discussed in Chap. 4

1.2.3 Lattices' geometry

The 532 nm lattice intensity is given by

$$\begin{aligned} I_{dip,532}(\mathbf{r}) = \Big\langle \Big| & \underbrace{E_{a_1}(\mathbf{r})\left(e^{i\left(k_{532,H}\mathbf{a}_1.\mathbf{r}+\omega_{532,H}t+\phi_1\right)}+c.c\right)\mathbf{e}_V + E'_{a_1}(\mathbf{r})\left(e^{i\left(k_{532,H}\mathbf{a}_1.\mathbf{r}-\omega_{532,H}t+\phi'_1\right)}+c.c\right)\mathbf{e}_V}_{H1} \\ & + \underbrace{E_{a_2}(\mathbf{r})\left(e^{i\left(k_{532,H}\mathbf{a}_2.\mathbf{r}+\omega_{532,H}t+\phi_2\right)}+c.c\right)\mathbf{e}_V}_{H2} \\ & + \underbrace{E_{a_3}(\mathbf{r})\left(e^{i\left(k_{532,V}\mathbf{a}_3.\mathbf{r}+\omega_{532,V}t+\phi_3\right)}+c.c\right)\mathbf{a}_3^{\perp} + E'_{a_3}(\mathbf{r})\left(e^{i\left(k_{532,V}\mathbf{a}_3.\mathbf{r}-\omega_{532,V}t+\phi'_3\right)}+c.c\right)\mathbf{a}_3^{\perp}}_{V532} \Big|^2 \Big\rangle \end{aligned} \tag{1.3}$$

---

[9] High Power Fiber Laser ALS-IR-1064-10-E-CC-SF provided by *AZURLIGHT SYSTEMS*

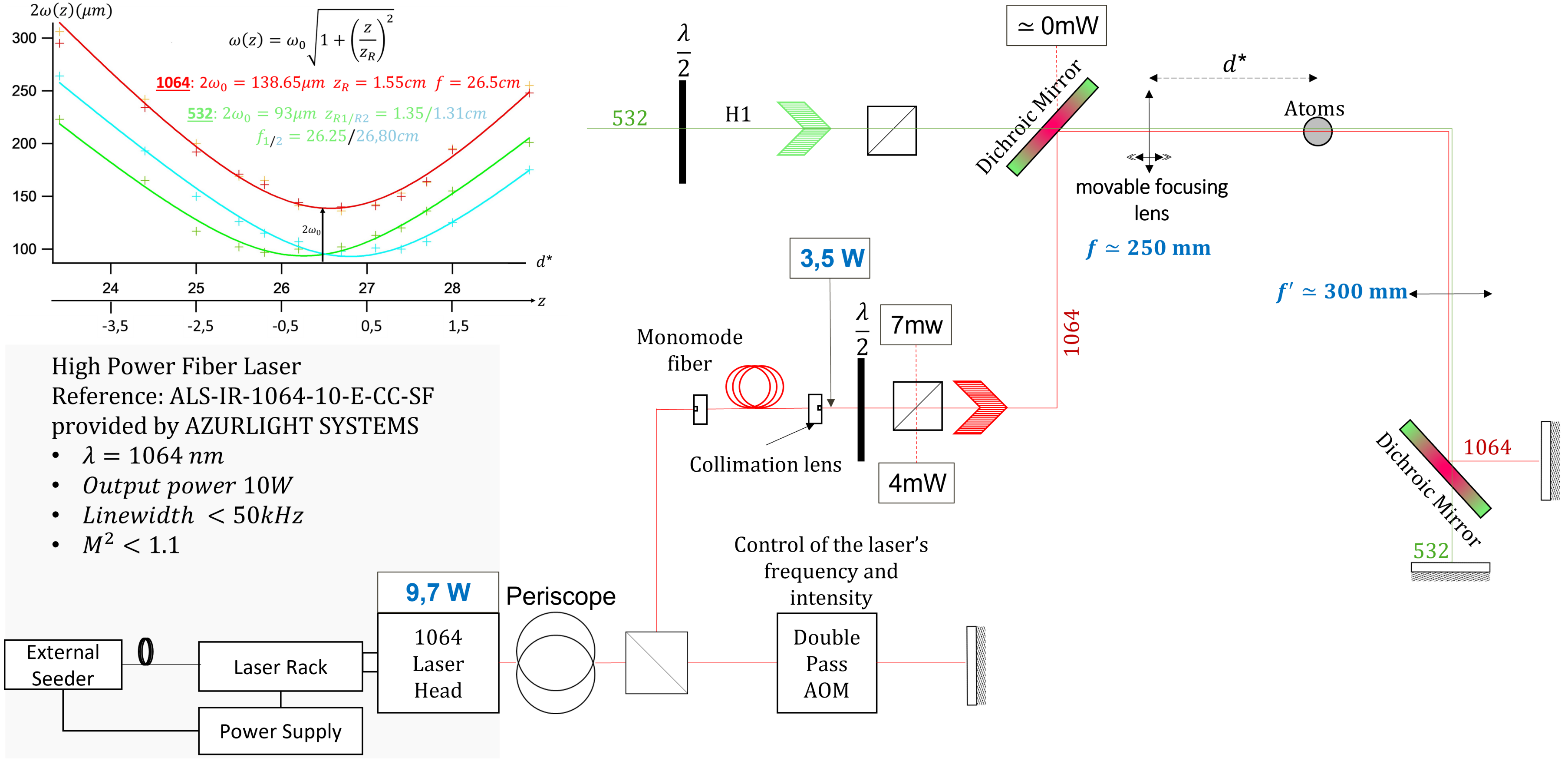

FIGURE 1.5: Bichromatic lattice optical setup: The waists of both lasers were measured some distance away from the focusing lens using a flipper mirror to redirect the beams. In practice, the position of this lens is still moved about using a micrometer screw gauge to fine tune and balance the diffraction of both lattices. Both lasers' focal points are made to coincide, despite the dispersive character of the focusing lens, using the collimation lens at the output of the monomode fiber outcoupling the 1064 nm laser.

While the 1064 nm lattice intensity is given by

$$I_{dip,1064}(\mathbf{r}) = \left\langle \left| E_{a_1,i}(\mathbf{r}) \left(e^{ik_{1064}\mathbf{a}_1.\mathbf{r}+\omega_{1064}t+\phi_i} + c.c \right) \mathbf{e}_V + E'_{a_1,i}(\mathbf{r}) \left(e^{ik_{1064}\mathbf{a}_1.\mathbf{r}-\omega_{1064}t+\phi'_i} + c.c \right) \mathbf{e}_V \right|^2 \right\rangle \tag{1.4}$$

Where

- The time average is taken over rapidly oscillating terms
- The ω_{xxxx} are the frequencies of the various beams, $\omega_{532,H}$ and $\omega_{532,V}$ are slightly different so that the vertical and horizontal beams may not create any relevant interference pattern
- The k_{xxxx} are the norms of the wavevectors of the various beams
- $\mathbf{a}_1$, $\mathbf{a}_2$, $\mathbf{a}_3$ are unit vectors corresponding to the travel direction of each of the H1(1064), H2 and 532V beams (see Fig. 1.6a, 1.6b). $\mathbf{e}_V$ and $\mathbf{a}_3^{\perp}$ are also shown in this figure.

Taking into account the fact that the lattice beams' detuning is much bigger than the fine structure's transitions' frequencies, the dipolar potential is still given by Eq.1.1, with $\alpha_{1064} \simeq 0.54\alpha_{532}$

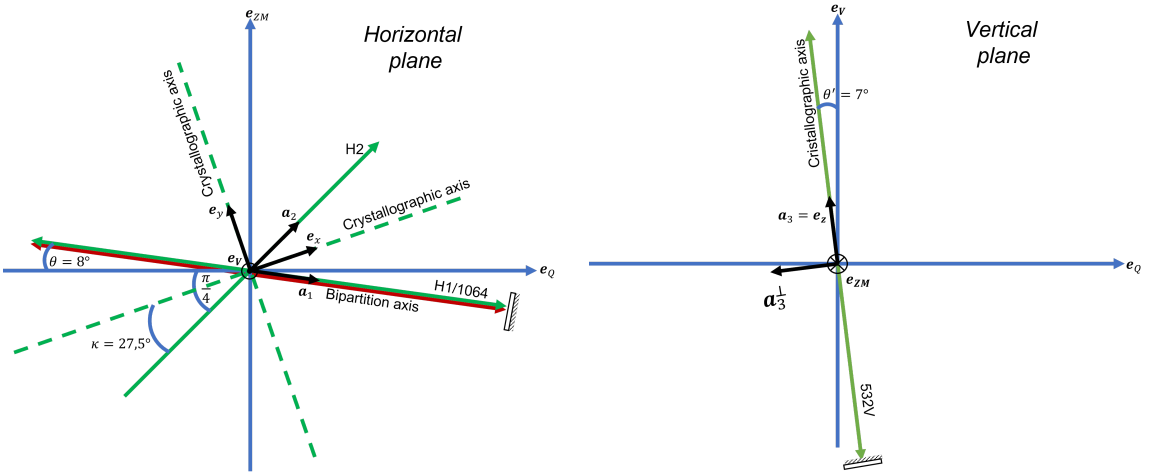

(A) View of the lattices' beams' arrangement in the horizontal plane i.e. parallel to the ground

(B) View of the lattices' beams' arrangement in the vertical plane

This expression can be further simplified by noticing that the condensate (5 μm) is small in comparison to the Rayleigh lengths ($\sim cm$) and the waists of the various beams ($\sim$ 50 μm), so that we may neglect the variation of the electric fields amplitudes across the region of interest[10]: $E(\mathbf{r}) \to E$, on the other hand the time averaging lets us omit all time dependent terms, which oscillate with characteristic frequencies much bigger than those that characterize the atom's center of mass' motion. The resulting potential landscape is depicted in Fig. 1.7b, 1.7a.

---

[10] We have experimentally observed the limitations of this approximation investigating tunnel effects in our system.

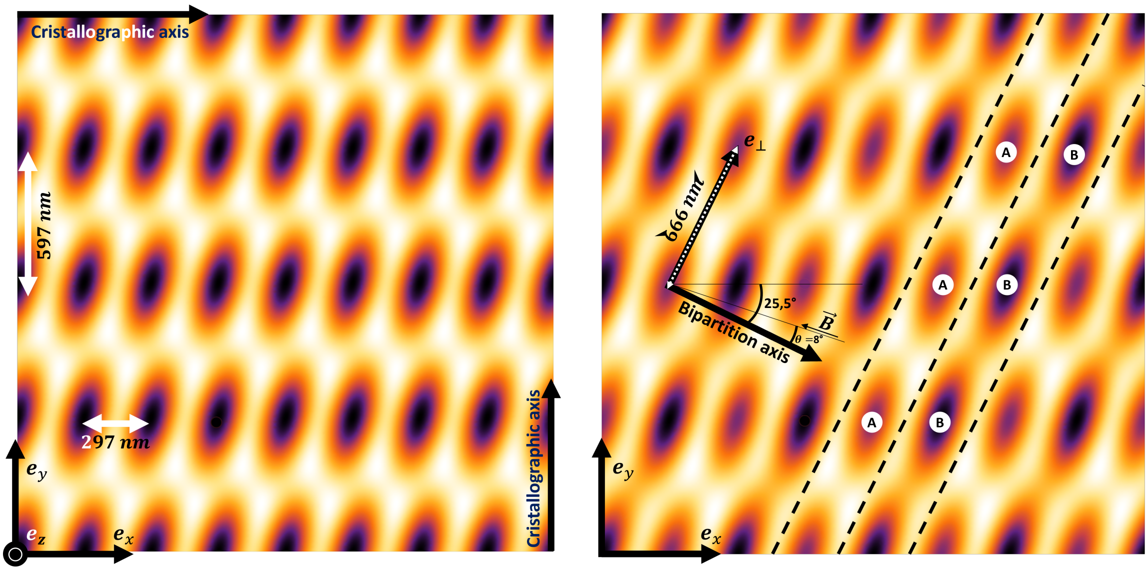

(A) Horizontal lattice potential landscape when the infrared laser is switched off. The vertical lattice's (along $\mathbf{e}_z$) period is 268 nm.

(B) Horizontal lattice potential landscape when the infrared laser is switched on ($\phi_i = 0$). There are now two distinct well families indexed by the A and B letters. The potential wells are anisotropic, moreover none of their main axes are aligned with the bipartition axis. This does not impair the bipartition process which still isolates atoms from the two well families shown above (A and B)

FIGURE 1.7: Bichromatic and monochromatic lattices' horizontal potential landscapes. The bipartition axis is given by the direction of propagation of the H_1 and $\mathbf{1064}$ beams, it indicates the direction along which the atoms are separated when bipartite measurements are performed (see Chap.4).

1.2.4 Loading routine

In order to load the BEC in the lattices, the lattice's lasers' powers is gradually ramped up, they are controlled by 3 sets of independent acousto-optic modulators (AOMs), with respective frequencies of 80, 80 and 110 MHz. The loading sequence of the condensate is depicted in Fig. 1.8. The release sequences are various and depend on the experiment that is carried out. Release sequences are detailed in each of Chap.3 and Chap.4.

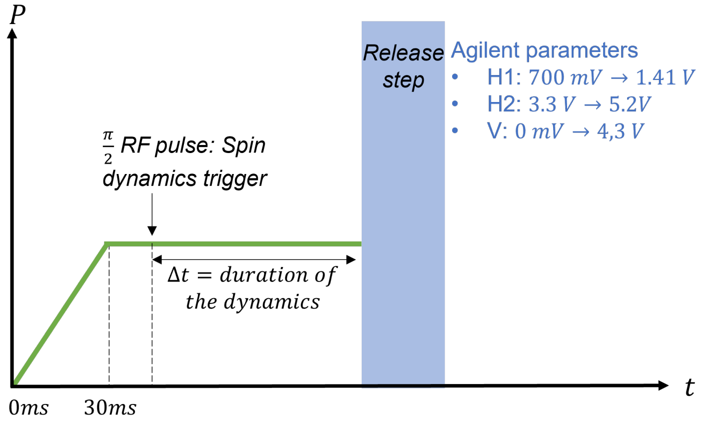

FIGURE 1.8: Loading sequence of the BEC. The power of the lasers is gradually increased[11], and we reach typical lattice depths of $22 \sim 28 E_r$ [12]. The duration of the spin dynamics in the lattice is fixed by the length of the power plateau Δt. The 30 ms (Δt_{inc}) duration over which the lasers' power is slowly increased is set by several constraints, one of which is the *adiabaticity condition* which must be fulfilled in order to fill low lying energy bands preferentially, according to this condition the increase rate of the lattice depth should be smaller than frequencies related to typical energy gaps (ΔE) between the ground motional states of the atoms in the lattice (first band) and the first excited states (second band) $\frac{dV}{dt} << \frac{\Delta E^2}{\hbar} \simeq 340 \times 10^3 E_r.s^{-1}$ [12]. Other conditions state that the ramp should let atoms fully explore the lattice potential to adequately rearrange themselves and homogeneously and regularly fill the lattice ($\Delta t_{inc} > \frac{1}{f_{\text{DipolarTrap}}} \simeq 5$ ms).

1.2.5 Atomic density pattern

The competition between various energy scales (atomic interactions and potential energy as dictated by the radial intensity patterns of the laser beams) is such that atoms end up in the well known wedding cake conformation: lattice sites in the inner core generally contain pairs of particles also called **doublons**, whereas lattice sites in the external shell are populated by single particles for the most part. This arrangement is specific to the Mott state and stems from the fact that number fluctuations are energetically unfavorable when the tunneling energy scales are smaller than the interatomic repulsions.

---

[12] What we show here are the typical voltage ramps programmed into the waveform generators controlling the lasers' intensities. While the derivatives of the wave forms shown here are discontinuous, the actual lasers' intensities evolve rather smoothly.

[12] The Mott transition happens at 8 E_r [49]

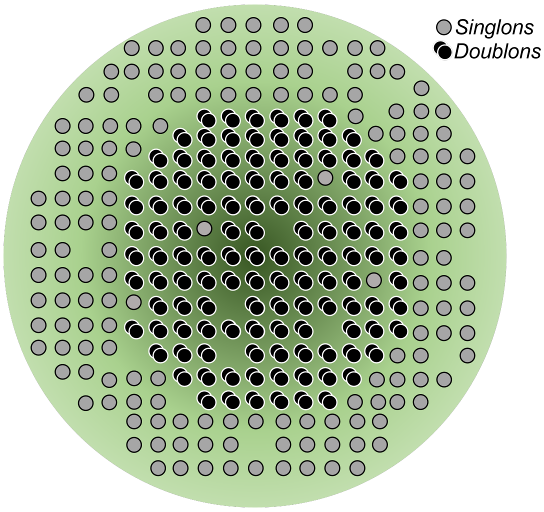

FIGURE 1.9: When the condensate is slowly loaded in the optical lattice, the competition between dipolar potential energy and interaction energy dictates the number of atoms in each lattice site. In the inner parts of the lattice, the dipole potential energy (≡ depth of the lattice) is such that doublons are energetically favoured: despite the adverse contribution of atom atom interactions, it is less costly energetically for atoms to form into particle pairs than to populate external wells which are more shallow

1.2.6 Triggering the dynamics : A spin's interaction with a magnetic field

After the condensate has been loaded in the lattice, all atoms are in the $\left(|^7P_3, m_s = -3\rangle\right)$ *spin state which, as an eigenstate of the interaction Hamiltonian* $\hat{H}_{\text{sec}} = \frac{1}{2}\sum_{i,j} V_{ij}\left[\hat{S}^z_i\hat{S}^z_j - \frac{1}{4}\left(\hat{S}^+_i.\hat{S}^-_j + \hat{S}^-_i\hat{S}^+_j\right)\right]$*), remains unchanged up to a global phase coefficient.*
In order to trigger the dynamics, we rely on radio frequency fields effect on the spins to ***quench*** *their internal degrees of freedom. In the following, we briefly review the spins interactions with radio frequency fields and the two techniques which we use to manipulate these atoms' internal states. A more detailed account of these aspects can be found in [50].*

The interaction Hamiltonian between a spin $\hat{\mathbf{S}}$ and a **static field** $\mathbf{B}_0$[13] along $\mathbf{e}_z$ is written:

$$\hat{H} = -\gamma\hat{\mathbf{S}}.\mathbf{B}_0 \tag{1.5}$$

where:

- $\gamma = -\frac{g_S\mu_B}{\hbar}$ is the gyromagnetic ratio.

The eigenstates of $\hat{H}$ are denoted $|m\rangle_{\mathbf{z}}$, corresponding eigenvalues are $E_m = mg_S\mu_B B_0$.
This expression remains the same when we consider an additional magnetic field oscillating at frequency ω comparable to ω_0 in a direction orthogonal to $\mathbf{e}_z$: $\mathbf{B}_1 = B_1\cos(\omega t)\mathbf{u}_x$. In this case however, $\hat{H}$ can be rewritten

$$\hat{H} = \epsilon\omega_0\hat{\mathbf{S}}_z + 2\epsilon\Omega\cos(\omega t)\hat{\mathbf{S}}_x \tag{1.6}$$

where:

- $\Omega = \frac{|g_S|\mu_B B_1}{2\hbar}$ is the Rabi frequency

---

[13] Note that $\mathbf{B}_0$ is space independent. In the case of space dependent magnetic fields, the external degrees of freedom of the atoms must be taken into account, the fact that $\hat{r}$ and $\hat{p}$ do not commute can for example lead to so-called Majorana losses [50]. In our case, for an individual atom space dependence can be neglected as it is pinned to the 3D lattice

- $\omega_0 = |\gamma| B_0$ is the Larmor frequency
- $\epsilon = \pm 1$ is the sign of the Landé factor

Using the usual scaling operator $\hat{S}_\pm$, we get :

$$\hat{H} = \underset{\text{Spin precession around }\mathbf{z}}{\epsilon\omega_0\hat{S}_z} + \epsilon\frac{\Omega}{2}\underset{\text{promotion terms}}{\left[e^{-i\omega t}\hat{S}_+ + e^{i\omega t}\hat{S}_- + e^{-i\omega t}\hat{S}_- + e^{i\omega t}\hat{S}_+\right]} \tag{1.7}$$

In the frame rotating at frequency $\epsilon\omega$, the interaction Hamiltonian takes the following **effective** form:

$$\hat{H} \longrightarrow \hat{H}_{\text{eff}} = -\epsilon\delta\hat{S}_z + \epsilon\frac{\Omega}{2}\left[e^{i(\epsilon-1)\omega t}\hat{S}_+ + e^{-i(\epsilon-1)\omega t}\hat{S}_- + e^{-i(\epsilon+1)\omega t}\hat{S}_- + e^{i(\epsilon+1)\omega t}\hat{S}_+\right] \tag{1.8}$$

Where $\delta = \omega - \omega_0$. Depending on the sign of ϵ, promotion terms in the equation 1.8 will be static or oscillate at frequency 2ω. Performing the so called *rotating wave approximation*[14], we drop these fast oscillating terms so that:

$$\hat{H}_{\text{eff}} = -\epsilon\delta\hat{S}_z + \epsilon\frac{\Omega}{2}\left[\hat{S}_+ + \hat{S}_-\right] = -\epsilon\delta\hat{S}_z + \epsilon\Omega\hat{S}_x = \sqrt{\delta^2 + \Omega^2}\,\hat{\mathbf{S}}.\mathbf{u} = \Omega_G\hat{\mathbf{S}}.\mathbf{u} \tag{1.9}$$

Where

- $\Omega_G = \sqrt{\delta^2 + \Omega^2}$ is the generalized Rabi frequency

In the rotating frame, the interaction between a spin and an oscillating magnetic field in the presence of a strong external static field reduces to its interaction with an effective static field $\mathbf{B}_{\text{eff}}$ given by.

$$\mathbf{B}_{\text{eff}} = \frac{\hbar\sqrt{\delta^2 + \Omega^2}}{g_S\mu_B}\mathbf{u} \tag{1.10}$$

$$\mathbf{u} = \cos(\theta)\mathbf{e}_z + \sin(\theta)\mathbf{e}_x \qquad \cos(\theta) = \frac{-\epsilon\delta}{\sqrt{\delta^2 + \Omega^2}} \qquad \sin(\theta) = \frac{\epsilon\Omega}{\sqrt{\delta^2 + \Omega^2}} \tag{1.11}$$

The spin flipping techniques used in the experiment are based on equation 1.9, these techniques are **rapid adiabatic passages** (RAP) and **Rabi pulses**.

In rapid adiabatic passages, an atom which we will assume, without loss of generality, has been prepared in the $|m\rangle_{\mathbf{z}}$ state is placed in a radio frequency field whose Rabi frequency is slowly increased from 0 to Ω_1. In doing so, the atomic state seamlessly transforms into $|m\rangle_{\mathbf{u}}$ such that $\mathbf{u.z} = \cos(\theta)$ with $\cos(\theta) \simeq 1$. Sweeping ω through the resonance from $\delta < 0, |\delta| \gg \Omega_1$ to $\delta > 0, |\delta| \gg \Omega_1$ increases θ from 0 to $\sim\pi$, switching off the RF field (slowly yet again) leaves the atom in the $|-m\rangle_z$ state, effectively flipping it.

---

[14] This approximation is valid if the generalized Rabi frequency is negligible in comparison to the Larmor frequency $\Omega_G = \sqrt{\delta^2 + \Omega^2} \simeq 50 - 100kHz \ll omega a_0 = 2\pi 2.2MHz$

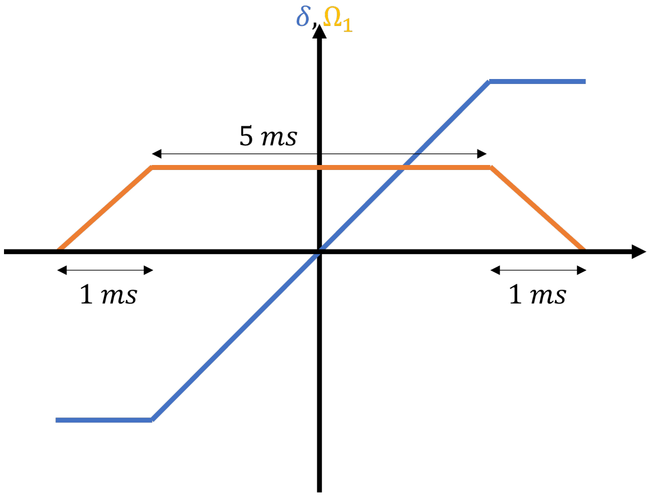

FIGURE 1.10: RAPs' power and detuning ramps. For the RAP procedure to be efficient, the spin must adiabatically follow the eigenstates of effective Hamiltonian. The *adiabaticity condition* writes $|\dot{\theta}| \ll \sqrt{\Omega^2+\delta^2} \equiv |\dot{\delta}\Omega+\delta\dot{\Omega}| \ll (\Omega^2+\delta^2)^{3/2}$ [50].

Rabi pulses, on the other hand, involve resonant RF pulses i.e. $\delta = 0$.
Consider, for the sake of simplicity, a spin $\frac{1}{2}$ particle prepared in the $|+\rangle_{\mathbf{z}}$ state, since $\delta = 0$, $\mathbf{u} = \mathbf{e}_x$ and the evolution of the spin under the influence of the RF field is given by the evolution operator $U = e^{-i\hat{H}t/\hbar}$ where

$$\hat{H} \equiv \frac{\hbar}{2}\begin{pmatrix} 0 & \Omega \\ \Omega & 0 \end{pmatrix} \tag{1.12}$$

Which leads to

$$\Psi(t) = e^{-i\hat{H}t/\hbar}|+\rangle_z = \frac{1}{2}\left[e^{-i\Omega t/2}|+\rangle_z + e^{+i\Omega t/2}|-\rangle_z\right] \tag{1.13}$$

For an interaction time $\Delta t = \frac{\pi}{\Omega}$ (π pulse), we get $\Psi(\frac{\pi}{\Omega}) \propto |-\rangle_{\mathbf{z}}$, we have flipped the spin population.
For $\Delta t = \frac{\pi}{2\Omega}$ $\left(\frac{\pi}{2}\text{ pulse}\right)$, we get an equal superposition of both $|+\rangle_{\mathbf{z}}$ and $|-\rangle_{\mathbf{z}}$ states.
For a spin 3 particle, the normalized populations' distribution as a function of the RF pulse angle read

$$N_{m_s}(0)/N = \begin{pmatrix} 6 \\ m_s+3 \end{pmatrix} \sin\left[\frac{\theta}{2}\right]^{6+2ms} \cos\left[\frac{\theta}{2}\right]^{6-2ms} \tag{1.14}$$

Where $\binom{n}{k} = \frac{n!}{k!(n-k)!}$

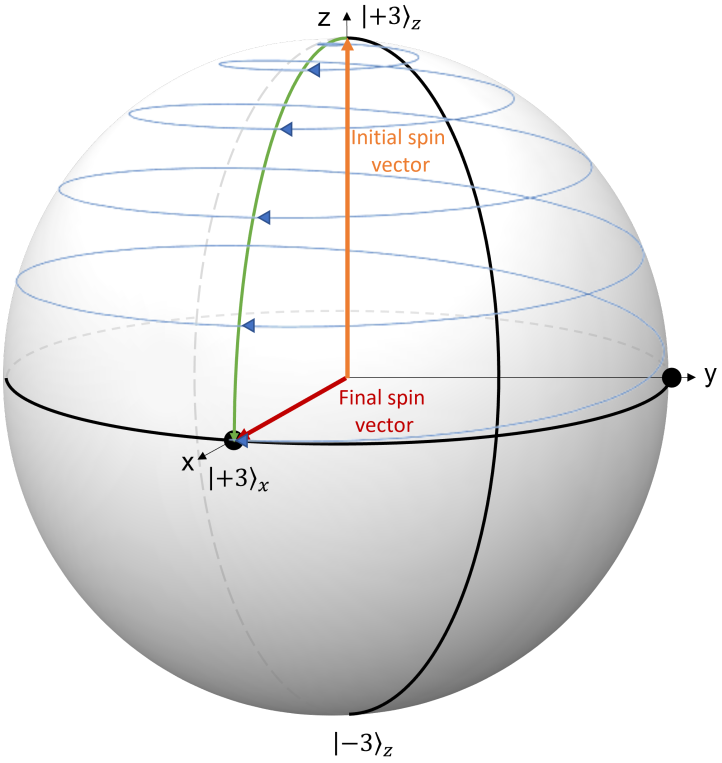

FIGURE 1.11: Blue trajectory: The spin vector trajectory in the laboratory frame during a $\frac{\pi}{2}$ pulse for a spin initially along **z**. Green trajectory: Its trajectory in the rotating frame. In practice, the quantization magnetic field's amplitude is about 0.79 Gauss which corresponds to a ~ 2.2 MHz Larmor frequency. Typical RF frequency detunings are on the order of the kHz which remains small compared to typical Rabi frequencies. In general, the Rabi frequency is finely adjusted so that RF pulses durations may always be an integer number N of Larmor periods. For a $\frac{\pi}{2}$ pulse $N = 5$, in which case $\Omega_R = \frac{2\pi}{5}\frac{f_0}{4} = 2\pi \times 105$ kHz. These high amplitudes are reached using a 30 watt RF amplifier.

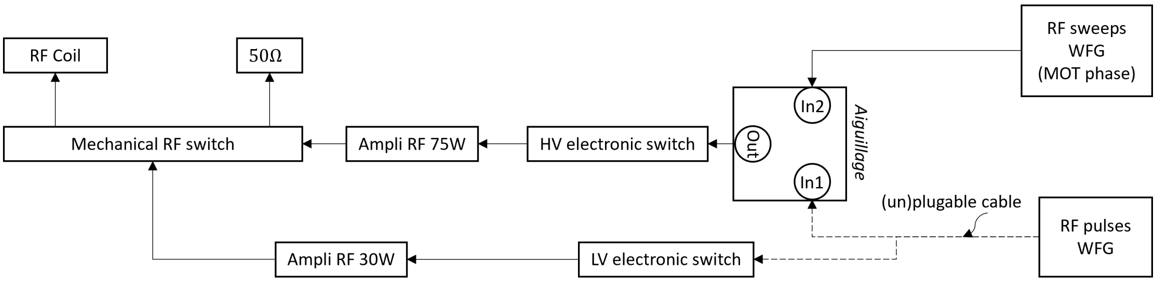

FIGURE 1.12: Architecture of the RF chain. The electronic switches allow for fast (≈ 5-15 ns) switch on and off of the signals generated by the waveform generators (WFG). These signals can be amplified by two distinct amplifiers both of which are connected to the same mechanical switch. Only one of these inputs (the 75 W amplifier's output or the 30 W amplifier's output) is sent to the RF coil that generates the RF field. The other input is connected to a 50 Ω termination.

1.3 Imaging techniques

*After triggering the dynamics, the atoms' internal state evolve under the influence of dipole dipole interactions. This evolution can be monitored through the measurement of the seven Zeeman populations of chromium. Several techniques are employed to do just that: first, the seven states are separated using the century old **Stern & Gerlach** technique, then, the atomic clouds thus obtained are imaged using either **absorption** or **fluorescence** imaging. These procedures are detailed in the following section.*

1.3.1 The Stern & Gerlach technique

The seven spin states of the chromium atoms are separated using a $\simeq 9$ G.cm^{-1} magnetic gradient generated by the MOT coils. The force thus felt by each spin state is proportional to their spin quantum number m_s. The separation of these spin states allows us to unravel the dynamics of the populations and to monitor the growth of correlations through time.

1.3.2 Absorption imaging

The so called *absorption imaging* technique focuses on the modification of the imaging beam's characteristics as it propagates through the atomic cloud to be observed.

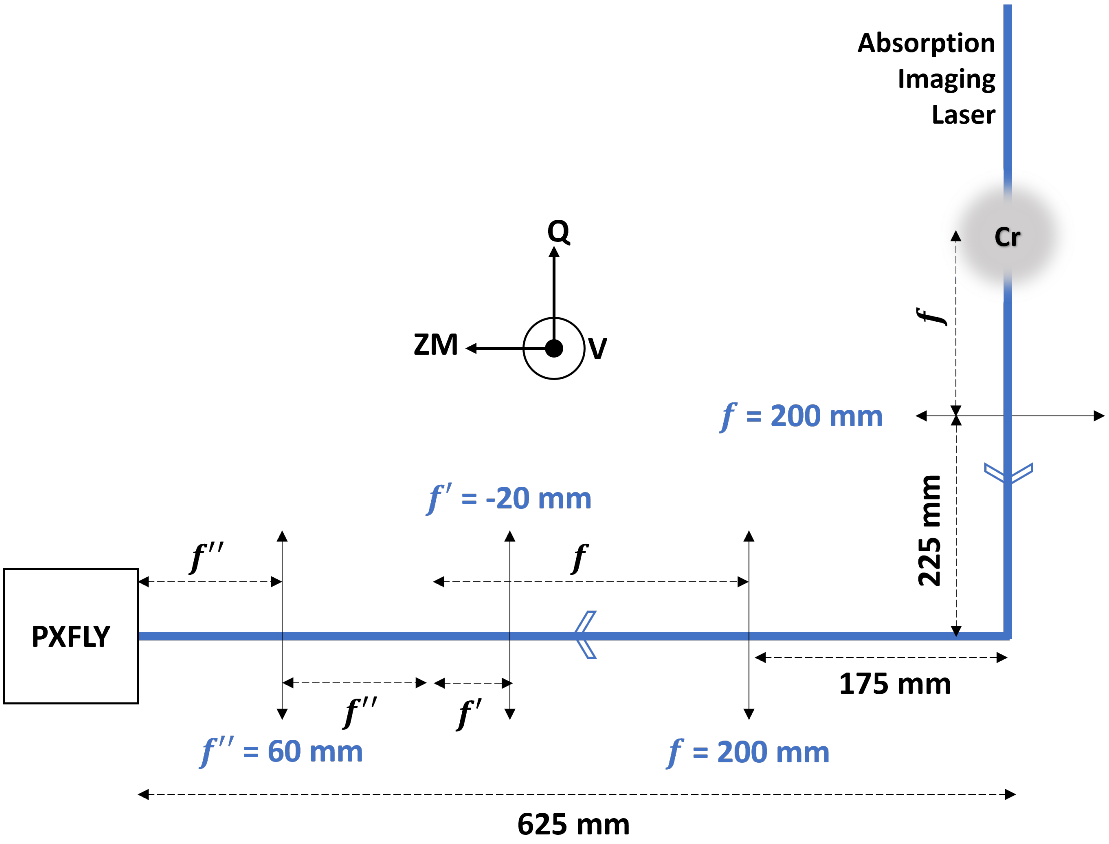

FIGURE 1.13: The absorption imaging setup is composed of two achromatic lenses and a telescope which allow for a global magnification factor of 3. The CCD camera used (the PixelFly) sports a 51% quantum efficiency @425 nm. The physical size of the pixels is 6.15 μm according to the manufacturer. The imaging beam is σ^- polarized, it is non saturating and tuned to the $|^7S_3, m_s = -3\rangle \rightarrow |^7P_4, m_s = -4\rangle$ transition. Imaging pulses' durations do not exceed ≈ 50 μs.

This technique builds upon the Beer-Lambert's law, which, when valid, predicts the exponential decrease of the laser's intensity as it goes through the atomic cloud. More specifically, we have [12]

$$N = -\frac{1}{\sigma_0} \iint_{\Delta_x \Delta_y} \ln\left(\frac{I_t}{I_i}\right) dydx \tag{1.15}$$

Where

- N is the number of atoms in a given cloud
- Δ_x, Δ_y are integration lengths spanning the atomic cloud's transverse area
- $\sigma_0 = \frac{3\lambda^2}{2\pi}$ is the absorption cross section
- I_i is the incident intensity. $I_i \sim 0.1 I_{\text{sat}}$ where $I_{\text{sat}} = \frac{\pi h c \Gamma}{3\lambda^3} = 8.503$ mW.cm^{-2} is the saturation intensity of the imaging transition
- I_t is the transmitted intensity

Strictly speaking, this equation only allows us to recover the number of constituents in the stretched state $\left|{}^7S_3, m_s = -3\right\rangle$. To recover the number of constituents of clouds corresponding to other spin momenta numbers, we use multiplicative factors, called *detectivity factors* accounting for the laser's detuning and the modification of the atoms' absorption cross section as they are optically pumped towards the $m_s = -3$ substate during the imaging process. Detectivity factors can be deduced by comparing the experimental populations found through Eq. 1.15 at time $t_{\text{dyn}} = 0$ ms to those given by Eq. 1.14.
As 52 chromium does not have any hyperfine structure and because the experimental clouds are in general not very dense, this imaging technique proved ideal for absolute atom number determination. Number uncertainties are estimated to about 10%.

1.3.3 Fluorescence imaging

Atomic clouds can also be characterized using the so-called *fluorescence imaging* technique. This technique focuses not on the characteristics of the transmitted imaging beam, but instead, on those photons spontaneously emitted by the atoms upon interaction with this beam.
By collecting and counting these photons one can recover some of the clouds' characteristics. More specifically, while it is hard, for example, to get quantitative estimates of N using fluorescence imaging, it is in theory possible to measure the ratios between the number of constituents in two distinct clouds with greater precision as this technique is less sensitive to the Zeeman structure of the imaging transition. This relative insensitivity stems from the conjunction of various factors:

1. *In theory*[15], the external magnetic field should be close to 0 during the imaging phase, so that the Zeeman induced frequency shifts remain small in comparison to the detuning between the imaging laser and the atomic transition.
2. The (red-)detuning of the imaging laser's frequency which makes it less sensitive to the details of the Zeeman structure. This detuning was experimentally optimized for each kind of experiment we carried. This optimization aimed at balancing the various clouds signals as well as their shapes and distances of separation. The red detuning coupled to the fact that we use the MOT's horizontal counterpropagating beams for

---

[15] In practice, the magnetic field parameters are adjusted so that the imaging of the clouds is as balanced as possible at $t_{dyn} = 0$ ms

imaging also entails a cooling effect similar to those at play in optical molasses and limits the expansion of the atomic clouds in the horizontal plane during the imaging phase[16].

3. The long time duration of the imaging pulses (750 μs -1.3 ms depending on the experiment at hand) which leads to complete spin scrambling within each individual cloud. This effect is supplemented by the fact that the imaging beams come from 4 different directions which makes for random polarizations and ultimately for smaller sensitivity to the spin degree of freedom and negligible transient imaging regimes which is in clear contrast with the absorption scheme wherein the various spin states are slowly pumped towards the resonant state $|^7S_3, m_s = -3\rangle$.

All in all, the imaging of the various spin states is more homogeneous as is evidenced by the measured *fluorescence detectivity factors* f_m whose dispersion around their mean value $\overline{f_m}$ is $\frac{\max(f_m)-\min(f_m)}{\overline{f_m}} \approx 0.25$ whereas it could reach values as high as 2.07 for absorption imaging [15].

The remaining inhomogneities can be linked to several limitations:

1. It is hard, if not impossible, using the current experimental set-up, the Stern & Gerlach characteristics, and the imaging time constraints, to enforce a zero magnetic field throughout the area over which the various atomic clouds spread ($\simeq 5 \times 3$ mm). This is mainly due to eddy currents which subside in times comparable to the time of flight (15 ms).

2. The complex intensity landscape of the **MOT's horizontal beams which are used for fluorescence imaging**. This landscape can be seen below, it is inhomogeneous by nature.

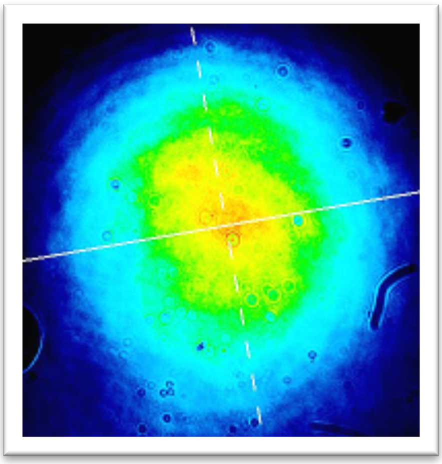

FIGURE 1.14: The waists of the horizontal MOT beams were evaluated to 1830 and 2160 μm. The limited size of these beams is such that all clouds cannot be illuminated uniformly after the *S&G* separation. This also limits TOF durations which can be used.

3. Photon collection efficiency is asymmetric, all else being equal, some clouds are better imaged than others. This defect is inherent to the imaging system and the many

---

[16] Using the MOT beams for imaging induces however undesirable couplings between the delicate MOT adjustments and the imaging process.

geometrical constraints we faced building it, as shown in the figure below it is due to limited numerical aperture of the imaging system we use.

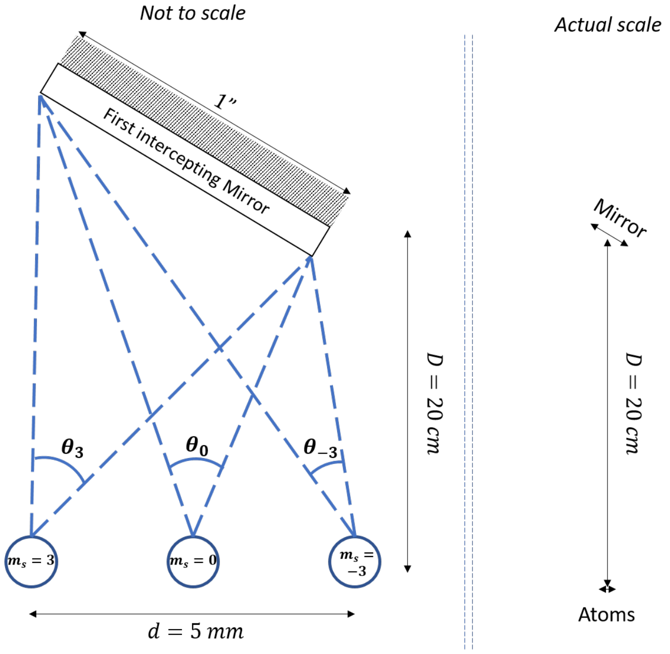

FIGURE 1.15: Because of the Stern & Gerlach technique used to separate the different clouds, the various *emission cones* intercepted by the first mirror of the imaging path and subsequent optical elements are different. Estimated atomic proportions are spoiled by this asymmetry.

4. The quality of the fits which are ultimately used to find out the atom numbers in each cloud depend on the shapes of these clouds, these shapes are dictated by the forces acting on the clouds during the time of flight. In general, extremal (±3) clouds' shapes can be a bit more... eccentric.

As mentioned above, in our experiment, the role of the imaging beam is played by the MOT's horizontal[17] beams. **In practice**, after a $\simeq$ 15 ms *time of flight* (TOF), these beams are shined upon the atomic samples, spontaneously emitted photons are then collected via the vertical porthole of the experimental chambers and redirected towards a water cooled EM-CCD ANDOR camera[18] via a system of achromatic 2 inch lenses whose total magnification factor is $\frac{4}{3}$. The collection efficiency of this setup is unfortunately quite low ($\epsilon \simeq 4 \times 10^{-3}$) and most photons emitted by the atoms are lost. The details of the imaging set-up are described in Fig. 1.16.
The camera's chip sports an 82% quantum efficiency at 425 nm, it is composed of 512×512 active pixels each of which is $16 \times 16\ \mu m$ large (magnification notwithstanding). The working temperature of the camera varies between $-80°C$ and $-90°C$, such low temperatures limit the generation of thermal electrons in the camera registers. These electrons, much like all other types of **spurious electrons**, can potentially distort experimental measurements, and deteriorate the camera's detectivity limit. This is because both spurious electrons and relevant electrons (i.e. those generated by the fluorescence photons after photoconversion), are indistinguishable and amplified independent of their physical origin. Therefore, the lower the count of spurious electrons, the smaller are detectable signals. Other than thermal electrons, *clock-induced charges* (CIC) and *stray light electrons* also contribute to the electronic

---

[17] The MOT's vertical beams induce undesirable parasitic reflections on the imaging camera's chip and can therefore not be used. During the imaging process, these beams are blocked using a shutter.
[18] iXon Ultra 897

camera background. CIC contribution is limited adjusting camera parameters, while stray light electrons numbers are curbed by carefully shielding the camera surroundings and by working in complete darkness. In our setup, the number of stray light photons does not exceed 0.7 photons per pixel for typical exposure times. The main stray light sources are the lasers which remain turned on (although not directly aimed at the atoms of course) during the imaging phase: the 532 nm laser, the 851 nm laser and the 1075 nm laser.

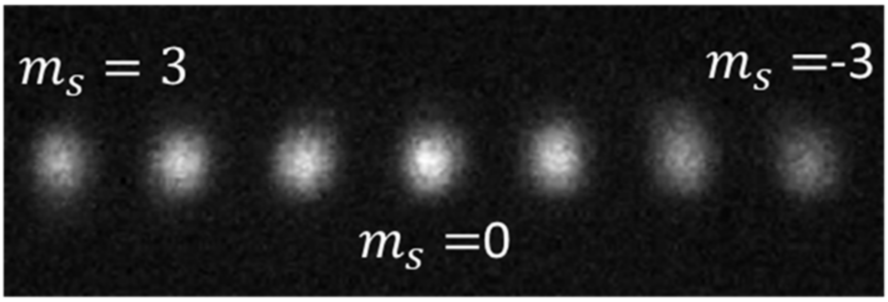

FIGURE 1.17: Fluorescence Imaging typical image (average over 10 images). After the Stern Gerlach, we get access to all seven Zeeman populations (C_{m_s} in Chap 2)

Comparison between absorption and fluorescence imaging

- The images obtained through absorption imaging are affected by the intensity fluctuations of the imaging lasers. Fluorescence imaging is less so affected by the fluctuations of the MOT lasers' power as these are *damped* by the saturation of the imaging transition[19].
- The signal obtained through fluorescence imaging can be concentrated on fewer number of pixels by adapting the magnification of the camera while allowing for long time of flights to better separate the Zeeman clouds. Focusing the clouds signal on a smaller area limits the impact of the pixel to pixel noise. This can not be done in absorption imaging for which detailed analysis shows that the potential signal to noise ratio gains are compensated by the decrease of the clouds' optical depth.
- Simple arguments reported in [51] show that the ratio between the fluorescence imaging SNR and the absorption imaging SNR is proportional to $\sqrt{\frac{\epsilon A}{N\sigma}}$ where N is the number of atoms, A the true pixel size of the camera, σ the scattering cross section and ϵ the collection efficiency of the fluorescence optics, showing that fluorescence is usually better suited for the imaging of small atom numbers.
- Absorption imaging generally requires that acquired images be defringed
- It is harder for big atomic samples to obtain quantitative data using fluorescence imaging
- The more or less isotropic character of spontaneous emission yields weak fluorescence signal unless high numerical aperture optics are used. On the other hand the choice of the optical axis is less stringent for fluorescence imaging than it is for absorption imaging.
- Detectivity factors are more homogeneous for fluorescence imaging

---

[19] For high laser intensities, the fluorescence of a two level atom is proportional to $\Gamma\times$ (Population of the excited state)$\simeq \frac{\Gamma}{2}$ and it does not follow intensity fluctuations of the laser anymore when the transition is saturated.

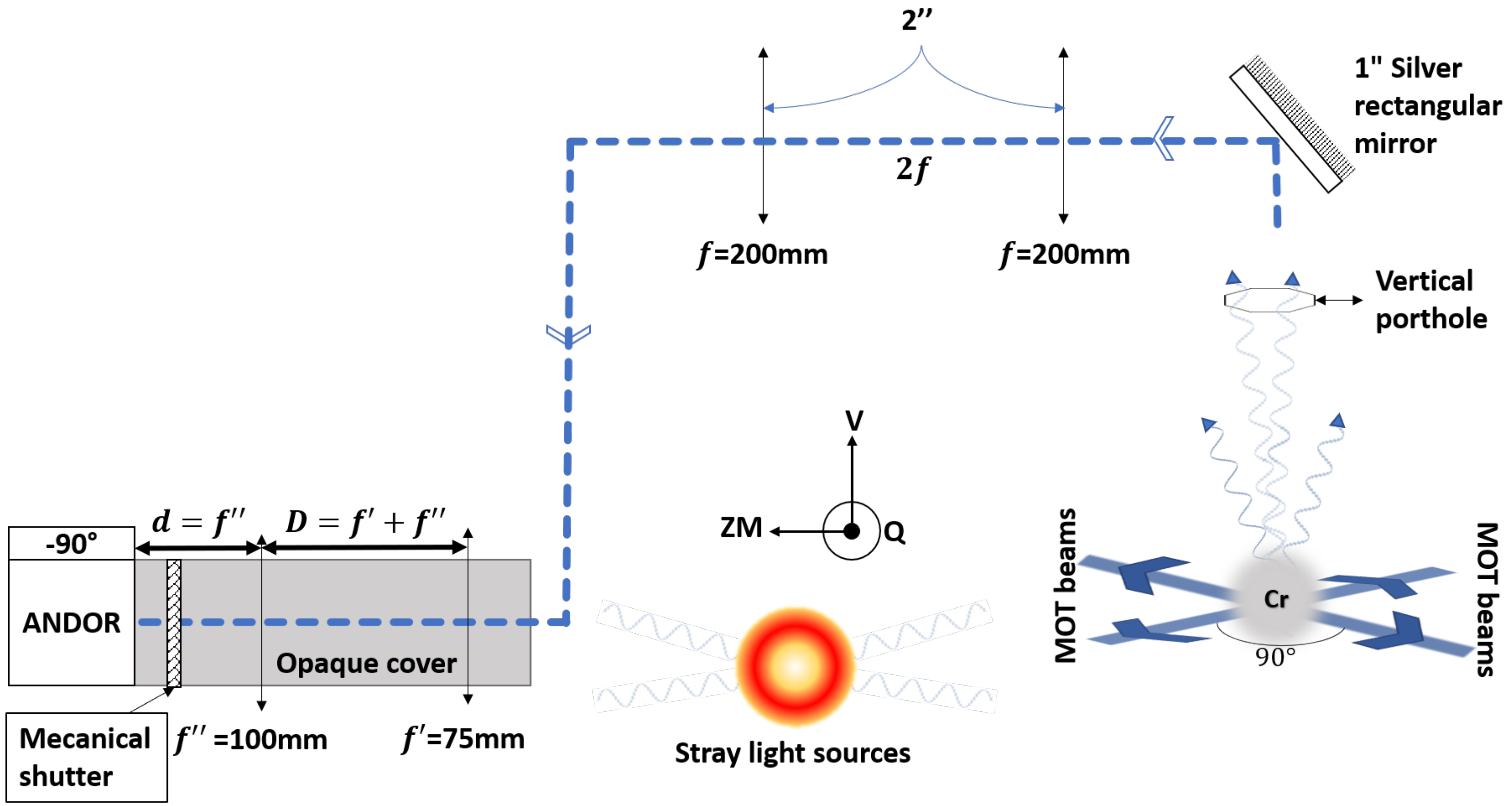

Figure 1.16: Fluorescence imaging setup. During imaging the MOT beams are shined upon the atoms, a small part of the scattered photons is collected through the vertical porthole of the science chamber and redirected towards a water cooled EM-CCD camera. All of the camera software parameters were experimentally optimized and are reported here.

.

Experimental snapshot: Some more photons

The collection efficiency of the current fluorescence route is far from satisfying $\epsilon = 4.10^{-3}$. To palliate this limitation, another collection circuit was built, the idea being to image the atoms through different paths on the **same** and only EM-CCD camera we have. Below a schematic representation of this alternative route.

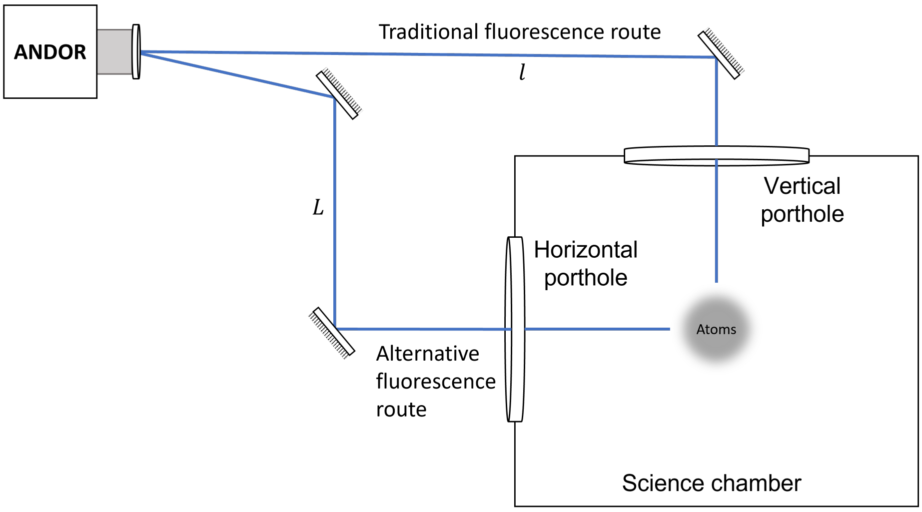

FIGURE 1.18: Schematic representation of the alternative fluorescence collection route. The geometrical length of this alternative route is much bigger than the traditional one $L \gg l$.

This endeavor however met with a small measure of success. Indeed, because of the greater geometrical length of this second path, the position dependent imaging inhomogeneities became, unforeseen to us, much more severe. In particular while atoms centered on the optical axis of the set up were adequately imaged, small displacements relative to this axis made them virtually disappear. This path could therefore not be used to track the dynamics of the seven spin states.

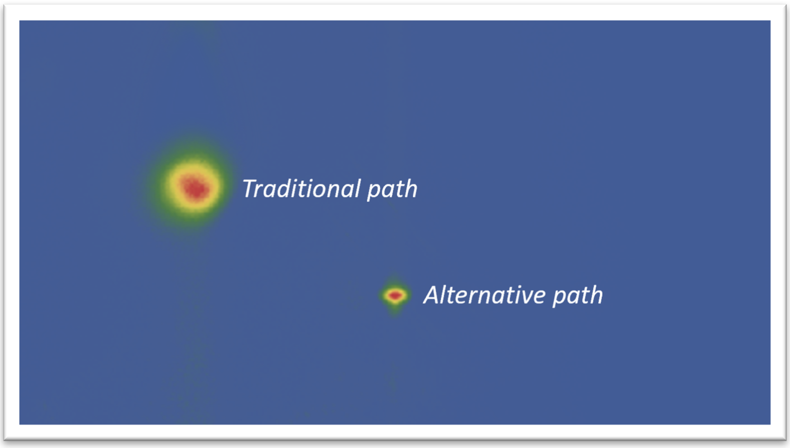

FIGURE 1.19: The same MOT, observed through both traditional and alternative fluorescence paths. The size difference is due to different focusing strategies: the traditional path is focused on the position of the condensate after time of flight, on the other hand the alternative path's optical axis being orthogonal to the fall trajectory of the atoms, the alternative set-up can be focused using the MOT's position which explains it small size on the image above.

2 Experimental noises and data statistical treatment

> *You cannot hear music and noise at the same time.*
>
> – Henry David Thoreau

As will be shown in Chap. 3, the build up of spin correlations between atoms is enclosed within the statistical distributions of Zeeman populations. These distributions however are distorted by various experimental noises. In this -***quite technical*** - *chapter we make an exhaustive inventory of these noises, their physical origin and their impact on the statistical properties of the Zeeman populations while at the same time giving a detailed account of the various methods used to apprehend experimental data and, if possible, unravel the role of the sole dipolar dynamics.*

Motivations and main results

It is common in experimental endeavors like ours which are based on the compilation of a great number of experimental shots that data be plagued with **shot to shot fluctuations of the total signal**[1]. It is also customary to normalize the data in order to get rid of the adverse impacts of these fluctuations.

In our case for example, each experimental realization provides us with a picture containing a certain number[2] of **clouds whose individual signals, hereafter denoted C_{m_s}, can be linked to the atomic Zeeman populations** i.e. the number of atoms in these clouds, hereafter denoted A_{m_s} and which we are interested in.

The fact is that these *Zeeman gray levels* or *Zeeman counts* (the C_{m_s}) **are not** the *Zeeman atomic* populations (A_{m_s}). **Zeeman counts carry with them the trace of the whole detection chain**, which, alas, **also contributes to their statistical properties**.

These **Zeeman counts can be seen as random variables**. This is the framework which we will be using in the totality of this chapter. When normalizing these Zeeman counts by their sum we obtain new random variables, the **normalized Zeeman counts** $C_{m_s}\Big/\sum_{m'_s} C_{m'_s}$.

This process is not trivial, in fact ratios of random variables are generally not well behaved (see sec. 2.2.6), and there are no generic relationships between the statistical properties of the non normalized variables and their normalized counterparts; and even if there were, one would still need to choose how to correct the normalized variables for the other statistical noises contributed by the detection chain. The statistical properties hence obtained are arguably different from those of the **normalized atomic populations**: $A_{m_s}\Big/\sum_{m'_s} A_{m'_s}$.

The main goal of this chapter is to circumvent all of the thorny issues which are brought about by this precocious normalization process: we want to **first get rid of the detection chain's contributions** *then* **perform the normalization process**. And this is exactly what we achieve.

The results presented in this chapter are based on the **systematic** use of **a single set of**

---

[1] In our case the shot to shot fluctuations of the total number of atoms in the condensate.

[2] $2S+1=7$ or 14 depending on whether or not we perform a bipartite measurement.

statistical theorems: the *law of total expectation*, the *law of total variance* and *the law of total covariance* (see sec. 2.1.3).
Repeatedly using these laws in **a reverse chronological way** and for each step of the detection process, we gradually recover the statistical properties (expected value, variance and covariances) of the *non normalized* atomic populations (the A_{m_s}). Then using the so called **Delta method** which only needs these exact statistical properties as inputs (and not the knowledge of each exact A_{m_s} for each single experimental shot) **we obtain the statistical properties of the normalized populations** $A_{m_s} \Big/ \sum_{m'_s} A_{m'_s}$ which are the variables we are interested in as they are immune to the atom number fluctuations.
We also provide a method for the **derivation of the effective gain** applied to **each and every experimental picture** we took using the amplification feature of our EM-CCD camera. We use this method to also take into account the fluctuations of this gain in our experiment, fluctuations which are mostly neglected in generic data treatment protocols.

2.1 Preliminary definitions

2.1.1 Expected values, variances and covariances

The **expected value** $\mathbb{E}(X)$ of a random variable X with a finite number of outcomes $x_1,...,x_k$ each of which has probability $p_1,...,p_k$ of occurring, is a weighted average of all these possible outcomes. It is defined as

$$\overline{X} = \mathbb{E}(X) = x_1 p_1 + ... + x_k p_k \tag{2.1}$$

The expected value is also called the *first moment* of the random variable X.

The **variance** of a random variable X is the expected value of the squared deviation of X from its expected value [52].

$$\text{Var}\,(X) = \mathbb{E}\left[(X - \mathbb{E}(X))^2\right] \tag{2.2}$$

The variance is also called the *second centered moment* of the random variable X.
In particular if X, Y are two independent random variables:

$$\text{Var}\,(XY) = \mathbb{E}(X)^2\text{Var}\,(Y) + \mathbb{E}(Y)^2\text{Var}\,(X) + \text{Var}\,(X)\,\text{Var}\,(Y) \tag{2.3}$$

This property is used in section 2.2.3.
The **covariance** of two -real valued- random variables X and Y is defined as the expected value of the product of their deviations from their respective expected values [53].

$$\text{cov}\,(X,Y) = \mathbb{E}\left[(X - \mathbb{E}(X))\,(Y - \mathbb{E}(Y))\right] \tag{2.4}$$

The covariance is also called the *central mixed moment of order two* relative to the X and Y variables.
If X and Y are independent variables then $\text{cov}\,(X,Y) = 0$

2.1.2 The conditional expected value

The **conditional expected value** of a random variable X is its expected value given that a certain set of "conditions" represented for example by a second random variable Y is known to occur. When the conditioning is done using this other random variable Y the conditional expected value will be denoted $\mathbb{E}(X \mid Y)$, similarly the conditioning can be done using the joint probability distribution of two random variables (Y,Z), in which case we will write $\mathbb{E}(X \mid (Y,Z))$ or $\mathbb{E}(X \mid Y,Z)$.
The conditional expected value can be seen as **a random variable or a function**: $\mathbb{E}(X \mid Y):$

$x \mapsto \mathbb{E}(X \mid Y = x)$.

Example [54]**:** Consider the roll of a fair die and let $A = 1$ if the number is even and $A = 0$ otherwise. Furthermore, let $B = 1$ if the number is prime and $B = 0$ otherwise

	1	2	3	4	5	6
A	0	1	0	1	0	1
B	0	1	1	0	1	0

$$\begin{aligned} \mathbb{E}(A) &= \frac{1}{2} \\ \mathbb{E}(A \mid B = 1) &= \frac{1}{3} \\ \mathbb{E}(A \mid B = 0) &= \frac{2}{3} \end{aligned} \tag{2.5}$$

The **conditional variance** is defined in the same manner.

2.1.3 Law of total...

...expectation

The *law of total expectation* (**LTE**) states that if X is a random variable whose expected value $\mathbb{E}(X)$ is defined, and Y is any random variable on the same probability space, then

$$\overline{X} = \mathbb{E}(X) = \mathbb{E}(\mathbb{E}(X \mid Y)) \tag{2.6}$$

...variance

The *law of total variance* (**LTV**) states that if X and Y are random variables on the same probability space, and the variance of X is finite, then

$$\mathrm{Var}\,(X) = \mathbb{E}[\mathrm{Var}\,(X \mid Y)] + \mathrm{Var}\,(\mathbb{E}[X \mid Y]) \tag{2.7}$$

...covariance

The *law of total covariance* (**LTC**) states that if X, Y, and Z are random variables on the same probability space, and the covariance of X and Y is finite, then

$$\mathrm{cov}\,(X, Y) = \mathrm{cov}(Y, X) = \mathbb{E}(\mathrm{cov}(X, Y \mid Z)) + \mathrm{cov}(\mathbb{E}(X \mid Z), \mathbb{E}(Y \mid Z)) \tag{2.8}$$

Graphical intuition

In this subsection we give, through a practical example, a graphical intuition of the law of total variance, the intuition behind the other laws is similar.

Let A be the random variable corresponding to the atomic population of a certain Zeeman cloud right after the system's quench. The distribution of the A variable is supposed (here) to be a function of the initial preparation angle $A = A(\theta)$.
Using the law of total variance, one has that:

$$\mathrm{Var}\,(A) = \mathrm{Var}\,(\mathbb{E}(A \mid \theta)) + \mathbb{E}(\mathrm{Var}\,(A \mid \theta)) \tag{2.9}$$

The first term $\mathrm{Var}\,(\mathbb{E}(A \mid \theta))$ represents the noise contribution of the θ variable as it would be zero if θ was a constant.
The second term is linked to the quantum fluctuations of the $\hat{A}$ observable and is non zero

even when θ is perfectly reproducible.

Below a graphical representation of both terms.

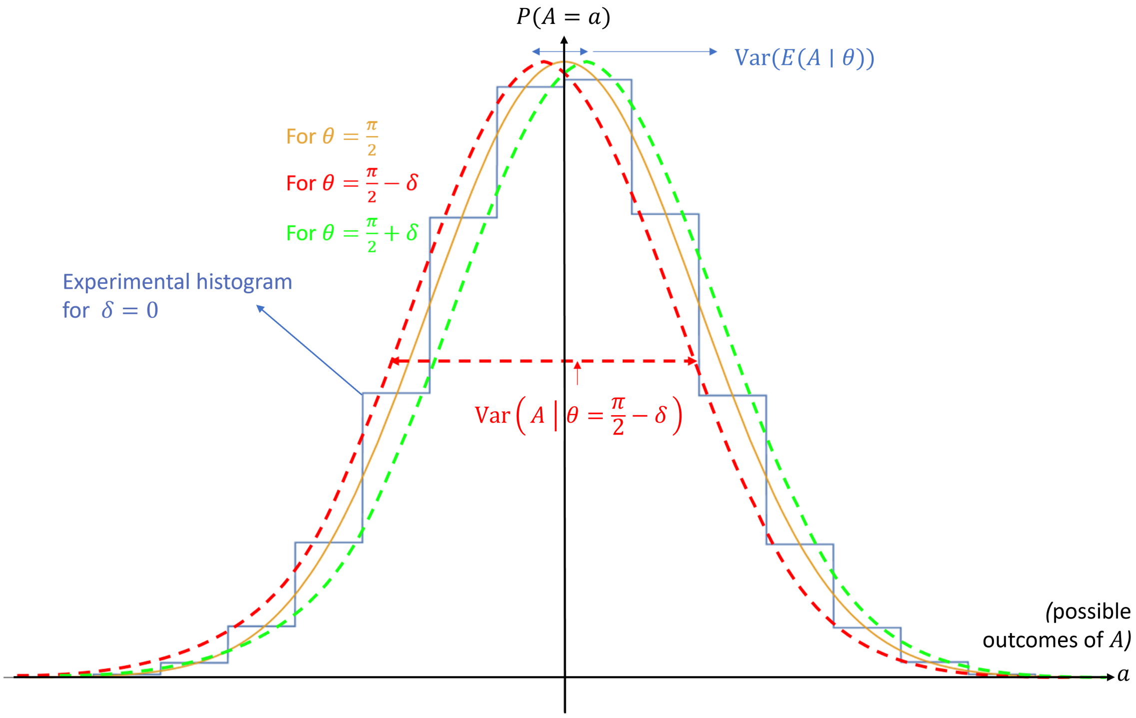

Figure 2.1: Representation of the distribution probability of A as a function of the initial preparation angle. Both noise contributions are shown. For a classical measurement, the **toy** Gaussian distribution above would transform into a Dirac distribution (no quantum fluctuations). We see then that only the $\mathrm{Var}(E(A|\theta))$ contribution would remain. If θ were constant, only the full line orange curve would be measured, and only the quantum fluctuations of the $\hat{A}$ observable would play a role. In the general case, the total variance is a sum of these two contributions

2.1.4 Recurrent probability distributions

The **Poisson distribution** noted Pois is a discrete probability distribution that expresses the probability of a given number of events occurring in a fixed interval of time or space if these events occur with a known constant mean rate λ and independently of the time since the last event [55].

$$X \sim \mathrm{Pois}(\lambda) \Leftrightarrow \mathbb{P}(X=k) = \frac{\lambda^k e^{-\lambda}}{k!} \tag{2.10}$$

For Poisson distributions, $\mathbb{E}(X) = \mathrm{Var}(X) = \lambda$.

Normal distributions are a type of continuous probability distribution which play an important role in statistics. They are noted $\mathcal{N}(\mu,\sigma)$, μ being the expected value of the distribution and σ its standard deviation.

$$X \sim \mathcal{N}(\mu,\sigma) \Leftrightarrow \mathbb{P}(X=x) = \frac{1}{\sqrt{2\pi}\sigma} e^{-\frac{(x-\mu)^2}{2\sigma^2}} \tag{2.11}$$

Bernoulli distribution represent the discrete probability distribution of a random variable which takes the value 1 with probability p and the value 0 with probability $q = 1-p$, for a fair coin flip $p = \frac{1}{2}$. p is the distribution's **parameter**. We also have $\mathbb{E}(X) = p$ and $\mathrm{Var}(X) = pq$.

2.1.5 On mixture distributions

In probability and statistics, a mixture distribution is the probability distribution of a random variable that is derived from a collection of other random variables as follows: first, a random variable is selected by chance from the collection according to given probabilities of selection, and then the value of the selected random variable is realized [56].

2.2 Experimental noises and data statistical treatment

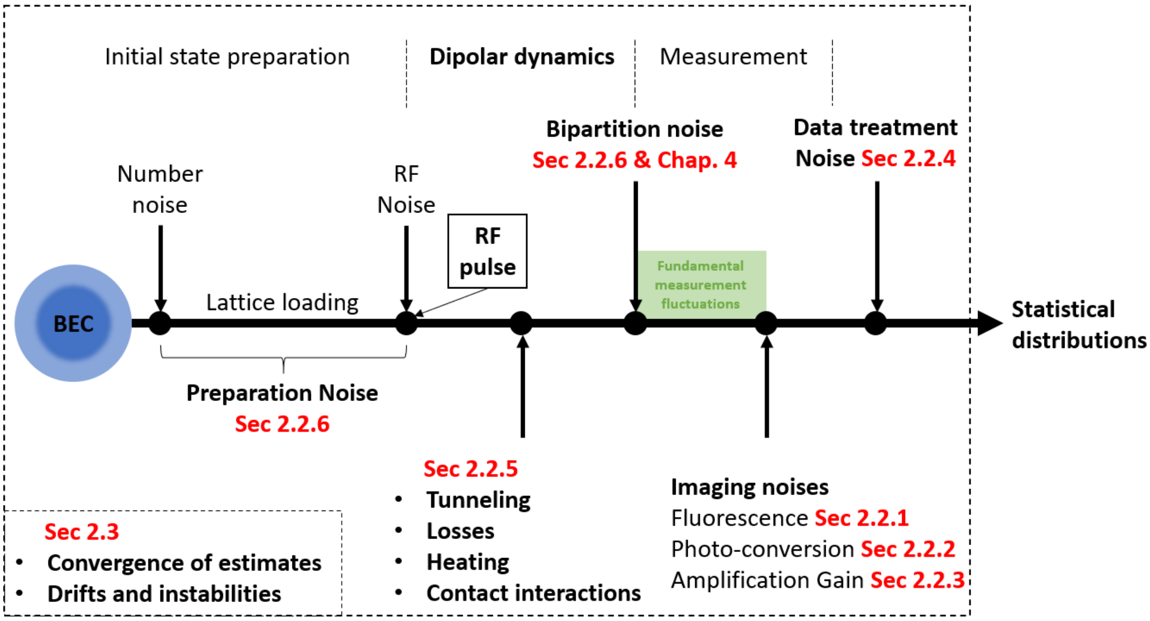

FIGURE 2.2: Chronological hierarchy of experimental noises. The fundamental measurement fluctuations also called in the following **quantum projection noise** are fluctuations of the measurement that arise whenever the system is in a superposition of eigenstates of the observable that is measured. All of these noises will be discussed in the coming pages. For convenience purposes, this discussion is carried in reverse chronological order. It starts with the imaging noises.

Our journey through noises starts shortly after the atoms have been released from the optical lattice, at this point the different spin states are separated using the Stern & Gerlach technique, and atoms are visualized through fluorescence imaging as described in Chap. 1 . ***It is at this stage that we encounter our first experimental noise***

2.2.1 Fluorescence noise and collection efficiency

In this first subsection we relate the statistical properties (first and second (mixed) moments) of the number of atoms in a given Zeeman cloud to the statistical properties of the number of spontaneous photons they emit.

Fluorescence is a stochastic phenomenon whose probability distribution for a two level atom is usually approximated by a **Poisson distribution**. Departures from this behavior when photon correlations are taken into account are small [57].

In the following, we'll suppose that chromium atoms' fluorescence obeys a Poisson distribution. Let $\tilde{n}_i$ be number of photons emitted by an atom i during time Θ. We'll assume that

$$\tilde{n}_i \sim \text{Pois}\left(f_i\Theta\right) \tag{2.12}$$

Where f_i depends on the nature of the transitions available to the decay process, as well as the **imaging** laser intensity.

Out of all emitted photons, only some travel towards the detector. When a photon is emitted by an atom it travels in a random direction $\vec{k}$. The random variable corresponding to the number of photons traveling to the detector is given by n_i

$$n_i = \sum_{k=1}^{\tilde{n}_i} \epsilon_k \tag{2.13}$$

Where the $\{\epsilon_k\}$ are **independent and identically distributed** (iid) Bernoulli variables of parameter ϵ. ϵ is nothing else but the collection efficiency of our imaging setup.

Notice that the sum's upper limit is given by $\tilde{n}_i$, it is itself a random variable, in other words the randomness of the n_i variable stems not only from the ϵ_k summands but also from the number of ϵ_k variables that are to be added together. We will face this kind of *double randomness* time and again in the following pages.

Using the results of sec. 2.1.4 we find

$$\begin{aligned} \overline{n_i} &\underset{\text{LTE}}{=} \mathbb{E}\left(\mathbb{E}\left(\sum^{\tilde{n}_i} \epsilon_k \mid \tilde{n}_i\right)\right) \\ \begin{array}{c}\text{Here}\tilde{n}_i\text{is temporarily fixed} \\ \text{because of the conditionning: the} \\ \text{number of summands} \\ \text{is no longer random}\end{array} \longrightarrow &= \mathbb{E}\left(\sum^{\tilde{n}_i} \mathbb{E}\left(\epsilon_k\right)\right) \\ &= \mathbb{E}\left(\tilde{n}_i\epsilon\right) \\ &= \epsilon f_i \Theta \end{aligned} \tag{2.14}$$

$$\begin{aligned} \text{Var}\left(n_i\right) &\underset{\text{LTV}}{=} \text{Var}\left(\mathbb{E}\left(\sum^{\tilde{n}_i} \epsilon_k \mid \tilde{n}_i\right)\right) + \mathbb{E}\left(\text{Var}\left(\sum^{\tilde{n}_i} \epsilon_k \mid \tilde{n}_i\right)\right) \\ &= \text{Var}\left(\tilde{n}_i\epsilon\right) + \mathbb{E}\left(\tilde{n}_i\epsilon\left(1-\epsilon\right)\right) \\ &= \epsilon^2 f_i\Theta + \epsilon(1-\epsilon) f_i\Theta \\ &= \epsilon f_i\Theta \end{aligned} \tag{2.15}$$

and as expected n_i **is again Poisson distributed**.

Consider now a random variable A **corresponding to a number of atoms subjected to the same experimental configuration (all atoms in a given Zeeman cloud for example)** then the f_i factor should be the same for all these atoms $f_i \to f$.

Further neglecting any sort of interactions between these ensembles of atoms make it so that the n_i variables are independent and identically distributed $(n_i \sim n)$. The sum total of photons emitted by this assembly of atoms is then $N = \sum_{i=1}^{A} n_i \equiv \sum_{i=1}^{A} n$ (notice that this sum is also *doubly random*). In the following N_i will be the number of photons emitted by the i^{th} Zeeman cloud constituted of A_i atoms.

As it turns out, while the sum of two independent Poisson distributions is also a Poisson distribution [3], the sum of a random number of Poisson variables is not a Poisson variable,

---

[3] Interestingly, according to Raikov's theorem, the converse is also true: *Suppose that a random variable ζ is Poisson distributed, suppose also that it can be decomposed into the sum $\zeta = \zeta_1 + \zeta_2$ of two independent random variables. Then the distribution of each summand is a shifted Poisson's distribution.*

indeed let us consider the characteristic function (cf) of the N variable, according to the law of total expectation

$$
\begin{aligned}
\mathrm{cf}(x) &= \mathbb{E}\left(e^{ixN}\right) = \mathbb{E}\left(\mathbb{E}\left(e^{ixN}|A\right)\right) \\
&= \mathbb{E}\left(\underbrace{\mathbb{E}\left(e^{ixnA} \mid A\right)}_{\substack{\text{characteristic function of} \\ \text{the nA Poisson variable} \\ \text{A is fixed}}}\right) \\
\mathrm{cf}_{\mathrm{Poiss}(\lambda)}(t) = e^{\lambda(e^{it}-1)} \longrightarrow &= \mathbb{E}\left(e^{\overline{n}A(e^{ix}-1)}\right) \\
&= \sum_{k=0}^{\infty} \frac{\left(\overline{n}\left(e^{ix}-1\right)\right)^k}{k!} \mathbb{E}\left(A^k\right)
\end{aligned}
\tag{2.16}
$$

A priori, this characteristic function is not the characteristic function of a Poisson Distribution which again is generally written: $\mathrm{cf}_{Poiss}(t) = e^{\lambda(e^{it}-1)}$ with λ the parameter of the distribution that is considered. N is therefore **not Poisson distributed**: **The light emitted by the atoms over a series of shots is not Poisson distributed**. Still, using the law of total expectation, we can calculate the expected value of N

$$
\overline{N} = \mathbb{E}\left(\epsilon f \Theta A\right) = \epsilon f \Theta \overline{A} = \overline{n}\overline{A}
\tag{2.17}
$$

Whereas using the law of total variance, we get the variance

$$
\begin{aligned}
\mathrm{Var}\left(N\right) &= \mathrm{Var}\left(\sum_{i}^{A} \overline{n}_i\right) + \mathbb{E}\left(\sum_{i}^{A} \mathrm{Var}\left(n_i\right)\right) \\
&= \overline{n}^2 \mathrm{Var}\left(A\right) + \overline{n}\overline{A}
\end{aligned}
\tag{2.18}
$$

Notice that if A were perfectly determined ($\mathrm{Var}\left(A\right) = 0$), N would indeed be Poisson distributed.
Using the law of total covariance, we get **for $\mathbf{i \neq j}$**

$$
\begin{aligned}
\mathrm{cov}\left(N_i, N_j\right) &= \mathrm{cov}\left(\sum^{A_i} n_i, \sum^{A_j} n_j\right) \\
&= \mathbb{E}\left(\mathrm{cov}\left(\sum^{A_i} n_i, \sum^{A_j} n_j | A_i, A_j\right)\right) + \mathrm{cov}\left(\mathbb{E}\left(\sum^{A_i} n_i | A_i, A_j\right), \mathbb{E}\left(\sum^{A_j} n_j | A_i, A_j\right)\right) \\
&= \mathbb{E}\left(\sum_{k,k'} \mathbb{1}_{k<A_i \cap k'<A_j} \underbrace{\mathrm{cov}\left(n_i, n_j\right)}_{0}\right) + \mathrm{cov}\left(\overline{n_i} A_i, \overline{n_j} A_j\right) \\
&= \overline{n_i}\ \overline{n_j} \mathrm{cov}\left(A_i, A_j\right)
\end{aligned}
\tag{2.19}
$$

Impact of

- Fluorescence noise

$$\begin{aligned}\overline{N} &= \overline{n}\overline{A}\\ \mathrm{Var}\left(N\right) &= \overline{n}^2\mathrm{Var}\left(A\right) + \overline{n}\overline{A}\\ \mathrm{cov}\left(N_i, N_j\right) &= \overline{n_i}\ \overline{n_j}\mathrm{cov}\left(A_i, A_j\right)\end{aligned} \tag{2.20}$$

These equations give the statistical relationships between the number of photons emitted by the atoms towards the camera, N, and the number of atoms in the Zeeman clouds, A.

The photons represented by the variable N are those that are intercepted by the camera's chip. The detection process involves the photoelectric process in which lies the second experimental noise we will analyze.

2.2.2 Photoconversion noise

In this second subsection we relate the statistical properties of the number of atoms in a given Zeeman cloud to the statistical properties of the electronic signal generated upon conversion of the photons to electrons in the camera's chip and before the amplification of this electronic signal in the gain register.

Let η be the random variable corresponding to the possible conversion of a photon hitting any given pixel, $\overline{\eta} = 0.82$ at 425 nm.
Let E_{px} be the random variable corresponding to the number of electrons generated through the photodetection of N_{px} impinging photons on pixel px

$$E_{px} = \sum_{k}^{N_{px}} \eta_k \tag{2.21}$$

In this formalism, the η_k are iid Bernoulli variables of parameter $\overline{\eta}$ and variance $\overline{\eta}(1-\overline{\eta})$.
Using the law of total expectation:

$$\overline{E_{px}} = \overline{\eta}\ \overline{N_{px}} \tag{2.22}$$

Using the law of total variance

$$\mathrm{Var}\left(E_{px}\right) = \overline{\eta}^2\mathrm{Var}\left(N_{px}\right) + \overline{\eta}(1-\overline{\eta})\overline{N_{px}} \tag{2.23}$$

Using the law of total covariance assuming the photoconversions in each pixel to be independent

$$\mathrm{cov}\left(E_{px}, E_{px'}\right) = \overline{\eta}^2\mathrm{cov}\left(N_{px}, N_{px'}\right) \tag{2.24}$$

Where px and px' designate two different pixels.
We have considered here that all photoconversion processes are independent of the number of

impinging photons, this is quite reasonable for small photon numbers and holds in our case as we are far from saturating the camera and related blooming effects.
Considering now an assembly of pixel illuminated by the light emitted by a single Zeeman

state, we have

$$E = \sum_{px} E_{px} \tag{2.25}$$

The average signal due to N impinging photons is given by

$$\overline{E} = \sum_{px} \overline{E_{px}} = \overline{\eta}\ \overline{N} = \overline{\eta}\ \overline{n}\overline{A} \tag{2.26}$$

The variance is

$$\begin{aligned}
\mathrm{Var}\,(E) = \sum_{px} \mathrm{Var}\left(E_{px}\right) + 2 \sum_{px<px'} \mathrm{cov}\left(E_{px}, E_{px'}\right) &= \overline{\eta}^2 \sum_{px} \mathrm{Var}\left(N_{px}\right) + \overline{\eta}(1-\overline{\eta})\overline{N} + 2 \sum_{px<px'} \overline{\eta}^2 \mathrm{cov}\left(N_{px}, N_{px'}\right) \\
&= \underbrace{\overline{\eta}^2 \sum_{px} \mathrm{Var}\left(N_{px}\right) + 2 \sum_{px<px'} \overline{\eta}^2 \mathrm{cov}\left(N_{px}, N_{px'}\right)}_{\overline{\eta}^2 \mathrm{Var}(N)} + \overline{\eta}(1-\overline{\eta})\overline{N} \\
&= \overline{\eta}^2 \mathrm{Var}\,(N) + \overline{\eta}(1-\overline{\eta})\overline{N} \\
&= \overline{\eta}^2 \left(\overline{n}^2 \mathrm{Var}\,(A) + \overline{n}\overline{A}\right) + \overline{\eta}(1-\overline{\eta})\overline{n}\overline{A} \\
&= \overline{\eta}^2\ \overline{n}^2 \mathrm{Var}\,(A) + \overline{\eta}\ \overline{n}\ \overline{A}
\end{aligned} \tag{2.27}$$

Is the camera's input electronic signal E Poisson distributed?
For E to be Poisson distributed its variance should be equal to its expected value, and therefore the first term of the previous equation should be negligible.
In our experiment, the total atom number fluctuations are about 10%, while atom numbers in a single cloud are ≈ 1000 in average which means that $\mathrm{Var}\,(A) \approx 10000$. On the other hand $\overline{\eta} = 0.8$, which implies that for the first term of this equation $\overline{\eta}^2\ \overline{n}^2 \mathrm{Var}\,(A)$ to be negligible, $\overline{n}$ should be $\ll 1$. This is not the case: indeed the number of photons scattered by an atom (assuming that we strongly saturate the imaging transition and that the MOT lasers are resonant) in Δt =1 ms (which is the approximate duration of the imaging pulses) is $\approx \frac{\Gamma}{2} \times \Delta t \simeq 1.5 \times 10^4$ where $\Gamma = 2\pi \times 5 \times 10^6$, taking into account the collection efficiency of our set-up,$\epsilon \simeq 4.10^{-3}$, the number of photons hitting the camera is $\overline{n} \simeq 60$ photons. Experimentally we find that the number of photons emitted by a single atom is $\approx 7-13$ which can be accounted for by the detuning of the imaging lasers. This implies in particular that **the E variables distribution are superpoissonian**. The contribution of this excess variance wherein hides the quantum projection noise - that we are looking for - increases with the detection efficiency.

The covariance between signals originating from two different clouds (i and j) (the derivation below is similar to the one detailed in 2.19)

$$\begin{aligned}
\mathrm{cov}(E_i, E_j) &= \sum_{px} \sum_{px'} \mathrm{cov}\Big(\sum^{N_{i,px}} \eta, \sum^{N_{j,px'}} \eta\Big) \\
&= \sum_{px} \sum_{px'} \overline{\eta}^2 \mathrm{cov}\left(N_{i,px}, N_{j,px'}\right) \\
&= \overline{\eta}^2 \mathrm{cov}\left(N_i, N_j\right) \\
&= \overline{\eta}^2 \overline{n_i}\ \overline{n_j} \mathrm{cov}\left(A_i, A_j\right)
\end{aligned} \tag{2.28}$$

Impact of

- Fluorescence noise
- Photoconversion noise

$$\begin{aligned}\overline{E} &= \overline{\eta}\ \overline{n}\overline{A}\\ \mathrm{Var}\left(E\right) &= \overline{\eta}^2\ \overline{n}^2\mathrm{Var}\left(A\right) + \overline{\eta}\ \overline{n}\ \overline{A} \qquad (2.29)\\ \mathrm{cov}\left(E_i, E_j\right) &= \overline{\eta}^2\overline{n_i}\ \overline{n_j}\mathrm{cov}\left(A_i, A_j\right)\end{aligned}$$

These equations give the relations between the input electronic signal of the camera E and the number of atoms A.

Remark: The structures of the Eqs. 2.20 and 2.29 are the same, this is because the two noises we have considered here are of the same nature and can be basically grouped together into a single Bernoulli variable with parameter $\overline{\eta}\ \overline{n}$. The amplification noise we discuss next is of different nature, and it is harder to predict the form these equations will take.

When the photons hit the camera's chip, some of them are transformed into electrons. This part we have just described. Afterwards, these so-called photo-electrons are dragged through the imaging chip into a gain register. Using high voltages and making use of impact ionization phenomena, the number of electrons is multiplied by a certain average factor we call gain. Impact ionizations may or may not happen as the electrons travel through the gain register, making this amplification process a stochastic one. This is the third noise that we consider.

2.2.3 EM-CCD camera basics, single shot gain computation algorithm, and amplification noise

In the first part of this section, we describe the basic architecture of the EM-CCD camera used in the experiment. This understanding allows us to devise a novel ***single shot gain computation algorithm*** *later used for the statistical treatment of experimental data. In the second part of this section, we relate the statistical properties of the number of counts (pixel's grey level intensity) to the atomic ones.*

Part 1: EM-CCD camera, from operation principles to single shot gain computation algorithm

We call *primary electrons* the mixture of all (spurious and photo) electrons reaching the read-out register (see Fig. 2.3). The particularity of EM-CCD camera lies not in this register but in the following one, the so called *gain register* wherein secondary electrons are spawned in great numbers through impact ionization. Primary and secondary electrons all add up to a certain number of *post-amplification electrons*.

Assuming that each pixel charge amplification happens independently of other pixels' amplification processes and that no spurious electrons are generated in the gain register, the probability distribution $\mathscr{F}$ describing the number of *post-amplification electrons*, n_{pe}, is given by [58][59].

$$\mathscr{F}\left(n_{pe} = x\right) = p_0\delta_{x,0} + \sum_{n_p} p_{n_p}\frac{x^{n_p-1}e^{-\frac{x}{g}}}{g^{n_p}\left(n_p-1\right)!} \tag{2.30}$$

Where

- p_{n_p} is the probability of getting a total pixel charge (i.e. a certain number of primary electrons) of n_p electrons
- g is the **mean gain**, that is the average of the amplification factors applied to all the pixels **in a single picture**

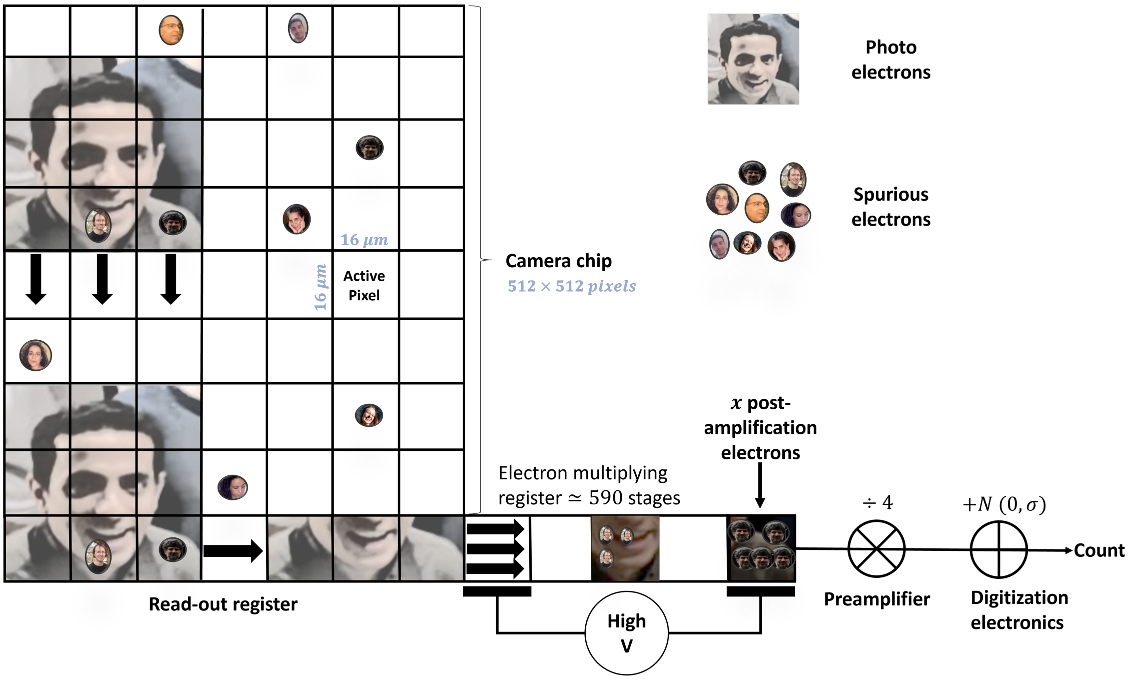

FIGURE 2.3: Photons impinging onto the camera's chip give birth to *photo-electrons* which are in turn brought down to the *gain register* together with spurious electrons (thermal electrons, CIC and such). At this point both kinds are indistinguishable. The black arrows indicate the direction in which pixels' charges are moved. In the case at hand there is only one Laurent[4]spurious electron before amplification and $x = 5$ Laurent spurious electrons after amplification, going through the preamplifier, these 5 Laurent electrons will be divided by 4 giving an **integer number** of counts equal to **1** and not **1.25**. The story is not finished yet as an additional Gaussian distributed random number of counts will be added to them when going through the digitization electronics (Read Noise)

After the amplification process these *post-amplification electrons* are *read-out*[5]. The read-out includes both the passage of electrons through the *preamplifier and the analog to digital conversion.*

As we understand it, these operations have two distinct effects, the first one is that every 4[6] charges are converted into a single count[7], this is the effect of the preamplifier (according to the manufacturer). The second effect is that this count reading is further blurred out by a Gaussian noise $\sim \mathcal{N}_{0,\sigma}$ whose origin lies in the workings of the digitization electronics.

All in all, the probability that a single pixel's charge correspond to "x counts" post readout is the probability of the digitization electronics producing "i" counts **times** the probability of having **not** "$4(x-i)$" **but** "$4(x-i)-2$", "$4(x-i)-1$", "$4(x-i)$", or "$4(x-i)+1$" electrons before the preamplifier. This is because all these charges are the same modulo 4 and will be read as $x-i$ after the preamplifier

---

[5] While the terms are similar, this specific reading-out happens not in the read-out register but in the output node

[6] 4.01 according to the manufacturer

[7] The discrete nature of the charges must be taken into account when making for this dubious "division operation"

All in all, these counts distribution probability is given by the Cauchy product:

$$\mathscr{C}(x) = \sum_{i=-i_{max}}^{i_{max}} \left[\mathscr{N}_{0,\sigma}(i) \times \sum_{j=-2}^{1} \mathscr{F}(4(x-i)+j) \right] \tag{2.31}$$

Where

- The sum over j accounts for the effect of the preamplifier and the discrete nature of the charges: here, we assume that the number of charge post division is round up. So for example $\frac{14e^-}{4} \equiv \frac{15e^-}{4} \equiv \frac{16e^-}{4} \equiv \frac{17e^-}{4} \equiv 4$

This theory can be checked against experimental data as $\mathscr{C}(x)$ should accurately describe the distribution of counts across all pixels, as long as the p_{n_p} are given.
Using this distribution function, we can surmise the gain effectively applied to each of the images composing the experimental data.
To do so, we consider image regions which are *mostly unexposed*[8] to the light scattered by the atoms. We call these regions *dark regions* as opposed to *bright regions* that contain the light scattered by the atoms. The total charge per pixel in these regions is low[9] and is in any case Poisson distributed (i.e. $p_{n_p} = \frac{\lambda^{n_p} e^{-\lambda}}{n_p!}$, where λ is the expected value of the distribution)[10].
For these pixels the model above is valid, still it contains too many variables (λ, σ, g) for fits to be efficient or reliable. Thankfully, all parameters can be expressed in terms of the mean gain g and the characteristics of the experimental data. Indeed one can easily show that (assuming the model to be right)

$$\begin{gathered} \text{Law of total expectation} \rightarrow \frac{\lambda g}{4.01} = \text{mean of empirical data} \\ \text{Law of total variance} \rightarrow \frac{2g^2\lambda}{4.01^2} + \sigma^2 \simeq \text{ variance of empirical data} \end{gathered} \tag{2.32}$$

With these equations, which relate λ and σ to g, the fits only depend on the single parameter g.

---

[8] This can be ascertained by checking the signal in said region against dark images, i.e. images collected by the camera when its internal shutter is closed.

[9] Which helps in truncating the sum in equation 2.30.

[10] The total charge per pixel in these regions is given by the sum of the spurious electrons whose distribution follows a Poisson law and the diffuse light falling on the sensor which also follows a Poisson law. The sum of two Poisson laws is also a Poisson law.

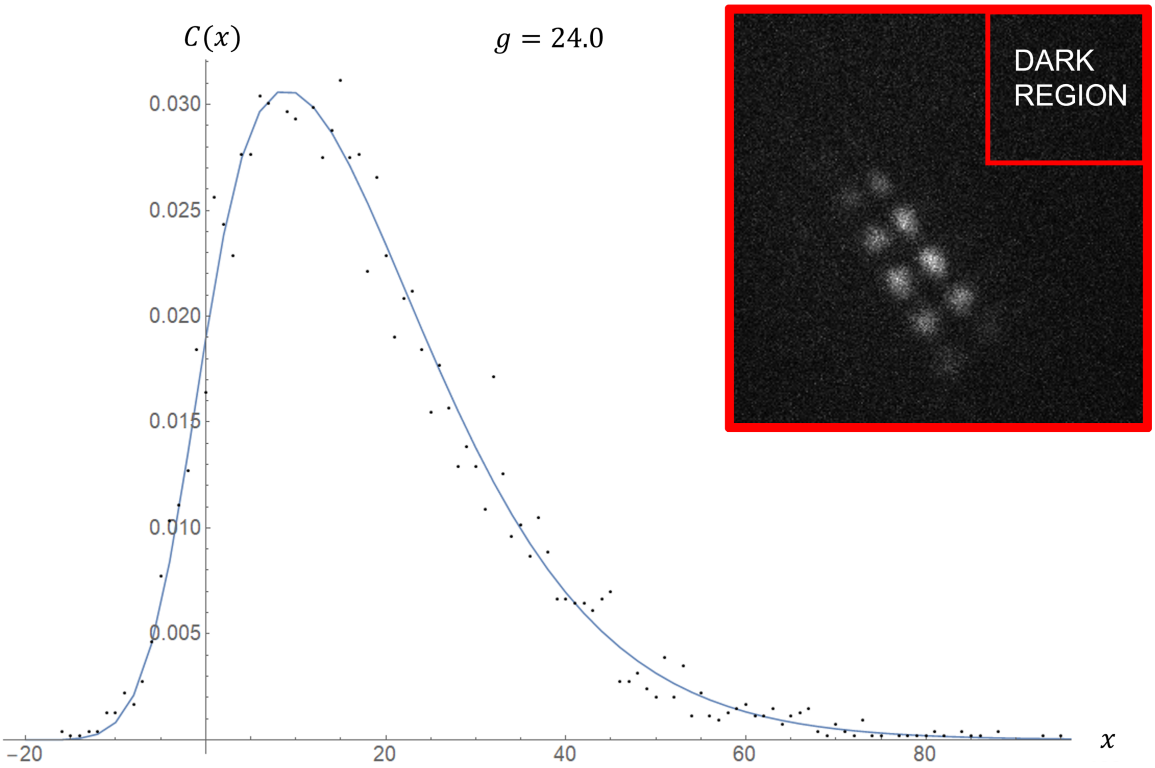

FIGURE 2.4: Fit of the $\mathscr{C}(x)$ distribution for a single picture dark region. The experimental data is given by the black points, the theoretical fit is given by the blue line. g is the gain found by the fitting process. This is the output of the **single shot gain algorithm** when applied to a single image. Notice that this image is an actual experimental image, the single shot gain algorithm does not need for secondary calibration images to be taken for it to work. The number of pixels in the dark region is greater than 5000. For this image the gain announced by the software is 30.

Typical gain statistical characteristics as derived by the single shot gain algorithm [11]:

$$\begin{aligned} \overline{g} &= 24.80 \\ \Delta g &= 0.72 \\ \overline{\delta g} &= 0.23 \\ \overline{\sigma} &= 5.03 \end{aligned} \tag{2.33}$$

Where

- $\overline{\delta g}$ is the mean fit standard error for g over a series of fits. Notice that $\overline{\delta g} < \Delta g$, this means that the standard error for individual fits is smaller than the standard deviation of the gain over the whole series: the shot to shot determination of the gain is precise enough and can indeed resolve the typical experimental fluctuations of the gain.

The mean value of the gain g was also checked using more down to earth methods (see caption of Fig. 2.5), in accordance with the single shot gain algorithm the values displayed by the camera software proved to be systematically overestimating the real gain applied by the camera.

---

[11] The statistics were derived from a series of 70 pictures taken for a software gain equal to 30, a preamplifier set to 4.9, and a readout rate of 1MHz

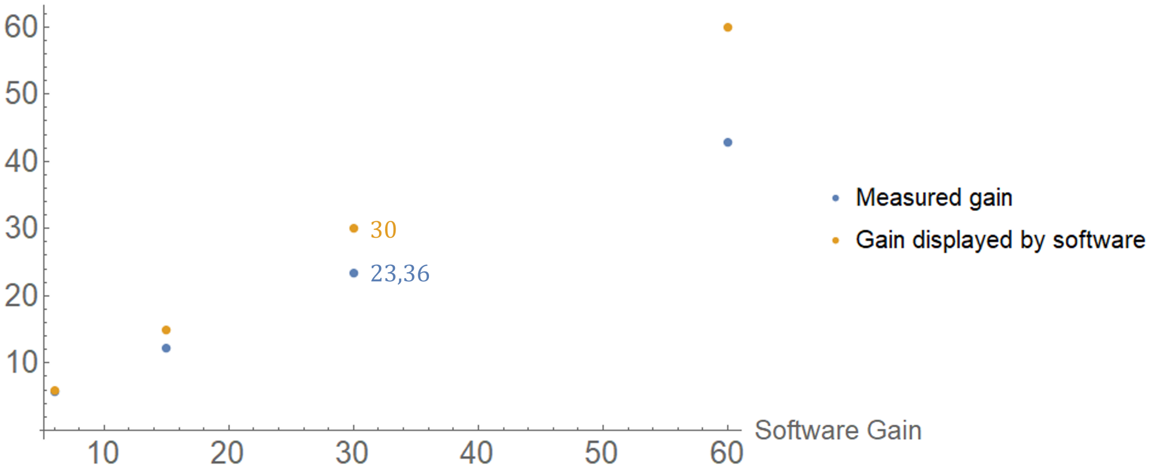

FIGURE 2.5: The mean gain applied by the camera was measured for different settings. This specific measurement relied on the comparison between laser signals' **averages** with and without amplification. The signal averages were computed over hundreds of shots. This measurement is spoiled by the laser power drifts and fluctuations. Still the results are very much in agreement with those found in Fig.2.4. Usually the software gain is set to 30, this value overestimates the real gain (23.36 as found using this method). This method is used as a confirmation test of the single shot gain algorithm, it cannot however be used to find the effective gain used for a given picture. Uncertainties on the values of the gain found through this method are also bigger than those of the single shot gain algorithm.

Part 2: Amplification noise

We have now better understood the workings of the EM-CCD camera, we have in particular observed that the electron amplification process is a stochastic one, and that it is characterized (over a series of pictures) by a mean gain $\overline{g}$ *and a standard deviation* Δg *which we can precisely compute using the single shot gain computation algorithm we have devised. We now move on to the impact of this amplification process on the various moments which we are interested in.*

After the amplification process electrons are converted into a certain number of counts. The final **count number for any given cloud** is given by:

$$C = \sum_{px} G(E_{px}) + RN \tag{2.34}$$

Where

- G is a *stochastic function* describing the complex operations happening within the camera
- RN is a normally distributed random variable accounting for the read noise, **this variable will be taken into account in the following section together with the data treatment noise**

Considering a single picture (i.e the gain is fixed and is the same for all pixels), we have

$$\begin{aligned} &\mathbb{E}\left(\sum_{px} G(E_{px})|(E_{px}, g)\right) = \sum_{px} \frac{g}{4.01} E_{px} \\ \Leftrightarrow &\mathbb{E}\left(\sum_{px} G(E_{px})|(E_{px}, g)\right) \simeq \frac{gE}{4.01} \\ \Rightarrow &\mathbb{E}\left(C|E, g\right) \simeq \frac{gE}{4.01} \end{aligned} \tag{2.35}$$

The conditioning here is done on two variables, but obeys the same principles as previous ones, in particular $G(E_{px})|(E_{px}, g)$ is a random variable whose, expected value for example, will depend on the outcome of the conditioning variables. It is clear for instance that $G(E_{px})|(E_{px} = 5, g = 30)$ is a random variable that is quite different from $G(E_{px})|(E_{px} = 0, g = 30)$ whose only possible outcome is 0 (if we neglect the RN variable).

In any case, using the law of total expectation and assuming that the gain, g, is independent from
the input signal we find that

$$\overline{C} = \overline{\frac{gE}{4.01}} = \frac{\overline{g}\;\overline{E}}{4.01} = \underbrace{\frac{\overline{g}}{4.01}\overline{\eta}\;\overline{n}}_{\alpha}\overline{A} = \alpha\overline{A} \tag{2.36}$$

Whereas[12], using the **law of total variance** on 2.35, and property 2.3

$$\operatorname{Var}\left(\mathbb{E}\left(C \mid E, g\right)\right) = \frac{\operatorname{Var}\left(g\right)\operatorname{Var}\left(E\right) + \overline{g}^2\operatorname{Var}\left(E\right) + \operatorname{Var}\left(g\right)\overline{E}^2}{4.01^2} \tag{2.37}$$

and following [60], we get the following sequences of equalities

$$\begin{aligned} \mathbb{E}\left(\operatorname{Var}\left(C|E, g\right)\right) &= \mathbb{E}\left(\sum \operatorname{Var}\left(G\left(E_{px}|E, g\right)\right)\right) \\ [60] \;\rightarrow &= \mathbb{E}\left(\frac{g^2}{4.01^2}E\right) \\ &= \frac{\overline{g^2}}{4.01^2}\overline{E} \end{aligned} \tag{2.38}$$

---

[12] Forgetting about the RN variable which will be included in the following section

Finally, we find using the law of total variance

$$\begin{aligned}
\mathrm{Var}\,(C) &= \mathrm{Var}\left(\mathbb{E}(C|E,g)\right) + \mathbb{E}\left(\mathrm{Var}\left(C|E,g\right)\right)\\
&= \frac{\mathrm{Var}\left(g\right)\mathrm{Var}\,(E) + \overline{g}^2\mathrm{Var}\,(E) + \mathrm{Var}\left(g\right)\overline{E}^2}{4.01^2} + \frac{\overline{g^2}}{4.01^2}\overline{E}\\
\mathrm{Var}\left(g\right) = \overline{g^2} - \overline{g}^2 \longrightarrow = &= \frac{\overline{g^2}\mathrm{Var}\,(E) + \mathrm{Var}\left(g\right)\overline{E}^2}{4.01^2} + \frac{\overline{g^2}}{4.01^2}\overline{E}\\
{*}{*}{*} &= \frac{\overline{g^2}\left(\overline{\eta}^2\ \overline{n}^2\mathrm{Var}\,(A) + \overline{\eta}\ \overline{n}\ \overline{A}\right) + \mathrm{Var}\left(g\right)\left(\overline{\eta}\ \overline{n}\overline{A}\right)^2}{4.01^2} + \frac{\overline{g^2}}{4.01^2}\left(\overline{\eta}\ \overline{n}\overline{A}\right)\\
&= \underbrace{\frac{\overline{g^2}}{\overline{g}^2}}_{\gamma}\ \frac{\overline{g}^2\left(\overline{\eta}^2\ \overline{n}^2\mathrm{Var}\,(A) + \overline{\eta}\ \overline{n}\ \overline{A}\right)}{4.01^2} + \frac{\mathrm{Var}\left(g\right)}{\overline{g}^2}\frac{\overline{g}^2\left(\overline{\eta}\ \overline{n}\overline{A}\right)^2}{4.01^2} + \frac{\overline{g^2}}{4.01^2}\left(\overline{\eta}\ \overline{n}\overline{A}\right)\\
&= \gamma\alpha^2\mathrm{Var}\,(A) + \frac{\overline{g}\gamma}{4.01}\alpha\overline{A} + \frac{\mathrm{Var}\left(g\right)}{\overline{g}^2}\alpha^2\overline{A}^2 + \frac{\overline{g}\gamma}{4.01}\alpha\overline{A}\\
&= \gamma\alpha^2\mathrm{Var}\,(A) + \frac{\mathrm{Var}\left(g\right)}{\overline{g}^2}\alpha^2\overline{A}^2 + 2\gamma\frac{\overline{g}}{4.01}\alpha\overline{A}\\
&= \gamma\alpha^2\mathrm{Var}\,(A) + \frac{\mathrm{Var}\left(g\right)}{\overline{g}^2}\overline{C}^2 + 2\gamma\frac{\overline{g}}{4.01}\overline{C}\\
\Leftrightarrow \gamma\alpha^2\mathrm{Var}\,(A) &= \mathrm{Var}\,(C) - \frac{\mathrm{Var}\left(g\right)}{\overline{g}^2}\overline{C}^2 - 2\gamma\frac{\overline{g}}{4.01}\overline{C}\\
\Leftrightarrow \mathrm{Var}\,(A) &= \frac{\mathrm{Var}\,(C) - \frac{\mathrm{Var}(g)}{\overline{g}^2}\overline{C}^2 - 2\gamma\frac{\overline{g}}{4.01}\overline{C}}{\gamma\alpha^2}
\end{aligned} \tag{2.39}$$

Notice that if we neglect the variance on the mean gain g then $\Delta g = 0$ and[13], $\overline{g^2} = \overline{g}^2$, taking $E_i \sim \mathrm{Pois}(\lambda)$, the third line (***) of the sequence above becomes:

$$\mathrm{Var}\,(C) = 2\frac{\overline{g^2}}{4.01^2}\overline{E} \tag{2.40}$$

The factor 2 here is the so-called excess noise factor discussed in previously referenced articles, in [60] and in most works dealing with EM-CCD amplification. As far as the variance of the input (E) and output (C) signals are concerned, this factor 2 is the main signature of the stochastic nature of the amplification process. Put otherwise, if the amplification could be reduced to a simple deterministic multiplication, the proportionality factor between both would simply be $\frac{\overline{g^2}}{4.01^2}$. The factor 2 in Eq. 2.40 is specific of Poisson distributed E inputs. **The laws that we derive (***) are however more general as they do not need the E input signal to be Poisson distributed**, which it is not as shown in 2.27. Moreover **the terms involving the variance of the gain Δg and γ are in general not discussed or even taken into account in the literature**.

What about covariances ? In this case, we know that $(i \neq j)$

$$\mathbb{E}(C_i C_j | E_i, E_j) = \frac{g^2 E_i E_j}{4.01^2} \tag{2.41}$$

---

[13] Actually $\gamma \simeq 1.002$

Therefore

$$\begin{aligned}
\operatorname{cov}\left(C_i,C_j\right) &= \frac{\overline{g^2}\,\overline{E_iE_j}}{4.01^2}-\frac{\bar{g}^2\,\overline{E_i}\;\overline{E_j}}{4.01^2}\\
\Leftrightarrow \overline{E_iE_j} &= \frac{4.01^2}{\overline{g^2}}\operatorname{cov}\left(C_i,C_j\right)+\frac{\bar{g}^2}{\overline{g^2}}\overline{E_i}\;\overline{E_j}\\
\Leftrightarrow \operatorname{cov}\left(E_i,E_j\right) &= \frac{4.01^2}{\overline{g^2}}\operatorname{cov}\left(C_i,C_j\right)+\left(\frac{1-\gamma}{\gamma}\right)\overline{E_i}\;\overline{E_j}\\
\Leftrightarrow \overline{n_i}\;\overline{n_j}\;\bar{\eta}\;\bar{\eta}\operatorname{cov}\left(A_i,A_j\right) &= \frac{4.01^2}{\overline{g^2}}\frac{\bar{g}^2}{\bar{g}^2}\operatorname{cov}\left(C_i,C_j\right)+\left(\frac{1-\gamma}{\gamma}\right)\frac{4.01^2}{\bar{g}^2}\overline{C_i}\;\overline{C_j}\\
\Leftrightarrow \operatorname{cov}\left(A_i,A_j\right) &= \frac{4.01^2}{\gamma\overline{n_i}\;\overline{n_j}\;\bar{\eta}\;\bar{\eta}\;\bar{g}^2}\operatorname{cov}\left(C_i,C_j\right)+\left(\frac{1-\gamma}{\gamma}\right)\frac{4.01^2}{\bar{g}^2\overline{n_i}\;\overline{n_j}\;\bar{\eta}\;\bar{\eta}}\overline{C_i}\;\overline{C_j}\\
\Leftrightarrow \operatorname{cov}\left(A_i,A_j\right) &= \frac{\operatorname{cov}\left(C_i,C_j\right)+(1-\gamma)\overline{C_i}\;\overline{C_j}}{\gamma\alpha_i\alpha_j}
\end{aligned}\tag{2.42}$$

Impact of

- Fluorescence noise
- Photoconversion noise
- Amplification noise

$$\begin{aligned}
\bar{A} &= \frac{\bar{C}}{\alpha}\\
\operatorname{Var}(A) &= \frac{\operatorname{Var}(C)-\frac{\operatorname{Var}(g)}{\bar{g}^2}\bar{C}^2-2\gamma\frac{\bar{g}}{4.01}\bar{C}}{\gamma\alpha^2}\\
\operatorname{cov}\left(A_i,A_j\right) &= \frac{\operatorname{cov}\left(C_i,C_j\right)+(1-\gamma)\overline{C_i}\;\overline{C_j}}{\gamma\alpha_i\alpha_j}
\end{aligned}\tag{2.43}$$

- $\alpha=\frac{\bar{g}}{4.01}\bar{\eta}\;\bar{n}$
- $\gamma=\frac{\overline{g^2}}{\bar{g}^2}$

These equations give the relations between the output electronic signal of the camera, i.e. the number of counts C and the number of atoms A.

The number of counts in each Zeeman cloud C_i whose statistics we have just derived is generally retrieved by fitting the clouds shape with a Gaussian model. This method comes with inherent uncertainty which adds together with the pixel to pixel noise captured by the RN variable mentioned in the beginning of this section. It is this uncertainty or data treatment noise that we now examine.

2.2.4 Data treatment and pixel to pixel noise

Images obtained through repeated experiments contain a certain amount of information which we can try to retrieve through various methods such as morphological analysis, 2D fitting and 1D fitting algorithms. Whatever the chosen method, the information retrieved is not equivalent to the information contained in the images which remains unknown. This distortion corresponds to what we call *data treatment noise*. In our case, we have chosen to use more or less sophisticated 1D fitting algorithms to retrieve the information enclosed in the images, the typical distortion[14], that is the typical error associated to the determination of the fit's parameters. Estimates for the fit's standard error can be found using bootstrapping (see [61]).

In any case, the effect of the data treatment process can be modeled by an additional Gaussian noise which, with the readout or pixel to pixel noise that we neglected in the previous section, still form into a Gaussian noise $W \sim \mathcal{N}(\mu = 0, w)$[15]. The only effect of this Gaussian noise is to modify the variance of the count populations as it should be equally probable to underestimate or overestimate the real signal ($\mu = 0$). All in all the atom/count statistical relationships are given by the following set of equations

Impact of

- Fluorescence noise
- Photoconversion noise
- Amplification noise
- Data treatment and pixel to pixel noise

$$\begin{aligned} \overline{A} &= \frac{\overline{C}}{\alpha} \\ \mathrm{Var}\left(A\right) &= \frac{\mathrm{Var}\left(C\right) - \frac{\mathrm{Var}(g)}{\overline{g}^2}\overline{C}^2 - 2\gamma\frac{\overline{g}}{4.01}\overline{C} - \overline{w^2}}{\gamma\alpha^2} \\ \mathrm{cov}\left(A_i, A_j\right) &= \frac{\mathrm{cov}\left(C_i, C_j\right) + \left(1-\gamma\right)\overline{C_i}\ \overline{C_j}}{\gamma\alpha_i\alpha_j} \end{aligned} \tag{2.44}$$

- $\alpha = \frac{\overline{g}}{4.01}\overline{\eta}\ \overline{n}$
- $\gamma = \frac{\overline{g^2}}{\overline{g}^2}$
- $\overline{w^2}$ is the average over all the experimental series of ^{2}.

These equations give the relation between the number of counts C and the number of atoms A corrected for the data treatment and the pixel to pixel noises. In the case of bipartite experiments the C variables must also be corrected for the bipartition noise (see Delta method).

Note that w does not affect the covariances, that is because estimation errors and pixel noise of two different clouds are not correlated.

At this stage, we have finally derived the set of statistical relations between the variables representing the number of constituents of each Zeeman cloud (the A variables) and the variables corresponding to the number of counts (the C ones) ***which are the only ones that are experimentally accessible****. The story however is not over, as moments and mixed moments of the A variables are yet still affected by many other noises amongst which*

---

[14] that comes with this method is encapsulated within the fit's *standard errors*

[15] The sum of two Gaussian distributions is a Gaussian distribution.

are the preparation noise, the dissipative and coherent processes occurring in the lattice and possibly the bipartition noise (see Fig. 2.2). This bipartition noise will be discussed in chap. 4. In the following section, we will directly tackle the thorny subject of the dissipative and coherent processes taking place when the atoms are still trapped in the optical lattices.

2.2.5 Contact interactions, tunneling, losses and heating

Contact interactions, tunneling, losses and heating are distinct phenomena which we have grouped together because all four are concomitant with the unfurling of the dipolar dynamics.

Contact interactions

Before discussing the effects of the contact interactions on our measurements, let us first introduce some useful operators [62].
First and foremost, the **field operator** $\hat{\Psi}(\mathbf{r})$ which describes the state of a spin S boson

$$\hat{\Psi}(\mathbf{r}) = \begin{pmatrix} \hat{\Psi}_S(\mathbf{r}) \\ . \\ \hat{\Psi}_0(\mathbf{r}) \\ . \\ \hat{\Psi}_{-S}(\mathbf{r}) \end{pmatrix} \tag{2.45}$$

where each of the $\hat{\Psi}_m$ obeys **bosonic commutation relationships**.

The exact form of these operators requires careful consideration of the trapping potential. For simplicity, we will assume this potential to be isotropic and harmonic along the three directions and we will therefore expand each of the $\hat{\Psi}_m(\mathbf{r})$ operators using the ansatz

$$\begin{aligned} \hat{\Psi}_m(\mathbf{r}) &= \sum_{n_x,n_y,n_z} h_{n_x}(x) h_{n_y}(y) h_{n_z}(z) \hat{h}^m_{n_x,n_y,n_z} \\ &= \sum_{\mathbf{n}} h_{\mathbf{n}}(\mathbf{r}) \hat{h}^m_{\mathbf{n}} \end{aligned} \tag{2.46}$$

Where

- $h_n(\mathbf{r}) = \langle \mathbf{r} | \mathbf{n} \rangle = h_n(\mathbf{r}) = h_{n_x}(x) h_{n_y}(y) h_{n_z}(z)$ are the Hermit functions [63]

  $$h_n(x) = \frac{1}{\sqrt{2^n n!}} \left(\frac{m\omega}{\pi\hbar} \right)^{\frac{1}{4}} e^{-\frac{m\omega x^2}{2\hbar}} H_n\left(\sqrt{\frac{m\omega}{\hbar}} x \right), \qquad n = 0, 1, 2... \tag{2.47}$$

  Where $H_n(x) = (-1)^n e^{x^2} \frac{d^n e^{-x^2}}{dx^n}$ is the n$^{\text{th}}$ Hermit polynomial
- $\hat{h}^m_{\mathbf{n}}$ are the bosonic annihilation operators associated to the single particle state $|h_n\rangle \otimes |S, m\rangle$

The annihilation operator $\hat{A}_{F,M}(x, x')$ which removes a pair of particles in the molecular state $|F, M\rangle$ at positions $\mathbf{r}$,$\mathbf{r}'$

$$\hat{A}_{F,M}(\mathbf{r}, \mathbf{r}') = \sum_{m,m'} \langle F, M | S, m, S, m' \rangle \hat{\Psi}_m(\mathbf{r}) \hat{\Psi}_{m'}(\mathbf{r}') \tag{2.48}$$

The **projection operator** $\hat{P}_F$ on the subspace of the molecular state of total spin F

$$\hat{P}_F = \sum_M |F, M\rangle \langle F, M| \tag{2.49}$$

Now to write the interaction potential between two spin S particles. This interaction potential is nothing but the sum over all molecular potentials

$$\begin{aligned}\hat{V}_c(\mathbf{r},\mathbf{r}') &= \sum_F \hat{V}_F(\mathbf{r},\mathbf{r}') \\ &= \sum_{F=0}^{2S} \underbrace{\frac{4\pi\hbar^2 a_F}{m}}_{g_F} \delta(\mathbf{r}-\mathbf{r}')\hat{P}_F \\ &= \sum_{F=0}^{2S} g_F \delta(\mathbf{r}-\mathbf{r}')\hat{P}_F\end{aligned} \tag{2.50}$$

Where a_F is the F molecular potential scattering length.
Moreover, for low energy collisions, (i.e. s waves collisional regime), only even potentials can be retained (this is because they are the only ones to be exchange symmetric, for more ample justification see [62] for example):

$$\hat{V}_c(\mathbf{r},\mathbf{r}') = \sum_{F_{even}=0}^{2S} g_F \delta(\mathbf{r}-\mathbf{r}')\hat{P}_F \tag{2.51}$$

It can be shown [64], that for **this low energy collisions approximation to be valid**, the typical motional energies of the interacting pair should be lower than the centrifugal barrier V_0

$$V_0 = \frac{2\hbar^3}{\sqrt{M^3 C_6}} \underset{[65]}{\simeq} k_B \times 0.8mK \gg \frac{\hbar\omega_{532}}{2} \tag{2.52}$$

which is indeed the case as $\hbar\omega_{532}/k_b \simeq 1\mu K$ even for ω_{532} (the oscillation frequency associated with the 532 nm lattice) as high as 500 kHz.

a_6	a_4	a_2	a_0
102.5±0.4	64±4	-7±20	$13.5^{+11}_{-10.5}$

Table 2.1: Chromium scattering lengths in units of a_B[12].

Finally, the **contact Hamiltonian** is

$$\hat{H}_c = \frac{1}{2}\sum_{F,M}\int d\mathbf{r}d\mathbf{r}' \hat{V}_c(\mathbf{r},\mathbf{r}')\,\hat{A}^\dagger_{F,M}(\mathbf{r},\mathbf{r}')\hat{A}_{F,M}(\mathbf{r},\mathbf{r}') \tag{2.53}$$

As we are interested in the effects of this Hamiltonian on the *atomic* states and not the *molecular* ones, we will use the alternative [62] form:

$$\hat{H}_c(t) = \frac{1}{2}\int d\mathbf{r} \sum_{m_1,m_2,m_1',m_2'} C^{m_1,m_2}_{m_1',m_2'} \hat{\Psi}^\dagger_{m_1}(\mathbf{r})\hat{\Psi}^\dagger_{m_2}(\mathbf{r})\hat{\Psi}_{m_2'}(\mathbf{r})\hat{\Psi}_{m_1'}(\mathbf{r}) \tag{2.54}$$

We can expand this Hamiltonian into a sum of harmonic level dependent elementary two body contact Hamiltonians as such

$$\begin{aligned}&= \sum_{m_1,m_2,m_1',m_2'} \frac{1}{2}C^{m_1,m_2}_{m_1',m_2'} \sum_{\mathbf{n_1},\mathbf{n_2},\mathbf{n}_1',\mathbf{n}_2'} \int d\mathbf{r} h^*_{\mathbf{n_1}}(\mathbf{r}) h^*_{\mathbf{n_2}}(\mathbf{r}) h_{\mathbf{n}_2'}(\mathbf{r}) h_{\mathbf{n}_1'}(\mathbf{r}) \hat{h}^{m_1,\dagger}_{\mathbf{n_1}} \hat{h}^{m_2,\dagger}_{\mathbf{n_2}} \hat{h}^{m_2'}_{\mathbf{n}_2'} \hat{h}^{m_1'}_{\mathbf{n}_1'} \\ &= \sum_{m_1,m_2,m_1',m_2'} \sum_{\mathbf{n_1},\mathbf{n_2},\mathbf{n}_1',\mathbf{n}_2'} \frac{1}{2}C^{m_1,m_2}_{m_1',m_2'} \eta_{\mathbf{n_1},\mathbf{n_2},\mathbf{n}_1',\mathbf{n}_2'} \hat{h}^{m_1,\dagger}_{\mathbf{n_1}} \hat{h}^{m_2,\dagger}_{\mathbf{n_2}} \hat{h}^{m_2'}_{\mathbf{n}_2'} \hat{h}^{m_1'}_{\mathbf{n}_1'}\end{aligned} \tag{2.55}$$

Where

- $\eta_{n_1,n_2,n'_1,n'_2} = \int d\mathbf{r} h^*_{\mathbf{n_1}}(\mathbf{r}) h^*_{\mathbf{n_2}}(\mathbf{r}) h_{\mathbf{n'_2}}(\mathbf{r}) h_{\mathbf{n'_1}}(\mathbf{r})$
- $C^{m_1,m_2}_{m'_1,m'_2} = \sum_F g_F \langle S, m_1, S, m_2 | \hat{P}_F \left| S, m'_1, S, m'_2 \right\rangle = \sum_F g_F \langle S, m_1, S, m_2 | F, M \rangle \left\langle F, M \middle| S, m'_1, S, m'_2 \right\rangle$

The intrasite contact dynamics can be computed using the full time dependent Hamiltonian as given by

$$\hat{H}(t) = \hat{H}_c(t) + \hat{H}_\omega \tag{2.56}$$

Where $\hat{H}_\omega$ accounts for the kinetic part of the total Hamiltonian and the trap's potential. We are however not interested in the full contact driven intrasite dynamics, instead we want to derive the typical timescales at which contact interactions affect the local spin projections of the doublons.

According to Eq. 2.55 these timescales are directly given by the $2h \Big/ \left(C^{m_1,m_2}_{m'_1,m'_2} \eta^*_{n_1} \eta^*_{n_2} \eta_{n'_2} \eta_{n'_1} \right)$ quantities. In particular, assuming that the atoms are initially loaded in the ground state of the harmonic

oscillator, the dynamics onset is governed by $2h \Big/ \left(C^{m_1,m_2}_{m'_1,m'_2} \eta^*_{n_1} \eta^*_{n_2} \eta_{\mathbf{0}} \eta_{\mathbf{0}} \right)$.

Computing these coefficients, we find that the contact driven dynamics timescales are on the order of a few hundred microseconds. We can therefore surmise that it will, when coupled to the other phenomena discussed below, contribute to the increase of the variability of the various measurements, **even** at very short times.

Tunneling

The effects of **transport phenomena** in the optical lattice are hard to assess - quantitatively speaking. In general still, tunneling changes the interaction environment of the hopping atom and therefore the subsequent evolution of its internal degrees of freedom. Tunneling however is suppressed in the Mott phase and related effects are quite negligible. In fact, experiments carried out using the bipartition set-up (see Chap. 4) which are not described in this manuscript have shown that tunneling is quite negligible, even at times exceeding 400 ms when the atoms are left in the $\left| {}^7S_3, m_s = -3 \right\rangle$ state[16] as soon as the depth of the lattice is greater than $8E_{r,532}5$. Various intensity and magnetic gradients also contribute to the reduction of tunneling by making it systematically non resonant.

Heating

For a two level atom in a far-off resonance trap, photon scattering related heating occurs at rate $\Gamma_{\text{heat}} = 2E_r\Gamma_{s.e} \propto \frac{\Omega_L^2}{\delta_L^2}$[47]. In our case, it was evaluated to 20 nK.s^{-1}. For 100 ms experiments, this leads to an increase of the temperature $\Delta T = 2$ nK which is small compared to the BEC's temperature (50 nK). Heating leads to an increase of the kinetic energy of the atoms and facilitates tunneling between sites, it can therefore increase the variability of the dynamics.

Losses

Losses increase the variability of the dipolar dynamics and related characterizations (variance of the magnetization, and other correlators introduced in Chap. 3). The basic principle behind this is represented in the figure below

---

[16] The timescales of tunneling may depend on the tilting angle of the spins as interactions also do

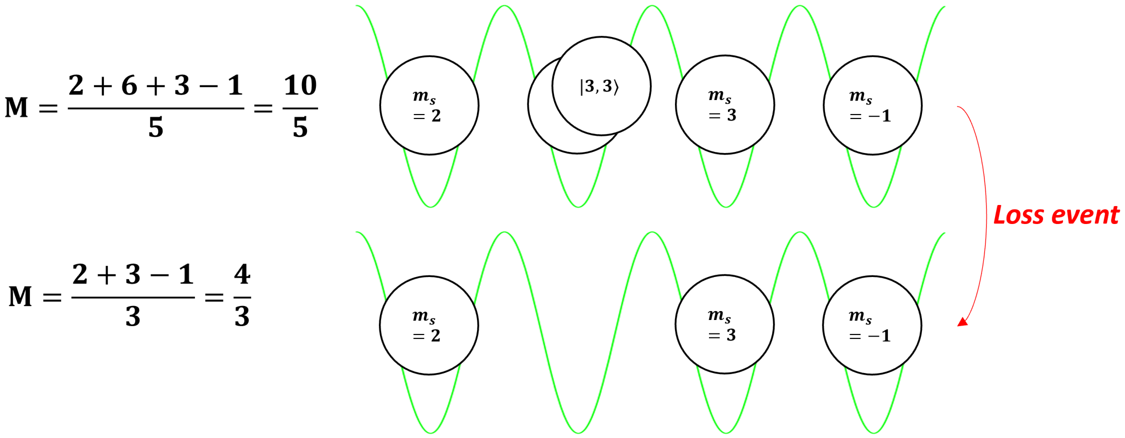

FIGURE 2.6: In the figure above, the loss of a doublon (through **local** dipolar relaxation) in the state $|m_{s,1}:3, m_{s,2}:3\rangle$ produces a state whose magnetization **M** is different from the initial state's magnetization. As the state in which doublons are lost is random, the post-dynamic state obtained at the end of each experiment we carry out is different even though the initial state is the same, in particular, the statistical properties of this end-state carry some level of variability within them which is due entirely to loss events. This variability affects all of the properties of our system, not only the magnetization. Of course this scenario builds on the fact that **doublons and singlons interact for some time**, if they didn't the properties of the end state would be independent of any doublons related processes.

The effect of losses have been studied through *exact numerical simulations* on a 2×6 plaquette, composed of 8 singlons and 4 spin 6 particles representing doublons. The results are detailed in appendix D. The main conclusion of this appendix being that while losses do mitigate the development of correlations to some extent, their effect is not strong enough to prevent us from observing their development, in accordance with the experimental results of Chap. 3 and 4

These four phenomena modify the unfurling of the dynamics between atoms which would otherwise be solely dictated by the initial state in which they are prepared. As it turns out this state's preparation is not perfectly reproducible. This is what we call the preparation noise

2.2.6 Preparation noise

In this section we focus on the preparation noise in which we include both the RF noise and number noise. We discuss the causes and the effects of these noises, and briefly touch on the subject of magnetic gradients. We then review the several data treatment schemes that can be used to deal with these noises as far as the statistical aspect is concerned.

The RF noise

The RF noise finds its root cause in the **shot-to-shot variability of the $\frac{\pi}{2}$ RF pulse** used to prepare the atomic sample in its initial state, this variability is ultimately linked to two factors: first is the imperfect reproducibility of the radio field pulse itself, second are the instabilities (drifts and fluctuations) of the dominant magnetic field which are caused by external factors such as the slow drifts of the earth's magnetic field and the erratic contributions of power line generated magnetic fields.

The reproducibility of the RF pulses was improved in several ways, for example RF pulses were previously characterized by their duration and the Rabi frequency (Ω of the RF field)would be adjusted so that the spin rotation is completed within this duration (5 μs in the case of a $\frac{\pi}{2}$ rotation).

Currently, **the pulses are characterized by the number of RF periods**: every experimental pulse correspond to the same number of RF periods. This ensures that the starting phase of the pulses is always the same. This also allows for early switch on and late switch off of the electronic switches (see Chap. 1 Fig. 1.12) and therefore for cleaner implementations of the RF pulses (see Fig. 2.7).

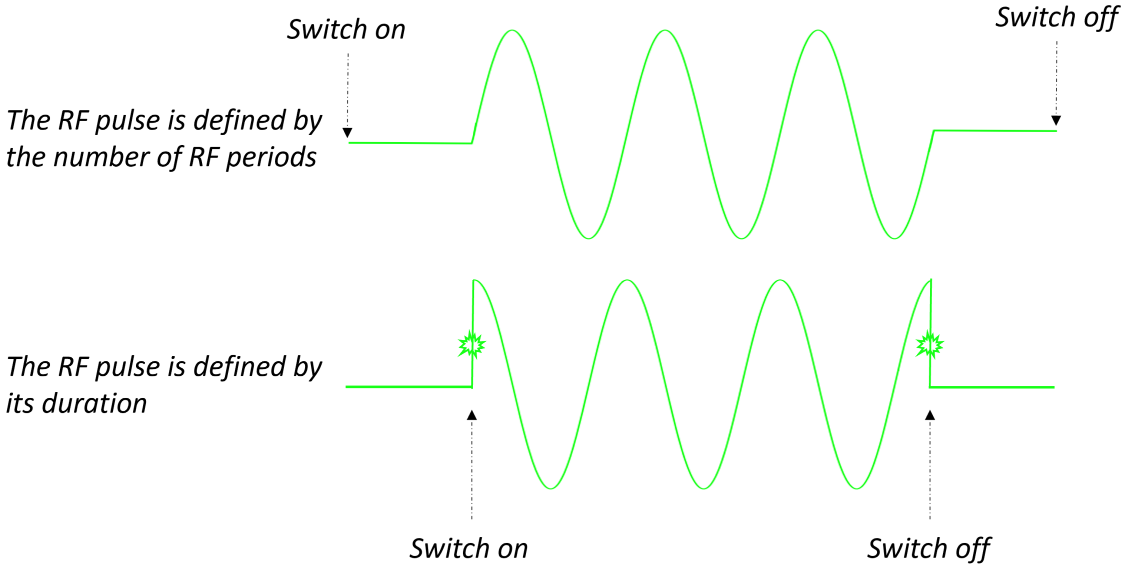

FIGURE 2.7: Comparison between early and late switch on/off of the electronic RF switches. In the first case, the RF pulse is defined by the number of RF periods, the starting phase of the pulses is always the same from shot to shot and the electronic switches can be switched on before the beginning of the pulses, in this case the flanks of these pulses are well defined and are always the same shot to shot. In the second case, the activation and deactivation of these switches defines the duration of the RF pulse and therefore the initial tilt angle of the spins. In this case however, the edges of the pulse display bigger variations from shot to shot which is detrimental to the reproducibility of the initial state. The shape of these pulses can be observed experimentally using a small pick-up coil close to the atomic chamber.

Increasing the Rabi frequency to values as high as 100 kHz also allowed for pulses more insensitive to magnetic inhomogeneities and fluctuations.

The drifts of the dominant magnetic field are fought against by a frequent calibration of the RF pulses. As for its fluctuations, they can be prevented using various locking schemes or through *active control* techniques which counter the effects of well identified fluctuations, for example the fluctuations of the Larmor frequency originating from the landlines' 50 Hz can be suppressed by a factor greater than 10 dB by feeding correction coils with 50 Hz current of appropriate amplitude and phase. The active control techniques are still being tested and were not implemented for the data that is presented in the Chaps. 3 and 4.

The atoms' preparation is also affected by **remnant magnetic gradients** which constitute a systematic source of inhomogeneity as far as spin preparation is concerned, this effect however is small as we now show.

Because of the magnetic gradients, the spins' Larmor frequency which is dictated by the local magnetic field amplitude displays a spatial dependence which in turn makes the radio field frequency detuning space-dependent: $\delta \rightarrow \delta(z)$. Ultimately, this makes for a spatially dependent generalized Rabi frequency (see chap.1)

$$\Omega_G(z) = \sqrt{\Omega^2 + \delta(z)^2} \tag{2.57}$$

This spatial dependence however is negligible, indeed in our experiment, the horizontal (ZQ plane) and vertical gradients were estimated to 26 mG.cm^{-1} and 117 mG.cm^{-1} respectively. For simplicity we will take $\nabla.B = 100$ mG.cm^{-1}.
An upper bound for the Mott state spatial extension being $\Delta_{Mott} = 10\ \mu$m, the local detuning should be bounded by

$$\Delta_{Mott}\nabla B = 10^{-4}\mathrm{G} \equiv 280\mathrm{Hz}. \tag{2.58}$$

Which for the usual Rabi frequencies we work with (50 -100 kHz) makes for negligible deviations of $\Omega_G(z)$ and therefore for negligible inhomogeneities of preparation.

The number noise

The number noise corresponds to the **shot-to-shot fluctuation of the number A_T of atoms in the condensate** (typically, $\Delta A_T \simeq 8\%$ within a single experimental series). This variability is due to the fluctuations of experimental parameters, mainly lasers' frequencies and power levels as well as the evergoing thermalization of the experiment. Amongst all technical noises, bipartition - when performed - and atom number noises have the heaviest impacts on absolute populations' variability.

Correction of the preparation noise at time $t_{\mathrm{dyn}} = 0$ ms

Much like other noises, one can try to get rid of the influence of the preparation noise through the use of total expectation, variance and covariance laws. In the case of covariances for example, one writes

$$\mathrm{cov}\left(A_i, A_j\right) = \underbrace{\mathbb{E}\left(\mathrm{cov}\left(A_i, A_j | A_T, \theta\right)\right)}_{\substack{\text{The quantum fluctuations contribution}\\ \text{hides in this term}}} + \underbrace{\mathrm{cov}\left(\mathbb{E}(A_i|A_T,\theta), \mathbb{E}(A_j|A_T,\theta)\right)}_{\substack{\text{Additional covariance contribution}\\ \text{due to the preparation noise}}} \tag{2.59}$$

Where θ is the random variable corresponding to the spin initial tilt.
Strictly speaking, this equation is only valid for 0 ms dynamics. Indeed, it is a fact that all phenomena occurring in the lattice, losses most notably, result in a shot-to-shot variability of the exact post-dynamics end-state **even when the initial state is perfectly reproducible**. It is therefore hard to assess how perturbations of the initial state (due to the preparation noise) translate when considering the final one, in particular the A entity should not be a random variable anymore but a statistical mixture 2.1.5 indeed, which, a priori, makes the $\mathbb{E}(A_i\,|\,\theta)$ quantity hard to interpret. The same could have been said of other noises, the number of spontaneously emitted photons by an atom for example, is a a statistical mixture of different Poisson laws: for each shot, one must choose the parameter of the Poisson law (which is dictated by, say, the power of the MOT lasers at that time), then the number of emitted photons according to this law - Eqs. 2.2.6 take this point into account. This aspect is even more glaring here as the power of the lasers can be more or less stabilized, whereas the details of the physical phenomena occurring in the lattice are harder to apprehend.
In any case at time $t_{\mathrm{dyn}} = 0$ ms at least, to model the effects of the RF noise, we will assume that the fluctuations of the initial tilt angle θ are normally distributed [17]:

$$\theta \sim \mathcal{N}\left(\frac{\pi}{2}, \Delta\theta\right) \tag{2.60}$$

---

[17] The standard deviation $\Delta\theta$ of the θ pulse has been evaluated to 2.5×10^{-3} rad.

In this case, the RF noise's contribution to the total covariance can be computed exactly as the expected populations are differentiable functions of the θ parameter (**for 0 ms dynamics times**). More specifically, **without bipartition**, the initial expected populations are

$$\mathbb{E}\left(A_{m_s}|A_T,\theta\right) = \left[\binom{6}{3+m_s}\left[\sin^2\left(\frac{\theta}{2}\right)\right]^{3+m_s}\left[\cos^2\left(\frac{\theta}{2}\right)\right]^{3-m_s}\right]A_T = a_{m_s}(\theta)A_T \tag{2.61}$$

Where A_T is the total number of atom and a_{m_s} the fractional population in the m_s Zeeman cloud. Writing $a'_{m_s} = \frac{da}{d\theta}$ and $a''_{m_s} = \frac{d^2a}{d\theta^2}$ and **independence** as well as **random variables Taylor expansions**, we have

$$\begin{aligned}\operatorname{cov}\left(\mathbb{E}\left(A_{m_s}|A_T,\theta\right),\mathbb{E}\left(A_{m'_s}|A_T,\theta\right)\right) &= a_{m_s}\left(\frac{\pi}{2}\right)a_{m'_s}\left(\frac{\pi}{2}\right)\operatorname{Var}\left(A_T\right) + a'_{m_s}\left(\frac{\pi}{2}\right)a'_{m'_s}\left(\frac{\pi}{2}\right)\operatorname{Var}\left(\theta\right)\overline{A_T^2} \\ &+ \left(a_{m'_s}\left(\frac{\pi}{2}\right)\frac{a''_{m_s}\left(\frac{\pi}{2}\right)}{2} + a_{m_s}\left(\frac{\pi}{2}\right)\frac{a''_{m'_s}\left(\frac{\pi}{2}\right)}{2}\right)\operatorname{Var}\left(\theta\right)\operatorname{Var}\left(A_T\right)\end{aligned} \tag{2.62}$$

This result encapsulates several intuitive facts: the first one is that the number noise correlates atomic populations positively $\left(a_{m_s}\left(\frac{\pi}{2}\right)a_{m'_s}\left(\frac{\pi}{2}\right) > 0\right)$. The second fact is that, at $\theta = \frac{\pi}{2}$ the RF noise correlates Zeeman populations corresponding to same sign spin quantum numbers whereas it anticorrelates Zeeman populations with spin quantum numbers of opposite signs (sign$\left(a'_{m_s}\left(\frac{\pi}{2}\right)a'_{m'_s}\left(\frac{\pi}{2}\right)\right) = \mathrm{sign}(m_s m'_s)$). The last term is a second order term which we've included for completeness, it can be neglected.

Impact of

- Fluorescence noise
- Photoconversion noise
- Amplification noise
- Fit noise
- Preparation Noise @ $t_{\text{dyn}} = 0$ ms

$$\begin{aligned}
\overline{A} &= \frac{\overline{C}}{\alpha} \\
\text{Var}\,(A) &= \frac{\text{Var}\,(C) - \frac{\text{Var}(g)}{\overline{g}^2}\overline{C}^2 - 2\gamma\frac{\overline{g}}{4.01}\overline{C} - \overline{w^2}}{\gamma\alpha^2} - \overline{a}^2\left(\frac{\pi}{2}\right)\text{Var}\,(A_T(0)) - \overline{a'}^2\left(\frac{\pi}{2}\right)\text{Var}\,(\theta)\,\overline{A_T(0)^2} \\
\text{cov}\left(A_i, A_j\right) &= \frac{\text{cov}\left(C_i, C_j\right) + (1-\gamma)\,\overline{C_i}\;\overline{C_j}}{\gamma\alpha_i\alpha_j} - \overline{a_i\left(\frac{\pi}{2}\right)}\;\overline{a_j\left(\frac{\pi}{2}\right)}\text{Var}\,(A_T(0)) - \overline{a'_i\left(\frac{\pi}{2}\right)}\;\overline{a'_j\left(\frac{\pi}{2}\right)}\text{Var}\,(\theta)\,\overline{A_T(0)^2}
\end{aligned} \tag{2.63}$$

- $\alpha = \frac{\overline{g}}{4.01}\overline{\eta}\;\overline{n}$
- $\gamma = \frac{\overline{g^2}}{\overline{g}^2}$

These equations give the relations between the number of counts C and the number of atoms A at time $t_{\text{dyn}} = 0$ ms corrected for the preparation, the data treatment and the pixel to pixel noises. In the case of bipartite experiments the C variables must also be corrected for the bipartition noise (see Delta method).

Remark: If we allow for variations of the f_i factor as possibly caused by variations of the imaging beams' powers from shot to shot, the n variable corresponding to the number of photons emitted by an atom is no longer Poisson distributed. In this case the $\frac{\text{Var}(C) - \frac{\text{Var}(g)}{\overline{g}^2}\overline{C}^2 - 2\gamma\frac{\overline{g}}{4.01}\overline{C} - \overline{w^2}}{\gamma\alpha^2}$ and the $\frac{\text{cov}(C_i,C_j)+(1-\gamma)\overline{C_i}\;\overline{C_j}}{\gamma\alpha_i\alpha_j}$ terms in Eqs. 2.62 change into $\frac{\text{Var}(C) - \frac{\text{Var}(g)}{\overline{g}^2}\overline{C}^2 - 2\gamma\frac{\overline{g}}{4.01}\overline{C} - \gamma\alpha\chi\overline{C} - \overline{w^2}}{\gamma\alpha^2}$ and $\frac{\text{cov}(C_i,C_j)+(1-\gamma-\gamma\chi_{ij})\overline{C_i}\;\overline{C_j}}{\gamma\alpha_i\alpha_j}$ respectively $\chi_{ij} = \frac{\text{cov}(n_i,n_j)}{\overline{n}_i\overline{n}_j}$, $\chi = \frac{\text{Var(n)} - \overline{n}}{\overline{n}^2}$

Correction of the RF noise at longer interaction times

The variance of the magnetization

In the third chapter of this manuscript, we track the evolution of the spin correlations in the evolution of the magnetization's variance. It is therefore necessary to go beyond the $t_{\text{dyn}} = 0$ case presented above. To do so **we claim that the contribution of the RF noise to the fluctuations of the magnetization is conserved throughout the dynamics modulo the change in the number of atoms**. This is because the variance of the magnetization itself is conserved at long times to a pretty good approximation despite the loss of doublons. This claim is supported by the following arguments:

- $\left[\hat{S}_z, \hat{H}_{\text{sec}}\right] = \hat{0}$ which implies that the magnetization and all its statistical moments remain constant once the doublons are lost.

- The spatial segregation of singlons and doublons in the Mott state limits the interaction between singlons and doublons.
- Doublons are lost relatively fast (in 10 ms which is similar to dipole dipole interactions timescales) which also limits spin exchange between singlons and doublons.

The conservation of the magnetization entails that the RF noise's contribution, hereafter denoted Δ_{RF}, is also somehow conserved throughout the evolution, modulo the change in the number of atoms. More specifically, when correcting the **normalized variance** $\mathrm{Var}\left(\hat{S}_z\right) \Big/ A_T$ we assume that

$$\Delta_{RF}^{t>0} = \Delta_{RF}^{t=0} \frac{A_T(t)}{A_T(0)} \tag{2.64}$$

At time $t_{\mathrm{dyn}} = 0$ ms the contribution of the RF noise $\Delta_{RF}^{t=0}$ is estimated by subtracting to the variance of the magnetization its theoretical value which is $\frac{3}{2}A_T$.

Other observables

This section is not meant to provide tight or realistic bounds for the contribution of the RF noise and should be seen as more of preliminary approach towards this objective.

Other observables such as the populations and the system's partial magnetizations are not conserved and it is harder to claim that the contribution of the RF noise to their fluctuations remains unchanged as the system evolves. Still, in the words of von Neuman, what cannot be predicted might still be controlled. One possible way of bounding the effect of the RF noise when considering observables that do not commute with the Hamiltonian lies in the unitarity of the evolution:

Let $\left|\psi(0)\right\rangle$ be the single particle initial state prepared in the experiment after an imperfect $\frac{\pi}{2}$ pulse.

$$\left|\psi(0)\right\rangle = e^{-\frac{i}{2}(\frac{\pi}{2}+\epsilon)\hat{S}_y} \left|-3\right\rangle_z \tag{2.65}$$

Where ϵ represents the difference of the initial tilt angle to $\frac{\pi}{2}$. In first order in ϵ the previous equation writes:

$$\begin{aligned}
\left|\psi(0)\right\rangle &= \left[e^{-\frac{i}{2}(\frac{\pi}{2})\hat{S}_y} e^{-\frac{i}{2}(\epsilon)\hat{S}_y}\right] \left|-3\right\rangle_z \\
&= \left[e^{-\frac{i}{2}(\frac{\pi}{2})\hat{S}_y}\left(1 - \frac{i}{2}\epsilon\hat{S}_y\right)\right] \left|-3\right\rangle_z \\
&= \left|-3\right\rangle_x - \frac{1}{4} e^{-\frac{i}{2}(\frac{\pi}{2})\hat{S}_y} \epsilon \hat{S}^+ \left|-3\right\rangle_z \\
&= \left|-3\right\rangle_x - \frac{1}{4} e^{-\frac{i}{2}(\frac{\pi}{2})\hat{S}_y} \epsilon \left|-2\right\rangle_z \\
&= \underbrace{\left|-3\right\rangle_x}_{\left|\psi_{\frac{\pi}{2}}(0)\right\rangle} - \underbrace{\frac{1}{4}\epsilon\left|-2\right\rangle_x}_{\left|\epsilon(0)\right\rangle}
\end{aligned} \tag{2.66}$$

Note that the contribution of the perturbation $\left|\epsilon(0)\right\rangle$ is initially orthogonal to the ideal initial spin state $\left|\psi_{\frac{\pi}{2}}(0)\right\rangle$.

When considering an initial many body state with N particles, $|\Psi(0)\rangle$, we have

$$\begin{aligned}
|\Psi(0)\rangle &= \underbrace{\otimes_{i=1}^{N} \left|\psi(0)\right\rangle_i}_{\Psi_{\frac{\pi}{2}}(0)} \\
&= \otimes_{i=1}^{N} \left|\psi_{\frac{\pi}{2}}(0)\right\rangle_i \\
&+ \underbrace{|\epsilon(0)\rangle_1 \left|\psi_{\frac{\pi}{2}}(0)\right\rangle_2 \ldots \left|\psi_{\frac{\pi}{2}}(0)\right\rangle_N}_{|\epsilon_1(0)\rangle} \\
&+ \underbrace{\left|\psi_{\frac{\pi}{2}}(0)\right\rangle_1 |\epsilon(0)\rangle_2 \ldots \left|\psi_{\frac{\pi}{2}}(0)\right\rangle_N}_{|\epsilon_2(0)\rangle} \\
&+ \ldots \\
&+ \underbrace{\left|\psi_{\frac{\pi}{2}}(0)\right\rangle_1 \ldots \left|\psi_{\frac{\pi}{2}}(0)\right\rangle_{N-1} |\epsilon(0)\rangle_N}_{|\epsilon_N(0)\rangle} \\
&+ \text{Higher order terms in } |\epsilon(0)\rangle
\end{aligned} \tag{2.67}$$

Because $|\epsilon(0)\rangle$ is orthogonal to $\left|\psi_{\frac{\pi}{2}}(0)\right\rangle$ the norm of the $|\epsilon_i(0)\rangle$ states is $\|\epsilon(0)\| = \|\epsilon\| = \frac{|\epsilon|}{4}$. In the following we assume that the evolution of the $|\epsilon_i(0)\rangle$ states is independent of i: $|\epsilon(0)\rangle_i \equiv |\epsilon(0)\rangle$. In this case, dropping the higher order terms and normalizing the resulting state, the evolution of $|\Psi(0)\rangle$ at first order is given by

$$\begin{aligned}
|\Psi(t)\rangle &= e^{it\hat{H}/\hbar}\left(\alpha \left|\Psi_{\frac{\pi}{2}}(0)\right\rangle + \alpha \sum_i |\epsilon_i(0)\rangle\right) \\
\text{translational invariance} \longrightarrow &= \alpha \underbrace{e^{it\hat{H}/\hbar}\left|\Psi_{\frac{\pi}{2}}(0)\right\rangle}_{\left|\Psi_{\frac{\pi}{2}}(t)\right\rangle} + \alpha N \underbrace{e^{it\hat{H}/\hbar}|\epsilon(0)\rangle}_{|\epsilon(t)\rangle}
\end{aligned} \tag{2.68}$$

Where α is the normalization constant, $\alpha = \frac{1}{\sqrt{1+N(\epsilon/4)^2}}$.
If we consider now an observable $\hat{O}$ that does not commute with the Hamiltonian, for example $\hat{S}_z^A$ (or $\hat{A}_m$), we have

$$\langle\Psi(t)|\hat{O}|\Psi(t)\rangle = \alpha^2 \left\langle \Psi_{\frac{\pi}{2}}(t) \middle| \hat{O} \middle| \Psi_{\frac{\pi}{2}}(t)\right\rangle + \alpha^2 N \left\langle \Psi_{\frac{\pi}{2}}(t) \middle| \hat{O} \middle| \epsilon(t)\right\rangle + \alpha^2 N \left\langle \epsilon(t) \middle| \hat{O} \middle| \Psi_{\frac{\pi}{2}}(t)\right\rangle + \alpha^2 N^2 \langle\epsilon(t)|\hat{O}|\epsilon(t)\rangle \tag{2.69}$$

If we let $|x_i\rangle$ be an orthonormal eigenbasis of $\hat{O}$ such that $\hat{O}|x_i\rangle = o_i\,|x_i\rangle$, $|\epsilon(t)\rangle = \sum_i \epsilon_i\,|x_i\rangle$ and $\left|\Psi_{\frac{\pi}{2}(t)}\right\rangle = \sum_i \psi_i\,|x_i\rangle$ then we can write

$$\begin{aligned}
\text{(Cauchy Schwarz)} \longrightarrow \left|\left\langle \epsilon(t) \middle| \hat{O} \middle| \Psi_{\frac{\pi}{2}}(t)\right\rangle\right| &\le \|\epsilon\| \left\| \hat{O} \left| \Psi_{\frac{\pi}{2}}(t)\right\rangle \right\| \\
\hat{O}|x_i\rangle = o_i\,|x_i\rangle \longrightarrow &\le \|\epsilon\| \left\| \sum_i \psi_i o_i\,|x_i\rangle \right\| \\
&\le \|\epsilon\| \sqrt{\sum_i \psi_i^2 o_i^2} \\
&\le \|\epsilon\| \sqrt{\langle \hat{O}^2 \rangle_{\left|\Psi_{\frac{\pi}{2}}\right\rangle}}
\end{aligned} \tag{2.70}$$

In the case where $\hat{O}$ has zero expectation value - for example $\hat{O} = \hat{S}_z^A$ - Eq. 2.70 can be rewritten

$$\left|\left\langle \epsilon(t)\middle|\hat{O}\middle|\Psi_{\frac{\pi}{2}}\right\rangle\right| \leq \mathrm{std}\left(\hat{O}_{\left|\Psi_{\frac{\pi}{2}}\right\rangle}\right)\|\epsilon\| \tag{2.71}$$

To benchmark this approach we can apply it to the $\hat{S}_z$ operator at time $t_{\mathrm{dyn}} = 0$ ms, as in this case we know the exact effect of the RF noise through Eqs. 2.63. These equations predict that the contribution of the RF noise to **the variance of the magnetization** is

$$\sum_{m=-3}^{3}\sum_{m'=-3}^{3} m m' \overline{a'_m\left(\frac{\pi}{2}\right)}\,\overline{a'_{m'}\left(\frac{\pi}{2}\right)}\mathrm{Var}\left(\theta\right) N^2 \tag{2.72}$$

For a total number of atoms $N = 10000$ and a standard deviation $\mathrm{std}\left(\theta\right) = 5 \times 10^{-3}$ we find a numerical value of 22500.

If we compute the 2.71 bound using the same inputs, and assuming that $\mathrm{std}\left(\hat{S}^z\right)_{\left|\Psi_{\frac{\pi}{2}}\right\rangle} = \sqrt{\frac{3N}{2}}$ we find

$$\left(2\alpha^2 N\|\epsilon\|\sqrt{\left\langle\hat{O}^2\right\rangle_{\left|\Psi_{\frac{\pi}{2}}\right\rangle}}\right)^2 = 2.5 \times 10^6 \gg 22500 \tag{2.73}$$

which makes this bound mostly irrelevant. More realistic bounds could be obtained by properly bounding the variance of observable $\hat{O}$ instead of bounding the term $\left|\left\langle \epsilon(t)\middle|\hat{O}\middle|\Psi_{\frac{\pi}{2}}\right\rangle\right|$, which only provides a rough overestimation of the effect. Proper bounding of the variance could be done using equations similar to 2.70 and general inequalities such as the Bathia Davis one. More realistic bounds should also keep higher order terms in ϵ as the first order approximation is obviously too crude. The contribution of these terms is not negligible given that their number grows as $\frac{N!}{t!(N-t)!}$ where t is the highest order of the development. It would also be desirable for this bound to have the same scaling as the theoretical effect at time $t_{\mathrm{dyn}} = 0$ ms (i.e. $\propto N^2$ instead of N^3).

Correction of the number noise at longer interaction times: The Delta method

In order to get rid of the adverse impacts of the number noise, it is customary to normalize each data point by its total signal. This **normalization** process when performed on the initial data enclosed in the images (the C_i variables) is not entirely satisfactory as it is hard if not impossible to rigorously relate the various moments of the $\frac{A_i}{\sum_j A_j}$ variables which represent the normalized **atomic** populations and the $\frac{C_i}{\sum_j C_j}$ variables which represent the normalized **count** populations[18]. This is because of the many stochastic processes involved in the detection chain (e.g. fluorescence, EM-CCD amplification...) which also contribute additional statistical relationships, so to speak, between count populations which do not exist between atomic ones. In general anyway, ratios of random variable are not necessarily well behaved and one must be careful when dealing with this kind of variables[19].
In our case, if we relent on normalizing count populations from the get go and first get rid of the impacts of the detection chain (through Eqs. 2.44), we can still make use of random

---

[18] This was in fact the route that was chosen for the presentation of our data in our article [66], wherein strictly speaking we look at the **normalized counts** distribution corrected for noises like the RF noise, the shot noise and so forth. here we present an alternative data treatment path

[19] One most striking illustration of the problems that crop up when dealing with quotient variables is the fact that the ratio of two Gaussian distribution (a Cauchy distribution) has no defined mean, variance or higher moments. This is because the Gaussian distribution at the denominator has a non negligible probability density in a neighborhood of 0. In practice, one can circumvent these problems by focusing on a restricted data sets (not containing 0).

variables
Taylor expansions to have a look at the statistical properties of the normalized atom populations.
For example the expected value of the normalized populations $\mathbb{E}\left(\frac{A}{A_T}\right)$ is found using second order Taylor approximations

$$\mathbb{E}\left(\frac{A}{A_T}\right) \simeq \frac{\mathbb{E}(A)}{\mathbb{E}(A_T)} - \frac{\operatorname{cov}(A, A_T)}{\mathbb{E}(A_T)^2} + \frac{\mathbb{E}(A)}{\mathbb{E}(A_T)^3}\operatorname{Var}(A_T) \tag{2.74}$$

The generalization of these expansions to the variance covariance matrix is called **Delta method**, it is also a second order approximation and is often used with the sole assumption that the variance of relevant variables is "small" [20] [67]. It can be used like so:
First let us denote

$$g : \vec{x} = (x, y, z) \mapsto \left(\frac{x}{z}, \frac{y}{z}\right) = \left(g_1(\vec{x}), g_2(\vec{x})\right)$$

such as

$$g(A_i, A_j, A_T) = \left(g_1\left(A_i, A_j, A_T\right), g_2\left(A_i, A_j, A_T\right)\right) = \left(\frac{A_i}{A_T}, \frac{A_j}{A_T}\right)$$

We have

$$\frac{\partial g_1}{\partial x} = \frac{1}{z}, \quad \frac{\partial g_1}{\partial z} = \frac{-x}{z^2}, \quad \frac{\partial g_2}{\partial y} = \frac{1}{z}, \quad \frac{\partial g_2}{\partial z} = \frac{-y}{z^2}$$

The Jacobian of g at point $\vec{x} = (x, y, z)$ is given by

$$\nabla g(x, y, z) = \begin{pmatrix} \frac{1}{z} & 0 & -\frac{x}{z^2} \\ 0 & \frac{1}{z} & -\frac{y}{z^2} \end{pmatrix}$$

so that

$$\nabla g(A_i, A_j, A_T) = \begin{pmatrix} \frac{1}{\overline{A_T}} & 0 & -\frac{\overline{A_i}}{\overline{A_T}^2} \\ 0 & \frac{1}{\overline{A_T}} & -\frac{\overline{A_j}}{\overline{A_T}^2} \end{pmatrix}$$

Then

$$\operatorname{Cov}[g(A_i, A_j, A_T)] = \operatorname{Cov}\left(\frac{A_i}{A_T}, \frac{A_j}{A_T}\right) \approx \nabla g(\overline{A_i}, \overline{A_j}, \overline{A_T})\operatorname{Cov}[(A_i, A_j, A_T)]\nabla g(\overline{A_i}, \overline{A_j}, \overline{A_T})^T$$

where $\operatorname{Cov}[(A_i, A_j, A_T)]$ is the covariance matrix of A_i, A_j and A_T
Below we present a brief numerical study of the validity of these methods at time $t_{\text{dyn}} = 0$ ms.

In this numerical study we have simulated the outcome of the experiment at time $t = 0$ ms when tainted by a given **number noise**. More specifically, we have set the number of atoms to be normally distributed $A_T \sim \mathcal{N}(10000, \Delta A_T)$. Much like the actual experiment we've divided the numerical results into packets of size 50, which is the average length of real experimental series. For each of these packets we compute

- The variance covariance matrix of the normalized populations as given by the Delta method (**which, from now on, we will call Delta populations**)
- The variance covariance matrix of the first order populations, that is the populations we find when we drop off all second order terms and beyond from the delta development

---

[20] Small enough so that following terms, which involve higher statistical moments, in the development become negligible

- The variance covariance matrix of the *true normalized* populations

In Fig. 2.8, we compare the **average** of the variance covariance matrices thus found for the true normalized and the Delta populations to the theoretical variance covariance[21] matrix expected at time $t_{\mathrm{dyn}} = 0$ ms. For two matrices U, V, this distance is given by:

$$Dist(U,V) = \sqrt{\sum (u_{i,j} - v_{i,j})^2} \tag{2.75}$$

This distance can be expressed in terms of percentage

$$Dist_{\%}(U,V) = \frac{\sqrt{\sum (u_{i,j} - v_{i,j})^2}}{\sqrt{\sum (u_{i,j})^2}} \tag{2.76}$$

In Fig. 2.9, we show that first order approximations cannot reproduce the results obtained through normalization.

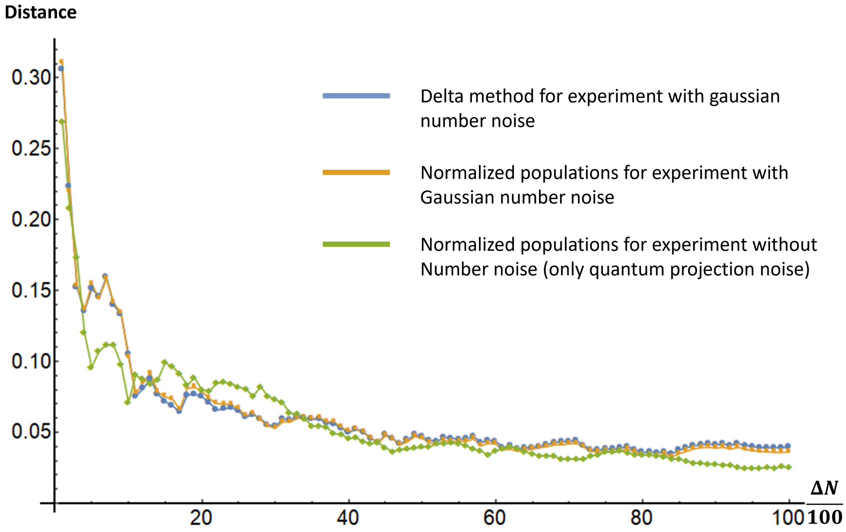

FIGURE 2.8: The yellow line represent the distance between the variance covariance matrix of the *true normalized* populations and the theoretical variance covariance matrix as a function of the number of experimental packets or sets taken into account, each packet contains 50 experimental shots. The blue line represents the distance between the variance covariance matrix of the Delta populations to the theoretical variance covariance matrix. The green line represents the results that would be found for a perfect experiment, that is an experiment affected by the sole quantum projection noise. All results are extremely similar which testifies to the quality of the Delta approximation, and to the fact that the results are limited by the **convergence of the statistical estimates** not by Delta scheme. This detail is of importance, strictly speaking experiments allow us to compute *estimators* of the various moments related to the atomic signals. These estimators' rate of **convergence** depend on the probability distribution of these signals. They make for irreducible estimation uncertainties of the true moments we are interested in.[22]

---

[21] The matrix M whose elements are given by $M_{m_s,m_{s'}} = a_{m_s}(\delta_{m_s,m_{s'}} - a_{m_{s'}})$, see Chap. 3

[22] In fact for larger experimental sets, the Delta method shows a slight over correction

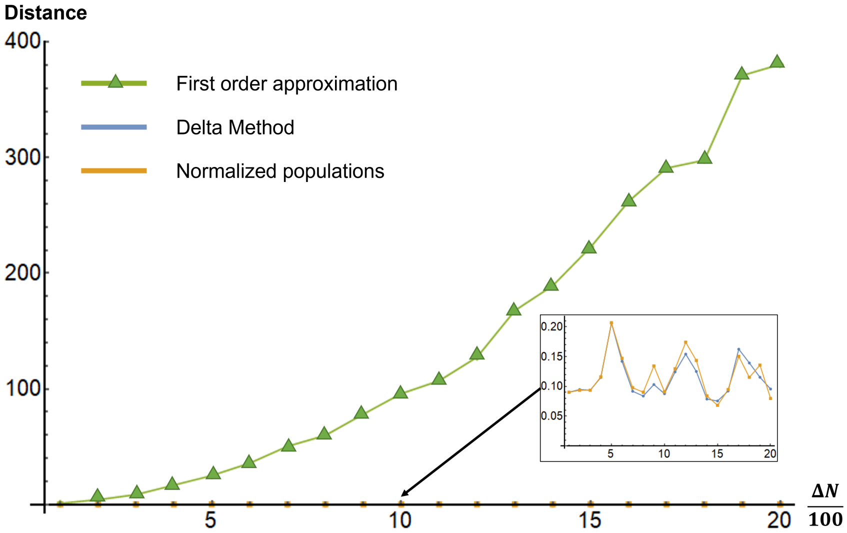

FIGURE 2.9: The green line represents the distance between the variance covariance matrix of normalized populations and the theoretical variance covariance matrix as a function of ΔA_T when the Delta method is truncated to first order. The inset shows the results for normalized populations and Delta populations. The results are obtained using 8 packets of 50 shots each, which is similar to the actual experiment. The results show that the second order corrections are necessary in reproducing the normalization process. The results also show that the Delta method is robust against number noises with standard deviations greater than ours (up to 20%).

For **bipartite measurements**, each family is normalized by the total number of atom of the family itself and the cross covariances are taken care of by considering $g(x, y, w, z) = \{\frac{x}{w}, \frac{y}{z}\}$ The Jacobian of g at point $\vec{x} = (x, y, w, z)$ is given by

$$\nabla g(x, y, w, z) = \begin{pmatrix} \frac{1}{w} & 0 & -\frac{x}{w^2} & 0 \\ 0 & \frac{1}{z} & 0 & -\frac{y}{z^2} \end{pmatrix} \tag{2.77}$$

so that

$$\nabla g(A_i, B_j, A_T, B_T) = \begin{pmatrix} \frac{1}{\overline{A_T}} & 0 & -\frac{\overline{A_i}}{\overline{A_T}^2} & 0 \\ 0 & \frac{1}{\overline{B_T}} & 0 & -\frac{\overline{B_j}}{\overline{B_T}^2} \end{pmatrix} \tag{2.78}$$

Side notes:

- Eqs. 2.63, the delta method (as well as the partial covariance presented in C) are handy statistical methods in that **they only require the knowledge of the statistically significant quantities** (the averages, variances and covariances of the intensity counts) to be applied, the exact knowledge of each data point value is not necessary.

- Another possible data treatment scheme consists in the computation of **partial covariances**. This scheme aims at the suppression of uninteresting common mode correlations between the A variables, common mode correlations being in the case at hand those indirect correlations generated by the variations of the A_T variable[23]. This is done by projecting the A variables onto what can be understood as a hyperplane orthogonal to the A_T variable. This concept is discussed at length in appendix C.

At this point, using Eqs. 2.63 and the Delta method, we have in principle gotten rid of the statistical influence of all tractable noises - we could think of. It is in these refined statistics

---

[23] When the number of atom increases, the magnitude of the A variables also increases which makes for trivial positive correlations

that we will track the growth of spin correlations. This is the subject of the next chapters. Below, the reader will find some other considerations on subsidiary statistical matters.

2.3 Other statistical considerations

The Delta method as well as Eqs. 2.63 are sensitive to the precise estimation of the counts distributions various statistical moments. These moments can easily be misestimated because of trivial phenomena such as signal drifts and signal jumps. Below we explain how these phenomena are addressed in the data treatment.

2.3.1 On drifts and instabilities of the total signal

Long experimental series are subject to drifts and other instabilities which spoil the estimation of statistical relationships between atomic populations. **Drifts** of a given Zeeman signal can be modeled, within a given experimental series, as a function of the time t by the following $A_i(t)$ **stochastic drift** [68]

$$A_i(t) = A_i(0) + a_i t \tag{2.79}$$

Where

- $A_i(0)$ is the random variable corresponding to the atomic signal in cloud i at time $t = 0$
- a_i is a cloud dependent drift coefficient

These drifts are due to the slow thermalization of the experimental set-up.
We compute the expected value of this drift process over a time duration $\Delta t = \underbrace{\text{Number of shots}}_{N_s} \times \underbrace{\text{cycling time}}_{\delta t}$ as follows

$$\begin{aligned}
\mathbb{E}_{\Delta t}(A_i(t)) &= \frac{1}{N_s}\sum_{k}^{N_s}\mathbb{E}\left(A_i(0) + a_i k \delta t\right) \\
&= \frac{1}{N_s}\sum_{k}^{N}\mathbb{E}\left(A_i(0)\right) + a_i \frac{\delta t}{N_s}\sum_{k}^{N} k \\
&\simeq \mathbb{E}\left(A_i(0)\right) + \underbrace{\frac{a_i \Delta t}{2}}_{\text{systematic deviation}}
\end{aligned} \tag{2.80}$$

Variances and covariances are computed in much the same manner and show systematic deviations from the relevant distribution which is that of $A_i(0)$.
To get rid of the trivial influence of these drifts, we subtract any linear contributions from the total signal sequence of the experimental series that is considered (see Fig. 2.10). In bipartite experiments, each family's signal is corrected individually.

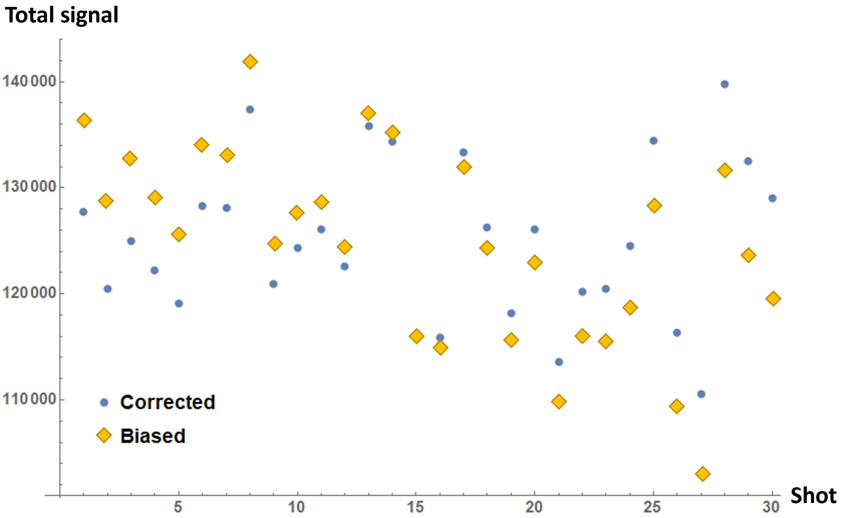

FIGURE 2.10: The data is corrected for atom number drifts by deleting linear contribution to said number through time. To do so we first fit the data with a function of the form $at+b$, we then subtract this contribution to the data before adding the initial average signal of the series to the data back again. For bipartite experiments, **it is not sufficient to correct for the total signal**, it is necessary that each family's signal drift be corrected for independently, as opposite drifts caused by the bipartition can cancel out making for a total signal constant through time.

In much the same way, sudden **signal jumps** lead to erroneous estimations of the statistical relationships between the A variables.

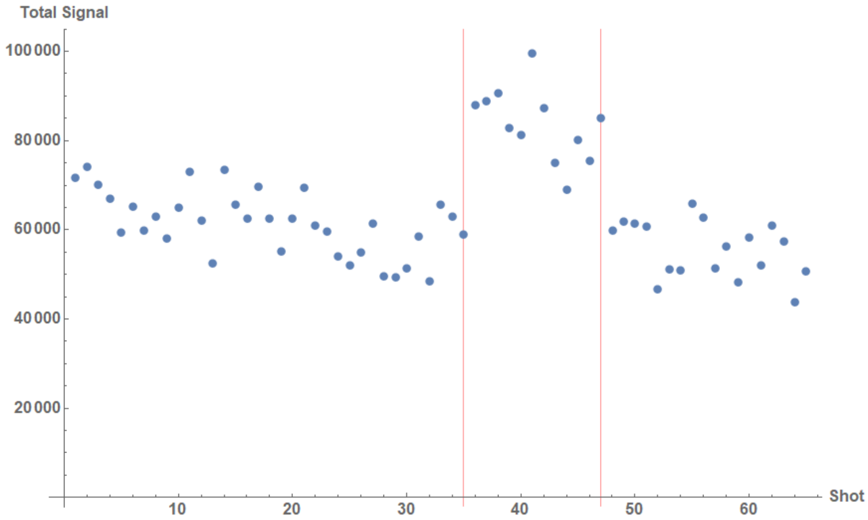

FIGURE 2.11: When an experimental sequence of shots displays a signal jump, the data is divided into several parts each of which is analyzed independently. In the case shown above, the data is sliced into three independent subpackets materialized by the red vertical lines.

2.4 General data treatment scheme

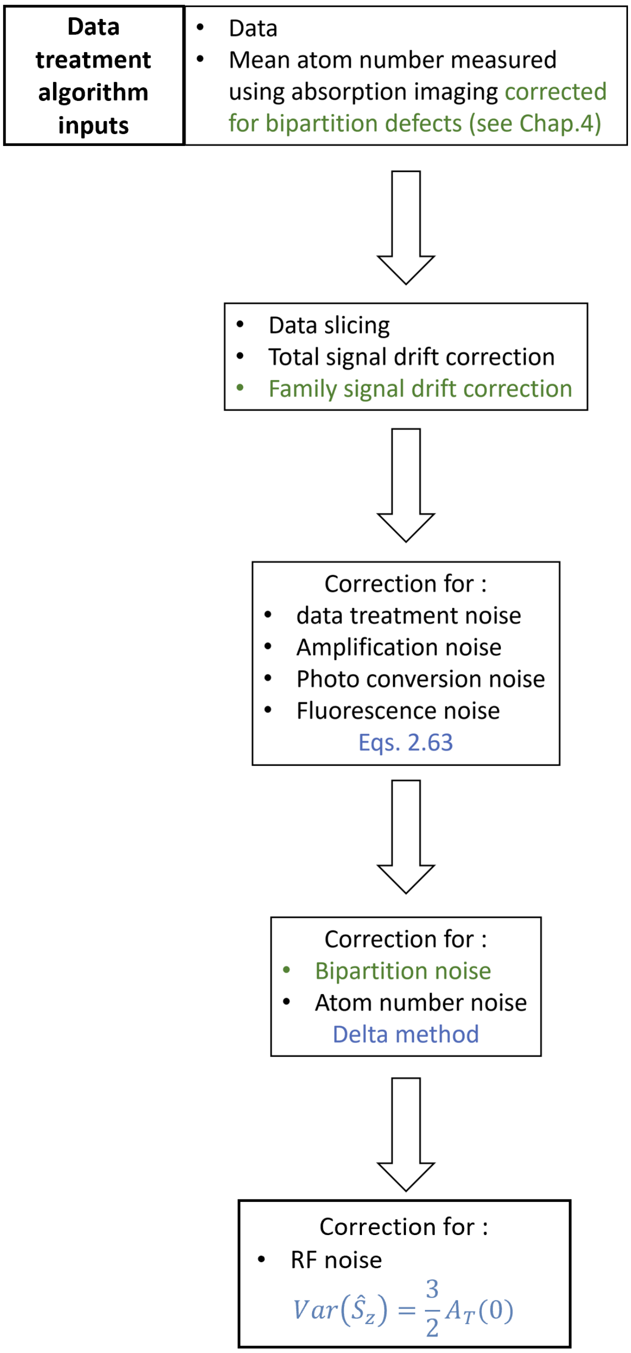

FIGURE 2.12: General data correction scheme. Green: treatments specific to the bipartition experiments. Blue: method used for the data treatment. The data treatment algorithm's inputs are the data (experimental images) and the mean atom number measured through absorption imaging. This atom number can be overestimated for bipartition experiments (see Chap. 4) and must be corrected for these experiments. The data is then sliced around signal jumps. Signal drifts are then corrected before equations 2.63 are applied to correct for detection, data treatment and pixel to pixel noises. The Delta method is then applied on the variance covariance matrices thus found to eliminate the spurious contributions of the bipartition and atom number noises. The RF noise's contribution is then measured at time $t = 0$ by assuming that the variance of the magnetization at 0 interaction time should be equal to $\frac{3}{2}A_T(0)$. At later times the RF noise's contribution to the total magnetization is modified according to the remaining number of atoms, see sec. 2.2.6.

3 Spin correlations from collective spin fluctuations

> *Allez en avant, et la foi vous viendra*
>
> – Jean le Rond d'Alembert

In this chapter we show that the growth of all sorts of correlations in our system is enclosed within the first and second - possibly mixed - moments of the Zeeman populations. By measuring these various statistical moments, focusing in particular on the variance of the total magnetization and the spin populations' averages, we give a direct experimental proof of the long time build up of spin correlations in our system. The method we propose circumvents the use of customary state tomography techniques.

3.1 Definitions

In all of the following

- $\hat{m}_i = |m\rangle_i \langle m|_i$ is the operator associated with the number of atoms in the spin state m in site i, for typographic reasons, in some equations, we will also write $\hat{m}_i = |m_i\rangle \langle m_i|$. When site i is doubly populated $\hat{m}_i = (|m\rangle_1 \otimes \mathbb{1} + \mathbb{1} \otimes |m\rangle_2)(\langle m|_1 \otimes \mathbb{1} + \mathbb{1} \otimes \langle m|_2)$
- $\hat{A}_m = \sum_i \hat{m}_i$ is the non normalized number of atoms in the m Zeeman cloud
- a_m is the ***expectation value*** of the normalized number of atoms in the m Zeeman cloud
- a_m^i is the ***expectation value*** of the non normalized number of atoms in the m spin state in the ***singlonic*** site i of the optical lattice $a_m^i = \langle \hat{m}_i \rangle$
- $a_m^{i,d}$ is the ***expectation value*** of the non normalized number of atoms in the m spin state in the ***doublonic*** site i of the optical lattice $a_m^{i,d} = \langle \hat{m}_i \rangle$
- The $C_{m,m'}^{M_S}$ symbol represents the $\left\langle S, M_S \middle| 3, m, 3, m' \right\rangle$ Clebsch-Gordan coefficient
- N_d is the number of **populated** doublonic ***sites*** in the lattice
- N_s is the number of **populated** singlonic ***sites*** in the lattice
- $N_S = N_s + N_d$ is the number of **populated** sites in the lattice
- $A_T = 2N_d + N_s$ is the number of atoms in the lattice

3.2 From the elementary spin correlators to the magnetization correlator and correlations lengths

3.2.1 Elementary correlators

In this first experiment we focus on the growth of global spin correlations.
For spin particles in a lattice, the following correlator is a most suited candidate to describe these spin correlations

$$C^{m,m'} = \sum_{i\neq j}^{N_S} \left\langle \hat{m}_i \hat{m}'_j \right\rangle - \langle \hat{m}_i \rangle \left\langle \hat{m}'_j \right\rangle \tag{3.1}$$

The $C^{m,m'}$ correlator, hereafter called elementary m,m' correlator is simply the sum over the whole lattice of individual non local ($i \neq j$) correlators.
In this section we show that this kind of correlators can be ***estimated under certain conditions (unit filling + homogeneity) simply by looking at the statistics of the Zeeman populations*** *.*
To do so, let us first rewrite the elementary correlator as follows

$$\begin{aligned} C^{m,m'} &= \sum_{i\neq j}^{N_S} \left\langle \hat{m}_i \hat{m}'_j \right\rangle - \langle \hat{m}_i \rangle \left\langle \hat{m}'_j \right\rangle \\ &= \sum_{i\neq j}^{N_S} \operatorname{cov}\left(\hat{m}_i, \hat{m}'_j\right) \\ &= \sum_{i,j}^{N_S} \operatorname{cov}\left(\hat{m}_i, \hat{m}'_j\right) - \sum_{i}^{N_S} \operatorname{cov}\left(\hat{m}_i, \hat{m}'_i\right) \end{aligned} \tag{3.2}$$

This quantity can be linked to the statistical properties of the populations in the following manner:
The **first term** is straightforwardly estimated from the **variance covariance matrix of the Zeeman populations**

$$\begin{aligned} \operatorname{cov}(A_m, A_{m'}) &= \operatorname{cov}\left(\sum_{i}^{N_S} \hat{m}_i, \sum_{j}^{N_S} \hat{m}'_i\right) \\ &= \sum_{i,j}^{N_S} \operatorname{cov}\left(\hat{m}_i, \hat{m}'_i\right) \end{aligned} \tag{3.3}$$

The relationship between the **on-site quantum correlations captured by the second term** and the Zeeman populations is less explicit and will require from us that we compute various on-site expectation values, which we now do:

Expression of a^i_m for singlons
Let the total many-body wavefunction be $|\Psi\rangle = \sum_\alpha \alpha |\alpha\rangle$ where $|\alpha\rangle$ is a state spanning the whole lattice of the form $\left| m^\alpha_1 ... m^\alpha_i ... m^\alpha_{N_S} \right\rangle$, m^a_i being a the spin projection of the singlon at

site i ($m_i \in [|-3,3|]$) and alpha is a complex number

$$\begin{aligned} a_m^i = \langle \hat{m}_i \rangle &= \sum_\alpha \sum_\beta \alpha^* \beta \langle \alpha | m_i \rangle \langle m_i | \beta \rangle \\ &= \sum_\alpha \sum_\beta \alpha^* \beta \left\langle m_1^\alpha .. m_i^\alpha ... m_{N_S}^\alpha \middle| m_i \right\rangle \left\langle m_i \middle| m_1^\beta .. m_i^\beta ... m_{N_S}^\beta \right\rangle \\ &= \sum_\alpha \sum_\beta \alpha^* \beta \delta_{m,m_i^\alpha} \delta_{m,m_i^\beta} \langle \alpha | \beta \rangle \\ &= \sum_\alpha |\alpha|^2 \delta_{m,m_i^\alpha} \end{aligned} \tag{3.4}$$

Expression of $\langle M | \hat{m}_i | M' \rangle$ for doublons

In all of the following, we assume that doublons are restricted to the S=6 manifold which is, because of local contact interactions, gap protected (for details see [49]). We therefore write the $|S,M\rangle$ state as simply $|M\rangle$. This *molecular* state can be developed using Clebsch Gordan coefficients in the *atomic* basis

$$|M\rangle = \sum_{m_a} C^M_{m_a, M-m_a} |m_a, M-m_a\rangle \tag{3.5}$$

And therefore

$$\begin{aligned} \langle M | \hat{m}_i | M' \rangle &= \sum_{m_a,m_b} C^M_{m_a,M-m_a} C^{M'}_{m_b,M'-m_b} \langle m_a, M-m_a | \Big(|m\rangle_1 \langle m|_1 + |m\rangle_2 \langle m|_2 \Big) | m_b, M'-m_b \rangle \\ &= \sum_{m_a,m_b} C^M_{m_a,M-m_a} C^{M'}_{m_b,M'-m_b} \left[(\delta_{m,m_a} \delta_{m,m_b} \delta_{M-m_a,M'-m_b}) + (\delta_{m_a,m_b} \delta_{m,M-m_a} \delta_{m,M'-m_b}) \right] \\ &= \sum_{m_a,m_b} C^M_{m_a,M-m_a} C^{M'}_{m_b,M'-m_b} \delta_{m,m_a} \delta_{m,m_b} \delta_{M-m_a,M'-m_b}) \\ &+ \sum_{m_a,m_b} C^M_{m_a,M-m_a} C^{M'}_{m_b,M'-m_b} \delta_{m,M-m_a} \delta_{m,M'-m_b} \delta_{m_a,m_b} \\ &= C^M_{m,M-m} C^{M'}_{m,M'-m} \delta_{M,M'} + C^M_{M-m,m} C^{M'}_{M'-m,m} \delta_{M,M'} \\ &= 2 \left(C^M_{m,M-m} \right)^2 \delta_{M,M'} \end{aligned} \tag{3.6}$$

Hence denoting by $|\psi\rangle = \sum_\alpha \alpha |\alpha\rangle = \sum_\alpha \alpha \Big| \overbrace{m_1^\alpha, m_2^\alpha, \ldots m_s^\alpha}^{\text{singlons}}, \overbrace{M_{s+1}^\alpha, \ldots, M_S^\alpha}^{\text{doublons}} \Big\rangle$ the full state wave-function of the whole many body system at hand, we obtain the following results

Expression of $a_m^{i,d}$ for doublons

$$\begin{aligned} a_m^{i,d} = \langle \hat{m}_i \rangle &= \sum_\alpha \sum_\beta \alpha^* \beta \langle m_1^\alpha, m_2^\alpha, \ldots m_s^\alpha, M_{s+1}^\alpha, \ldots M_i^\alpha \ldots, M_S^\alpha | \hat{m}_i \left| m_1^\beta, m_2^\beta, \ldots m_s^\beta, M_{s+1}^\beta, \ldots M_i^\beta \ldots, M_S^\beta \right\rangle \\ 3.6 \rightarrow &= 2 \sum_\alpha \sum_\beta \alpha^* \beta \left(C^{M_i^\alpha}_{m,M_i^\alpha - m} \right)^2 \delta_{\alpha,\beta} \\ &= 2 \sum_\alpha |\alpha|^2 \left(C^{M_i^\alpha}_{m,M_i^\alpha - m} \right)^2 \end{aligned} \tag{3.7}$$

Expression of $\langle \hat{m}_i \hat{m}'_i \rangle$ for singlons

$$\begin{aligned}
\langle \hat{m}_i \hat{m}'_i \rangle &= \sum_{\alpha}\sum_{\alpha'} \alpha^* \alpha' \langle \alpha | m_i \rangle \langle m_i | m'_i \rangle \langle m'_i | \alpha' \rangle \\
&= \sum_{\alpha}\sum_{\alpha'} \alpha^* \alpha' \langle m_1^{\alpha} .. m_i^{\alpha} ... m_N^{\alpha} | m_i \rangle \langle m_i | m'_i \rangle \left\langle m'_i \middle| m_1^{\alpha'} .. m_i^{\alpha'} ... m_N^{\alpha'} \right\rangle \\
&= \sum_{\alpha}\sum_{\alpha'} \alpha^* \alpha' \delta_{m,m'} \langle m_1^{\alpha} .. m_i^{\alpha} ... m_N^{\alpha} | m_i \rangle \left\langle m'_i \middle| m_1^{\alpha'} .. m_i^{\alpha'} ... m_N^{\alpha'} \right\rangle \\
&= \sum_{\alpha}\sum_{\alpha'} \alpha^* \alpha' \delta_{m,m'} \delta_{m,m_i^{\alpha}} \delta_{m',m_i^{\alpha'}} \langle \alpha | \alpha' \rangle \\
&= \delta_{m,m'} \sum_{\alpha} |\alpha|^2 \delta_{m,m_i^{\alpha}} \\
&= \delta_{m,m'} a_m^i
\end{aligned} \tag{3.8}$$

Expression of $\langle M | \hat{m}_i \hat{m}'_i | M' \rangle$ for doublons

$$\begin{aligned}
\langle M | \hat{m}_i \hat{m}'_i | M' \rangle = &\sum_{m_a,m_b} C^{M}_{m_a,M-m_a} C^{M'}_{m_b,M'-m_b} \langle m_a, M-m_a | \\
&\left[(|m\rangle_1 \langle m|_1 + |m\rangle_2 \langle m|_2) \left(|m'\rangle_1 \langle m'|_1 + |m'\rangle_2 \langle m'|_2 \right) \right] |m_b, M'-m_b\rangle \\
&= \sum_{m_a,m_b} C^{M}_{m_a,M-m_a} C^{M'}_{m_b,M'-m_b} \langle m_a, M-m_a | \left[\left(|m_1\rangle \langle m_1 | m'_1 \rangle \langle m'_1 | + \right.\right. \\
&|m_1\rangle \langle m_1 | m'_2 \rangle \langle m'_2 | + |m_2\rangle \langle m_2 | m'_1 \rangle \langle m'_1 | + |m_2\rangle \langle m_2 | m'_2 \rangle \langle m'_2 | \, |m_b, M'-m_b\rangle \\
&= \sum_{m_a,m_b} C^{M}_{m_a,M-m_a} C^{M'}_{m_b,M'-m_b} \Big[(\delta_{m,m_a} \delta_{m,m_b} \delta_{M-m_a,M'-m_b} \delta_{m,m'}) + (\delta_{m,m_a} \delta_{m,m_b}) \times \\
&(\delta_{m',M-m_a} \delta_{m',M'-m_b}) + (\delta_{m',m_a} \delta_{m',m_b})(\delta_{m,M'-m_b} \delta_{m,M-m_a}) + (\delta_{m,M-m_a} \delta_{m,M'-m_b} \delta_{m_a,m_b} \delta_{m,m'}) \Big] \\
&= \sum_{m_a,m_b} C^{M}_{m_a,M-m_a} C^{M'}_{m_b,M'-m_b} (\delta_{m,m_a} \delta_{m,m_b} \delta_{M-m_a,M'-m_b} \delta_{m,m'}) \\
&+ \sum_{m_a,m_b} C^{M}_{m_a,M-m_a} C^{M'}_{m_b,M'-m_b} (\delta_{m,m_a} \delta_{m,m_b})(\delta_{m',M-m_a} \delta_{m',M'-m_b}) \\
&+ \sum_{m_a,m_b} C^{M}_{m_a,M-m_a} C^{M'}_{m_b,M'-m_b} (\delta_{m',m_a} \delta_{m',m_b})(\delta_{m,M'-m_b} \delta_{m,M-m_a}) \\
&+ \sum_{m_a,m_b} C^{M}_{m_a,M-m_a} C^{M'}_{m_b,M'-m_b} (\delta_{m,M-m_a} \delta_{m',M'-m_b} \delta_{m_a,m_b} \delta_{m,m'}) \\
&= C^{M}_{m,M-m} C^{M'}_{m,M'-m} \delta_{M,M'} \delta_{m,m'} + C^{M}_{m,M-m} C^{M'}_{m,M'-m} (\delta_{m',M-m} \delta_{m',M'-m}) \\
&+ C^{M}_{m',M-m'} C^{M'}_{m',M'-m'} (\delta_{m,M'-m'} \delta_{m,M-m'}) + C^{M}_{M-m,m} C^{M'}_{M'-m,m} \delta_{M,M'} \delta_{m,m'} \\
&= 2 \left(C^{M}_{m,M-m} \right)^2 \delta_{M,M'} \delta_{m,m'} + \left(C^{M}_{m,M-m} \right)^2 \delta_{M,m'+m} \delta_{M,M'} + \left(C^{M}_{m',M-m'} \right)^2 \delta_{M,m'+m} \delta_{M,M'} \\
&= 2 \left(C^{M}_{m,M-m} \right)^2 \delta_{M,M'} \delta_{m,m'} + \left[\left(C^{m'+m}_{m,m'} \right)^2 + \left(C^{m'+m}_{m',m} \right)^2 \right] \delta_{M,M'} \delta_{M,m'+m} \\
&= 2 \left[\left(C^{M}_{m,M-m} \right)^2 \delta_{M,M'} \delta_{m,m'} + \left(C^{m'+m}_{m,m'} \right)^2 \delta_{M,M'} \delta_{M,m'+m} \right]
\end{aligned} \tag{3.9}$$

Expression of $\langle \hat{m}_i \hat{m}'_i \rangle$ for doublons

$$\begin{aligned}
\langle \hat{m}_i \hat{m}'_i \rangle &= \sum_\alpha \sum_\beta \alpha^* \beta \quad \langle m_1^\alpha, m_2^\alpha, \dots m_s^\alpha, M_{s+1}^\alpha, \dots M_i^\alpha \dots, M_S^\alpha | \, \hat{m}_i \hat{m}'_i \, \Big| m_1^\beta, m_2^\beta, \dots m_s^\beta, M_{s+1}^\beta, \dots M_i^\beta \dots, M_S^\beta \Big\rangle_i \\
&= 2 \sum_\alpha \sum_\beta \alpha^* \beta \left[\left(C_{m, M_i^\alpha - m}^{M_i^\alpha} \right)^2 \delta_{\alpha,\beta} \delta_{m,m'} + \left(C_{m,m'}^{m'+m} \right)^2 \delta_{M_i^\alpha, m'+m} \delta_{\alpha,\beta} \right] \\
&= 2 \sum_\alpha |\alpha|^2 \left(C_{m, M_i^\alpha - m}^{M_i^\alpha} \right)^2 \delta_{m,m'} + \underbrace{2 \left(C_{m,m'}^{m'+m} \right)^2 \sum_\alpha |\alpha|^2 \delta_{M_i^\alpha, m'+m}}_{\Xi_{m+m'}^{i,d}} \\
3.7 \rightarrow &= a_m^{i,d} \delta_{m,m'} + \Xi_{m+m'}^{i,d}
\end{aligned} \tag{3.10}$$

Hence, we obtain the following expression for the second term of Eqs. 3.2

$$\begin{aligned}
\sum_i^{N_S} \mathrm{cov}\left(\hat{m}_i, \hat{m}'_i \right) &= \sum_i^{N_s} \left(\delta_{m,m'} a_m^i - (a_m^i a_{m'}^i) \right) + \sum_i^{N_d} \left(\delta_{m,m'} a_m^{i,d} - (a_m^{i,d} a_{m'}^{i,d}) + \Xi_{m+m'}^{i,d} \right) \\
&= \sum_i^{N_s} \left(a_m^i (\delta_{m,m'} - a_{m'}^i) \right) + \sum_i^{N_d} \left(a_m^{i,d} (\delta_{m,m'} - a_m^{i,d}) + \Xi_{m+m'}^{i,d} \right)
\end{aligned} \tag{3.11}$$

And all in all we obtain the following **expression for the elementary m,m' correlator**

$$C^{m,m'} = \sum_{i \neq j}^{N_s} \langle \hat{m}_i \hat{m}'_i \rangle - \langle \hat{m}_i \rangle \langle \hat{m}'_i \rangle = \mathrm{cov}\left(A_m, A_{m'} \right) - \sum_i^{N_s} \left(a_m^i (\delta_{m,m'} - a_{m'}^i) \right) - \sum_i^{N_d} \left(a_m^{i,d} (\delta_{m,m'} - a_m^{i,d}) + \Xi_{m+m'}^{i,d} \right) \tag{3.12}$$

The distinction between a_m^d and a_m is necessary as, a priori, doublons undergo dynamical processes which are different from those of singlons. In particular the dipolar dynamics undergone by doublons are faster.

In any case, the sum terms involving the precise knowledge of the number and states of doublons or singlons at time t are not experimentally accessible. This limitation of course is not specific to our experiment and is not of huge concern anyway as we are mostly interested in the long time build up of the quantum correlations, moreover the number of doublons decreasing with time means that the contribution of these terms to the $C^{m,m'}$ correlator quickly becomes negligible. In practice, in our setup, doublons are completely dropped within the first 10 ms, at which point the correlator can be written

$$C_{t>10ms}^{m,m'} = \sum_{i \neq j}^{N} \langle \hat{m}_i \hat{m}'_i \rangle - \langle \hat{m}_i \rangle \langle \hat{m}'_i \rangle = \mathrm{cov}\left(A_m, A_{m'} \right) - \sum_i^{N_s} a_m^i (\delta_{m,m'} - a_{m'}^i) \tag{3.13}$$

This expression can be linked to the following **fictitious product state $|\Psi\rangle$ built on the single particle wave function whose average spin populations are given by the Zeeman populations**:

$$|\Psi\rangle = \big|1 : \psi\big\rangle \dots \big|N_S : \psi\big\rangle \tag{3.14}$$

Where

- $\big| i : \psi \big\rangle = \sum_m \sqrt{a_m^i} \, |m\rangle$

For this state

$$\begin{aligned}\langle \hat{A}_m \hat{A}_{m'} \rangle_\Psi &= \sum_{i\neq i'} \langle i:\psi | m_i \rangle \langle m_i | i:\psi \rangle \langle i':\psi | m'_{i'} \rangle \langle m'_{i'} | i':\psi \rangle + \sum_{i'=i} \langle i:\psi | m_i \rangle \langle m'_i | i:\psi \rangle \\ &= \sum_{i\neq i'} a^i_m a^{i'}_{m'} + \sum_i a^i_m \delta_{m,m'}\end{aligned} \tag{3.15}$$

Similarly, we get

$$\langle \hat{A}_m \rangle_\Psi = \sum_i a^i_m \tag{3.16}$$

Using these equations we define cov_{prod} as

$$\begin{aligned}\mathsf{cov}_{prod}\left(\hat{A}_m, \hat{A}_{m'}\right) = \operatorname{cov}\left(\hat{A}_m, \hat{A}_{m'}\right)_\Psi &= \sum_{i\neq i'} a^i_m a^{i'}_{m'} + \sum_{i'=i} a^i_m \delta_{m,m'} - \sum_i a^i_m \sum_j a^j_{m'} \\ &= \sum_i a^i_m (\delta_{m,m'} - a^i_{m'})\end{aligned} \tag{3.17}$$

And

$$C^{m,m'}_{t>10ms} = \operatorname{cov}\left(\hat{A}_m, \hat{A}_{m'}\right) - \mathsf{cov}_{prod}(\hat{A}_m, \hat{A}_{m'}) \tag{3.18}$$

This equation shows that covariances assuming values different than those associated with the product state $|\Psi\rangle$ is a proof of correlations developing in the sample.

Assuming homogeneity i.e. $\left| i:\psi \right\rangle = \sum_m \sqrt{\frac{A_m}{N_s}} |m\rangle = \sum_m \sqrt{a_m} |m\rangle$, the $\mathsf{cov}_{prod}(\hat{A}_m, \hat{A}_{m'})$ term becomes entirely deducible from the global spin populations averages (because a^i_m is then equal to $\frac{A_m}{N_s}$), and in turn, **the elementary correlator $C^{m,m'}_{t>10ms}$ becomes entirely deducible from the statistics of the populations**, as was announced in the beginning of this section

Side note: If we do not assume homogeneity, we can still reorder the labeling of the sites so that, $a^1_m \leq \ldots \leq a^{N_S}_m$. Using the Chebyshev's sum inequality [69], we get

$$\begin{aligned} \frac{1}{N_S} \sum_i^{N_S} a^i_m a^i_m \geq \left(\frac{1}{N_S} \sum^{N_S} a^i_m \right)^2 = a^2_m \\ \Leftrightarrow -\frac{1}{N_S} \sum^{N_S} a^i_m a^i_m \leq -a^2_m \\ \Leftrightarrow \frac{1}{N_S} \sum^{N_S} a^i_m - \frac{1}{N_S} \sum^{N_S} a^i_m a^i_m \leq a_m - a^2_m \\ \Leftrightarrow \mathsf{cov}_{prod}\left(\hat{A}_m, \hat{A}_m\right) \leq N_S (a_m - a^2_m) \\ \Leftrightarrow \operatorname{cov}\left(\hat{A}_m, \hat{A}_m\right) - \mathsf{cov}_{prod}\left(\hat{A}_m, \hat{A}_m\right) \geq \operatorname{cov}\left(\hat{A}_m, \hat{A}_m\right) - N_S (a_m - a^2_m) \end{aligned} \tag{3.19}$$

So that the statistical properties of the populations provide lower bounds for the diagonal correlators:

$$C^{m,m}_{t>10ms} \geq \operatorname{cov}\left(\hat{A}_m, \hat{A}_m\right) - N_S (a_m - a^2_m) \tag{3.20}$$

3.2.2 Magnetization correlator

Other relevant correlations can be obtained using these elementary correlators as building blocks, for example ***local magnetization correlations****.*

A measure of the local magnetizations correlations is given by the so called **magnetization correlator, C_z, which takes into account all the pairwise connected correlations associated with magnetization** in our system:

$$C_z = \sum_{i\neq j}^{N} \left\langle \hat{s}_z^i \hat{s}_z^j \right\rangle - \left\langle \hat{s}_z^i \right\rangle \left\langle \hat{s}_z^j \right\rangle \tag{3.21}$$

where $\hat{s}_z^i = \sum_m m\hat{m}_i$ is operator associated with the local magnetization of the **particle** in the i^{th} site of the lattice. Yet again, depending on the filling of lattice site i, the $\hat{s}_z^i$ operator applies either to a single atom or a pair of atom.

This correlator is also given by the elementary correlators:

$$\begin{aligned} C_z = \sum_{m,m'} mm' C^{m,m'} &= \sum_{m,m'} mm' \sum_{i\neq j}^{N} \left\langle \hat{m}_i \hat{m}'_j \right\rangle - \langle \hat{m}_i \rangle \left\langle \hat{m}'_j \right\rangle \\ &= \sum_{i\neq j}^{N} \left\langle \sum_{m,m'} mm' \hat{m}_i \hat{m}'_j \right\rangle - \left\langle \sum_m m\hat{m}_i \right\rangle \left\langle \sum_{m'} m' \hat{m}'_j \right\rangle \\ &= \sum_{i\neq j}^{N} \left\langle \hat{s}_z^i \hat{s}_z^j \right\rangle - \left\langle \hat{s}_z^i \right\rangle \left\langle \hat{s}_z^j \right\rangle \end{aligned} \tag{3.22}$$

In particular, using 3.18, we find

$$\begin{aligned} C_z^{t>10ms} = \sum_{m,m'} mm' C^{m,m'}_{t>10ms} &= \sum_{m,m'} mm' \mathrm{cov}\left(A_m, A_{m'}\right) - \sum_{m,m'} mm' \mathrm{cov}_{prod}(A_m, A_{m'}) \\ &= \sum_{m,m'} mm' \mathrm{cov}\left(A_m, A_{m'}\right) - \sum_{m,m'} mm' \sum_i a^i_m (\delta_{m,m'} - a^i_{m'}) \\ &= \underbrace{\sum_{m,m'} mm' \mathrm{cov}\left(A_m, A_{m'}\right)}_{\Delta^2 \hat{S}_z} + \sum_i \left(\sum_m m a^i_m\right)^2 - \sum_i \sum_m m^2 a^i_m \\ \text{homogeneity} \rightarrow &= \mathrm{Var}\hat{S}_z + \underbrace{N_S \left(\sum_m m a_m\right)^2 - N_S \sum_m m^2 a_m}_{-\Sigma_z \equiv \text{ on-site spin fluctuations}} \end{aligned} \tag{3.23}$$

Which is the correlator used in our article [66].

Σ_z represents the on site site fluctuations of the local magnetization $\Sigma_z = \sum_i \mathrm{Var}\left(\hat{s}_z^i\right)$.

In this chapter we have shown that the information encoded in this correlator and others is entirely found in the elementary correlator $C^{m,m'}_{t>10ms}$, which is readily obtained from the populations statistics.

While the link between the elementary correlators and the magnetization correlator is of theoretical interest, experimental results **focus on the latter** $C_z^{t>10ms}$ as there is no obvious way to correct the individual population covariances $\mathrm{cov}\left(A_m, A_{m'}\right)$ for the RF noise as was explained in Chap. 2 for interaction times $t_{\mathrm{dyn}} > 0$ ms whereas it is possible to do it for the variance of the magnetization.

Final notes:

- The method we propose here requires that populations be measured in a **single basis** only.
- The method requires that homogeneity be assumed to retrieve quantum correlations. This condition is in fact not too stringent as our experimental results are not significantly affected by typical experimental gradients as suggested by numerical simulations, see sec. 3.3.5

3.3 Results

3.3.1 Experimental protocol

In order to estimate the **magnetization correlator**,C_z, discussed above as a function of time, the results of the dipolar dynamics must be measured a great many number of times. The results presented in this chapter are based on the analysis of $5\times$ 40 shots per point (i.e. per interaction time - Δt in the figure below -). The limited size of the subpackets speaks of the necessity to regularly check and compensate for any experimental drift.

Typical experiments start out with a condensate ($N \sim 10^4$), which we load into a 3D anisotropic lattice (see Chap. 1). Particular care is taken calibrating the lattices, the depth of which is measured using 2 μs diffraction sequences and subsequently monitored using dedicated photodiodes[1]. We made sure that the depth of the lattices was always above 20 $E_{r,532}$, typically 22 $E_{r,532}$ for the horizontal lattices and 28 $E_{r,532}$ for the vertical one, such lattice depths ensure that all tunneling related processes are suppressed, their constancy across the various experimental series guarantees on the other hand that the so called *quadratic Zeeman fields* generated by lattice induced tensorial light shifts [15] are constant.

The atoms always spend the same time in the optical lattice independent of the actual duration of the dynamics which is determined by the triggering RF pulse. This helps limit systematic heating or tunneling related biases. Once the chosen dynamic time has elapsed, the atoms are slowly released (in 300 μs) from the hold of the lattice, at the same time the dipolar laser (1075 nm) is abruptly switched off and on again. This technique, termed δ-kick cooling [70], reduces the velocity dispersion of the atoms and makes for smaller and better fitted clouds. The atoms are then imaged after a $\approx$ 14 ms time of flight using a 1 ms off-resonant pulse to make them fluoresce. Each experimental shot provides us with seven spin populations for the chosen interaction time t_{dyn}, the compilation of which lets us estimate the spin population variance covariance matrix of the populations for this specific interaction time, and more importantly in the case at hand the variance of the global magnetization and the average fractional populations.

All of these experiment are carried in the dark for better performances of the fluorescence imaging as was explained in Chap. 1.

---

[1] While the photodiode signal informs us on the power of the light actually hitting the atoms, it may well happen that the spectral purity of the 532 nm laser worsens with time, which can not be detected by the photodiodes. The spectral coherence of the lattice lasers should therefore be frequently checked using diffraction, and improved using the ETALON CAPTURE feature of the Verdi system.

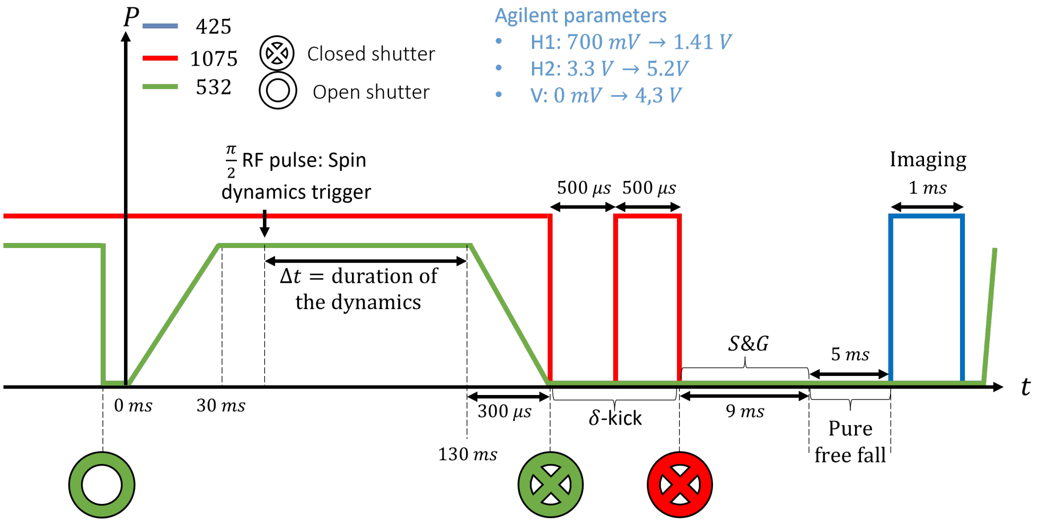

FIGURE 3.1: Schematic power ramps for the various laser involved in the experiments described in the present chapter.

3.3.2 Data treatment protocol

The information enclosed in the data is retrieved by fitting the clouds' intensity profiles with 1D Gaussian functions. These fits provide us with the clouds' total signals and the related standard errors.

To analyze the data we use the scheme referenced at the end of Chap. 2. First, total signal drifts are corrected for as they can fictitiously increase the variances of the various quantities that are measured (the A_{m_s}). Next, we compute the detectivity factors (the so called αs of Eq; 2.63 for example) using the data points at time $t_{\text{dyn}} = 0$ ms so that the average fractional populations are symmetric at all times and equal to those theoretically predicted for a $\frac{\pi}{2}$ pulse. At this point the Eqs. 2.63 are applied to get rid of the noises linked to the detection chain. To get rid of the number noise we then use the Delta scheme presented in Eqs. 2.2.6 on the non normalized variance covariance matrices obtained at the previous step.

We then compute the variance of the magnetization -$\mathrm{Var}\left(\hat{S}_z\right)$- as well as the corresponding onsite fluctuations Σ_z. We finally compute the contribution of the RF noise ($\Delta_{RF}^{t=0}$) for each data point at time $t_{\text{dyn}} = 0$ ms by forcing the normalized variance of the global system $\frac{\mathrm{Var}(\hat{S}_z)}{A_T(0)}$ to $3/2$. In other words we have $\Delta_{RF}^{t=0} = \frac{\mathrm{Var}(\hat{S}_z)}{A_T(0)} - 3/2$. This value is used to correct the variances at greater interaction times by an amount that is proportional to the remaining number of atoms $\Delta_{RF}^{t>0} = \Delta_{RF}^{t=0}\frac{A_T(t)}{A_T(0)}$.

Orders of magnitude for the various noises are *similar* to those found in [66][2]. For the reader to get an idea of the different orders of magnitude, we report this articles' numbers here: the RF noise's contribution is approximately $0.7 \times \sqrt{\frac{3}{2A_T}}$ (where $\sqrt{\frac{3}{2A_T}}$ is the expected variance of the normalized magnetization at time $t_{\text{dyn}} = 0$ ms). The initial data treatment and pixel to pixel noise contribution is similar $0.6 \times \sqrt{\frac{3}{2A_T}}$ and the contribution of the detection chain related noises is about $0.6 \times \sqrt{\frac{3}{2A_T}}$ initially. Using the corrected variances and on site fluctuations we compute the time evolution of the magnetization correlator C_z. This time evolution is presented below.

---

[2] In this article a different data treatment approach was chosen: the normalization process was carried first, then the detection noises were removed in quadrature.

3.3.3 Results

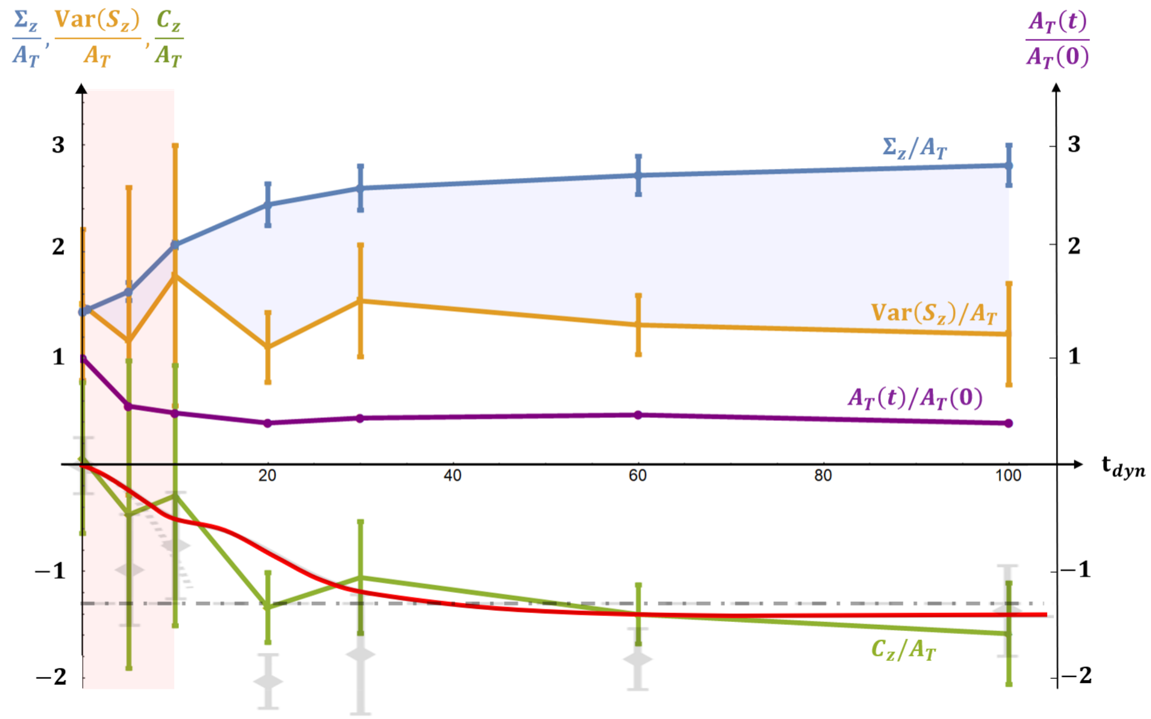

FIGURE 3.2: Green: Normalized magnetization correlator C_z/A_T time evolution. Black transparent points: Normalized magnetization correlator C_z/A_T time evolution using the methods developed in [66], these methods subtract in quadrature the various noises presented in the previous chapter to the normalized intensity count populations. Orange: time evolution of the normalized on site fluctuations Σ_z/A_T. Blue: time evolution of the magnetization's variance $\mathrm{Var}(\hat{S}_z)$. Purple: time evolution of the number of atoms at time t_{dyn} divided by the number of atoms at time $t_{\mathrm{dyn}} = 0$. Red: Numerical time evolution of C_z/A_T, these GDTWA numerical simulations made by our collaborators Sean Muleady, Bihui Zu and Ana Maria Rey do not take losses into account. Black/Dashed: Long time expectation value of C_z/A_T found through high temperature expansions [66]. Red shaded area: "short time" domain, **the discussions of the previous sections are valid beyond t=10 ms**. **The growth of the C_z correlator testifies to the build up of correlations between particles in the lattice**. The rather good agreement with theoretical predictions shows that dissipative phenomena do not impair the development of these correlations, as is also supported by the simulations reported in App. D. The agreement with theory also hints at the **quantum nature of these correlations** while at the same time validating the approach of Chap. 2. The relatively good agreement of the experimental points found through the methods developed in Chap. 2 and those found using the scheme of our article [66] confirms the validity of the methods used in this article.

A more proper monitoring of the quantum correlations' growth as caused by the sole dipole dipole interactions would require doublons to be removed before the beginning of the dynamics. This can be achieved making use of dipolar relaxation [15]. Filtering out doublons requires a preliminary π RF pulse, which transfers all the atom in the coherent state $|m_s = +3\rangle$. In this configuration, doublons undergoing dipolar relaxation leave the lattice. On the other hand singlons remain in the $|m_s = +3\rangle$ state. After 10 ms doublons have mostly left the lattice, at this point a $\frac{\pi}{2}$ pulse can trigger the quench dynamics. This scheme however increases the preparation noise when compared to a single $\frac{\pi}{2}$ pulse and ultimately produces data of lesser quality.

3.3.4 Estimation of quantum correlation lengths

The measured correlators may be used to estimate various kinds of correlation lengths. To do so, one must first specify the distance dependence of the relevant correlation functions. Let us take the example of the following $c_z(i,j)$

$$c_z(i,j) = \left\langle \hat{s}_z^i \hat{s}_z^j \right\rangle - \left\langle \hat{s}_z^i \right\rangle \left\langle \hat{s}_z^j \right\rangle \tag{3.24}$$

For a thermalized spin system we can in general expect this correlator to be exponentially decaying with the distance between sites [71], with a decay rate given by the correlation length ξ.
If we additionally neglect the anisotropy of the dipolar interactions and that of the lattice configuration (single correlation length) and assume that the system is translationally invariant
$(c_z(i,j) \longrightarrow c_z(r_{ij}))$, then we can posit the following functional form for $c_z(r)$

$$c_z(r>0) \approx -c_z(0)e^{-r/\xi} \tag{3.25}$$

Where the $-$ sign is motivated by the fact that C_z is negative.
Here, the $c_z(0)$ constant corresponds to zero range correlations, it should therefore coincide with the on-site fluctuations given by $\frac{\Sigma_z}{N}$ quantity. Hence by summing over all particles in the lattice, we end up with (i_0 is fixed)

$$\begin{aligned} \frac{C_z}{N} &= \sum_{j\neq i} c_z(r_{i_0 j}) = -c_z(0)\sum_{r>0} e^{-r/\xi} \\ \Leftrightarrow \frac{C_z}{N} &= -\frac{\Sigma_z}{N}\sum_{r>0} e^{-r/\xi} \\ \Leftrightarrow -\frac{C_z}{\Sigma_z} &= \sum_{r>0} e^{-r\xi} \end{aligned} \tag{3.26}$$

This integral equation can be solved numerically: in our case, at long times ($t = 100$ ms), we measure $C_z/N \approx -1.37$ and $\Sigma_z/N \approx 3.24$. Using the true lattice geometry and solving for ξ, **we obtain the value**

$$\xi = 0.39\frac{\lambda_{532}}{2}$$

instead of 0.3 for the cubic lattice assumed in [66] which means that, in the extent in which the hypotheses we made hold true, **local magnetization correlations in our system mainly involve neighboring entities**.

This kind of reasoning can be extended to population correlations by focusing on the local population correlator $c^{m,m'}(i,j)$

$$c^{m,m'}(i,j) = \left\langle \hat{m}_i \hat{m}'_j \right\rangle - \langle \hat{m}_i \rangle \left\langle \hat{m}'_j \right\rangle \tag{3.27}$$

Assuming in the same way isotropy, translational invariance and exponential decay we get

$$c^{m,m'}(i,j) = \epsilon c^{m,m'}(0)e^{-r_{ij}/\xi_{m,m'}} \tag{3.28}$$

Where

- $\epsilon = \pm 1$ accounts for the sign of the correlation function

- $c^{m,m'}(0) = \mathrm{cov}_{prod}(A_m, A_{m'})$ accounts for on site fluctuations which as proven above are given by the product variance covariance matrix

Using Eq. 3.18 we get another integral relation (i_0 is fixed)

$$\begin{aligned}\sum_{j\neq i_0}^{N_s} c^{m,m'}(i_0, j) = \epsilon c^{m,m'}(0) \sum_{j\neq i_0}^{N_s} e^{-r_{i_0 j}/\xi_{m,m'}} &= \frac{1}{N}\left(\mathrm{cov}\left(\hat{A}_m, \hat{A}_{m'}\right) - \mathrm{cov}_{prod}(\hat{A}_m, \hat{A}_{m'})\right) \\ \Leftrightarrow \epsilon \sum_{j\neq i_0}^{N_s} e^{-r_{i_0 j}/\xi_{m,m'}} &= \frac{1}{N}\left(\frac{\mathrm{cov}\left(\hat{A}_m, \hat{A}_{m'}\right)}{\mathrm{cov}_{prod}(\hat{A}_m, \hat{A}_{m'})} - 1\right)\end{aligned} \tag{3.29}$$

3.3.5 Effect of inhomogeneities

The effect of magnetic inhomogeneities was numerically investigated, it was confirmed by collaborators through GTWDA simulations (~ 70 atoms) that their effect on the measured correlators was small, that is that the difference between the real inhomogeneous system and the perfect (without gradients) spin system remains small as far as the C_z correlator is concerned, see Fig. 3.3.

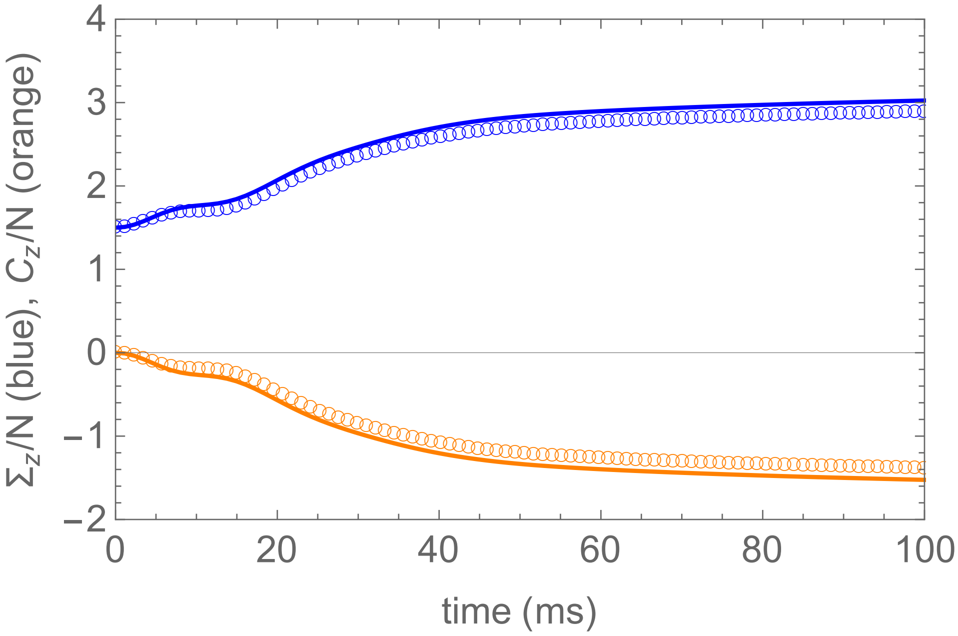

FIGURE 3.3: The effect of inhomogeneities on the development of correlations is negligible. Solid lines correspond to a homogeneous system, circles assume inhomogeneities comparable to those that were experimentally measured. It is intriguing that the correlations which might classically speaking be seen as a measurement of the *relative orientation of the spins* are negligibly affected by the gradients given that the differential rotation between neighboring entities ($\Delta\omega_{Larmor} \simeq 8$ Hz) in our lattice - induced by these gradients - is not negligible on the time scale of the experiment (100 ms). This result can be understood by realizing that the evolution of the C_z correlator is driven by the values of the fractional populations (the variance remains mostly constant throughout the dynamics) and that magnetic gradients do not affect much the evolution of these populations on the time scale of the experiment carried here, a fact which was observed experimentally before [72] and checked numerically on large atomic samples.

4 Spin correlations from bipartite measurements

> *Les idiots. Ils ne savent pas à quel point la moitié est plus que le tout, et ils ne savent pas non plus à quel point il y a dans la mauve et l'asphodèle un immense avantage.*
>
> – Hesiod (Les travaux et les jours)

The range of the dipole dipole interactions between chromium atoms is such that it is reasonable to believe that the spin correlations observed in our system involve neighboring entities mainly, be they singlons or doublons. This proposition is in some sense supported by the spin correlation length found in the previous chapter $\xi = 0.39\lambda/2$. *The experiment presented in Chap. 3 was not designed to take this specificity into account. In this chapter we present a novel bipartition method based on position to momentum mapping techniques which can be used to probe, more finely, the correlations between these neighboring entities. We show that, in our system, there develops correlations of more intricate nature than can be, a priori, surmised from the negative value of* C_z.

4.1 A practical example

To illustrate the possible usefulness of bipartite measurements, let us consider the following hypothetical state

$$|\Psi\rangle = \frac{|1_A:+3, 1_B:-3 ... N_A:+3, N_B:-3\rangle + |1_A:-3, 1_B:+3 ... N_A:-3, N_B:+3\rangle}{\sqrt{2}}$$

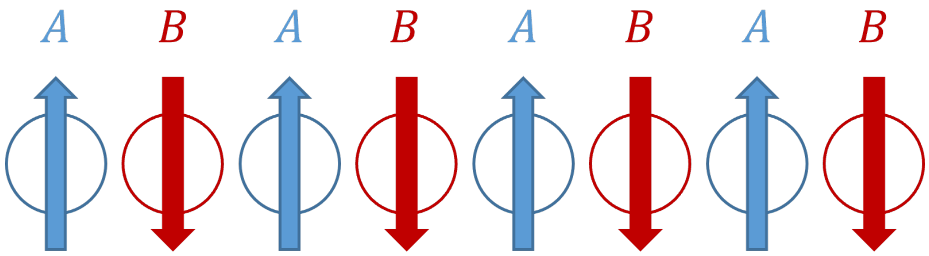

FIGURE 4.1: Representation of state $|\Psi\rangle$

$|\Psi\rangle$ describes a spin ensemble prepared in an **antiferromagnetic state**. Let us consider the global spin correlation function C_z introduced in the previous chapter and rewrite it so as to take into account the bipartite nature of this state

$$
\begin{aligned}
C_z &= \sum_{i\neq j} \left\langle \hat{s}_z^i \hat{s}_z^j \right\rangle - \left\langle \hat{s}_z^i \right\rangle \left\langle \hat{s}_z^j \right\rangle \\
&= \sum_{i_A\neq j_A} \left(\left\langle \hat{s}_z^{i_A} \hat{s}_z^{j_A} \right\rangle - \left\langle \hat{s}_z^{i_A} \right\rangle \left\langle \hat{s}_z^{j_A} \right\rangle \right) + \sum_{i_A, j_B} \left(\left\langle \hat{s}_z^{i_A} \hat{s}_z^{j_B} \right\rangle - \left\langle \hat{s}_z^{i_A} \right\rangle \left\langle \hat{s}_z^{j_B} \right\rangle \right) \\
&+ \sum_{i_B, j_A} \left(\left\langle \hat{s}_z^{i_B} \hat{s}_z^{j_A} \right\rangle - \left\langle \hat{s}_z^{i_B} \right\rangle \left\langle \hat{s}_z^{j_A} \right\rangle \right) + \sum_{i_B\neq j_B} \left(\left\langle \hat{s}_z^{i_B} \hat{s}_z^{j_B} \right\rangle - \left\langle \hat{s}_z^{i_B} \right\rangle \left\langle \hat{s}_z^{j_B} \right\rangle \right) \\
&= \underbrace{\sum_{i_A\neq j_A} \left\langle \hat{s}_z^{i_A} \hat{s}_z^{j_A} \right\rangle - \left\langle \hat{s}_z^{i_A} \right\rangle \left\langle \hat{s}_z^{j_A} \right\rangle}_{C_z^A} + \underbrace{\sum_{i_B\neq j_B} \left\langle \hat{s}_z^{i_B} \hat{s}_z^{j_B} \right\rangle - \left\langle \hat{s}_z^{i_B} \right\rangle \left\langle \hat{s}_z^{j_B} \right\rangle}_{C_z^B} + \underbrace{2 \sum_{i_A, j_B} \left\langle \hat{s}_z^{i_A} \hat{s}_z^{j_B} \right\rangle - \left\langle \hat{s}_z^{i_A} \right\rangle \left\langle \hat{s}_z^{j_B} \right\rangle}_{2C_z^{AB}}
\end{aligned}
\tag{4.1}
$$

The first two terms relate to the growth of correlations within a single spin family, while the second term relates to interfamilly spin correlations. For the $|\Psi\rangle$ state we are considering (assuming $N_A = N_B$)

$$
\begin{aligned}
C_z^A &= \frac{1}{2} \sum_{i_A\neq j_A} (3 \times (3) + (-3) \times (-3)) - 0 \times 0 = 9N_A(N_A - 1) \\
C_z^B &= \frac{1}{2} \sum_{i_B\neq j_B} (-3 \times (-3) + (3) \times (3)) - 0 \times 0 = 9N_B(N_B - 1) \\
C_z^{AB} &= \frac{1}{2} \sum_{i_A, j_B} (3 \times (-3) + (-3) \times 3) - 0 \times 0 = -9N_A N_B \\
C_z &= 9(N_A^2 + N_B^2 - 2N_A N_B) - 9(N_A + N_B) = 9((N_A - N_B)^2 - (N_A + N_B)) \simeq -9N
\end{aligned}
\tag{4.2}
$$

Total measurements such as those performed in Chap. 3 **can not resolve the particular nature** of this state's spin spin correlations which is **better deciphered by the partial measurements made possible by the bipartition process**. Notice in particular that intra and inter family correlations are of opposite signs, and that $\left|C_z^{AB}\right|, \left|C_z^{A/B}\right| \gg |C_z|$

As it turns out, our **system is also susceptible of developing such short scale textured spin spin correlations** see Fig. 4.2.

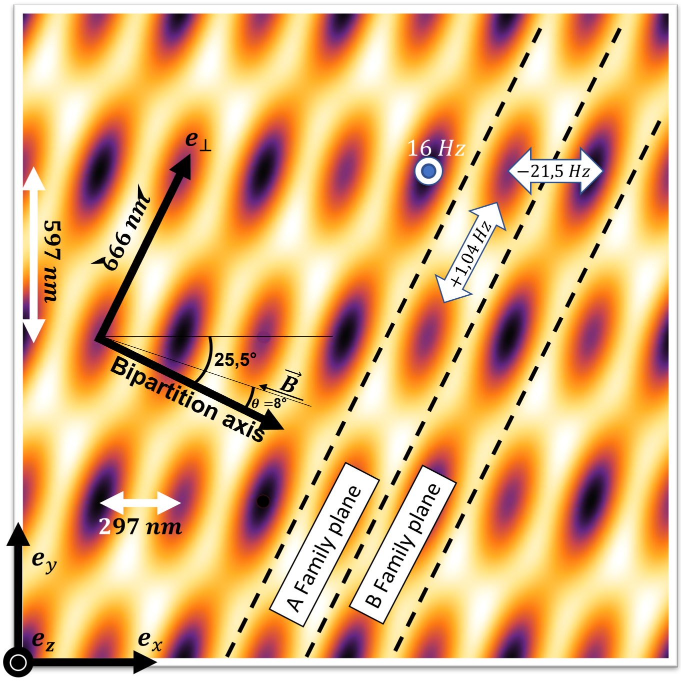

FIGURE 4.2: The bipartition technique we used fits the sign of the **DDI next neighbor couplings** of our system. As can be seen from the horizontal potential which is reproduced here when the 1064 nm laser is switched on, the A and B families' intra and extra next neighbors couplings which are proportional to $\frac{d^2}{r_{ij}^3}\left(1-3\cos(\theta_{ij})^2\right)$ are of opposite signs : the next neighbors couplings internal to each family are +16 Hz (along e_z) and 1.04 Hz (along $e_\perp$), while the external ones are −21.5 Hz. In a system where Ising type interactions prevail, such couplings would probably result in some kind of alternate spin ordering as far as thermodynamics are concerned. More generally, the anisotropy of the dipole dipole interactions and the anisotropy of the lattice also suggest that intra-family and inter-family correlations of different nature should emerge.

To better track these bipartite correlations i.e. the correlations between the A and B family, we focus on the C_z^{AB} correlator:

$$2C_z^{AB} = C_z - C_z^A - C_z^B \tag{4.3}$$

Where

- $C_z = \mathrm{Var}\left(\hat{S}_z\right) - \Sigma_Z$ (see Chap. 3)
- $C_z^A = \mathrm{Var}\left(\hat{S}_z^A\right) - \Sigma_z^A$
- $C_z^B = \mathrm{Var}\left(\hat{S}_z^B\right) - \Sigma_z^B$

We also have

$$\begin{aligned} C_z^{AB} &= \sum_{i_A, j_B} \left\langle \hat{s}_z^{i_A} \hat{s}_z^{j_B} \right\rangle - \left\langle \hat{s}_z^{i_A} \right\rangle \left\langle \hat{s}_z^{j_B} \right\rangle \\ &= \left\langle \sum_{i_A} \hat{s}_z^{i_A} \sum_{j_B} \hat{s}_z^{j_B} \right\rangle - \left\langle \sum_{i_A} \hat{s}_z^{i_A} \right\rangle \left\langle \sum_{j_B} \hat{s}_z^{j_B} \right\rangle \\ &= \langle \hat{S}_z^A \hat{S}_z^B \rangle - \langle \hat{S}_z^A \rangle \langle \hat{S}_z^B \rangle \\ &= \mathrm{cov}\left(\hat{S}_z^A, \hat{S}_z^B\right) \end{aligned} \tag{4.4}$$

The same kind of decomposition is available for the elementary correlators $C_{t>10ms}^{m,m'}$.

4.2 The bipartition process

4.2.1 Physical principles of bipartition

The bipartition technique that has been implemented draws on known position to momenta mapping methods which we have adapted to our system. These techniques build on the equivalence between the momentum and the position of a particle trapped in a harmonic potential.

In the following we take a brief look at the mathematical fundaments of these techniques. For a more detailed derivation see [73], [74], for an alternative one see [75].

A single particle in a 1D harmonic trap can be described by its quasi probability distribution as given by the **Wigner function** , which is defined as

$$W(x,p,t) = \int_{-\infty}^{\infty} d\epsilon \frac{e^{i\epsilon p/\hbar}}{2\pi\hbar} \Psi^* \left(x+\epsilon/2, t\right) \Psi(x-\epsilon/2, t) \tag{4.5}$$

Where

- Ψ is the corresponding single body wavefunction

The momentum distribution W_p of the particle can be found integrating its Wigner function over x. The evolution equation for the Wigner function derives from the time dependent equation[1]

$$i\hbar \frac{\partial \Psi}{\partial t} = -\frac{\hbar^2}{2m} \frac{\partial^2 \Psi}{\partial x^2} + V(x)\Psi \tag{4.6}$$

---

[1] Barring any kind of particle interaction, which justifies the single body aspect of this derivation.

In the case of a harmonic potential $V(x) = \frac{1}{2}m\omega^2 x^2$, assuming $W(x,p,t) = W(f(x,p,t), g(x,p,t))$ we find

$$\begin{aligned} \frac{\partial W}{\partial f}\left[\frac{\partial f}{\partial t} + \frac{p}{m}\frac{\partial f}{\partial x} - m\omega^2 x \frac{\partial f}{\partial p}\right] = 0 \\ \frac{\partial W}{\partial g}\left[\frac{\partial g}{\partial t} + \frac{p}{m}\frac{\partial g}{\partial x} - m\omega^2 x \frac{\partial g}{\partial p}\right] = 0 \end{aligned} \tag{4.7}$$

Which leads to

$$\begin{aligned} f(x,p,t) &= x\cos(\omega t) - \frac{p}{m\omega}\sin(\omega t) \\ g(x,p,t) &= m\omega x \sin(\omega t) + p\cos(\omega t) \end{aligned} \tag{4.8}$$

Denoting T is the oscillation period of the harmonic trap, we obtain

$$W\left(x, p, \frac{T}{4}\right) = W\left(-\frac{p}{m\omega}, m\omega x, t = 0\right) \tag{4.9}$$

As mentioned before, the momentum distribution W_p is found integrating over x

$$W_p\left(p, \frac{T}{4}\right) = \frac{1}{m\omega} W_x\left(x = -\frac{p}{m\omega}, t = 0\right) \tag{4.10}$$

We see that **the normalized momentum distribution at time $\frac{T}{4}$ is equal to the normalized position distribution at time $t = 0$ with a scaling factor $-\frac{1}{m\omega}$** (see Fig.4.3).

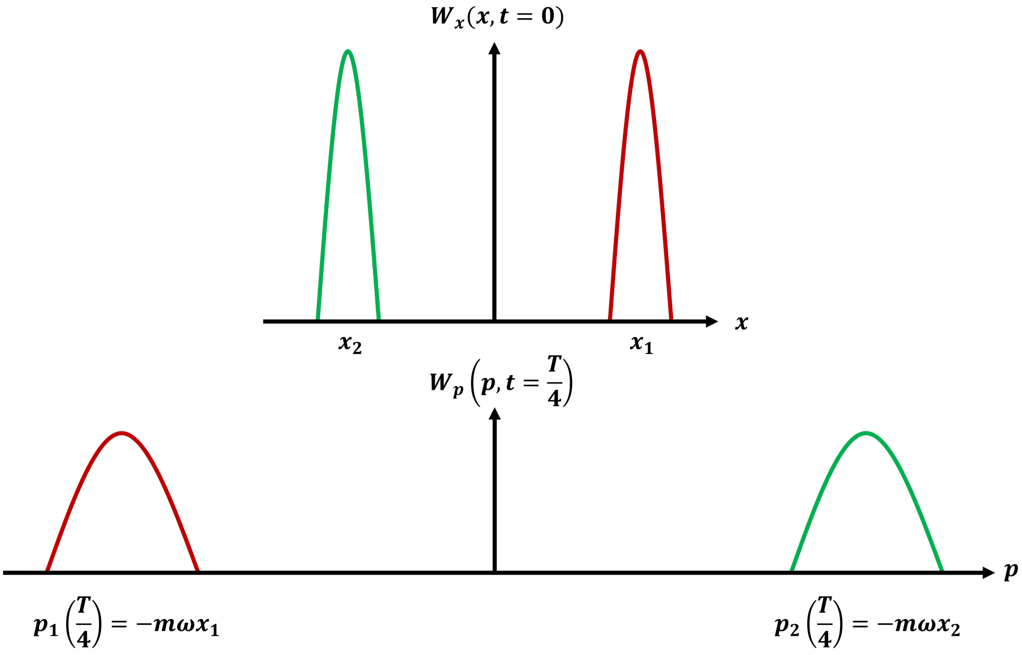

FIGURE 4.3: Comparison of the momentum and position distributions of two **non interacting** particles in a harmonic trap. After a quarter period, the momentum and position distributions of particles in a harmonic trap are exchanged, the magnification factor depends on the frequency of the trap.

This process can be understood looking at the equation of motion of **classical particle in a harmonic trap**.

$$x(t) = x_0 \cos(\omega t + \phi) \tag{4.11}$$

from which we see, by differentiation, that **the momentum and position of the particle evolve in quadrature**.

4.2.2 The bipartition in practice : Laser sequence

The experimental protocol for bipartite experiments is similar to the one described in the previous chapter, the only difference resides in the release step.

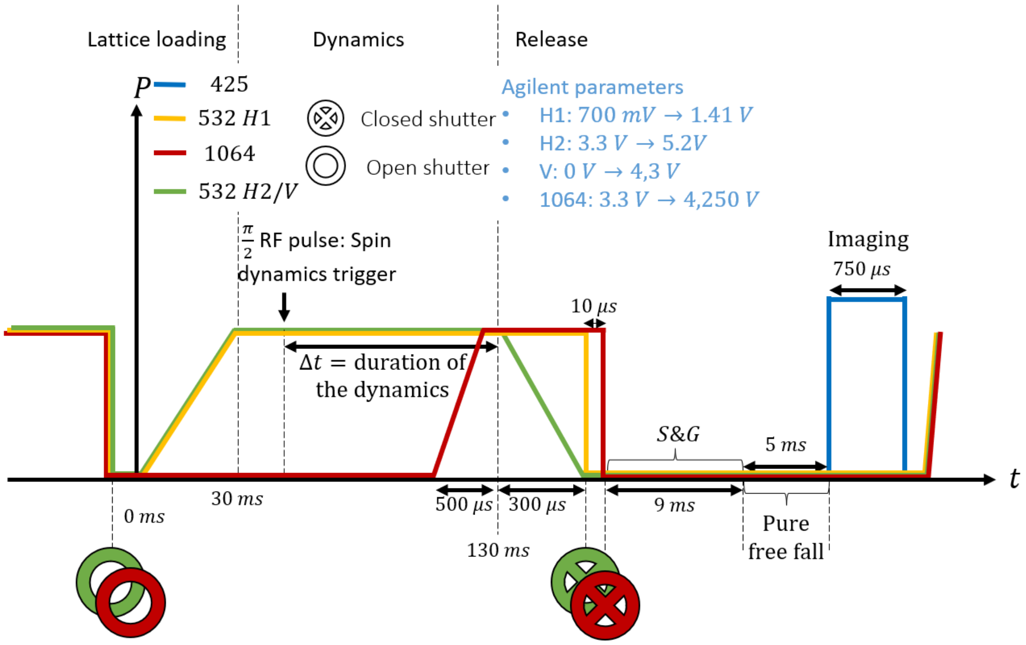

FIGURE 4.4: Compared to the experiments described in Chap.3, the 1064 nm is ramped up in 0.5 ms at the end of the dynamics. H_2 and V are then switched off in 300 μs at which point the bipartition is performed: H_1 is switched off abruptly using the RF switch of the AOM which controls the injection of the laser into its dedicated fiber. $\frac{T_{1064}}{4} = 10\ \mu s$ later approximately, depending on its power, the 1064 nm laser is also switched off. Atoms are then observed using fluorescence imaging as described in Chap. 1. The δ-kick step, which is not represented here, is much less efficient than it is for other experiments and is usually performed using the horizontal dipolar trap only, as the vertical one prevents the atoms from expanding and separating along the bipartition axis.

Below a pictorial perspective of the laser sequence

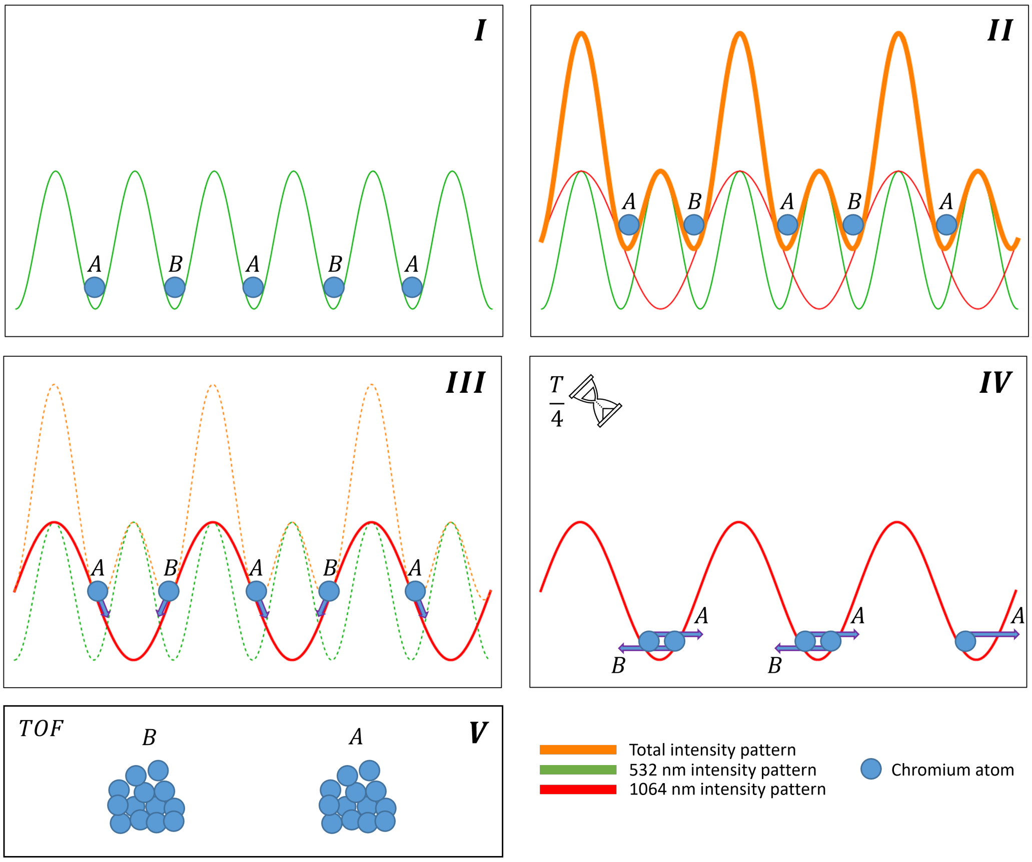

Figure 4.5: The total dipole potential (Orange) is the incoherent sum of the two potentials created by each of the two 1064 and 532 nm lasers. In the first step of the bipartition, the atoms sit in the potential wells created by the 532 nm laser. In the second step, the infrared potential enters the fray, the atoms are then transferred to a series of double wells. In the third step the 532 nm laser is abruptly switched off, the A and B labeled atoms are then driven by the harmonic-like potential of the 1064 nm laser. After a quarter period (10 μs) of this harmonic-like potential has elapsed the infrared laser is also switched off abruptly, this timing is such that the initial positions of the atoms are mapped into their respective momenta. All in all, after time of flight we end up with two distinct ensembles of atoms corresponding to each of the two families.

When coupled to the Stern & Gerlach technique, we can decouple the seven Zeeman states of chromium and access the full bipartite statistics of our system

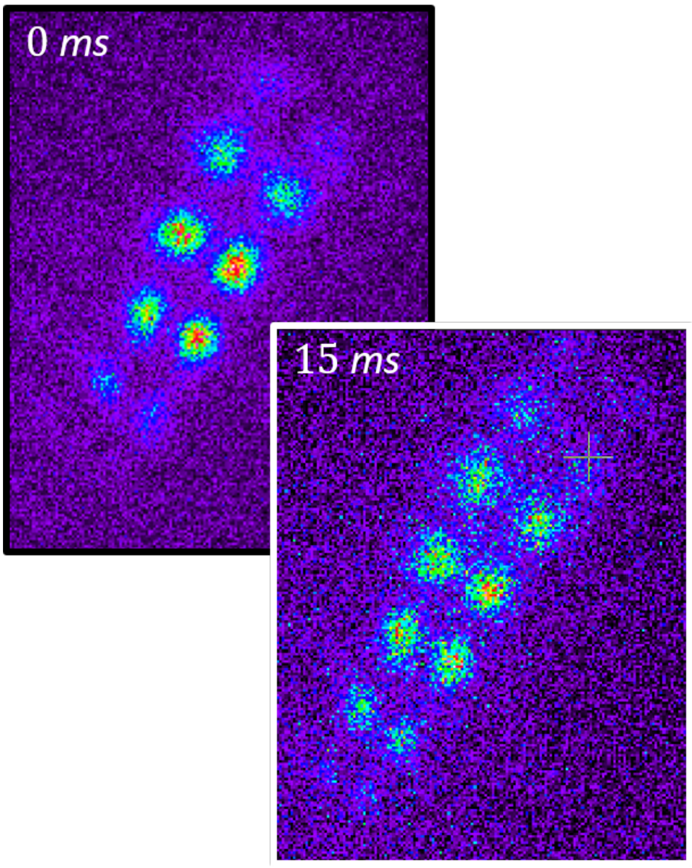

Figure 4.6: Above two photos taken after an interaction time of 0 and 15 ms respectively following a $\frac{\pi}{2}$ pulse. The Stern Gerlach technique is compatible with the bipartition technique we employ.

4.2.3 Bipartition pitfalls

The bipartition noise

The intensity patterns created by the 532 nm laser and the 1064 nm laser can drift relative to each other, this is, among other reasons[2], because these lasers are not ***frequency*** **locked**, as such, at the position of the BEC, the bichromatic intensity landscape (in orange below) varies with each experimental realization. This **shot-to-shot variability of the bichromatic dipole potential** is what we call the **bipartition noise**.

---

[2] Differential mechanical vibrations, temperature, pressure conditions... on the path of the 1064 nm and 532 nm beam can all contribute to this drift

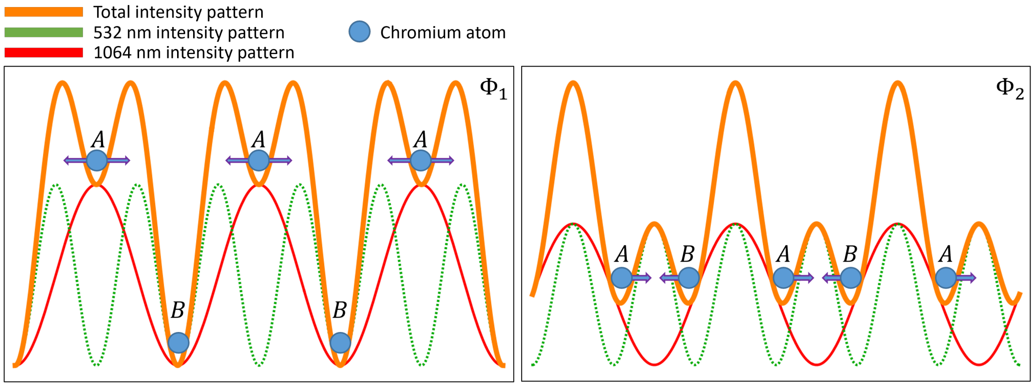

FIGURE 4.7: The 532 nm laser and the 1064 nm laser are not frequency locked, therefore the intensity pattern they create varies from shot to shot. The panel on the right (Φ_2) shows an intensity pattern for which the two atomic families are well separated. The configuration on the left leads to **three atomic clouds**: the atoms in the A family can either travel to the left or the right direction, whereas the B family atoms stay put.

The control and the stability of this pattern are paramount to the success of the bipartite measurement, fortunately this pattern proved to be quite *stable* through time, more so than erratic fluctuations, it was shown to slowly evolve in a pseudo-periodic fashion ($T \simeq 330s$) despite both reflected beams being decoupled.

The evolution of this intensity pattern was such that it became possible to *stabilize it by hand* using a 200 MHz double pass acousto-optic modulator: by fine tuning the 1064 nm beam's frequency (or equivalently its wavelength), and given the 50 cm distance that separates the retroreflection mirror (see Chap. 1) from the BEC, one can effectively shift the nodes and antinodes of the 1064 nm lattice and in final analysis control the intensity pattern under consideration. From the statistical analysis point of view, the bipartition noise can be dealt with using **normalization** (i.e. the Delta method) or **partial covariances**.

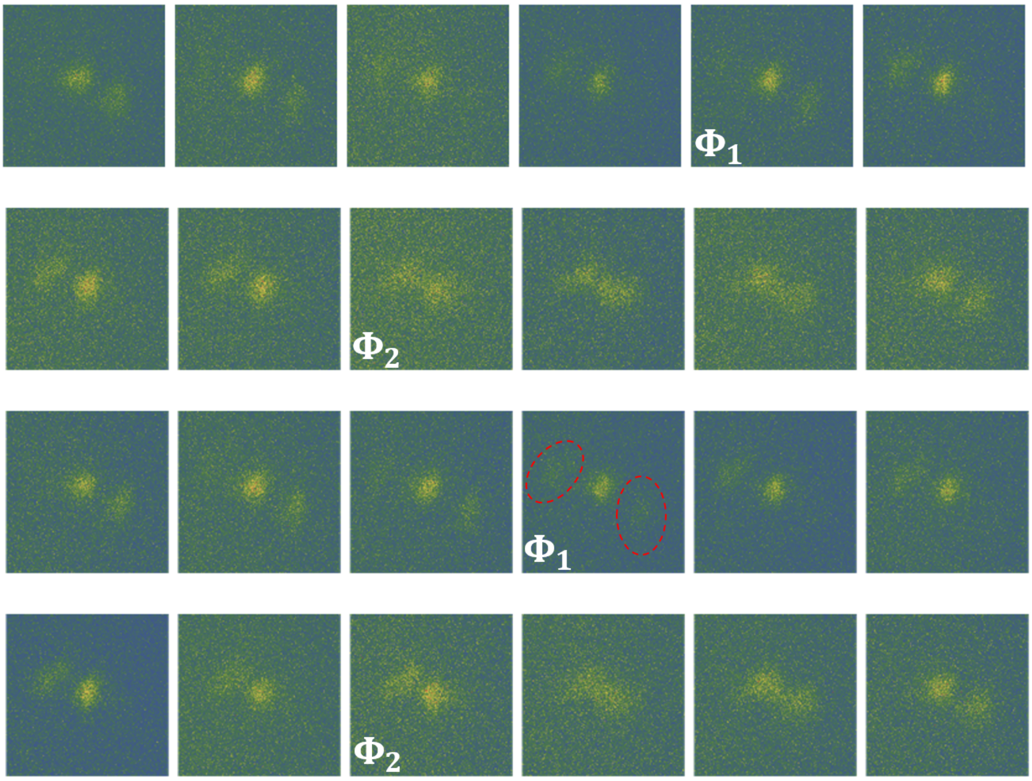

FIGURE 4.8: Early days bipartition photo gallery for a freely evolving phase or more precisely a freely evolving intensity landscape at the level of the atoms. These pictures were taken in less than ten minutes. We see that the 1064/532 intensity pattern evolves in an almost periodic fashion. At phase Φ_1 (see Fig.4.7), three clouds are apparent. At phase Φ_2, the bipartition produces two connected clouds.

The photo gallery above tells of an omnipresent *subsidiary family* A_{Bis}, wherein atoms can end up being projected. This particular defect is highlighted when considering average images of the bipartition, see the Fig.4.9 below. **This defect must be taken into account when treating the data**, as it may lead to an overestimation of the number of atoms contributing to the fluorescence signal.

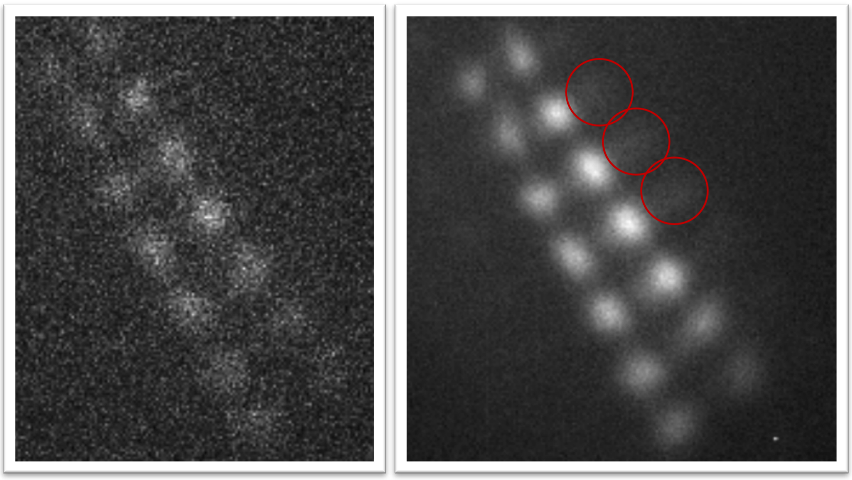

FIGURE 4.9: Right: average over 40 pictures at time $t_{\text{dyn}} = 30$ ms. Left: single shot at time $t_{\text{dyn}} = 30$ ms. The imperfections of the bipartition are highlighted by the averaging. A substantial part of the atoms (evaluated to 14%) is not taken into account when fitting the data. The number of atoms measured using absorption imaging is corrected by this factor of 14% when analyzing the data.

Effects of anharmonicity

The premise according to which momentum and position distributions are switched at $\frac{T}{4}$ is only valid for a harmonic oscillator. For a sinusoidal potential, the equation of motion of a classical particle read

$$\ddot{X} = -A' \sin(kX) \text{ for } -\frac{\pi}{2k} < X < \frac{\pi}{2k} \tag{4.12}$$

This can be rewritten as

$$\ddot{x} = -A \sin(x) \text{ for } -\frac{\pi}{2} < x < \frac{\pi}{2} \tag{4.13}$$

Where $A = A'k$. Multiplying this equation by the particle's velocity $\dot{x}$, we find that

$$\begin{aligned} \frac{1}{2}\dot{x}^2 &= A\cos(x) + B \\ \dot{x}(0) = 0 \longrightarrow &= A\left(\cos(x) - \cos(x_0)\right) \end{aligned} \tag{4.14}$$

In particular, we have

$$\begin{aligned} dt &= \frac{dx}{\sqrt{2A\left(\cos x - \cos x_0\right)}} \\ \Longrightarrow T &= \frac{4}{\sqrt{2A}} \int_0^{x_0} \frac{dx}{\sqrt{\cos x - \cos x_0}} \\ &= \frac{4}{\sqrt{2A}} \mathscr{F}\left(\frac{\pi}{2}, \sin\left(\frac{x_0}{2}\right)\right) \end{aligned} \tag{4.15}$$

Where $\mathscr{F}$ is the *incomplete elliptic integral of first kind*

$$\mathscr{F}(\rho, k) = \int_0^{\rho} \frac{du}{\sqrt{1 - k^2 \sin^2 u}}$$

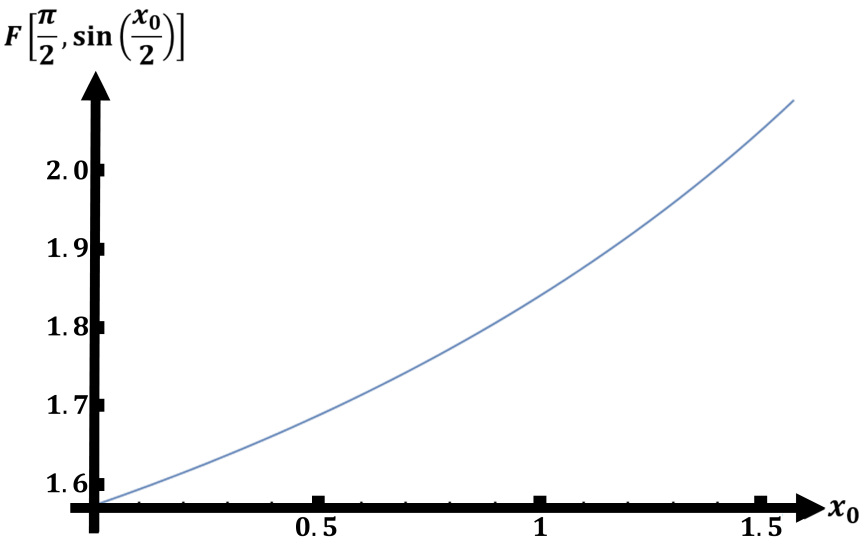

FIGURE 4.10: Plot of the incomplete elliptic integral of first kind for an initial position $x \in [|0, \frac{\pi}{2}|]$. **The period of the particles' oscillation within a sinusoidal trap depend on their initial position**. The period differences induced by this function are small, as the particles are initially extremely well localized within the 1064 well: if we neglect the non zero extension of the particles Wannier function all particles in the A (resp. B) wells share the same initial position x_0 modulo the lattice step.

This is to say that there is no global $\frac{T}{4}$ time per-se for all particles in the lattice, and the final position to momentum mapping is more complicated, in particular there are now two scaling factors instead of one, which induces additional asymmetries between the A and B families' clouds. These two scaling factors collapse back into a single one in the favorable symmetric intensity pattern case Φ_2 shown in Fig. 4.7: two initially symmetrically positioned particles will still end up acquiring perfectly antisymmetric momenta, despite the anharmonicity of the well.

Effect of exchange contact interaction during the release step

The timescales of inelastic interactions were computed in Chap. 2. It takes a few hundred microseconds for two particles trapped in a 532 nm well to undergo a spin changing collision. The release step only lasts 10 μs. It is therefore unlikely that contact interactions occur during the bipartition process (i.e. during the release step where particles share the same lattice site and are traveling towards each other) and end up affecting its outcome.

Tunneling effects during the ramp up of the 1064 nm laser

During the ramp up of the 1064 nm laser, restricting this theoretical venture to the symmetric intensity

pattern which corresponds to the data that was taken and neglecting interactions, tunneling processes can be modeled - crudely - by the following tight binding Hamiltonian

$$\hat{H} = \sum_{n,j=0}^{N-1} E_n \hat{a}^\dagger_{j,n} \hat{a}_{j,n} - \left[\sum_{j=0}^{N-1} J^+ \hat{a}^\dagger_{j,B} \hat{a}_{j,A} + J^- \hat{a}^\dagger_{j-1,B} \hat{a}_{j,A} + h.c \right] \tag{4.16}$$

Where

- $n \in \{A, B\}$
- N is the number of lattice cells (each cell contain two sites)

- J^+ and J^- are effective tunneling parameters (see Fig.4.11)
- $\hat{a}^\dagger_{n,j}$ ($\hat{a}_{n,j}$) are the creation (annihilation) operator of a particle in site n of lattice cell j

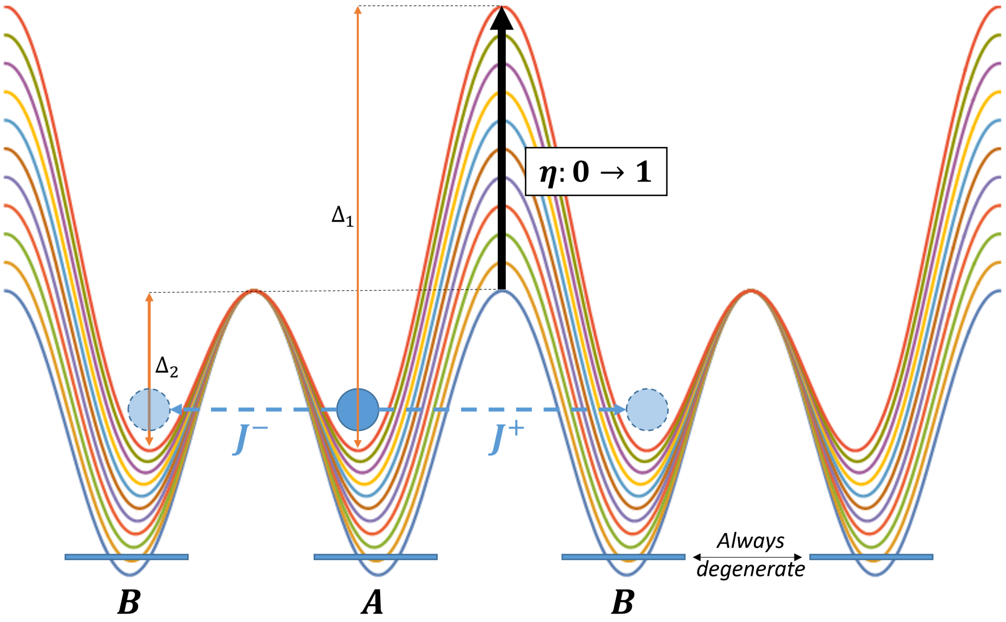

FIGURE 4.11: Intensity pattern's evolution when the 1064 nm laser is ramped up, η is the depth ratio of the 532 nm and 1064 nm lattices. The blue horizontal bars represent the energy levels of the wells in the harmonic approximation. The pattern - as far as the *phase* is concerned - corresponds to the one used for the experimental data that was taken. When ramping up the 1064 nm laser ($\eta\ _0\nearrow^1$) the Δ_1 potential barrier increases, whereas the Δ_2 potential barrier decreases. Tunneling process depend not only on the height of these barriers but also - within the isolated well approximation - on the energy discrepancy between the harmonic levels of each site. In the process described above all these harmonic levels are and remain degenerate. The evolution of the tunneling parameters J^+ and J^- will therefore only depend on the evolution of the barriers' heights. In the process described by the image above, we expect J^+ to decrease, and J^- to increase.

To **estimate the typical number of atom tunneling out of the initially populated site** A **during the ramp up phase**, let us introduce the Fourier transform of the $\hat{a}$ operators:

$$\hat{b}_n(q) = \frac{1}{\sqrt{N}} \sum_j e^{iqjd} \hat{a}_{n,j} \leftrightarrow \hat{a}_{n,j} = \frac{1}{\sqrt{N}} \sum_{q \in BZ} e^{-iqjd} \hat{b}_n(q) \tag{4.17}$$

Where

- d is the lattice step

In particular, by symmetry of the Brillouin zone, we have the following relations

$$\begin{aligned}
\sum_{j=0}^{N-1} \hat{a}^\dagger_{j,n} \hat{a}_{j,n} &= \frac{1}{N} \sum_{q,q' \in BZ} \sum_{j=0}^{N-1} e^{i(q-q')jd} \hat{b}^\dagger_n(q) \hat{b}_n(q') = \sum_{q \in BZ} \hat{b}^\dagger_n(q) \hat{b}_n(q) \\
\sum_{j=0}^{N-1} \hat{a}^\dagger_{j,B} \hat{a}_{j,A} &= \frac{1}{N} \sum_{q,q' \in BZ} \sum_{j=0}^{N-1} e^{i(q-q')jd} \hat{b}^\dagger_B(q) \hat{b}_A(q') = \sum_{q \in BZ} \hat{b}^\dagger_B(q) \hat{b}_A(q) \\
\sum_{j=0}^{N-1} \hat{a}^\dagger_{j-1,B} \hat{a}_{j,A} &= \frac{e^{-iqd}}{N} \sum_{q,q' \in BZ} \sum_{j=0}^{N-1} e^{i(q-q')jd} \hat{b}^\dagger_B(q) \hat{b}_A(q') = \sum_{q \in BZ} e^{-iqd} \hat{b}^\dagger_B(q) \hat{b}_A(q)
\end{aligned} \tag{4.18}$$

Using equation 4.17, $\hat{H}$ can be rewritten :

$$\begin{aligned}
\hat{H} &= \sum_{n,j=0}^{N-1} E_n \hat{a}^{\dagger}_{j,n}\hat{a}_{j,n} - \sum_{j=0}^{N-1}\left(J^{+}\hat{a}^{\dagger}_{j,B}\hat{a}_{j,A} + J^{-}\hat{a}^{\dagger}_{j-1,B}\hat{a}_{j,A} + h.c\right) \\
&= \sum_{q\in BZ} E_n \hat{b}^{\dagger}_{n,q}\hat{b}_n(q) - \left(J^{+}\sum_{q\in BZ}\hat{b}^{\dagger}_B(q)\hat{b}_A(q) + J^{-}\sum_{q\in BZ} e^{-iqd}\hat{b}^{\dagger}_B(q)\hat{b}_A(q) + h.c\right) \\
&= \sum_{q\in BZ}\left[E_n\hat{b}^{\dagger}_n(q)\hat{b}_n(q) - J^{+}\hat{b}^{\dagger}_B(q)\hat{b}_A(q) + J^{-}e^{-iqd}\hat{b}^{\dagger}_B(q)\hat{b}_A(q) + h.c\right] \\
&= \sum_{q\in BZ}\left(\hat{b}^{\dagger}_A(q)\hat{b}^{\dagger}_B(q)\right) h(q)\begin{pmatrix}\hat{b}_A(q)\\ \hat{b}_B(q)\end{pmatrix}
\end{aligned} \tag{4.19}$$

Where

$$h(q) = \begin{pmatrix} E_A & T(q) \\ T(q)^* & E_B \end{pmatrix}$$

with

$$T(q) = -(J^{+} + J^{-}e^{+iqd}) \tag{4.20}$$

and $E_{A/B}$ the energies defined by the tight binding Hamiltonian 4.16. Diagonalizing this Hamiltonian we end up with the following band structure:

$$\epsilon_{\pm}(q) = \overline{E} \pm \sqrt{E_{\Delta}^2 + \left|T(q)\right|^2} \tag{4.21}$$

Where :

$$\overline{E} = \frac{E_A + E_B}{2} \quad \text{and} \quad E_{\Delta} = \frac{E_A - E_B}{2} \tag{4.22}$$

The band gap is given by $\Delta(q) = \epsilon_{+}(q) - \epsilon_{-}(q) = 2\sqrt{E_{\Delta}^2 + \left|T(q)\right|^2}$, so that:

$$\left|T(q)\right|^2 = (J^{+})^2 + (J^{-})^2 + 2J^{+}J^{-}\cos(qd) = \frac{\Delta(q)^2 - 4E_{\Delta}^2}{4} \tag{4.23}$$

Assimilating this band gap to the one between the two lowest bands of the lattice Hamiltonian
structure and fitting the $\frac{\Delta(q)^2-4E_{\Delta}^2}{4}$ function to the band gap thus found, we can derive both tunneling parameters J^{+} and J^{-}. Put otherwise, we choose J^{+} and J^{-} such that the 4.16 model reproduces the lattice's band structure.

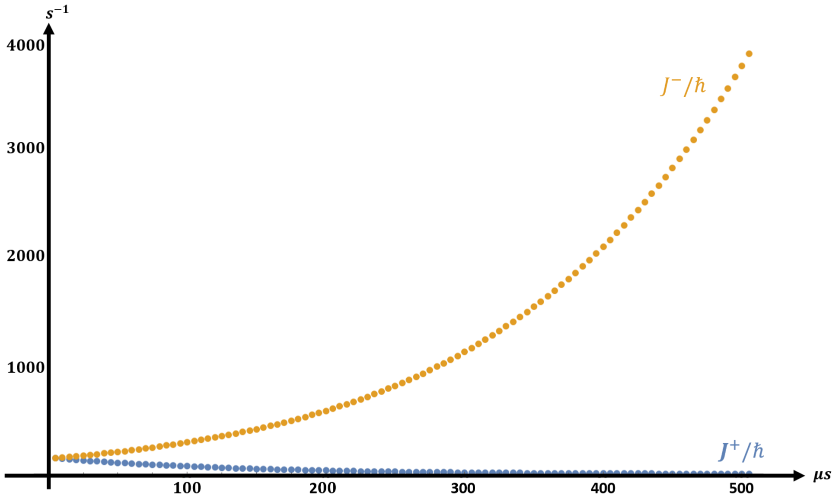

FIGURE 4.12: Evolution of the $\left(J^+, J^-\right)$ parameters as a function of time when the 1064 nm laser is ramped up $(\eta = 0 \rightarrow \eta = 1)$ in 500 μs.

Assuming the number of atoms tunneling from site A to the B sites is:

$$N_A = \int_0^{T_{ramp}} \frac{J^+(t)}{\hbar} dt + \int_0^{T_{ramp}} \frac{J^-(t)}{\hbar} dt \tag{4.24}$$

We find that the total number of atoms tunneling out of the A lattice site in 500 μs is **0.64**. This number is quite big, we have moreover not taken into account the 300 μs phase during which $H2$ and V are ramped down.

This derivation shows that the 1064 nm laser should be ramped up **as fast as possible**, to power values as low as possible [3]. Let us temper this result by noting that all sorts of gradients, interactions and asymmetries (notably in terms of well depths asymmetry (see Fig. 4.13) which can easily reach a few kHz) can in fact suppress the number of atom tunneling out of site A by making tunneling non resonant even when the power of the lasers is being ramped down. Experiments supporting this claim, not reported in this manuscript, wherein atoms are loaded in every other lattice site along the bipartition axis have shown that tunneling remains negligible during the bipartition step.

---

[3] i.e. these power values, although low, should still correspond to high enough scaling factors (see sec. 4.2.1) and oscillation periods small in comparison to on-site interaction time scales

Experimental snapshot: an alternative bipartition route

The initially envisioned bipartition protocol did not build on position to momentum mapping techniques. It was in fact based on well known **band mapping** methods. Band mapping is a technique which reveals the quasi momentum distribution of the atoms. It requires that the atoms be freed from the lattice fast enough that they don't have time to move from their initial positions, and slow enough so that band structure is mapped onto the free particles parabola (dispersion relation). This is different from time of flight techniques which reveal the momentum distribution of the particles [47].

The **band mapping bipartition technique** uses the correspondence, in the deep lattice limit, between the wells' energy levels (as given by the harmonic approximation) and the various bands of the band structure.

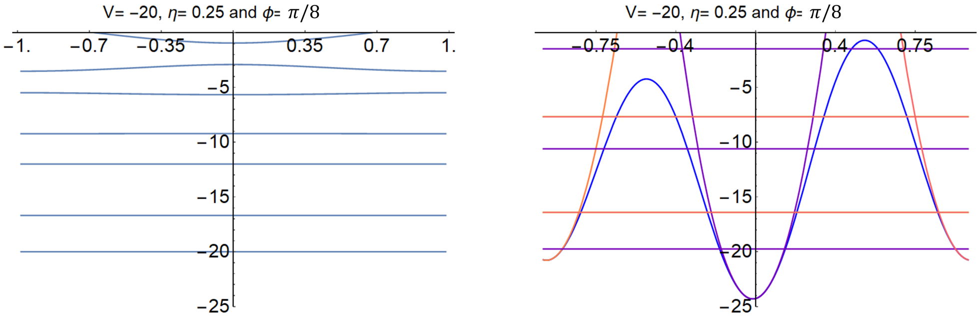

FIGURE 4.13: V,η and ϕ represent respectively the depth of the 532 nm lattice in units of recoil energy at 532 nm, the depth ratio between the 1064 nm and 532 nm lattices and the *phase* between both which sets the general shape and symmetry of the lattice. Left: The lattice band structure for the parameters shown above. Right: In blue the total dipolar potential for the parameters shown above: only one lattice site (two wells) is shown, the purple horizontal lines correspond to energy levels of the center well as given by the harmonic approximation, the orange horizontal lines correspond to energy levels of the well on the edge as given by the harmonic approximation, purple and orange parabolas are the osculating parabolas of the right and left wells as given by the harmonic approximation. The oscillation frequency ω of the trap is related to the second derivative of the potential energy at the bottom of the trap $\omega = \sqrt{\frac{1}{m}\frac{d^2E}{dx^2}}$. For the deep 1D bichromatic lattice shown above there is a rather clear correspondence between harmonic energy levels and the lattice band structure.

This correspondence meant that unraveling the quasi-momentum distribution was akin to unraveling the bipartite nature of the system, since, in some configurations like the one shown above, every other atom populates a different band. Contrary to the symmetric configurations for which the T/4 bipartition works, the bandmapping bipartition favors asymmetric potentials.

Unfortunately, while this may be true for a 1D lattice, this feature is hard to generalize, let alone to observe for a 3D anisotropic bichromatic lattice. This is due to the rather complicated shapes of the such lattices' Brillouin zones, the various and sometimes incompatible (a)diabaticity conditions that must be fulfilled, and the inadequacy of our imaging set-up. Moreover, because of the symmetry of the quasi momentum distribution (with respect to $q = 0$), the band mapping bipartition always generates (at least) three clouds, which is detrimental to signal to noise ratio.

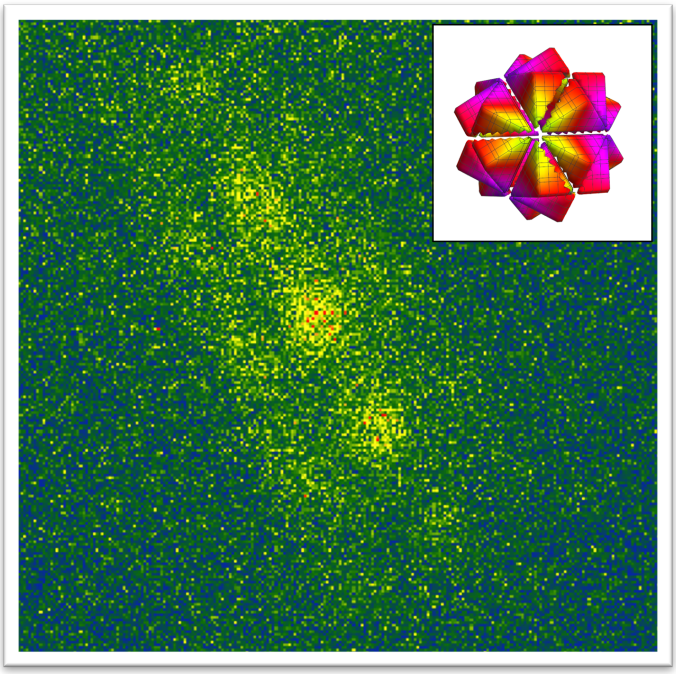

Figure 4.14: Inset: The third Brillouin zone of the lattice, the precise visualization of such 3D regions is beyond current imaging capabilities. Right: band mapping bipartition coupled to the Stern & Gerlach technique. This alternative route was abandoned because of the poor imaging quality

4.3 Results

4.3.1 Experimental protocol

In order to estimate the various quantities discussed in the beginning of this chapter C_z, $C_z^{A/B}$ and C_z^{AB} as a function of time, the dipolar dynamics must be observed a great many number of times. For the experiments discussed in this chapter, we've decided to focus on three interaction times $t_{\text{dyn}} = 0, 15$ and 30 ms. For each of these interactions times a total of 463, 502 and 457 photos were taken respectively while only 200 were taken for every interaction time studied in Chap. 3. This decision was motivated by the slow convergence of the variance and covariances estimators: by accumulating more photos for fewer interaction times we are able to construct more reliable estimators of the three chosen variance covariance matrices. These photos are the compilation of subpackets of 35 pictures each taken over 4 days. The limited size of the subpackets speaks of the necessity to regularly check and compensate for any experimental drift.

Typical experiments start out with a condensate ($N \sim 10^4$). The experimental precautions taken for the 532 nm lattices (see sec 3.3.1) extend to the 1064 nm lattice whose average depth is $\approx 80 - 100\ E_{r,1064}$.

The experimental laser sequence is shown in sec. 4.2.2.

4.3.2 Data treatment protocol

The information enclosed in the data is retrieved by fitting the clouds' intensity profiles with 1D Gaussian functions. These fits provide us with the clouds' total signals and the related standard errors (see Fig. 4.15).

To analyze the data we use the scheme referenced at the end of Chap. 2. As such we first correct the number of atoms found using absorption imaging by a factor of 14% accounting for the atoms ending up in the subsidiary A_{Bis} family (see Fig. 4.9). Total signal drifts are then corrected for as they can fictitiously increase the variances of the various quantities that are measured (the A_{m_s}). Drifts are corrected for each family independently. Next, we compute the detectivity factors (the so called αs of Chap. 2) ($30 \leq \alpha \leq 60$) using the data points at time $t_{\text{dyn}} = 0$ ms so that the average fractional populations are symmetric at all times and equal to those theoretically predicted for a $\frac{\pi}{2}$ pulse. At this point the Eqs. 2.63 are applied to get rid of the noises linked to the detection chain. To get rid of the number and bipartition noises we then use the bipartite Delta scheme presented in Eqs. 2.77 on the non normalized variance covariance matrices obtained at the previous step.

At this point, we compute the variances of each family's magnetization -$\text{Var}\left(\hat{S}_z^{A/B}\right)$- and that of the total system -$\text{Var}\left(\hat{S}_z\right)$- as well as the corresponding onsite fluctuations $\Sigma_z^{A/B}$ and Σ_z. We then compute the contribution of the RF noise ($\Delta_{RF}^{t=0}$) for each data point at time $t_{\text{dyn}} = 0$ ms by forcing the normalized variance of the global system $\frac{\text{Var}(\hat{S}_z)}{A_T(0)}$ to $3/2$. In other words we have $\Delta_{RF}^{t=0} = \frac{\text{Var}(\hat{S}_z)}{A_T(0)} - 3/2$. This value is used to correct the variances at greater interaction times by an amount that is proportional to the remaining number of atoms $\Delta_{RF}^{t>0} = \Delta_{RF}^{t=0} \frac{A_T(t)}{A_T(0)}$. The same atom number proportionality rule is used to correct the magnetization variances for the subfamilies at all times $\Delta_{RF}^{t\geq 0} = \Delta_{RF}^{t=0} \frac{A_{A/B}(t)}{A_T(0)}$.

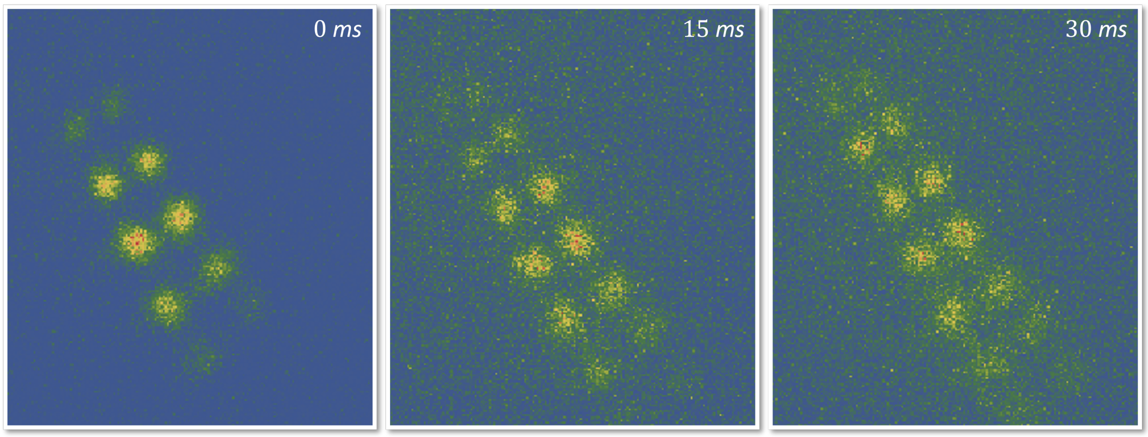

FIGURE 4.15: The clouds get larger and larger as their spin goes from +3 to -3, clouds on the bottom of typical pictures (±3, ±2) are quite big, this is detrimental to the reliable estimation of these clouds' signal, which in turn affect the whole properties of the variance covariance matrix via, notably, the detectivity factors. The reliability of these estimations is quantified by these clouds' fits' standard error to signal ratios ϵ, $\epsilon = \frac{\text{std. err of the fit}}{\text{fit signal}}$. For example we have at time $t_{\text{dyn}} = 0$ ms $\{\epsilon_{-3} = 14.3\%,\ \epsilon_{-2} = 3.1\%,\ \epsilon_{-1} = 1.7\%,\ \epsilon_0 = 1.7\%,\ \epsilon_1 = 1.8\%,\ \epsilon_2 = 3.1\%,\ \epsilon_3 = 19.9\%\}$ to be compared with the experiments of Chap.3 where at time $t_{\text{dyn}} = 0$ ms, we had $\{\epsilon_{-3} = 8.1\%,\ \epsilon_{-2} = 2.3\%,\ \epsilon_{-1} = 1.5\%,\ \epsilon_0 = 2\%,\ \epsilon_1 = 2\%,\ \epsilon_2 = 2.6\%,\ \epsilon_3 = 5.6\%\}$. The relative estimation of the number of atoms in each clouds at 30 ms is better and the fits' standard errors to signal ratios are $\{\epsilon_{-3} = 4\%, \epsilon_{-2} = 2.8\%,\ \epsilon_{-1} = 2.4\%,\ \epsilon_0 = 2.1\%,\ \epsilon_1 = 2.4\%,\ \epsilon_2 = 3.5\%,\ \epsilon_3 = 6\%\}$. The decrease of the fitting uncertainty shows that the reliability of the determination of each cloud's total signal is dictated not by the sole size of the clouds but rather by the *signal per pixel* quantity which is governed by both the cloud's size and the number of photons emitted.

4.3.3 Results

The average atom numbers at time $t_{\text{dyn}} = 0$, 15 and 30 ms are 10000, 6200, 4950[4] respectively. The average over all data points of the RF contribution at time $t_{\text{dyn}} = 0$ ms to the normalized variance $\text{Var}(\hat{S}_z)/A_T$ of the magnetization is 0.9×1.5 where 1.5 represents the expected normalized variance of the magnetization at time $t_{\text{dyn}} = 0$ ms. This value is comparable to the experiment presented in Chap. 3.

Results are summarized in the table and graphics below

Bipartite experiments results			
Interaction time (ms)	0	15	30
$\text{Var}(\hat{S}_z)/A_T$	1.5(± 0.7)	2.1(±1.2)	1.5(±0.8)
$\text{Var}(\hat{S}_z^A)/A_T^A$	1.7(±1.3)	7.8(±3.8)	4.8(±0.6)
$\text{Var}(\hat{S}_z^B)/A_T^B$	1.9 (±1.6)	4.3(±1.3)	5.2(±1.7)
C_z/A_T	0.1(±0.7)	-0.3(±1.1)	-1.4(±0.8)
C_z^A/A_T^A	0.2 (±1.2)	5.2(±3.7)	1.7(±0.7)
C_z^B/A_T^B	0.6(±1.6)	2.1(±1.2)	2.4(±1.7)
C_z^{AB}/A_T	-0.2(±0.3)	-2.1(±1.5)	-1.8(±0.7)
$a_{\pm 3}$	0.016	0.055	0.082
$a_{\pm 2}$	0.081	0.12	0.13
$a_{\pm 1}$	0.24	0.20	0.18
a_0	0.33	0.24	0.21

---

[4] These numbers should be multiplied by a factor 0.86 to account for the bipartition defects

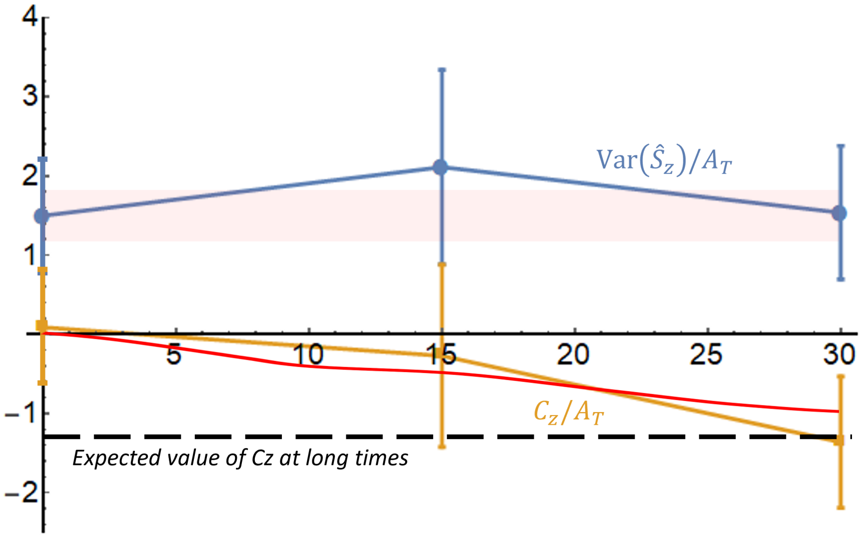

FIGURE 4.16: Blue: Time evolution of the whole system's magnetization variance. Yellow: Time evolution of the whole system's magnetization correlator C_z/A_T (see Eqs. 4.3). The variance is compatible with 1.5 at all times, while the evolution of C_z is compatible with the results of the previous chapter, and numerical predictions (red). The shaded area corresponds to the expected dispersion zone of the variance data points for the perfect experiment (i.e. with the sole quantum projection noise at time $t_{\text{dyn}} = 0$ ms). Error bars correspond to two standard deviations.

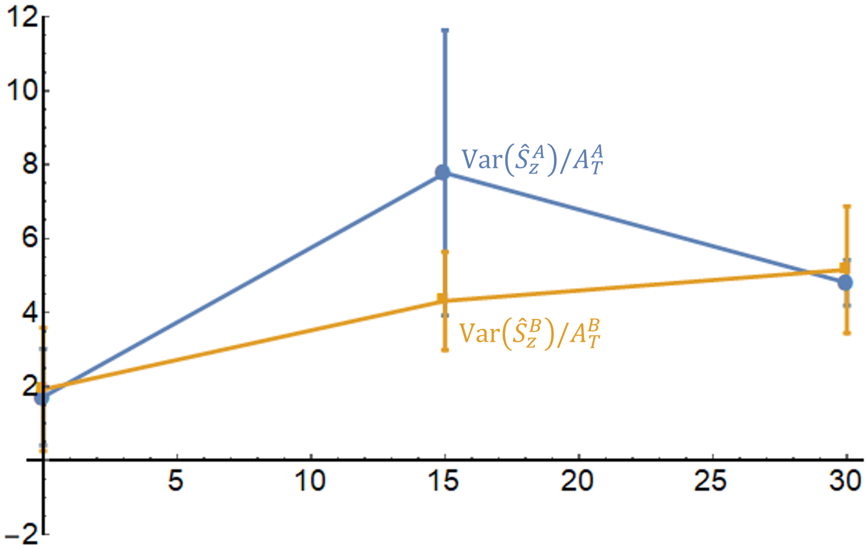

FIGURE 4.17: Time evolution of the variance of the magnetizations of both A and B families. The initial values of the variances are compatible with the theoretical value $\mathrm{Var}\left(\hat{S}_z^{A,B}\right)/N^{A/B} = 1.5$. Error bars correspond to two standard deviations.

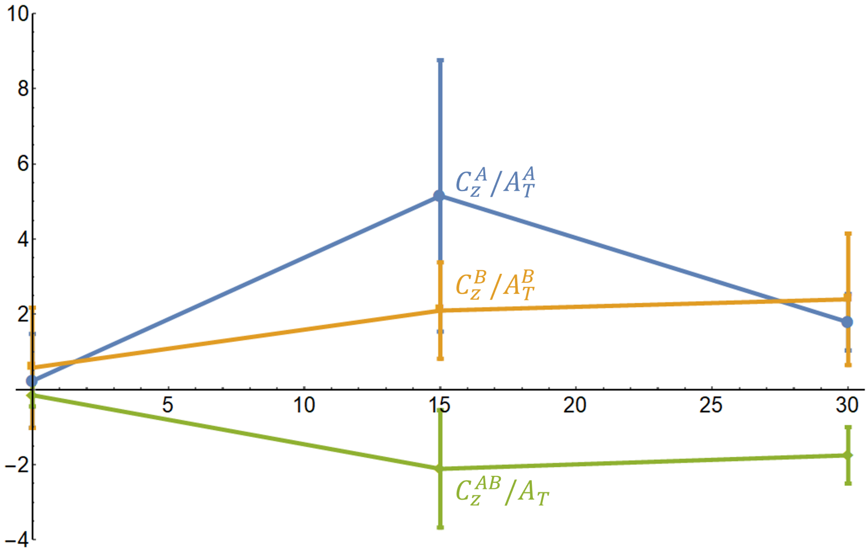

FIGURE 4.18: Time evolution of the bipartite correlators C_z^A, C_z^B, and C_z^{AB}. The intra and inter-familly correlations are of opposite signs. The A and B family correlators evolution is compatible at all times as can be expected from symmetry arguments.

The data which we present here has not yet been compared to theoretical predictions. We can however already conclude to the development of **bipartite spin correlations** of different natures within ($C_z^{A/B} > 0$) and between ($C_z^{AB} < 0$) the two atomic families that compose our system. This shows that correlations in our system are more intricately textured than can be presumed from the negativity of the global correlator $C_z < 0$.

Extending the spin correlation length analysis of the previous chapter to these data we find a mean intra-family spin correlation length

$$\frac{\xi_A + \xi_B}{2} = 0.56\frac{\lambda}{2}$$

and a inter-family spin correlation length

$$\xi_{AB} = 0.62\frac{\lambda}{2}$$

where we have assumed $c_z^{AB}(0) = \frac{\frac{\Sigma_z^A}{N_A} + \frac{\Sigma_z^B}{N_B}}{2}$ in Eqs. 3.26. The inter-family spin length designates the spatial scale over which the correlations between an atom belonging to the A family and an atom belonging to the B family extends.

Conclusion

> *T'imaginais-tu donc l'univers autrement ?*
> – Victor Hugo (Les contemplations - Ce que dit la bouche d'ombre)

In the course of my PhD, I have studied the development of spin correlations in an ensemble of lattice trapped dipolar atoms.

In this manuscript I have reported on two complementary experiments in which we tracked the growth of these correlations without relying on tomography like techniques. These experiments built on the repeated measurements of global Zeeman populations and the estimation of these observables' first and second statistical moments.

As it turns out, these statistical moments are affected by many phenomena, some of which are of physical significance (dipolar dynamics), and some of which are mostly irrelevant (e.g. preparation or fluorescence noise) to our experimental endeavor. In the second chapter of this manuscript, I have shown how to extract the sole contribution of the quantum projection noise from our data in a mathematically rigorous way.

In the third chapter of this manuscript, we prove -*experimentally*- that spin correlations do indeed develop in our system as it thermalizes through dipole dipole interactions. The quantum nature of these correlations is supported by the relatively good agreement of the experimental data with numerical simulations and theoretical predictions. The results of this chapter illustrate the correlation tracking possibilities offered by platforms involving higher spin particles. Indeed, for spin $\frac{1}{2}$ particles, C_z is zero as in this case the on site fluctuations accounted for by $\Sigma_z = \sum_i \left\langle \left(s_i^z\right)^2 \right\rangle - \left\langle s_i^z \right\rangle^2$ are constant[5].

In the fourth chapter we probe at these correlations using a novel bipartition method. We show that the correlations developing in our system are more finely structured than what might, a priori, be inferred from the results of the third chapter's experiment. This structure is in part related to the anisotropy of the dipole dipole interactions governing in our system. The results of this second experiment have not been confronted to theoretical predictions yet.

In conclusion still, we can positively say that thermalization of isolated quasi-pure dipole dipole coupled systems like ours goes with the growth of spin correlations and that this growth is negligibly modified by dissipative phenomena. This is reminiscent of quantum thermalization scenarios - previously demonstrated for smaller systems in [76] - wherein isolated pure systems evolve towards a steady state through the entanglement of their various components. Contrary to classical thermalization scenarios in which thermalization happens through interaction with another system, the thermalization that is discussed here only involves processes (spin exchanges) internal to the system.

Many questions remain to be answered in the short term: can there be, for systems with finite temperature, thermalization without entanglement? Are weaker kinds of quantum correlations sufficient? How *much* of these correlations should develop before the system

---

[5] $\left\langle \left(s_i^z\right)^2 \right\rangle = \frac{1}{4}$

reaches a steady state? On what spatial scale? Are there universal features to these phenomena?

These question are out of the reach of the current experimental set up. Answering them requires the ability to better track **quantum** correlations and or entanglement. The quantumness of correlations is in general estimated by the so called quantum discord quantity, this quantity however is ill-suited to experimental endeavors involving as many atoms as ours. The quantum covariance on the other hand only extends to systems having reached thermal equilibrium. Measuring entanglement is feasible, it would however require a greater stability of the magnetic field permeating the science chamber. This could be achieved through active regulation schemes, which are in part impeded by the metallic cell we use and the inability to measure the magnetic field's amplitude in regions close to the condensate.

The constancy of this field would not be the only technical obstacle to overcome either, going forward the quality of the imaging should be improved. Decoupling the magneto-optical trap and imaging beams, and using larger beams to illuminate the atoms could be the way to go in order to achieve higher signal to noise ratios and a more homogeneous imaging, this however would render the experiment even more complex, which is not desirable. A complete overhaul of the imaging system would perhaps be a more sensible alternative.

It would otherwise be beneficial to rein in more efficiently the intensity fluctuations of the main laser system (425 nm) and address the signal drifts problems by aiming at shorter cycling times.

These upgrades would certainly allow the chromium experiment to explore other facets of isolated systems' thermalization. Further down the road other related research paths could be trod upon, one can wonder for example how is quantum thermalization modified in the presence of disorder [77] [2]? Is our platform a good candidate for the study of itinerant ferromagnetism, as would be suggested by the *local ferromagnetism* protection properties reported in [78]? And finally (or not) can the correlations we observe be used, in particular for interferometric purposes?

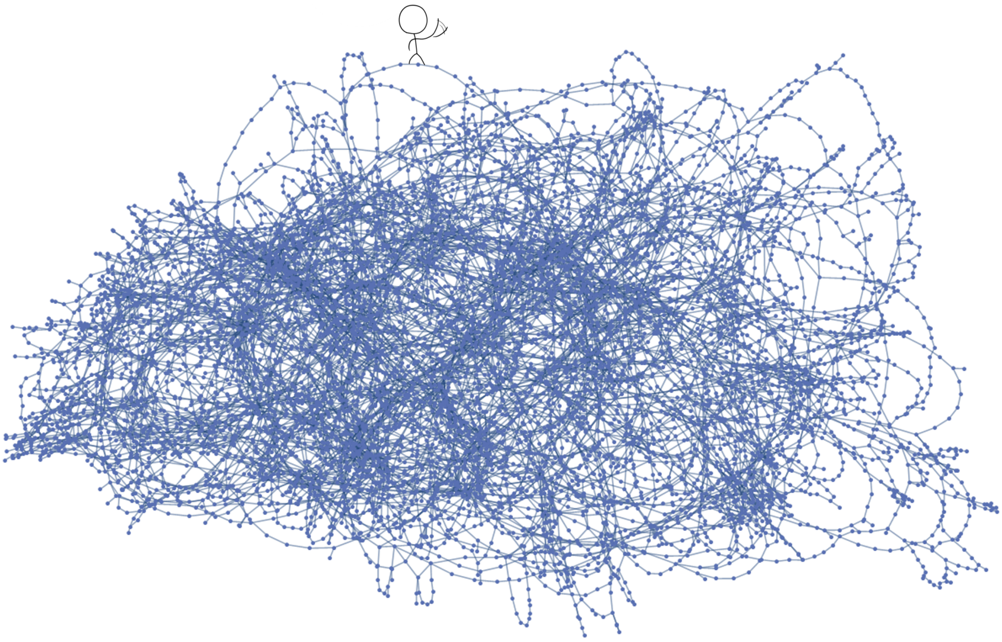

A The 851-425 nm laser chain

Toute votre félicité
Sujette à l'instabilité

– Pierre Corneille (Polyeucte martyr)

The cooling and imaging beams at 425 nm are generated through the frequency doubling of 851 nm laser. This light was formerly produced by a Ti:Sa device. In the early stages of this PhD, this system was replaced by a master diode - tapered amplifier assembly whose workings are described in this appendix. We also discuss the intricate locking schemes relative to this laser system.

A.1 Master oscillator - Tapered amplifier system

The 425 nm laser is generated through frequency doubling of a 1.5 W 851.104 nm laser which is output by a dedicated diode - tapered amplifier system.

The **Master Diode** (MD) is the first building block of this laser system. This particular MD is a frequency stabilized laser diode, it is stabilized using a Littrow type external cavity, its theoretical linewidth is evaluated to 50 kHz. Its lasing threshold is 54 mA, and it is usually working at 126 mA input current which corresponds to an approximate 30 mW output power.
The 851.1 nm laser produced by the MD is mode adapted using a telescope.

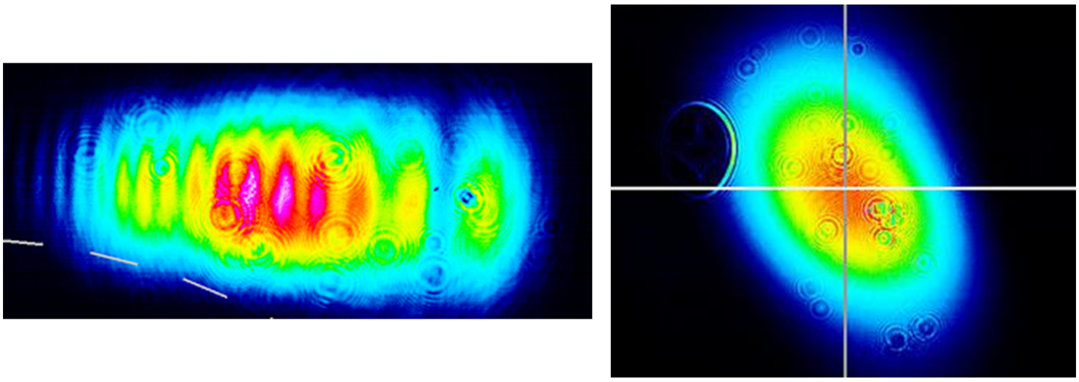

Figure A.2: Left: The MD initial output mode. Right: the final output mode after setting up the adequate cylindrical telescope. The telescope's lenses ($f = 25/-10$) were chosen to produce a transverse mode best suited to the tapered amplifier's input monomode fiber. The distance between the telescope's lenses was chosen to best collimate the laser beam. At 150 cm from the telescope the $\frac{1}{e^2}$ radii are 1014 and 1115 μm(images are not on the same scale). Circle like defaults are belong to the camera screen

The laser is then split into two parts of unequal power. The first part (few mW) follows the locking path (in green in Fig. A.1) (EOM+AOM) and is further split into two parts one of which goes to a wavemeter (purple path in Fig. A.1) and gives us the value of the laser's

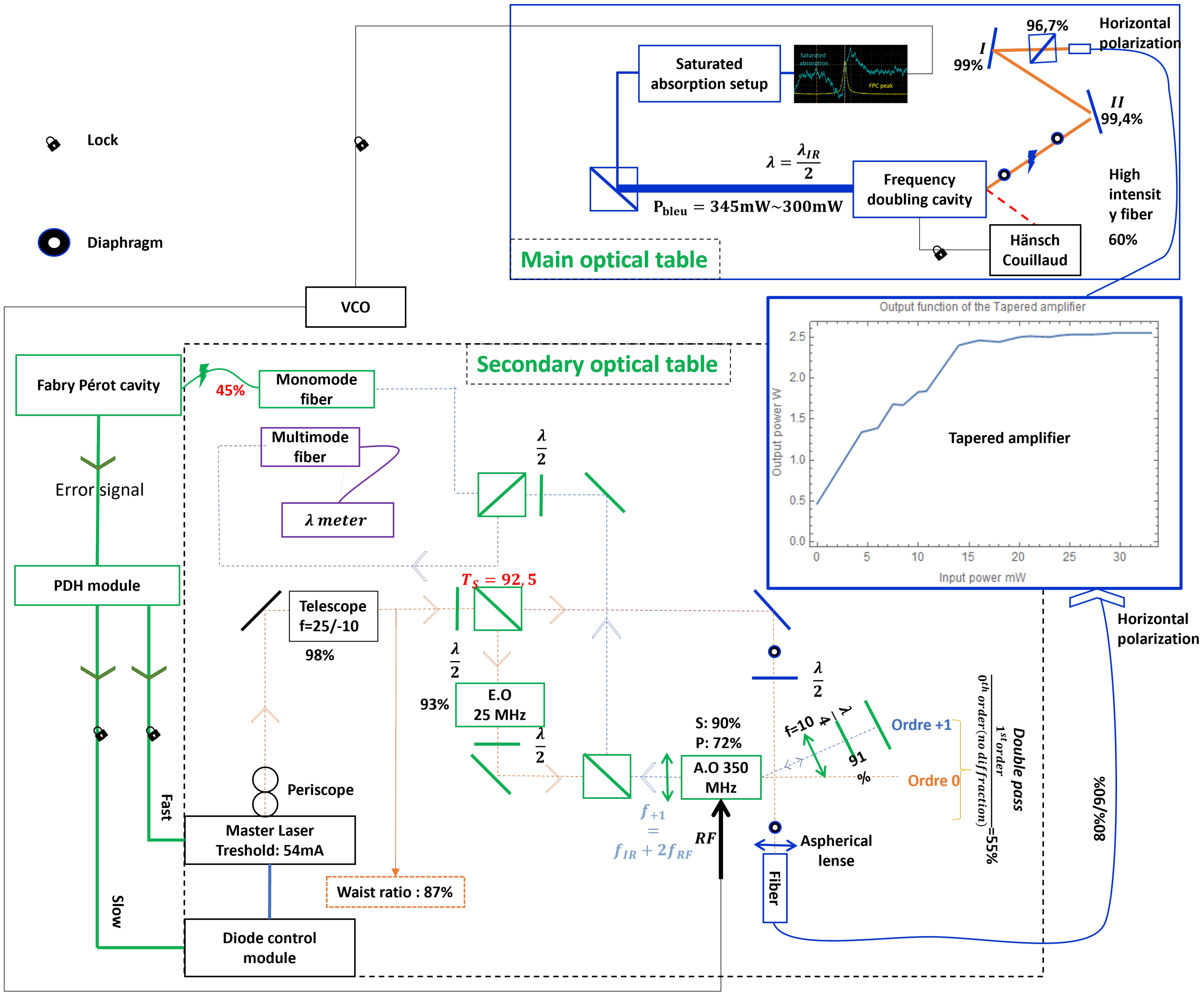

Figure A.1: Optical and locking paths related to the 425 nm light generation. The *"starting point"* (the MD) corresponds to the bottom left corner of the schematics.

wavelength (to picometric precision), while the other goes to a Fabry Perot cavity (FPC)[1] and serves the actual locking purpose. In our case we stabilized the MD's frequency using the Pound-Drever-Hall (PDH) technique.

In order to implement the PDH method, we use an electro optic modulator. An EOM is basically a crystal whose refractive index can rapidly change in response to an electrical stimuli. This index variation will imprint a phase modulation on any light wave traveling the crystal medium. In this way, the laser we use can be phase modulated, in particular a sinusoidal phase modulation will add mainly two sidebands (an infinity in fact with decreasing amplitudes) to the spectral decomposition of the laser light.

In practice, once it passes the EOM the 851 nm laser light comprises three frequencies : the carrier at $4.42910^{15} Hz$, and two other frequencies (at $\pm 25 MHz$ from the main one in our case) which constitute the so-called sidebands.

These sidebands do not share the incident beam's frequency, but the phase relation between them is well defined. If the sidebands are made to interfere with the fundamental component of the reflected beam for example, the sum will display a beat pattern at the modulation frequency which is collected and analyzed using a phase shifter, a mixer and a low pass filter. The phase of the beat pattern gives the phase of the reflected beam, thus informing us on the position of the laser frequency with respect to the cavity resonance.

In practice, the signal reflected off the cavity and onto a photo-diode (cf. fig. A.1) is transmitted to a PDH module, a component which allows us to create, shape and improve the error signal by tuning three parameters (CH0: The amplitude of the demodulation signal sent to the multiplier / CH1: The amplitude of the modulation sent to the EOM and also the relative phase between both).

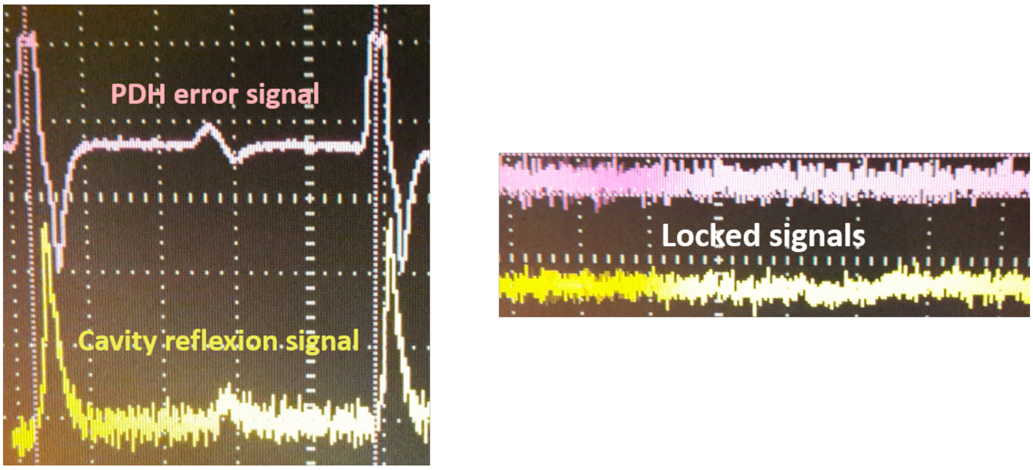

Figure A.3: Left: The PDH error signal and cavity reflection peaks of the 851.1 nm laser. Right: The residual frequency fluctuations are evaluated to less than (≃) 0.4 MHz.

This was for the locking to the FPC, the other part of the laser, the most powerful one (25 mW) actually follows the amplifying and frequency doubling path (in blue in Fig. A.1).

This part of the laser is first used to seed a tapered amplifier (TA) (TOPTICA Boosta Pro) through specifically designed fiber and fiber input port. The beam generated by the TA then goes through a double stage optical isolator (Transmittance = 85%) before connecting to a high power tolerant fiber; the injection efficiency of this fiber which was evaluated to 60% is quite good given that the transverse mode of the light emitted by the TA is not

---

[1] In practice, we use an ultra low expansion (ULE) cavity as a reference. It uses a material which expansion coefficient changes sign at a given temperature (around 20 °C in theory), the cavity is subjected to a servo loop locking it to this critical temperature (10 mK precision). This ensures an almost constant cavity length, and all in all, a stable laser frequency at ±1 MHz

Gaussian. The typical output power of this whole system is 1.5 W, which is identical to that of the Ti:Sa laser at maximum efficiency, moreover this system displays an output power plateau for seed powers higher than 15 mW, which is a great stability feature.

A.1.1 The frequency doubling process

The frequency doubling occurs in an external four-mirror ring commercial cavity (model FD–SF–07), produced by Tekhnoscan. The second harmonic is generated in a 15-mm-long lithium triborate (LBO) crystal.

The efficiency of the doubling mechanism depends on the quality of the laser injection into the cavity. Since the Ti:Sa laser was already injected into said cavity, we started by checking the good correspondence between the two lasers' modes then aligned the TA's beam on the Ti:Sa one.

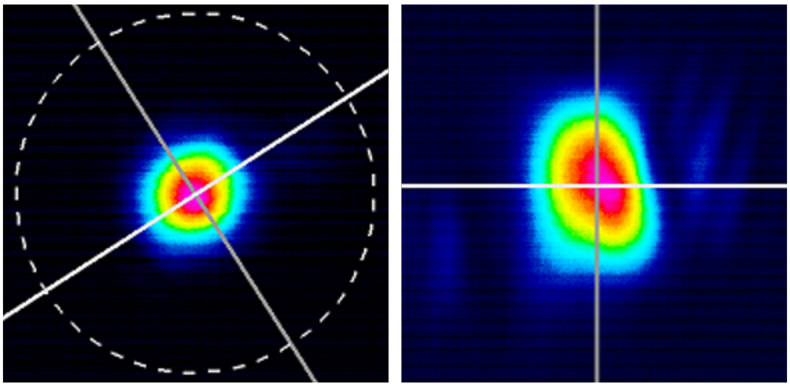

FIGURE A.4: Comparison of both laser modes. Left: MD/TA laser beam. Right: the Ti:Sa mode. The two images are not at the same scale. At 54 cm from the TA's output fiber the two waists of the TA laser are respectively 500 and 530 μm, while those of the Ti:Sa beam are measured to be 405 and 580 μm at 60 cm . These distances correspond to the rough position of the cavity injection lens. Due to the careful choice of the collimating lenses of the TA output fiber, the two modes show good correspondence, in fact the DM/TA system produces a laser of lower ellipticity.

The typical output power of the doubling cavity is 330 mW.

We should report here that the cavity length is itself subjected to a servo-loop based on the Hänsch Couillaud method. The Hänsch Couillaud method is a polarization sensitive locking technique. Here it allows us to control the doubling cavity length through a piezoelectric component so that the IR laser stays resonant, this guarantees that slow and small amplitude drifts of the IR laser do not affect the production of the 425.5 nm light too greatly.

The Hänsch Couillaud error signal has proven to be extremely sensitive to the polarization of the infrared laser at 851.105 nm, in particular its offset varied periodically as the polarization did too, this problem was solved placing a cleanup PBS after the high power tolerant fiber.

At this point, the 425 nm light has no reason to match the $|{}^7S_3\rangle \rightarrow |{}^7P_4\rangle$ cooling transition. To make it so, we use use a hollow cathode lamp and a saturated absorption based lock scheme.

The saturated absorption signal provides us with a dispersive atomic signal informing us on the detuning of the laser with respect to the cooling transition. This information we use to fine tune the 851 nm laser frequency using an acousto-optic modulator. To further counter any slow frequency wanders, of the FPC in particular, the voltage control oscillator which controls the RF frequency fed to the acousto-optic modulator is retroacted upon -using the same saturated absorption error signal- so that the laser stays resonant with the cooling frequency[2].

---

[2] The sum frequency of the 851 nm laser and the RF frequency is given by Fabry Perot cavity lock scheme ($f_{851} + 2f_{AOM} = f_{cavity}$), changing the AOM's frequency will make the PDH system described above act on the infrared frequency so that this equation stays true. In this way, the 425 nm light always matches the cooling transition.

B The bichromatic lattice: alignment procedures

Il n'existe aucune organisation qui puisse se protéger d'un grain de sable.
– Michel Tournier

B.1 Bichromatic lattice alignment procedures

The alignment of the bichromatic lattice comes down to the alignment of both green and infrared lattices.

B.1.1 532 nm lattice alignment

To align the 532 nm lattice, one can start by forming a cloud of magnetically trapped atoms, which are then aimed at using the 532 nm beam.

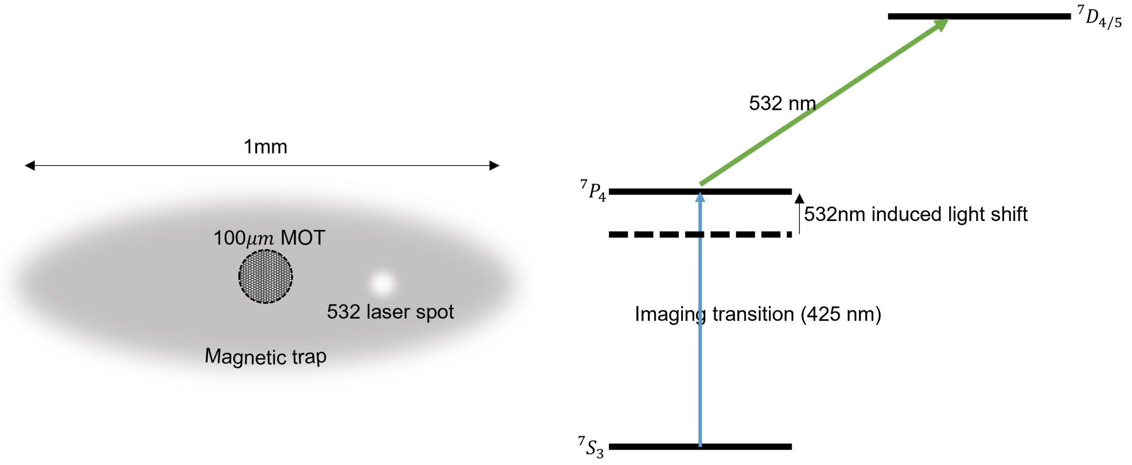

FIGURE B.1: In order to align the 532 nm laser beam, we use magnetically trapped atoms (see Chap.1). As it turns out the 532 nm light couples the $^7P_4$ level to the $^7D_{3/4/5}$ levels, this coupling induces a certain light shift which impairs the proper imaging of the atoms (the $^7P_4$ level is involved in the imaging transition). As a result, we visualize the position of the 532 nm beam directly on the cloud of magnetically trapped atoms in the form of a whitish spot.

Once this rough adjustment has been made, it is further refined by trapping the atoms in the dipolar dimple presented in the first chapter which is also aimed at the 532 nm beam. At this stage of course we do not trigger the evaporation process, this is because the propensity of thermal gases to expand make them easier to aim at.

After centering the incident beam, we carefully align the reflected one, by reinjecting it in the 532 nm fiber as shown in the following schematics

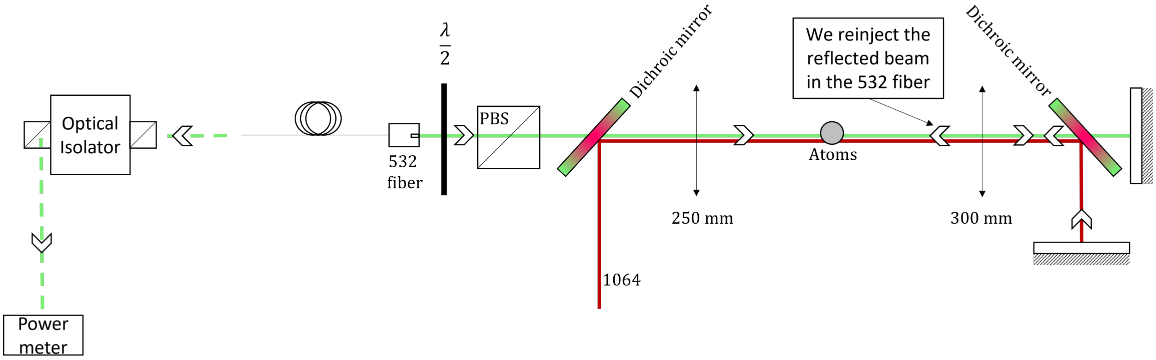

FIGURE B.2: We realign the reflected 532 nm beam by re-injecting it in the fiber outputting the outgoing beam

Finally, we measure the depth of thus created 532 nm lattice by checking for atomic diffraction. This alignment is then gradually improved through fine alignment of the reflected beam.

B.1.2 1064 nm lattice alignment

Once the 532 nm lattice has been set up, the 1064 nm outgoing beam is aligned on the 532 nm trajectory using a pair of distant diaphragms. The 1064 nm laser is also reinjected back into the dedicated output fiber.

Final notes:

- The voltage command sent to the AOMs controlling the lattice beams' powers is increased after the atoms have been released from the lattices and the Verdi shutter closed, so that these AOMS remain *warm*
- The beams should be injected in their dedicated fiber at low laser power. The corresponding AOMs however should always be used at maximum RF power
- Non linear power related effects in the lattices' injection fibers make it so that the adequate position of these fibers' injection lenses depend on the injected beams' power

B.2 Double lattice benchmark : Alternated loading

The structure of the double lattice can be ascertained by loading atoms in every other lattice site along the bipartition axis. The sequence leading to this alternated loading is quite simple as it only requires to invert the order in which the 1064 nm and 532 nm lasers are switched on.

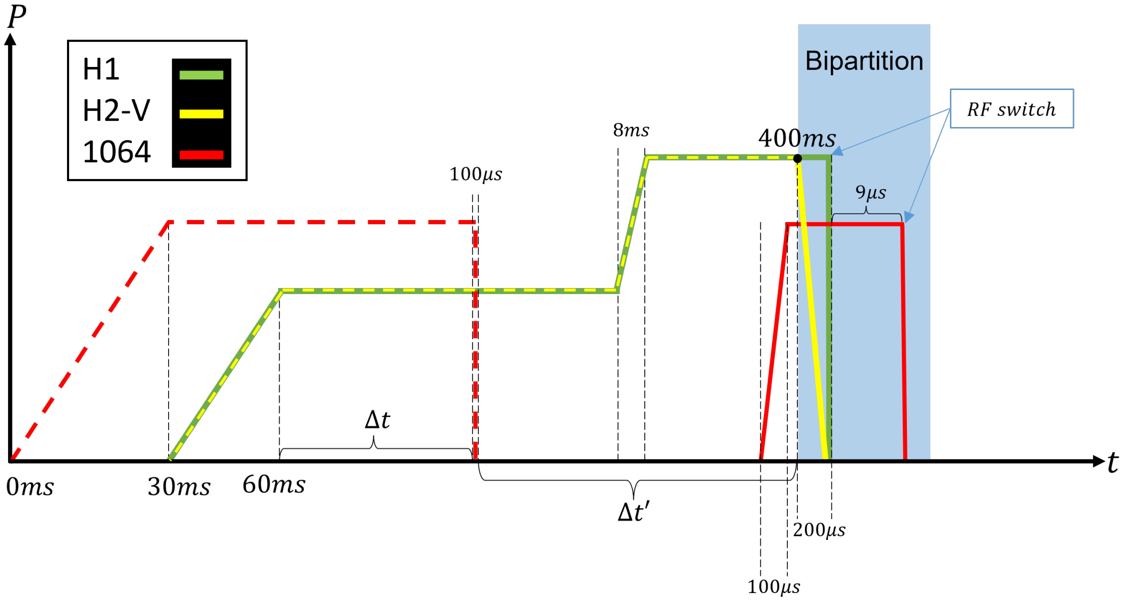

Figure B.3: The laser ramps used to load every other lattice site

The number of families upon bipartition depends on the order in which the lasers are switched on. When the atoms are first loaded in the 1D 1064 nm lattice, only one family can be observed after the bipartition step. When this step is omitted, two atomic families can be seen.

C The partial covariance

> *All models are wrong, but some are useful.*
>
> – George E. P. Box

In this appendix we present the partial covariance technique which gets rid of irrelevant common mode correlations between given random variables.

C.1 The partial covariance technique

C.1.1 Definition

When two stochastic variables X and Y are indirectly correlated via a third variable[1] Z, it is customary to correct for these unwanted correlations using partial covariance schemes as is done in [79][80].

The general idea is to consider X, Y and Z as vectors of an Euclidean space whose inner product is given by the covariance.

$$\langle X, Y \rangle = \operatorname{cov}(X, Y) \tag{C.1}$$

In this space we can write

$$\begin{aligned} X &= \alpha Z + X' \\ Y &= \alpha' Z + Y' \end{aligned} \tag{C.2}$$

Where

- X' and Y' are orthogonal to Z
- $\alpha = \frac{\operatorname{cov}(X,Z)}{\operatorname{Var}(Z)}$
- $\alpha' = \frac{\operatorname{cov}(Y,Z)}{\operatorname{Var}(Z)}$

This gives

$$\begin{aligned} \operatorname{cov}(X, Y) &= \alpha\alpha' \operatorname{Var}(Z) + \operatorname{cov}\left(X', Y'\right) \\ &= \frac{\operatorname{cov}(X, Z)\operatorname{cov}(Y, Z)}{\operatorname{Var}(Z)} + \operatorname{cov}\left(X', Y'\right) \end{aligned} \tag{C.3}$$

The total covariance between X and Y is in part explained by the first term of the right hand side which represents their non zero projection on vector Z, we call this contribution to the covariance a *common mode* correlation.

In the case where this common mode corresponds to uninteresting correlation biases, (for example the fluctuations of the total number of atoms), then the *residual* or *partial covariance* $\operatorname{cov}\left(X', Y'\right)$ makes for a somewhat more insightful measurement of the correlations. This residual part is the **partial covariance**, hereafter denoted **pcov**, of X and Y with respect to Z

---

[1] In the following, this third variable will be called *fluctuating parameter or control parameter*

$$\mathrm{pcov}(X,Y;Z) = \mathrm{cov}\left(X',Y'\right) \tag{C.4}$$

Similarly we define the partial variance **pvar** as

$$\mathrm{pvar}(X;Z) = \mathrm{pcov}(X,X;Z) \tag{C.5}$$

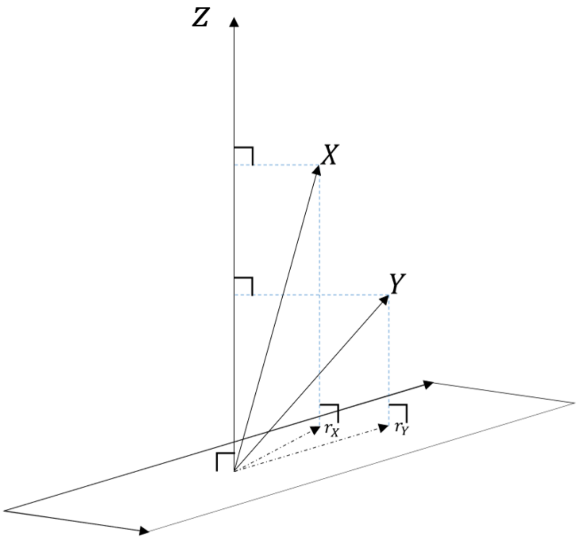

FIGURE C.1: Geometrically the partial covariance can be seen as what remains of the covariance, when the X and Y variables are projected onto the subspace orthogonal by the fluctuating parameters, that is $\mathrm{cov}\left(r_X, r_Y\right)$

Note that in general, the experimental application of partial covariance schemes **requires the careful monitoring of the control parameter Z.**

This formalism can be extended to several control parameters, for example the partial variance covariance matrix of the two variables X and Y corrected for both I and J is given by

$$\Sigma_p = \Sigma - \Sigma_V \Sigma_{I,J} \Sigma_V^T \tag{C.6}$$

Where Σ is the variance covariance matrix of variables X and Y and

$$\begin{aligned}
\Sigma_p &= \begin{pmatrix} \mathrm{pvar}(X;I,J) & \mathrm{pcov}(X,Y;I,J) \\ \mathrm{pcov}(X,Y;I,J) & \mathrm{pvar}(Y;I,J) \end{pmatrix} \\
\Sigma_V &= \begin{pmatrix} \mathrm{cov}\left(X,I\right) & \mathrm{cov}\left(X,J\right) \\ \mathrm{cov}\left(Y,I\right) & \mathrm{cov}\left(Y,J\right) \end{pmatrix} \\
\Sigma_{I,J} &= \begin{pmatrix} \mathrm{Var}\left(I\right) & \mathrm{cov}\left(I,J\right) \\ \mathrm{cov}\left(J,I\right) & \mathrm{Var}\left(J\right) \end{pmatrix}
\end{aligned} \tag{C.7}$$

and Σ_V^T is the transpose of Σ_V.

In our case, there are several fluctuating parameters, amongst which **the total number of atoms in the condensate A_T and the number of atoms in each of the A/B families A_T^A/A_T^B.** It is not possible to monitor these parameters during the experiment, however as one can see from Eq. C.6, **the exact knowledge of the control variables is not required in order to compute the partial variance covariance matrix, only a few particular statistical properties**

are needed. Moreover as it turns out

$$A_T = \sum_i A_i$$
$$A_T^A = \sum_i^{F_A} A_i \tag{C.8}$$

Where F_A is the A family and A_i the number of atoms in cloud i. This means that the variances and covariances of these parameters can easily be computed using experimental data, for example

$$\mathrm{Var}\left(A_T\right) = \sum_i \mathrm{Var}\left(A_i\right) + 2\sum_{i \neq j} \mathrm{cov}\left(A_i, A_j\right) \tag{C.9}$$

Since these corrections **do not require the additional monitoring of the fluctuating parameters**, the partial covariance used here is called **self corrected partial covariance**.

C.1.2 Aparté on constant correlation noises and variable correlation noises

Correlations

The correlation between two variables X and Y is defined as

$$\mathrm{corr}(X, Y) = \frac{\mathrm{cov}\left(X, Y\right)}{\sqrt{\mathrm{Var}\left(X\right)}\sqrt{\mathrm{Var}\left(Y\right)}} \tag{C.10}$$

In the euclidean space wherein the covariance plays the role of the inner product, these correlation matrices **represent the cosine of the angle between basis vectors**.

Constant correlation noises

Preliminary note: All the correlations matrices shown below are obtained through numerical experiments similar to those presented in Chap. 2. The results of these experiments are covariance or correlation matrices mimicking those obtained in the real lab experiment at time $t_{\mathrm{dyn}} = 0$ ms. Depending on the situation, we include either or all of the quantum projection noise, the number noise or the bipartition noise in these numerical experiments. We do not include the detection chain noises.

Correlation matrices of populations affected solely by constant correlation noises are always the same (contrary to the covariances matrices) and do not depend on the specific experiment. These noises are for example the bipartition noise (Bip) and the atom number noise (NN).

For the sake of concreteness, let us consider the latter, its effect on the $t_{\mathrm{dyn}} = 0$ ms populations can be described via the transformation

$$A_i \rightarrow \alpha A_i \quad \forall i \in [|1, 7|] \tag{C.11}$$

Where α is some random real number.

The covariances between populations are affected as follows

$$\mathrm{cov}\left(A_i, A_j\right) \rightarrow \alpha^2 \mathrm{cov}\left(A_i, A_j\right) \tag{C.12}$$

If we take into account the fact that A_i can be written at time $t_{\mathrm{dyn}} = 0$ ms $A_i = \beta_{ij} A_j$, we get

$$\mathrm{cov}\left(A_i, A_j\right) \rightarrow \alpha^2 \mathrm{cov}\left(A_i, A_j\right) = \alpha^2 \beta_{ij} \mathrm{Var}\left(A_j\right) \tag{C.13}$$

The correlations between populations on the other hand are insensitive to this noise and we have

$$\operatorname{corr}\left(A_i, A_j\right) \to \frac{\alpha^2 \operatorname{cov}\left(A_i, A_j\right)}{\alpha^2 \sqrt{\operatorname{Var}\left(A_i\right) \operatorname{Var}\left(A_j\right)}} = \operatorname{corr}\left(A_i, A_j\right) \tag{C.14}$$

If we take into account the fact that A_i can be written at time $t_{\text{dyn}} = 0$ ms $A_i = \beta_{ij} A_j$, we see that these correlations are in fact all equal to 1

$$\operatorname{corr}\left(A_i, A_j\right) = \frac{\alpha^2 \operatorname{cov}\left(A_i, A_j\right)}{\alpha^2 \beta_{ij} \operatorname{Var}\left(A_j\right)} = 1 \tag{C.15}$$

This means that the population **correlation matrix**, $\mathscr{C}_{\text{NN}}$, is in this case full of ones, expressing the fact that the space spanned by the 14 populations is but a line

$$\mathscr{C}_{\text{NN}} = \begin{pmatrix}
1 & 1 & 1 & 1 & 1 & 1 & 1 & 1 & 1 & 1 & 1 & 1 & 1 & 1 \\
1 & 1 & 1 & 1 & 1 & 1 & 1 & 1 & 1 & 1 & 1 & 1 & 1 & 1 \\
1 & 1 & 1 & 1 & 1 & 1 & 1 & 1 & 1 & 1 & 1 & 1 & 1 & 1 \\
1 & 1 & 1 & 1 & 1 & 1 & 1 & 1 & 1 & 1 & 1 & 1 & 1 & 1 \\
1 & 1 & 1 & 1 & 1 & 1 & 1 & 1 & 1 & 1 & 1 & 1 & 1 & 1 \\
1 & 1 & 1 & 1 & 1 & 1 & 1 & 1 & 1 & 1 & 1 & 1 & 1 & 1 \\
1 & 1 & 1 & 1 & 1 & 1 & 1 & 1 & 1 & 1 & 1 & 1 & 1 & 1 \\
1 & 1 & 1 & 1 & 1 & 1 & 1 & 1 & 1 & 1 & 1 & 1 & 1 & 1 \\
1 & 1 & 1 & 1 & 1 & 1 & 1 & 1 & 1 & 1 & 1 & 1 & 1 & 1 \\
1 & 1 & 1 & 1 & 1 & 1 & 1 & 1 & 1 & 1 & 1 & 1 & 1 & 1 \\
1 & 1 & 1 & 1 & 1 & 1 & 1 & 1 & 1 & 1 & 1 & 1 & 1 & 1 \\
1 & 1 & 1 & 1 & 1 & 1 & 1 & 1 & 1 & 1 & 1 & 1 & 1 & 1 \\
1 & 1 & 1 & 1 & 1 & 1 & 1 & 1 & 1 & 1 & 1 & 1 & 1 & 1 \\
1 & 1 & 1 & 1 & 1 & 1 & 1 & 1 & 1 & 1 & 1 & 1 & 1 & 1
\end{pmatrix} \tag{C.16}$$

The same reasoning stands for the bipartition noise and we can show that correlations between populations plagued by this noise can only take two values : ±1. The correlation matrix, $\mathscr{C}_{\text{Bip}}$ in this case is given by

$$\mathscr{C}_{\text{Bip}} = \begin{pmatrix}
1 & 1 & 1 & 1 & 1 & 1 & 1 & -1 & -1 & -1 & -1 & -1 & -1 & -1 \\
1 & 1 & 1 & 1 & 1 & 1 & 1 & -1 & -1 & -1 & -1 & -1 & -1 & -1 \\
1 & 1 & 1 & 1 & 1 & 1 & 1 & -1 & -1 & -1 & -1 & -1 & -1 & -1 \\
1 & 1 & 1 & 1 & 1 & 1 & 1 & -1 & -1 & -1 & -1 & -1 & -1 & -1 \\
1 & 1 & 1 & 1 & 1 & 1 & 1 & -1 & -1 & -1 & -1 & -1 & -1 & -1 \\
1 & 1 & 1 & 1 & 1 & 1 & 1 & -1 & -1 & -1 & -1 & -1 & -1 & -1 \\
1 & 1 & 1 & 1 & 1 & 1 & 1 & -1 & -1 & -1 & -1 & -1 & -1 & -1 \\
-1 & -1 & -1 & -1 & -1 & -1 & -1 & 1 & 1 & 1 & 1 & 1 & 1 & 1 \\
-1 & -1 & -1 & -1 & -1 & -1 & -1 & 1 & 1 & 1 & 1 & 1 & 1 & 1 \\
-1 & -1 & -1 & -1 & -1 & -1 & -1 & 1 & 1 & 1 & 1 & 1 & 1 & 1 \\
-1 & -1 & -1 & -1 & -1 & -1 & -1 & 1 & 1 & 1 & 1 & 1 & 1 & 1 \\
-1 & -1 & -1 & -1 & -1 & -1 & -1 & 1 & 1 & 1 & 1 & 1 & 1 & 1 \\
-1 & -1 & -1 & -1 & -1 & -1 & -1 & 1 & 1 & 1 & 1 & 1 & 1 & 1 \\
-1 & -1 & -1 & -1 & -1 & -1 & -1 & 1 & 1 & 1 & 1 & 1 & 1 & 1
\end{pmatrix} \tag{C.17}$$

Adding up both noise, we end up with a two sets of non colinear vectors: this time, the subspace spanned by all 14 populations is in fact 2D dimensional, it is a plane.

$$\mathscr{C}_{\text{NN, Bip}} = \begin{pmatrix}
1 & 1 & 1 & 1 & 1 & 1 & 1 & x & x & x & x & x & x & x \\
1 & 1 & 1 & 1 & 1 & 1 & 1 & x & x & x & x & x & x & x \\
1 & 1 & 1 & 1 & 1 & 1 & 1 & x & x & x & x & x & x & x \\
1 & 1 & 1 & 1 & 1 & 1 & 1 & x & x & x & x & x & x & x \\
1 & 1 & 1 & 1 & 1 & 1 & 1 & x & x & x & x & x & x & x \\
1 & 1 & 1 & 1 & 1 & 1 & 1 & x & x & x & x & x & x & x \\
1 & 1 & 1 & 1 & 1 & 1 & 1 & x & x & x & x & x & x & x \\
x & x & x & x & x & x & x & 1 & 1 & 1 & 1 & 1 & 1 & 1 \\
x & x & x & x & x & x & x & 1 & 1 & 1 & 1 & 1 & 1 & 1 \\
x & x & x & x & x & x & x & 1 & 1 & 1 & 1 & 1 & 1 & 1 \\
x & x & x & x & x & x & x & 1 & 1 & 1 & 1 & 1 & 1 & 1 \\
x & x & x & x & x & x & x & 1 & 1 & 1 & 1 & 1 & 1 & 1 \\
x & x & x & x & x & x & x & 1 & 1 & 1 & 1 & 1 & 1 & 1 \\
x & x & x & x & x & x & x & 1 & 1 & 1 & 1 & 1 & 1 & 1
\end{pmatrix} \tag{C.18}$$

Where x is a random number between 1 and -1, whose actual value is random.

Variable correlation noises

Variable correlation noises are characterized by the fact that the entries of their correlations matrices are different as soon as the number of shots taken to build the correlation matrix is limited. The quantum projection noise is a variable correlation noise. Below, we give two correlation matrices built on a series of 50 realizations of the numerical experiment with the quantum projection noise being the only noise to be included. These correlation matrices are denoted $\mathscr{C}_{QN}$

$$\mathscr{C}^1_{QN} = \begin{pmatrix}
1. & -0.04 & -0.38 & -0.06 & -0.2 & 0.06 & -0.06 & -0.1 & -0.14 & 0.38 \\
-0.04 & 1. & -0.48 & -0.2 & -0.24 & -0.06 & -0.14 & 0.16 & 0.06 & -0.08 \\
-0.38 & -0.48 & 1. & -0.44 & -0.16 & -0.1 & 0.04 & 0.1 & 0. & -0.14 \\
-0.06 & -0.2 & -0.44 & 1. & -0.2 & 0.14 & 0.08 & -0.04 & 0.02 & -0.2 \\
-0.2 & -0.24 & -0.16 & -0.2 & 1. & 0.02 & 0.04 & -0.24 & 0.04 & 0.26 \\
0.06 & -0.06 & -0.1 & 0.14 & 0.02 & 1. & -0.4 & 0.02 & -0.24 & 0.02 \\
-0.06 & -0.14 & 0.04 & 0.08 & 0.04 & -0.4 & 1. & -0.38 & -0.42 & 0.04 \\
-0.1 & 0.16 & 0.1 & -0.04 & -0.24 & 0.02 & -0.38 & 1. & -0.32 & -0.56 \\
-0.14 & 0.06 & 0. & 0.02 & 0.04 & -0.24 & -0.42 & -0.32 & 1. & -0.14 \\
0.38 & -0.08 & -0.14 & -0.2 & 0.26 & 0.02 & 0.04 & -0.56 & -0.14 & 1.
\end{pmatrix} \tag{C.19}$$

$$\mathscr{C}^2_{QN} = \begin{pmatrix}
1. & -0.04 & -0.34 & -0.14 & -0.14 & 0.1 & -0.06 & -0.16 & -0.02 & 0.22 \\
-0.04 & 1. & -0.38 & -0.48 & -0.16 & -0.1 & 0.2 & -0.12 & 0.18 & -0.22 \\
-0.34 & -0.38 & 1. & -0.3 & -0.18 & -0.1 & -0.14 & 0.3 & -0.14 & 0.02 \\
-0.14 & -0.48 & -0.3 & 1. & -0.2 & 0.16 & -0.1 & -0.06 & -0.04 & 0.1 \\
-0.14 & -0.16 & -0.18 & -0.2 & 1. & -0.06 & 0.12 & -0.04 & 0. & -0.04 \\
0.1 & -0.1 & -0.1 & 0.16 & -0.06 & 1. & -0.1 & -0.2 & -0.36 & -0.2 \\
-0.06 & 0.2 & -0.14 & -0.1 & 0.12 & -0.1 & 1. & -0.42 & -0.22 & -0.34 \\
-0.16 & -0.12 & 0.3 & -0.06 & -0.04 & -0.2 & -0.42 & 1. & -0.42 & -0.18 \\
-0.02 & 0.18 & -0.14 & -0.04 & 0. & -0.36 & -0.22 & -0.42 & 1. & 0.04 \\
0.22 & -0.22 & 0.02 & 0.1 & -0.04 & -0.2 & -0.34 & -0.18 & 0.04 & 1.
\end{pmatrix} \tag{C.20}$$

C.2 Benchmark

To benchmark the partial covariance scheme we use those same numerical experiments we have already used in the previous section. We remind the reader that these experiments mimic the results of the actual lab experiment at time $t_{\text{dyn}} = 0$ ms. For each realization of the experiment we choose a random number of atoms according to the distribution $\mathcal{N}(10000, 700)$, these atoms are then divided into two families according to the distribution $\mathcal{N}(50\%, 3\%)$, and then for each family we produce a random sample of 14 Zeeman clouds according to the theoretical populations of the initial experiment state (the one obtained after a $\frac{\pi}{2}$ pulse).
The general idea of this benchmark is to **try to recreate variance covariance matrices similar to those engendered by the sole projection noise by applying the partial covariance scheme to variance covariance matrices containing the additional contributions of the bipartition and number noises**. The criterion we have retained to test the efficiency of the partial covariance is the distance between the partial covariance matrices (or corrected covariance matrices) and the *quantum projection matrices* (that is those containing the sole contribution of the quantum projection noise).
In all of the following the distance between two matrices M and N is given by

$$|M - N| = \sqrt{\sum_{i,j} (M_{i,j} - N_{i,j})^2} \tag{C.21}$$

In a first attempt we show the result of the partial covariance scheme when **only** the atom number (NN) and bipartition (Bip) noises are taken into account without the projection noise. In this case, to get rid of all the randomness in the data it is necessary to compute the partial covariance with respect to the subspace generated by the 14 populations, which as you remember is plane! The initial variance covariance matrix[2]

$$\mathbf{Cov}_{\text{NN,Bip}} = \begin{pmatrix}
2211 & 5529 & 7371 & 5529 & 2211 & 81 & 203 & 271 & 203 & 81 \\
5529 & 13823 & 18430 & 13823 & 5529 & 202 & 507 & 676 & 507 & 202 \\
7371 & 18430 & 24572 & 18430 & 7371 & 270 & 675 & 900 & 675 & 270 \\
5529 & 13823 & 18430 & 13823 & 5529 & 202 & 507 & 676 & 507 & 202 \\
2211 & 5529 & 7371 & 5529 & 2211 & 81 & 203 & 271 & 203 & 81 \\
81 & 202 & 270 & 202 & 81 & 2200 & 5499 & 7331 & 5499 & 2200 \\
203 & 507 & 675 & 507 & 203 & 5499 & 13747 & 18328 & 13747 & 5499 \\
271 & 676 & 900 & 676 & 271 & 7331 & 18328 & 24436 & 18328 & 7331 \\
203 & 507 & 675 & 507 & 203 & 5499 & 13747 & 18328 & 13747 & 5499 \\
81 & 202 & 270 & 202 & 81 & 2200 & 5499 & 7331 & 5499 & 2200
\end{pmatrix} \tag{C.22}$$

---

[2] For convenience, we show a 10 by 10 matrix corresponding to the -2 to 2 spin states only instead of the full 14 by 14 matrix corresponding to -3 to 3 spin states

becomes when computing the partial covariance with respect to A^A_{-3} (or A^A_{-2}, orA^A_{-1} or $A^A_{-3}+A^A_1$ which are all colinear)

$$\mathbf{Cov}_{\text{NN,Bip}}^{A^A_{-3}corrected} = \begin{pmatrix} 0 & 0 & 0 & 0 & 0 & 0 & 0 & 0 & 0 & 0 \\ 0 & 1 & 1 & 1 & 0 & 0 & 0 & 0 & 0 & 0 \\ 0 & 1 & 1 & 1 & 0 & 0 & -1 & -1 & -1 & 0 \\ 0 & 1 & 1 & 1 & 0 & 0 & 0 & 0 & 0 & 0 \\ 0 & 0 & 0 & 0 & 0 & 0 & 0 & 0 & 0 & 0 \\ 0 & 0 & 0 & 0 & 0 & 2163 & 5406 & 7208 & 5406 & 2163 \\ 0 & 0 & -1 & 0 & 0 & 5406 & 13516 & 18020 & 13516 & 5406 \\ 0 & 0 & -1 & 0 & 0 & 7208 & 18020 & 24026 & 18020 & 7208 \\ 0 & 0 & -1 & 0 & 0 & 5406 & 13516 & 18020 & 13516 & 5406 \\ 0 & 0 & 0 & 0 & 0 & 2163 & 5406 & 7208 & 5406 & 2163 \end{pmatrix} \tag{C.23}$$

Complete correction using Eq.C.6 leads to

$$\mathbf{Cov}_{\text{NN,Bip}}^{corrected} = \begin{pmatrix} 0.1 & 0. & 0. & 0. & 0.1 & 0. & 0. & 0. & 0. & 0. \\ 0. & 0. & 0. & 0. & 0. & 0. & 0. & 0. & 0. & 0. \\ 0. & 0. & 0.1 & 0. & 0. & 0. & 0. & 0. & 0. & 0. \\ 0. & 0. & 0. & 0. & 0. & 0. & 0. & 0. & 0. & 0. \\ 0.1 & 0. & 0. & 0. & 0.1 & 0. & 0. & 0. & 0. & 0. \\ 0. & 0. & 0. & 0. & 0. & 0.1 & 0. & 0. & 0. & 0.1 \\ 0. & 0. & 0. & 0. & 0. & 0. & 0. & 0. & 0. & 0. \\ 0. & 0. & 0. & 0. & 0. & 0. & 0. & 0.1 & 0. & 0. \\ 0. & 0. & 0. & 0. & 0. & 0. & 0. & 0. & 0. & 0. \\ 0. & 0. & 0. & 0. & 0. & 0.1 & 0. & 0. & 0. & 0.1 \end{pmatrix} \tag{C.24}$$

Which means that our data does not contain any sort of randomness anymore. We have computed the orthogonal projection of our data to all the basis vectors, we are left with the 0 vector.

When **the quantum projection noise is included**, the uncorrected covariance matrix is given by

$$\begin{pmatrix} 2647 & 5441 & 7263 & 5440 & 2179 & 72 & 180 & 246 & 168 & 69 \\ 5441 & 14762 & 18138 & 13578 & 5437 & 170 & 425 & 591 & 406 & 166 \\ 7263 & 18138 & 25786 & 18119 & 7261 & 220 & 567 & 785 & 541 & 219 \\ 5440 & 13578 & 18119 & 14742 & 5433 & 169 & 436 & 596 & 412 & 166 \\ 2179 & 5437 & 7261 & 5433 & 2643 & 65 & 170 & 233 & 161 & 68 \\ 72 & 170 & 220 & 169 & 65 & 2660 & 5471 & 7302 & 5478 & 2189 \\ 180 & 425 & 567 & 436 & 170 & 5471 & 14836 & 18239 & 13684 & 5458 \\ 246 & 591 & 785 & 596 & 233 & 7302 & 18239 & 25895 & 18244 & 7287 \\ 168 & 406 & 541 & 412 & 161 & 5478 & 13684 & 18244 & 14860 & 5463 \\ 69 & 166 & 219 & 166 & 68 & 2189 & 5458 & 7287 & 5463 & 2652 \end{pmatrix} \tag{C.25}$$

Upon correction (for the bipartition and the number noises) we find

$$\begin{pmatrix}
421 & -114 & -152 & -111 & -44 & 2 & 1 & 0 & -2 & -1 \\
-114 & 887 & -378 & -282 & -114 & 3 & -3 & 0 & 0 & 0 \\
-152 & -378 & 1062 & -383 & -149 & -2 & -1 & 2 & 2 & 0 \\
-111 & -282 & -383 & 888 & -113 & -1 & 3 & -1 & 0 & -2 \\
-44 & -114 & -149 & -113 & 420 & -1 & 1 & -1 & 0 & 2 \\
2 & 3 & -2 & -1 & -1 & 422 & -115 & -151 & -112 & -43 \\
1 & -3 & -1 & 3 & 1 & -115 & 881 & -374 & -276 & -116 \\
0 & 0 & 2 & -1 & -1 & -151 & -374 & 1056 & -382 & -150 \\
-2 & 0 & 2 & 0 & 0 & -112 & -276 & -382 & 885 & -115 \\
-1 & 0 & 0 & -2 & 2 & -43 & -116 & -150 & -115 & 423
\end{pmatrix} \tag{C.26}$$

Whereas the expected matrix[3] is given by

$$\mathbf{Cov}_{QN} = \begin{pmatrix}
425 & -110 & -146 & -110 & -44 & 0 & 0 & 0 & 0 & 0 \\
-110 & 897 & -366 & -275 & -110 & 0 & 0 & 0 & 0 & 0 \\
-146 & -366 & 1074 & -366 & -146 & 0 & 0 & 0 & 0 & 0 \\
-110 & -275 & -366 & 897 & -110 & 0 & 0 & 0 & 0 & 0 \\
-44 & -110 & -146 & -110 & 425 & 0 & 0 & 0 & 0 & 0 \\
0 & 0 & 0 & 0 & 0 & 425 & -110 & -146 & -110 & -44 \\
0 & 0 & 0 & 0 & 0 & -110 & 897 & -366 & -275 & -110 \\
0 & 0 & 0 & 0 & 0 & -146 & -366 & 1074 & -366 & -146 \\
0 & 0 & 0 & 0 & 0 & -110 & -275 & -366 & 897 & -110 \\
0 & 0 & 0 & 0 & 0 & -44 & -110 & -146 & -110 & 425
\end{pmatrix} \tag{C.27}$$

The mean distance convergence as a function of the number of experimental series is shown in the following figure

---

[3] This second matrix is the average of the covariance matrices related to the sole contribution of the quantum projection noise for the same experiments.

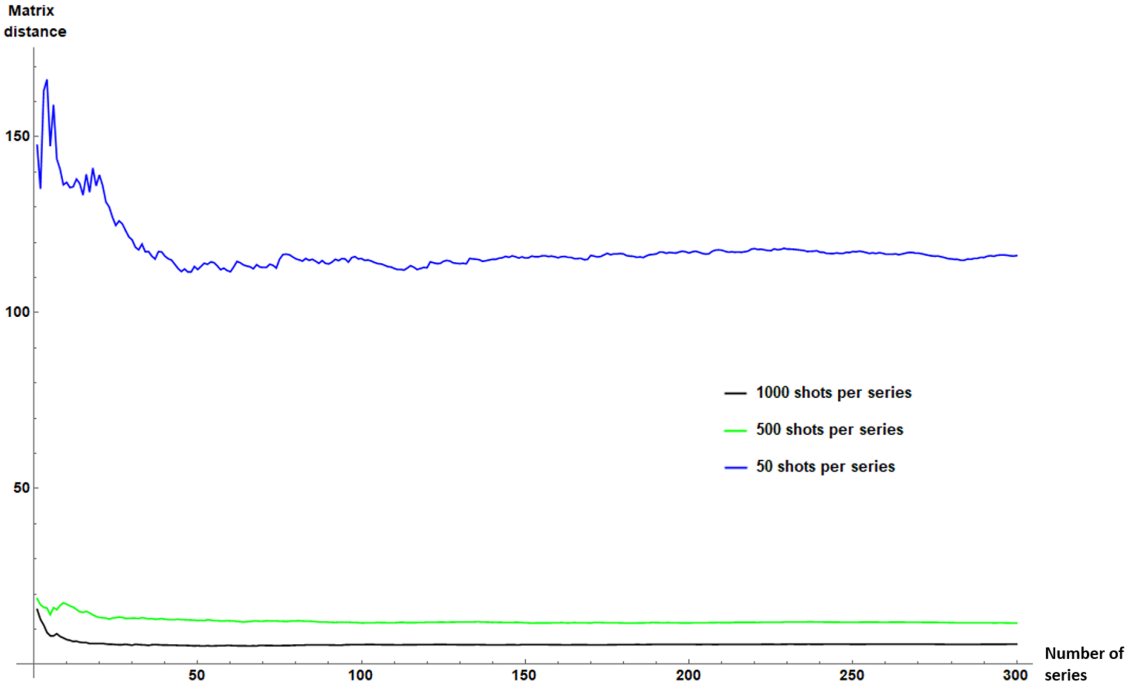

FIGURE C.2: Distance between the average of the matrices corrected for both atom number and bipartition noises to the expected correlation matrix[4]. The asymptotic value depends on the number of shots per series. **The uncorrected distance is** $\simeq 80000$, to be compared to the values shown here (150,20,10): the scheme works quite well.

In conclusion, the partial covariance scheme works quite well when it comes to the correction of constant correlation noises.

---

[4] Which is different from the correction of the average of the noisy matrices.

D Numerical simulations of dissipative dipolar dynamics

> *Debugging is twice as hard as writing the code in the first place. Therefore, if you write the code as cleverly as possible, you are, by definition, not smart enough to debug it.*
>
> – Brian W. Kernighan

In this appendix we investigate atomic losses' impact on the statistical distributions of the Zeeman populations. We compute the ***exact*** *evolution of a system of 8 singlons and 4 doublons, the four of which are lost throughout the dynamics. Thankfully, the algorithm used to do so was not written as cleverly as possible, which made it debuggable.*

D.1 System and assumptions

We simulate the dissipative dipolar interactions unfurling in a 2×6 rectangular plaquette, composed of eight singlons and 4 doublons. This system is represented in D.1

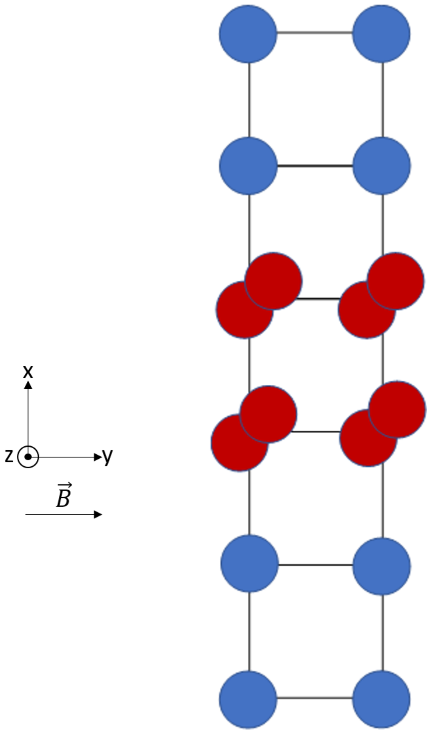

FIGURE D.1: The system is composed of 4 doublons and 8 singlons. They form a rectangular lattice

Assumptions

- The magnetic field runs along one of the lattice's "crystallographic" axes: this is not true in the actual experiment in which the magnetic field forms an ≈ 19° angle with one of the axes. We believe that this choice does not have any significant impact on the qualitative results of the simulations, on the other hand, it allows for faster and more efficient computations.

- The range of the interactions is limited: atoms only interact with the closest and second closest entities.
- The doublons are treated as spin 6 particles, the spin degree of freedom is constrained to the J=6 manifold.
- The singlons are initialized in the $|S=3, m_s=2\rangle$ whereas the doublons are initialized in $|S=6, m_s=4\rangle$ state. In the real system the atoms are prepared in the 0 magnetization manifold, the dimension of the Hilbert space relevant to this preparation entails prohibitively expensive calculations. The dimension of the chosen Hilbert space is D=11694943.

D.2 Simulation's principles

D.2.1 Master equation

The algorithm used to compute the dissipative dynamics of our system makes intensive use of the dimensional reduction principles underlined in section D.2.3, it also adapts known *quantum trajectories* or *quantum jumps* methods developed in the early nineties in the field of quantum optics to the problem at hand [81][82][83].

The main difference between these works and the results presented below being **the nature of the dissipative process investigated, here we are interested in particle losses rather than spontaneous emission induced decoherence**.

The main advantage of such methods is that one needs not evolve the whole density matrix ρ of the system that is considered but rather **a statistically significant set of wavefunctions** $|\Psi_k\rangle$ according to the protocol detailed below.

Following [84][85], we suppose that the dissipative dynamics of our system are given by the general

master equation:

$$\frac{d\hat{\rho}}{dt} = -\frac{i}{\hbar}[\hat{H}_{dd}, \hat{\rho}] - \frac{1}{2}\sum_i \left(\hat{L}_i^\dagger \hat{L}_i \hat{\rho} + \hat{\rho}\hat{L}_i^\dagger \hat{L}_i - 2\hat{L}_i \hat{\rho}\hat{L}_i^\dagger\right) \tag{D.1}$$

Where

- $\hat{\rho}$ is the density matrix of the system under consideration
- $\hat{H}_{dd}$ is the dipolar interaction Hamiltonian, for two particles it is written:

$$\begin{aligned}\hat{H}_{dd,12} &= \hat{H}_{Ising,12} + \hat{H}_{exchange,12} \\ &= \frac{\mu_0(1-3\cos\theta^2_{\vec{B},\vec{12}})}{4\pi r_{12}^3}(g_s\mu_B)^2\left(\hat{S}_{1z}\hat{S}_{2z} - \frac{1}{4}(\hat{S}_{1+}\hat{S}_{2-} + \hat{S}_{1-}\hat{S}_{2+})\right) \\ &= \chi\frac{1-3\cos\theta^2_{\vec{B},\vec{12}}}{\left(\frac{r_{12}}{a}\right)^3}\left(\hat{S}_{1z}\hat{S}_{2z} - \frac{1}{4}(\hat{S}_{1+}\hat{S}_{2-} + \hat{S}_{1-}\hat{S}_{2+})\right)\end{aligned} \tag{D.2}$$

- The i index runs over doubly occupied sites
- The $\hat{S}_i$ operators are dimensionless spin operators

- $\hat{L}_i$ describes two body inelastic collisions leading to the loss of the doublonic particle in site i at rate γ, by coupling to any of the unbound states of the continuum. These operators will be called Lindblad or jump operators.

The derivation of this equation is based on a series of assumptions (see [84]) notably the assumption that the environment is Markovian, that is that the time during which internal correlations exist within the environment is much smaller than the system-environment interaction time scales.

D.2.2 Wavefunction evolution protocol

Preliminary definitions

Consider the lattice model represented in D.1, we associate number operators $\hat{n}_i$ to each site and devise annihilation and creation operators $\hat{a}_i$, $\hat{a}_i^{\dagger}$[1] such as:

$$\begin{aligned}\hat{a}_i \left|n_1, ..., n_i, ...n_k\right\rangle &= \sqrt{n_i}\left|n_1 ..., n_i - 1, ...n_k\right\rangle \\ \hat{a}_i^{\dagger} \left|n_1, ..., n_i ..., n_k\right\rangle &= \sqrt{n_i + 1}\left|n_1, ..., n_i + 1, ..., n_k\right\rangle\end{aligned} \tag{D.3}$$

In this framework, the loss operators $\hat{L}_i$ are given by

$$\hat{L}_i = \sqrt{\gamma}\hat{a}_i^2 \tag{D.4}$$

Since these can only be applied to doubly occupied sites, we have:

$$\hat{L}_i^{\dagger}\hat{L}_i \left|\Psi\right\rangle = 2\gamma\left|\Psi\right\rangle \tag{D.5}$$

Finally, we define the *jump total probability* [2]

$$\delta p = \sum_i \delta p_i \tag{D.6}$$

where:

- $\delta p_i = \left\langle\Psi(t)\right|\hat{L}_i^{\dagger}\hat{L}_i\left|\Psi(t)\right\rangle\delta t$ relates to the probability of loosing doublon i within[3] δt

Evolution of a single wavefunction Ψ

The evolution of the single wavefunction Ψ is in fact divided in a series of discrete time steps, in each step we consider a randomly generated number $\epsilon \in [0,1]$ such that if :

- $\epsilon > \delta p$, the state $\left|\Psi(t)\right\rangle$ evolves continuously with the effective Hamiltonian

$$\hat{H}_{\text{eff}} = \hat{H}_{dd} - \frac{i\hbar}{2}\sum_i \hat{L}_i^{\dagger}\hat{L}_i \tag{D.7}$$

---

[1] In the actual algorithm, this approach is generalized to all spin states accessible to the atoms

[2] Numerically speaking, δp is calibrated so that all doublons be lost in 20 ms **on average**, therefore mimicking experimental observations. Actually for the results presented below, the average loss time for the first doublon is 2 ms, the second one is 5.6 ms, the third one is 11.7 ms, the last one is 20.11 ms

[3] δt which represents the time step of the simulations must be chosen so that $\delta p \ll 1$ for each time step

- $\epsilon \leq \delta p$, the state performs a so-called *jump* across the $\hat{L}_i$ channel. The probability of this channel being chosen is $P_i = \frac{\delta p_i}{\delta p}$, in this case we have

$$|\Psi(t+\delta t)\rangle = \frac{\hat{L}_i|\Psi(t)\rangle}{\sqrt{\delta p_i/\delta t}} \tag{D.8}$$

The first alternative leads to

$$|\Psi(t+\delta t)\rangle = \frac{1}{\sqrt{1-\delta p}}\left(1-\frac{i}{\hbar}\hat{H}_{\text{eff}}\delta t\right)|\Psi(t)\rangle \tag{D.9}$$

Developing $|\Psi(t)\rangle$ in the orthogonal basis of pure Zeeman states $|\alpha\rangle$[4] we get

$$|\Psi(t)\rangle = \sum_\alpha \alpha(t)|\alpha\rangle \tag{D.10}$$

And D.9 becomes

$$\begin{aligned}\sum_\alpha \alpha(t+dt)|\alpha\rangle &= \frac{1}{\sqrt{1-\delta p}}\left(1-\frac{i}{\hbar}\left(\sum_{\beta,\beta'} h_d^{\beta,\beta'}|\beta\rangle\langle\beta'| - \frac{i\hbar}{2}\sum_i 2\gamma\sum_\beta|\beta\rangle\langle\beta|\right)\delta t\right)\sum_\alpha \alpha(t)|\alpha\rangle \\ &= \frac{1}{\sqrt{1-\delta p}}\left(\sum_\alpha \alpha(t)|\alpha\rangle - \frac{i}{\hbar}\left(\sum_{\beta,\alpha}\alpha(t)h_d^{\beta,\alpha}|\beta\rangle - \frac{i\hbar}{2}\sum_i 2\gamma\alpha(t)\sum_\alpha|\alpha\rangle\right)\delta t\right)\end{aligned} \tag{D.11}$$

Projecting on $|\alpha\rangle$

$$\begin{aligned}\alpha(t+dt) &= \frac{1}{\sqrt{1-\delta p}}\left(\alpha(t)-\frac{i}{\hbar}\left(\sum_{\alpha'}\alpha'(t)h_d^{\alpha,\alpha'} - \frac{i\hbar}{2}\sum_i 2\gamma\alpha(t)\right)\delta t\right) \\ &= \frac{1}{\sqrt{1-\delta p}}\left(\alpha(t)\left(1-\sum_i \gamma\delta t\right) - \frac{i}{\hbar}\sum_{\alpha'}\alpha'(t)h_d^{\alpha,\alpha'}\delta t\right)\end{aligned} \tag{D.12}$$

Equation D.12: Weight evolution equation

which can be rewritten $\left(\text{with } \tilde{h}_d^{\alpha,\alpha'} \equiv \frac{h_d^{\alpha,\alpha'}}{\chi} \text{ and } \delta T = \frac{\chi}{\hbar}\delta t = 17.73\delta t \leftrightarrow \delta t = 0.0564\delta T\right)$

$$\begin{aligned}\alpha(t+dt) &= \frac{1}{\sqrt{1-\delta p}}\left(\alpha(t)\left(1-\sum_i \gamma\delta t\right) - \frac{i\chi}{\hbar}\sum_{\alpha'}\alpha'(t)\tilde{h}_d^{\alpha,\alpha'}\delta t\right) \\ &= \frac{1}{\sqrt{1-\delta p}}\left(\alpha(t)\left(1-\sum_i \frac{\gamma\hbar}{\chi}\delta T\right) - i\sum_{\alpha'}\alpha'(t)\tilde{h}_d^{\alpha,\alpha'}\delta T\right)\end{aligned} \tag{D.13}$$

---

[4] Pure Zeeman states are states where each no atom have well defined spin momenta numbers, for two chromium atoms $|m_s=-3, m_s=2\rangle$ is a pure Zeeman state whereas $|m_s=-3, m_s=2\rangle + |m_s=3, m_s=1\rangle$ is not.

constant	value	unit
$\hbar$	1.055×10^{-34}	J.s
g_s	2.002	
μ_B	9.274×10^{-24}	$\mathrm{J.T}^{-1}$
μ_0	$4\pi \times 10^{-7}$	$\mathrm{T.m.A}^{-1}$
a	264×10^{-9}	m
$\chi = \frac{\mu_0}{4\pi}\frac{(g_s\mu_b)^2}{a^3}$	1.86975×10^{-33}	J
$\frac{\chi}{\hbar} = \frac{\mu_0}{4\pi}\frac{(g_s\mu_b)^2}{\hbar a^3}$	17.73	s^{-1}
γ	20	s^{-1}

TABLE D.1: Some constants, some values and some units

On the weight evolution equation

1. Eq. D.12 can be interpreted as such : the weight of the node/state α in Eq. D.10 at time $t+dt$ depends on its weight at time t and the weights/couplings of the adjacent states, that is those pure Zeeman states which can be reached through a single two-particle exchange interaction ($h_d^{\alpha,\alpha'} \neq 0$). This is very reminiscent of the way heat diffuses in a graph, the main difference being that the Hamiltonian couplings are complex (eigenstate evolve with an oscillating phase instead of decaying to 0 when $t \to \infty$). The algorithm used to compute the evolution of single wavefunctions is based on this graph-like vision of the dipolar evolution.

2. **The $\frac{1}{\sqrt{1-\delta p}}$ prefactor** ensures the normalization of the wavefunction, keeping in mind that the effective Hamiltonian $\hat{H}_{\text{eff}}$ is non unitary

3. **The mere eventuality of a dissipative phenomenon can impact the system**, indeed, as can be seen in Eq.. D.12, The γ factor contributes to the weight evolution equation even when losses do not in fact occur. This effect which has been observed experimentally is illustrated in sec. D.3.1

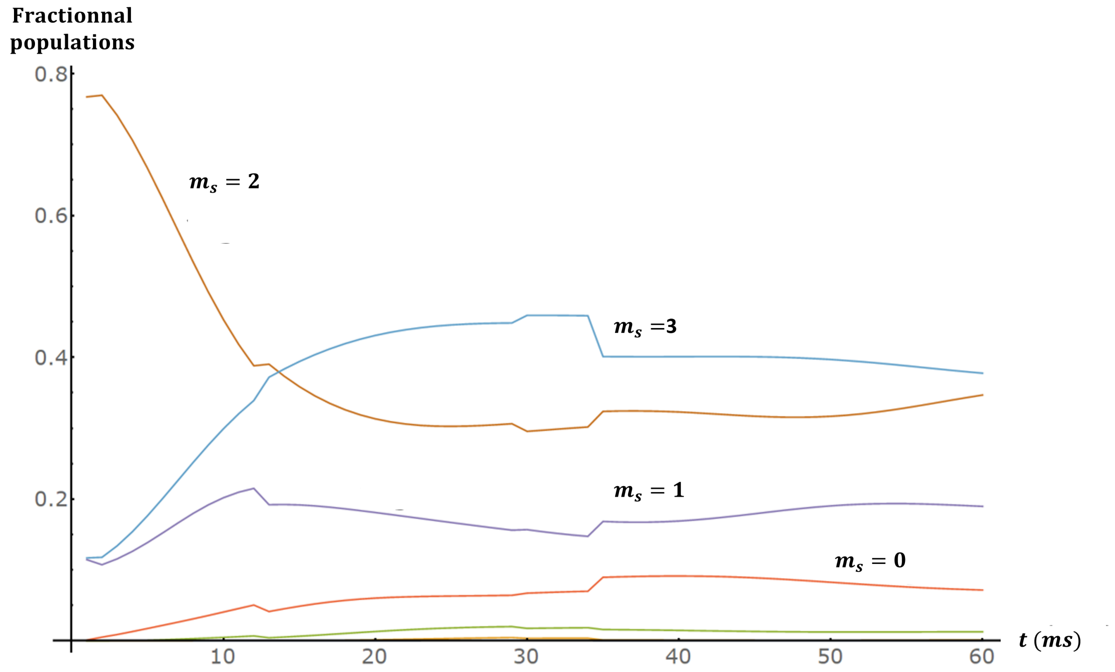

FIGURE D.2: Normalized spin populations time evolution for a single quantum trajectory, the small bumps correspond to loss events.

Evolution of the complete density matrix

The full density matrix at time t is obtained by averaging the above procedure up to time t on a sufficient number of trials N_t.

$$\hat{\rho}(t) \simeq \frac{1}{N_t}\sum_{k}^{N_t} |\Psi_k(t))\rangle \langle\Psi_k(t)| \xrightarrow[N_t\to\infty]{} \hat{\rho}(t) \tag{D.14}$$

The main advantage of this method proceeds from the fact that, in practice, convergence of the observables of interest is obtained for N_t (see D.2.4), therefore $N_t D$ which is the number of necessary runs is greatly inferior to $D^2 \simeq (12\times 10^6)^2$, that is, the cost of evolving the whole density matrix ρ.

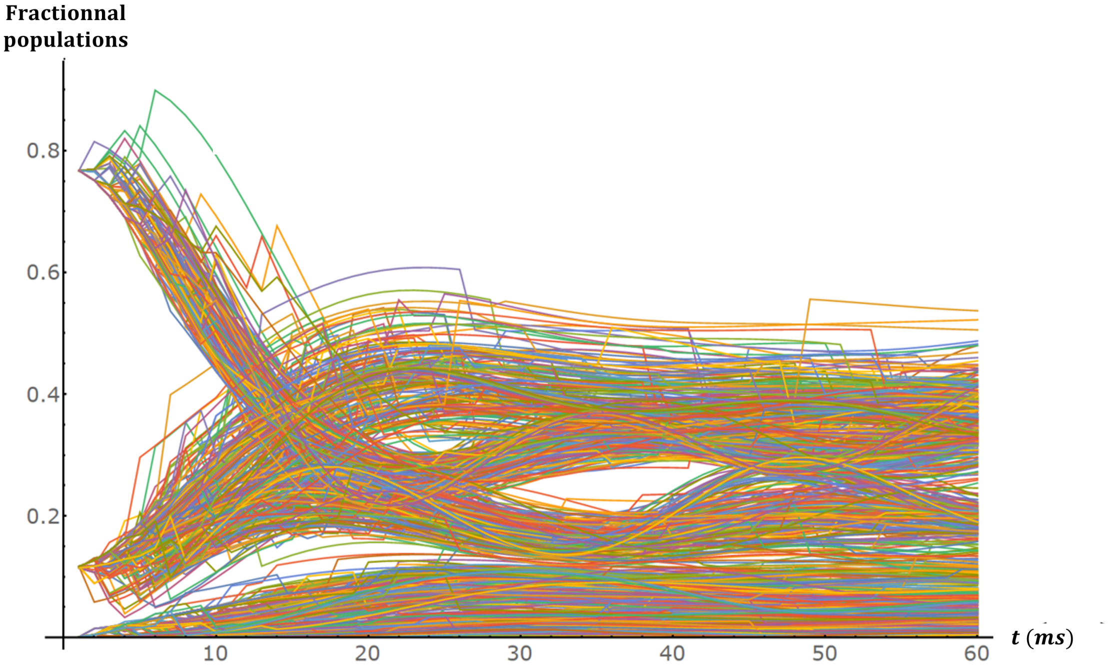

Figure D.3: Many trajectories must be computed for the convergence of the statistical averaging

Computation of observables' quantum expectation values

All other observables are computed in the same way, that is statistical averaging :

$$\langle \hat{A}(t) \rangle \simeq \frac{1}{N_t} \sum_{k}^{N_t} \langle \Psi_k(t) | \hat{A} | \Psi_k(t) \rangle \tag{D.15}$$

Algorithmic scheme

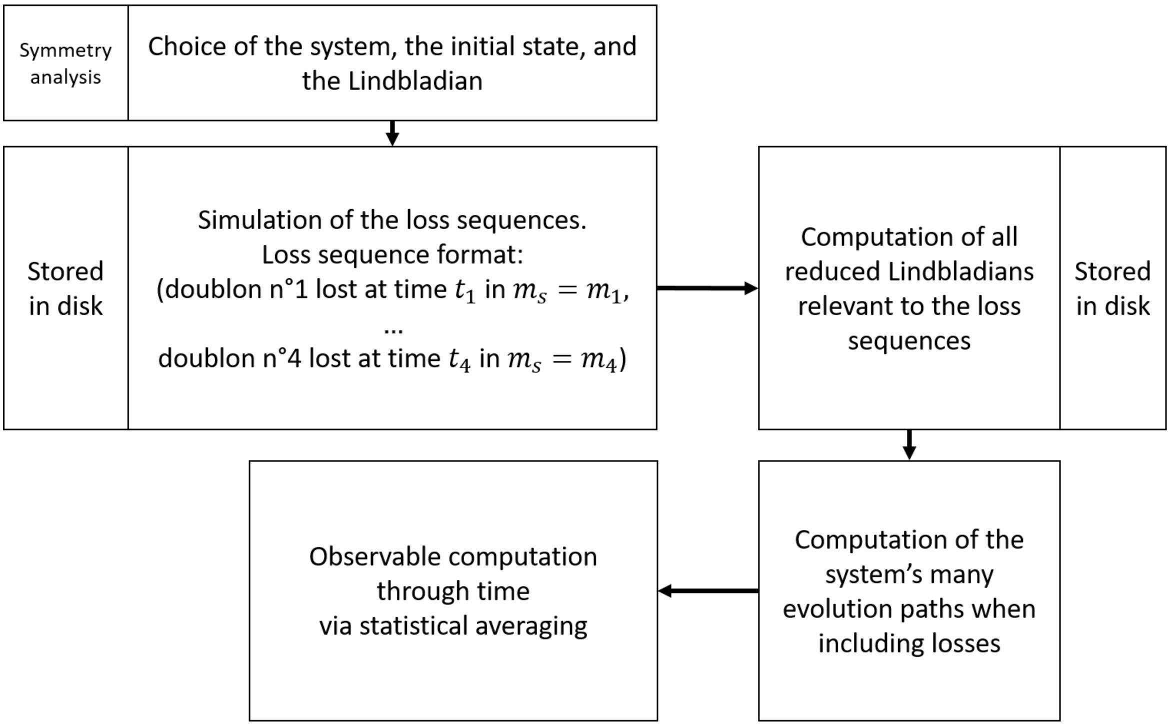

FIGURE D.4: The algorithmic scheme: The system is the one represented in D.1, the initial state is symmetric: this is important for the dimensional reduction process, as in this case geometrically symmetric nodes are equivalent, that is, they share the same weight history. The loss sequences are then computed according to the loss rates found in [62] (p.86) and making intensive use of the symmetries found in the previous step. Next, all relevant Lindbladians are computed, these of course have varying dimensions depending on the number of particles, and the magnetization at time t. Using these Lindbladians, we compute ~ 175 trajectories thanks to which we compute expectation values of all interesting observables through time see Eq. D.15

D.2.3 On the use of symmetries

The dimension of the chosen Hilbert space specific to the initial state described in Sec. D.1 is $D \simeq 12 \times 10^6$. In practice however, we make use of the system's symmetries to work on relatively smaller spaces ($\approx 3 \times 10^6$). These aspects are summarized in the figures below.

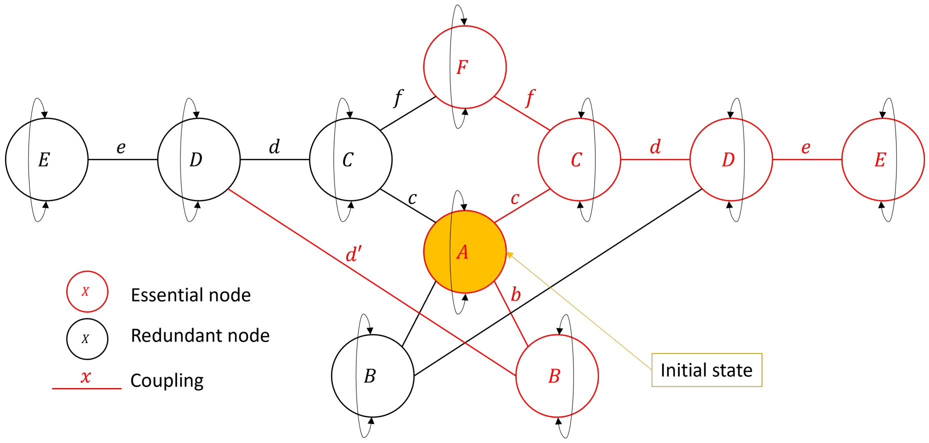

FIGURE D.5: The algorithm used to compute the wavefunction evolution uses graph-like structures. Above is a schematic view of such structures. The graph's nodes are pure Zeeman states (i.e. states wherein each atom has a well defined spin projection along the quantization axis). Depending on the system's and the initial state's symmetries some of these states become in fact equivalent, put otherwise they share the same weight history throughout the evolution. Instead of computing the weights of all nodes at time t, it is therefore enough to compute the weight associated to the equivalence class to which they belong. Doing so efficiently requires the use of a more condensed graph shown below.

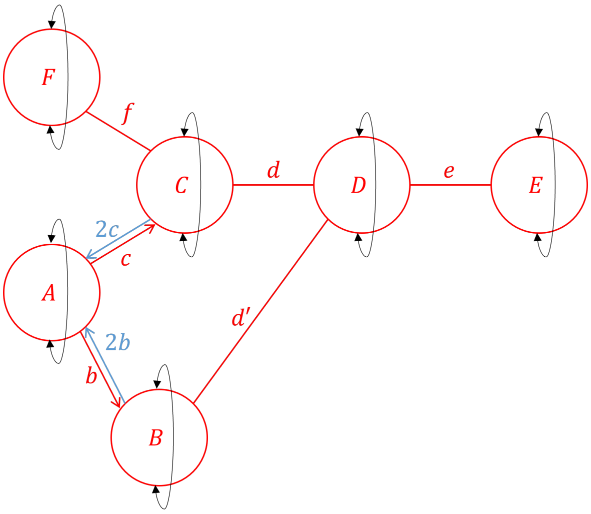

Figure D.6: It is computationally inefficient to even consider redundant nodes as is done when using symmetric matrices for calculations. It is better to (almost) forget about them altogether. This however requires the careful reexamination of the graph's *couplings* or *edges*. Above is the *essential graph* corresponding to the one shown in D.5, note that the graph is now *directed* which correspond to a *non hermitian Hamiltonian*, this trick which **makes for computationally more efficient algorithms** is based on the understanding of the node weight evolution equation: for example, when considering the graph of Fig. D.5, we see that the weight of node A at time $t+dt$ will be updated by considering the weight of two C nodes (the essential one and the redundant one), in the second graph, it is updated by considering the weight of one single node C but with twice the coupling which is better in terms of computational speed and memory usage. The forgotten nodes are summoned back to life once the computations are done with, to recover the exact properties of the system.

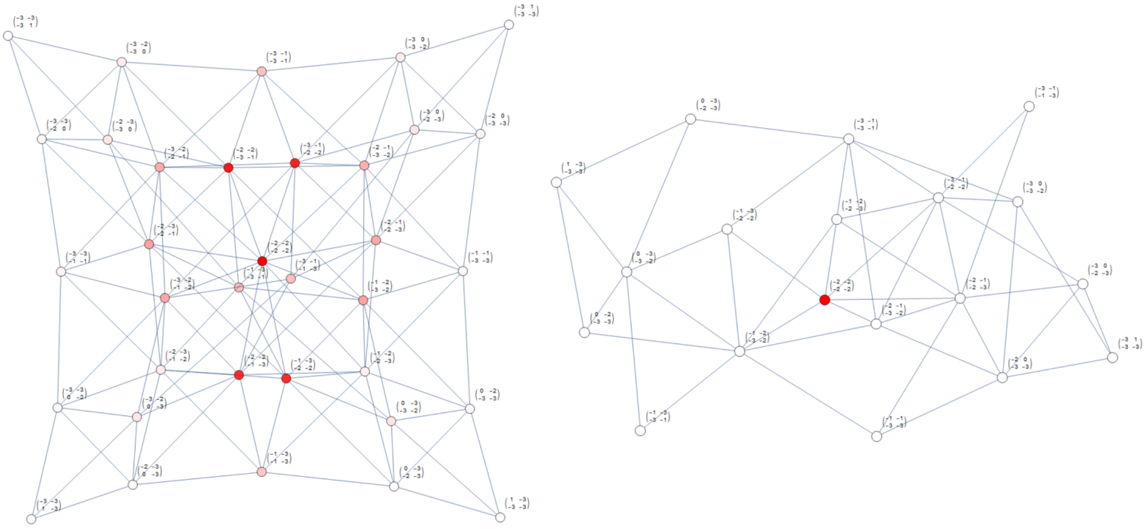

Figure D.7: Left: The full graph of a 2×2 square lattice with 4 singlons initialized in the $m_s = 2$ state. This graph contains 35 states, by considering appropriate symmetries, it can be condensed into a more efficient graph containing 19 states. The color gradient on the left hand graph represents the diffusion of the initially point like weight distribution in the graph: as time passes, more states are populated, the system explores the totality of the accessible magnetization manifold.

D.2.4 Benchmark

To test the reliability of the algorithm we compute the evolution of populations when all doublons are dropped (the system is then constituted of two isolated two by two square lattices filled with singlons). We then compare this simulation with the results of straightforward diagonalization of an equivalent singlon filled two by two square lattice. As shown below the results are in perfect agreement.

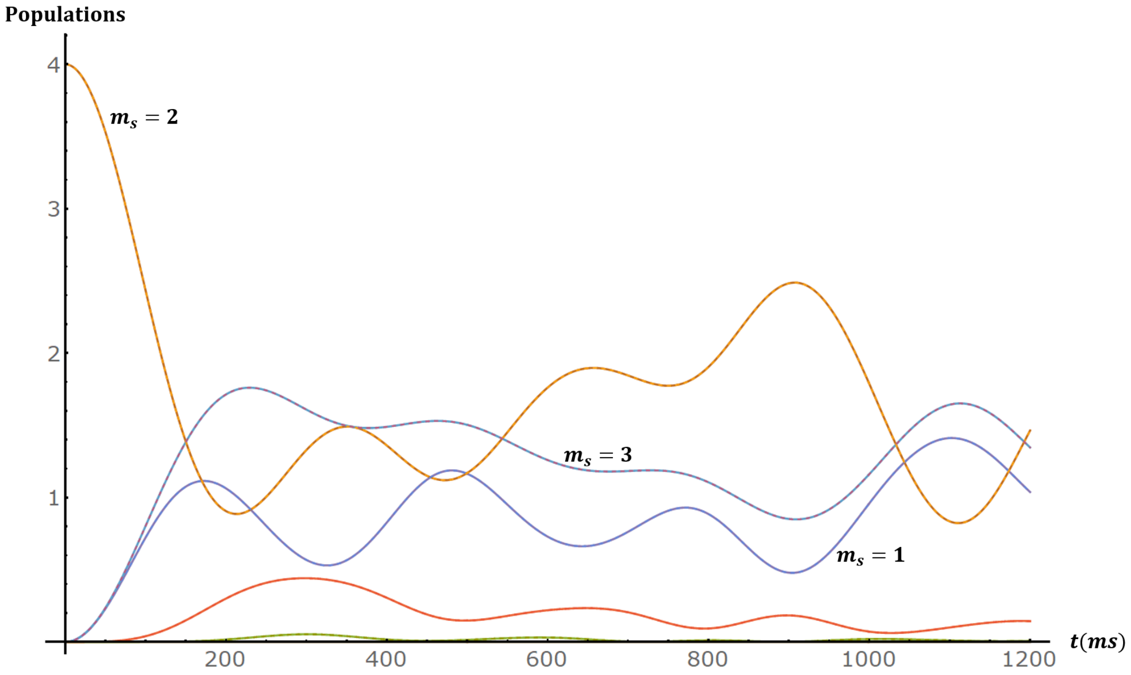

FIGURE D.8: Comparison between the normalized spin populations' evolution predicted by straight diagonalization of a 2×2 square lattice (dashed lines) with the results of the algorithm when all doublons are dropped (thick lines). The dashed lines are hardly visible as they are hidden in the thick ones: results are in perfect agreement.

We've also checked the convergence of some observables as a function of N_t, for populations the results are shown below.

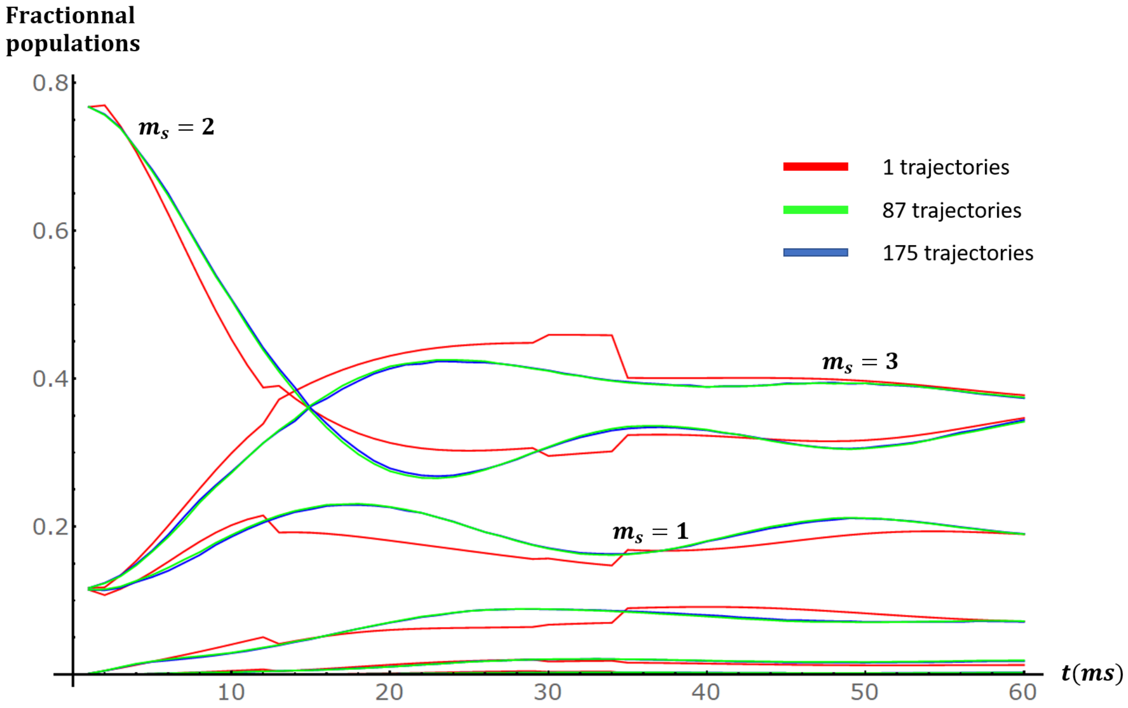

Figure D.9: As the number of trajectories increases, the difference between statistical averages of normalized populations becomes negligible.

D.3 Results

D.3.1 Impact of losses' eventuality

As mentioned in the paragraph D.2.2, the mere eventuality of dissipative phenomena alters the system's state

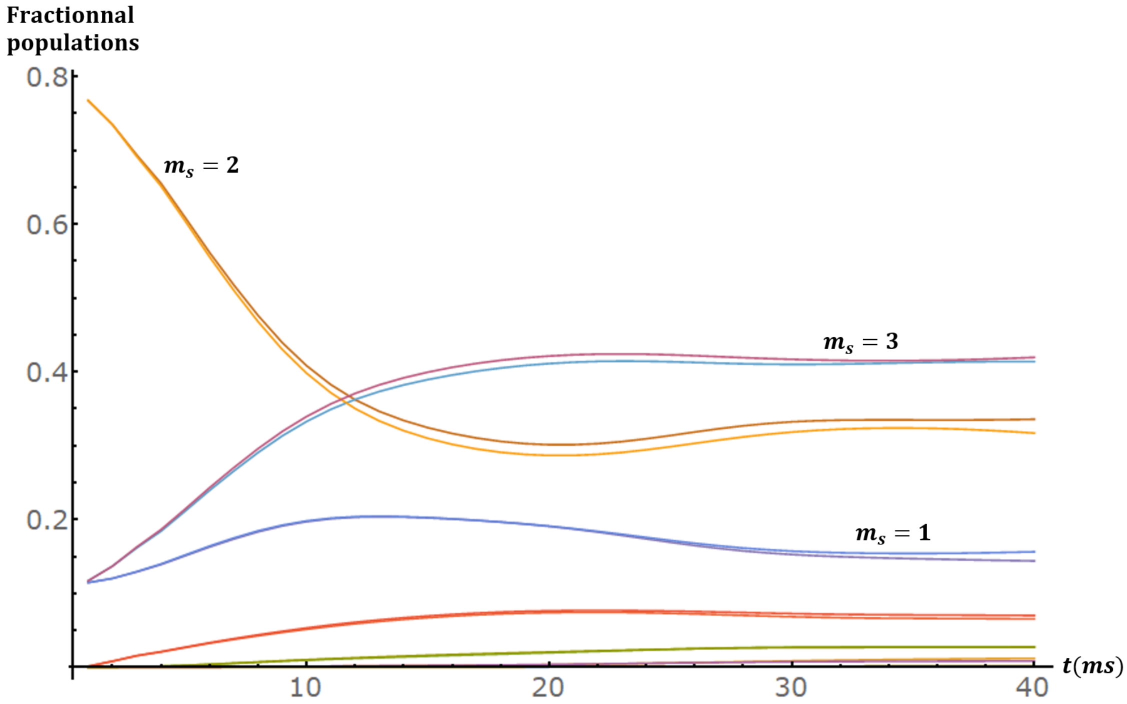

Figure D.10: Effect of losses' eventuality on normalized populations. The two sets of curves correspond to the normalized populations with and without the possibility of doublonic losses. The two sets of curves are different even when no losses actually happen. This effect is induced in our simulations by the γ factor in equation D.13. Intuitively, one can understand this effect by saying that the absence of particles leaving the lattice gives us some degree of information on the system that is considered, which in turn can affect its evolution.

D.3.2 Impact of losses

On populations' evolution

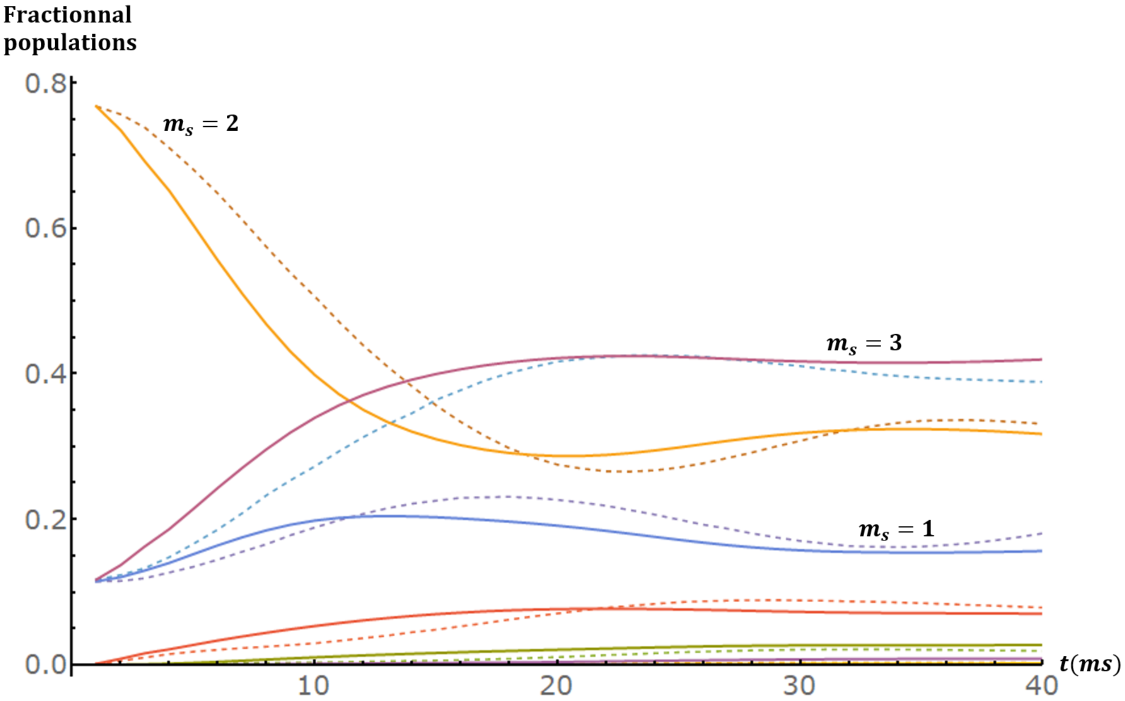

Figure D.11: Dashed: Evolution of populations when losses are taken into account. Thick: Evolution of populations when losses are not permitted

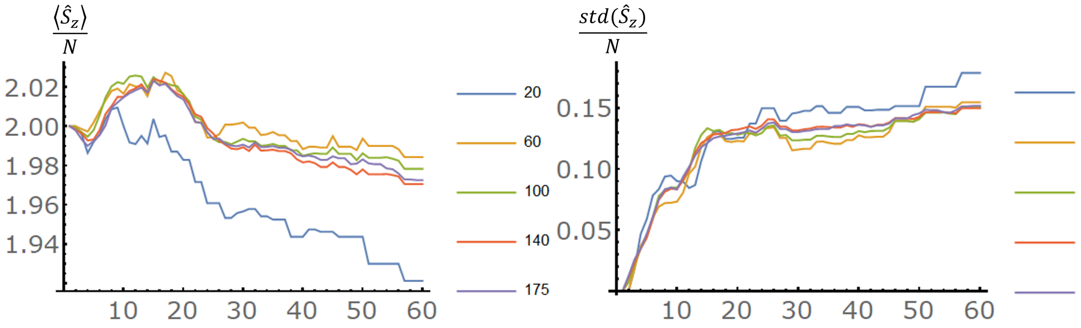

Figure D.12: Left: Evolution of the normalized magnetization quantum expectation value through time for 20,60,100,140 and 175 trajectories. Right: Evolution of the normalized magnetization standard deviation value through time for 20,60,100,140 and 175 trajectories

Since the variance of the magnetization for the chosen initial state is 0, we can compare the above shown dissipative contribution to the variance of the magnetization of the uncorrelated state state whose average populations are those of the correlated one. This comparison is made in the Fig. D.13

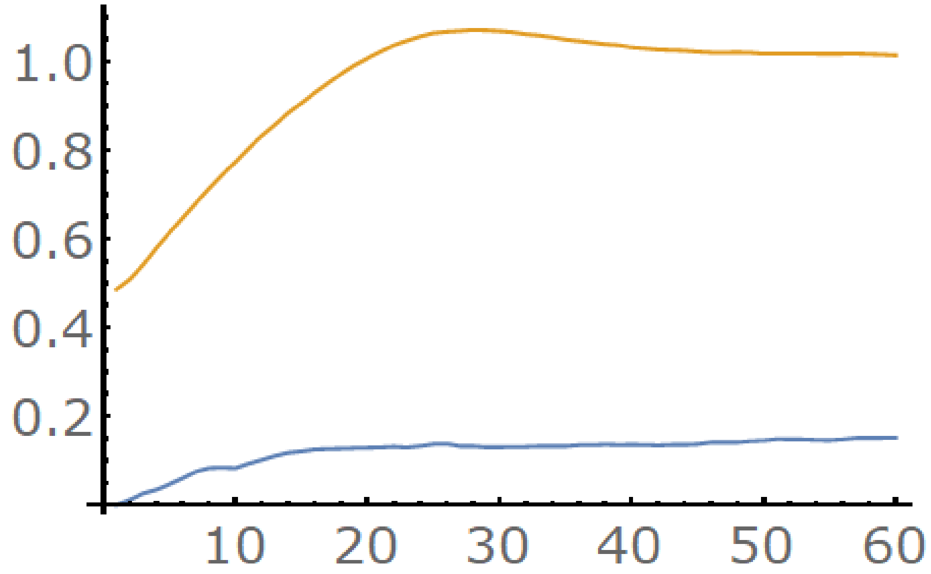

Figure D.13: Yellow: Evolution of the magnetization's standard deviation uncorrelated state whose average populations are those of the correlated one (i.e. the one computed using the algorithm). Blue: Evolution of the normalized magnetization standard deviation value through time for 175 trajectories. The effects of the losses remain small compared to the magnetization standard deviation of the uncorrelated state which can be thought of as the standard quantum noise in this case.

Conclusion: on the C_z correlator

From results of the previous sections we see that, at long times, the fractional populations are not heavily affected by losses. The variance of the magnetization on the other hand increases when losses are taken into account, as could have been expected considering the loss induced variability of the post dynamic end state, this increase however remains **small when compared to the standard deviations that can be expected from completely uncorrelated states** and is anyway **small compared to the precision of the experiment**. In general, we can expect the same type of effects for the actual system, keeping in mind that the spatial segregation of doublons and singlons in the real system might further mitigate the increase of the magnetization's variance since in this case one can argue that singlons are *less* affected by the departure of doublons from the lattice. **As far as the $C_z = \mathbf{Var}\left(\hat{S}_z\right) + N\left(\sum_m m a_m\right)^2 - N\sum_m m^2 a_m$ correlator is concerned (see Chap. 3), its time evolution should not be much affected by the loss of doublons, and in any case the effects of these losses should remain small compared to the standard quantum noise.**

Bibliography

[1] Lauriane Chomaz et al. “Dipolar physics: a review of experiments with magnetic quantum gases”. In: *Reports on Progress in Physics* 86.2 (2022), p. 026401. DOI: `10.1088/1361-6633/aca814`. URL: `https://dx.doi.org/10.1088/1361-6633/aca814`.

[2] G. Kucsko et al. “Critical Thermalization of a Disordered Dipolar Spin System in Diamond”. In: *Phys. Rev. Lett.* 121 (2 2018), p. 023601. DOI: `10.1103/PhysRevLett.121.023601`. URL: `https://link.aps.org/doi/10.1103/PhysRevLett.121.023601`.

[3] Antoine Browaeys and Thierry Lahaye. “Many-body physics with individually controlled Rydberg atoms”. In: *Nature Physics* 16.2 (2020), pp. 132–142. DOI: `10.1038/s41567-019-0733-z`. URL: `https://doi.org/10.1038%2Fs41567-019-0733-z`.

[4] Steven A. Moses et al. “New frontiers for quantum gases of polar molecules”. In: *Nature Physics* 13.1 (2016), pp. 13–20. DOI: `10.1038/nphys3985`. URL: `https://doi.org/10.1038%2Fnphys3985`.

[5] T Lahaye et al. “The physics of dipolar bosonic quantum gases”. In: *Reports on Progress in Physics* 72.12 (2009), p. 126401. DOI: `10.1088/0034-4885/72/12/126401`. URL: `https://doi.org/10.1088/0034-4885/72/12/126401`.

[6] T. Cantat-Moltrecht et al. “Long-lived circular Rydberg states of laser-cooled rubidium atoms in a cryostat”. In: *Physical Review Research* 2.2 (2020). DOI: `10.1103/physrevresearch.2.022032`. URL: `https://doi.org/10.1103%2Fphysrevresearch.2.022032`.

[7] Thomas Hartke et al. “Quantum register of fermion pairs”. In: *Nature* 601.7894 (2022), pp. 537–541. DOI: `10.1038/s41586-021-04205-8`. URL: `https://doi.org/10.1038%2Fs41586-021-04205-8`.

[8] Kaden R. A. Hazzard et al. “Quantum correlations and entanglement in far-from-equilibrium spin systems”. In: *Physical Review A* 90.6 (2014). ISSN: 1094-1622. DOI: `10.1103/physreva.90.063622`. URL: `http://dx.doi.org/10.1103/PhysRevA.90.063622`.

[9] Axel Griesmaier et al. “Bose-Einstein Condensation of Chromium”. en. In: *Phys. Rev. Lett.* 94.16 (Apr. 2005), p. 160401. ISSN: 0031-9007, 1079-7114. DOI: `10.1103/PhysRevLett.94.160401`. arXiv: `cond-mat/0503044`.

[10] J.Dalibard. *DEA Atomes froids, notes de cours*. URL: `http://www.phys.ens.fr/~dalibard/Notes_de_cours/DEA_atomes_froids_actuel.pdf`.

[11] K. Huang. *Statistical mechanics*. en. wiley, 1987.

[12] Lucas Gabardos. “Dynamique hors équilibre de spins couplés par interaction dipolaire en condensat de Bose-Einstein et en réseau optique”. PhD thesis. Université Paris 13, 2020.

[13] B. Pasquiou et al. “Control of dipolar relaxation in external fields”. In: *Physical Review A* 81.4 (2010). ISSN: 1094-1622. DOI: `10.1103/physreva.81.042716`. URL: `http://dx.doi.org/10.1103/PhysRevA.81.042716`.

[14] A. Patscheider et al. “Controlling dipolar exchange interactions in a dense three-dimensional array of large-spin fermions”. In: *Phys. Rev. Res.* 2 (2 2020), p. 023050. DOI: 10.1103/PhysRevResearch.2.023050. URL: https://link.aps.org/doi/10.1103/PhysRevResearch.2.023050.

[15] S. Lepoutre et al. “Out-of-equilibrium quantum magnetism and thermalization in a spin-3 many-body dipolar lattice system”. In: *Nature Communications* 10.1 (2019). ISSN: 2041-1723. DOI: 10.1038/s41467-019-09699-5. URL: http://dx.doi.org/10.1038/s41467-019-09699-5.

[16] A. de Paz et al. “Nonequilibrium Quantum Magnetism in a Dipolar Lattice Gas”. In: *Physical Review Letters* 111.18 (2013). DOI: 10.1103/physrevlett.111.185305. URL: https://doi.org/10.1103%2Fphysrevlett.111.185305.

[17] *ETH.* https://en.wikipedia.org/wiki/Eigenstate_thermalization_hypothesis.

[18] James Robert Garrison. “Thermalization and its breakdown in isolated quantum systems”. University of Santa Barbara. PhD thesis. 2016.

[19] Rahul Nandkishore and David A. Huse. “Many-Body Localization and Thermalization in Quantum Statistical Mechanics”. In: *Annual Review of Condensed Matter Physics* 6.1 (2015), pp. 15–38. DOI: 10.1146/annurev-conmatphys-031214-014726. URL: https://doi.org/10.1146%2Fannurev-conmatphys-031214-014726.

[20] Michael Redhead. “Models in Physics”. In: *British Journal for the Philosophy of Science* 31 (), pp. 145–163. DOI: 10.1093/bjps/31.2.145.

[21] F. A. Muller and Gijs Leegwater. “The Case Against Factorism: On the Labels of ⊗ -Factor Hilbert-Spaces of Similar Particles in Quantum Mechanics”. In: *Journal for General Philosophy of Science / Zeitschrift für Allgemeine Wissenschaftstheorie* (forthcoming), pp. 1–16. DOI: 10.1007/s10838-020-09514-6.

[22] James A C Ladyman, Oystein Linnebo, and Tomasz F Bigaj. “Entanglement and non-factorizability”. English. In: *Studies In History and Philosophy of Science Part B: Studies In History and Philosophy of Modern Physics* 44.3 (Aug. 2013). ISSN: 1355-2198.

[23] Sebastian Fortin and Olimpia Lombardi. “Entanglement and Indistinguishability in a Quantum Ontology of Properties”. In: *Studies in History and Philosophy of Science Part A* 91 (2022), pp. 234–243. DOI: 10.1016/j.shpsa.2021.11.017.

[24] GianCarlo Ghirardi and Luca Marinatto. “General criterion for the entanglement of two indistinguishable particles”. In: *Phys. Rev. A* 70 (1 2004), p. 012109. DOI: 10.1103/PhysRevA.70.012109. URL: https://link.aps.org/doi/10.1103/PhysRevA.70.012109.

[25] Nan Li and Shunlong Luo. “Classical states versus separable states”. In: *Phys. Rev. A* 78 (2 2008), p. 024303. DOI: 10.1103/PhysRevA.78.024303. URL: https://link.aps.org/doi/10.1103/PhysRevA.78.024303.

[26] Irenee Frérot. “Corrélations quantiques : une approche de physique statistique”. Thèse de doctorat dirigée par Roscilde, Tommaso Physique Lyon 2017. PhD thesis. 2017. URL: http://www.theses.fr/2017LYSEN061.

[27] Harold Ollivier and Wojciech H. Zurek. “Quantum Discord: A Measure of the Quantumness of Correlations”. In: *Physical Review Letters* 88.1 (2001). DOI: 10.1103/physrevlett.88.017901. URL: https://doi.org/10.1103%2Fphysrevlett.88.017901.

[28] Jian-Song Zhang and Ai-Xi Chen. “Review of quantum discord in bipartite and multipartite systems”. In: (2012).

[29] Giuseppe Vitagliano et al. “Spin Squeezing Inequalities for Arbitrary Spin”. In: *Phys. Rev. Lett.* 107 (24 2011), p. 240502. DOI: `10.1103/PhysRevLett.107.240502`. URL: `https://link.aps.org/doi/10.1103/PhysRevLett.107.240502`.

[30] *Private communication, Spin dynamics in lattice: quest for entanglement witnesses, Note by Laurent Vernac.*

[31] F. T. Arecchi et al. “Atomic Coherent States in Quantum Optics”. In: *Phys. Rev. A* 6 (6 1972), pp. 2211–2237. DOI: `10.1103/PhysRevA.6.2211`. URL: `https://link.aps.org/doi/10.1103/PhysRevA.6.2211`.

[32] Masahiro Kitagawa and Masahito Ueda. “Squeezed spin states”. In: *Phys. Rev. A* 47 (6 1993), pp. 5138–5143. DOI: `10.1103/PhysRevA.47.5138`. URL: `https://link.aps.org/doi/10.1103/PhysRevA.47.5138`.

[33] Giuseppe Vitagliano et al. “Spin squeezing and entanglement for an arbitrary spin”. In: *Physical Review A* 89.3 (2014). DOI: `10.1103/physreva.89.032307`. URL: `https://doi.org/10.1103%2Fphysreva.89.032307`.

[34] *Private communication, simulations performed by Bihui Zhu.*

[35] *Private communication with Irénée Frérot on the quantum covariance.*

[36] *Local hidden-variable theory.* [Online; accessed 4-July-2022]. 2022. URL: `https://en.wikipedia.org/w/index.php?title=Local_hidden-variable_theory&oldid=1084297805`.

[37] Quentin Beaufils. “Condensation de Bose Einstein du chrome”. PhD thesis. Université Paris 13, 2009.

[38] Radu Chicireanu. “Studies of cold chromium atoms in magnetic and optical traps: Steps towards Bose Einstein condensation”. PhD thesis. Université Paris 13, 2007.

[39] Aurélie De Paz. “Échange de spin et dynamique d’aimantation d’un gaz quantique dipolaire”. PhD thesis. Université Paris 13, 2015.

[40] Arnaud Pouderous. “Refroidissement et Piégeage d’atomes de Chrome”. PhD thesis. Université Paris 13, 2007.

[41] Jürgen Stuhler. “Kontinuierliches Laden einer Magnetfalle mit lasergekühlten Chromatomen”. PhD thesis. 2001.

[42] K. M. O’Hara et al. “Loading dynamics of CO_2 laser traps”. In: *Phys. Rev. A* 63 (4 2001), p. 043403. DOI: `10.1103/PhysRevA.63.043403`. URL: `https://link.aps.org/doi/10.1103/PhysRevA.63.043403`.

[43] Piet O Schmidt et al. “Continuous loading of cold atoms into a Ioffe–Pritchard magnetic trap”. In: *Journal of Optics B: Quantum and Semiclassical Optics* 5.2 (2003), S170. DOI: `10.1088/1464-4266/5/2/376`. URL: `https://dx.doi.org/10.1088/1464-4266/5/2/376`.

[44] G. Bismut et al. “Optimized loading of an optical dipole trap for the production of chromium BECs”. In: *Applied Physics B* 102.1 (2010), pp. 1–9. DOI: `10.1007/s00340-010-4171-y`. URL: `https://doi.org/10.1007%2Fs00340-010-4171-y`.

[45] Q. Beaufils et al. “All-optical production of chromium Bose-Einstein condensates”. In: *Phys. Rev. A* 77 (6 2008), p. 061601. DOI: `10.1103/PhysRevA.77.061601`. URL: `https://link.aps.org/doi/10.1103/PhysRevA.77.061601`.

[46] M. Fattori et al. “Demagnetization cooling of a gas”. In: *Nature Physics* 2.11 (2006), pp. 765–768. DOI: `10.1038/nphys443`. URL: `https://doi.org/10.1038%2Fnphys443`.

[47] Fabrice Gerbier. *Quantum Gases in Optical Lattices.* URL: http://www.lkb.upmc.fr/boseeinsteincondensates/wp-content/uploads/sites/10/2018/03/OL2018.pdf.

[48] A. de Paz et al. "Nonequilibrium Quantum Magnetism in a Dipolar Lattice Gas". In: *Phys. Rev. Lett.* 111 (18 2013), p. 185305. DOI: 10.1103/PhysRevLett.111.185305. URL: https://link.aps.org/doi/10.1103/PhysRevLett.111.185305.

[49] Petra Fersterer et al. "Dynamics of an itinerant spin-3 atomic dipolar gas in an optical lattice". In: *Physical Review A* 100.3 (2019). DOI: 10.1103/physreva.100.033609. URL: https://doi.org/10.1103%2Fphysreva.100.033609.

[50] Perrin Hélène. "Spins and fields". Les houches, Sept. 2013.

[51] Andrian Harsono. "Dipole trapping and manipulation of ultra-cold atoms". PhD thesis. University of Oxford, 2006.

[52] *Variance.* [Online; accessed 13-May-2022]. 2022. URL: https://en.wikipedia.org/w/index.php?title=Variance&oldid=1086943695.

[53] *Covariance.* https://en.wikipedia.org/w/index.php?title=Covariance&oldid=1080635706. [Online; accessed 13-May-2022]. 2022.

[54] *Conditional expectation.* [Online; accessed 13-May-2022]. 2022. URL: https://en.wikipedia.org/w/index.php?title=Conditional_expectation&oldid=1086432783.

[55] *Poisson distribution.* [Online; accessed 13-May-2022]. 2022. URL: https://en.wikipedia.org/w/index.php?title=Poisson_distribution&oldid=1087395759.

[56] *Mixture distribution — Wikipedia, The Free Encyclopedia.* [Online; accessed 25-June-2022]. 2022. URL: https://en.wikipedia.org/w/index.php?title=Mixture_distribution&oldid=1091582237.

[57] Robertsen A. Riehle and Henk F. Arnoldus. "Probability Densities for Fluorescent Photons Emitted by a Two-State Atom Driven by a Laser". en. In: *ISRN Optics* 2012 (Dec. 2012), pp. 1–6. ISSN: 2090-7826. DOI: 10.5402/2012/745871.

[58] R Bücker et al. "Single-particle-sensitive imaging of freely propagating ultracold atoms". In: *New Journal of Physics* 11.10 (2009), p. 103039. DOI: 10.1088/1367-2630/11/10/103039. URL: https://doi.org/10.1088/1367-2630/11/10/103039.

[59] A. G. Basden, C. A. Haniff, and C. D. Mackay. "Photon counting strategies with low-light-level CCDs". In: *Monthly Notices of the Royal Astronomical Society* 345.3 (Nov. 2003), pp. 985–991. ISSN: 0035-8711. DOI: 10.1046/j.1365-8711.2003.07020.x. eprint: https://academic.oup.com/mnras/article-pdf/345/3/985/2958818/345-3-985.pdf. URL: https://doi.org/10.1046/j.1365-8711.2003.07020.x.

[60] Michael Hirsch et al. "A Stochastic Model for Electron Multiplication Charge-Coupled Devices – From Theory to Practice". In: *PLOS ONE* 8.1 (Jan. 2013), pp. 1–13. DOI: 10.1371/journal.pone.0053671. URL: https://doi.org/10.1371/journal.pone.0053671.

[61] *Standard error.* https://www.real-statistics.com/distribution-fitting/distribution-fitting-confidence-intervals/fitted-parameters-standard-error/.

[62] Kaci KECHADI. "Analyse théorique des excitations et des instabilités des condensats de Bose-Einstein spinoriels dipolaires". Theses. Université Paris 13, Nov. 2019. URL: https://tel.archives-ouvertes.fr/tel-02386895.

[63] *Second Quantization.* http://eduardo.physics.illinois.edu/phys561/non_relativistic_final.pdf.

[64] Jean Dalibard. *Les interactions entre particules dans les gaz quantiques*. `https://www.college-de-france.fr/media/jean-dalibard/UPL543750239129031574_chap2..pdf`.

[65] B. Pasquiou et al. "Control of dipolar relaxation in external fields". In: *Phys. Rev. A* 81 (4 2010), p. 042716. DOI: `10.1103/PhysRevA.81.042716`. URL: `https://link.aps.org/doi/10.1103/PhysRevA.81.042716`.

[66] Youssef Aziz Alaoui et al. "Measuring Correlations from the Collective Spin Fluctuations of a Large Ensemble of Lattice-Trapped Dipolar Spin-3 Atoms". In: *Phys. Rev. Lett.* 129 (2 2022), p. 023401. DOI: `10.1103/PhysRevLett.129.023401`. URL: `https://link.aps.org/doi/10.1103/PhysRevLett.129.023401`.

[67] *Delta method*. `https://en.wikipedia.org/wiki/Delta_method`.

[68] *Stochastic drift — Wikipedia, The Free Encyclopedia*. [Online; accessed 19-May-2022]. 2020. URL: `https://en.wikipedia.org/w/index.php?title=Stochastic_drift&oldid=965832796`.

[69] *Chebyshev's sum inequality*. [Online; accessed 19-May-2022]. 2022. URL: `https://en.wikipedia.org/w/index.php?title=Chebyshev%27s_sum_inequality&oldid=1068380153`.

[70] Hubert Ammann and Nelson Christensen. "Delta Kick Cooling: A New Method for Cooling Atoms". In: *Phys. Rev. Lett.* 78 (11 1997), pp. 2088–2091. DOI: `10.1103/PhysRevLett.78.2088`. URL: `https://link.aps.org/doi/10.1103/PhysRevLett.78.2088`.

[71] *Private communication, Discussions on spin correlation length with Tommaso Roscilde.*

[72] Lucas Gabardos et al. "Relaxation of the Collective Magnetization of a Dense 3D Array of Interacting Dipolar $S = 3$ Atoms". In: *Phys. Rev. Lett.* 125 (14 2020), p. 143401. DOI: `10.1103/PhysRevLett.125.143401`. URL: `https://link.aps.org/doi/10.1103/PhysRevLett.125.143401`.

[73] Chingyun Cheng. "Ultracold Fermi Gases in a Bichromatic Optical Superlattice". Duke University. PhD thesis. 2016.

[74] K. Bencheikh and L.M. Nieto. "Exact results for nonequilibrium dynamics in Wigner phase space". In: *Physics Letters A* 384.25 (2020), p. 126599. DOI: `10.1016/j.physleta.2020.126599`. URL: `https://doi.org/10.1016%2Fj.physleta.2020.126599`.

[75] P. A. Murthy et al. "Matter-wave Fourier optics with a strongly interacting two-dimensional Fermi gas". In: *Physical Review A* 90.4 (2014). DOI: `10.1103/physreva.90.043611`. URL: `https://doi.org/10.1103%2Fphysreva.90.043611`.

[76] Adam M. Kaufman et al. "Quantum thermalization through entanglement in an isolated many-body system". In: *Science* 353.6301 (2016), pp. 794–800. DOI: `10.1126/science.aaf6725`. URL: `https://doi.org/10.1126%2Fscience.aaf6725`.

[77] A. Signoles et al. "Glassy Dynamics in a Disordered Heisenberg Quantum Spin System". In: *Phys. Rev. X* 11 (1 2021), p. 011011. DOI: `10.1103/PhysRevX.11.011011`. URL: `https://link.aps.org/doi/10.1103/PhysRevX.11.011011`.

[78] S. Lepoutre et al. "Spin mixing and protection of ferromagnetism in a spinor dipolar condensate". In: *Physical Review A* 97 (May 2017). DOI: `10.1103/PhysRevA.97.023610`.

[79] Taran Driver et al. “Two-Dimensional Partial-Covariance Mass Spectrometry of Large Molecules Based on Fragment Correlations”. In: *Phys. Rev. X* 10 (4 2020), p. 041004. DOI: `10.1103/PhysRevX.10.041004`. URL: `https://link.aps.org/doi/10.1103/PhysRevX.10.041004`.

[80] V. Zhaunerchyk et al. “Theory and simulations of covariance mapping in multiple dimensions for data analysis in high-event-rate experiments”. In: *Phys. Rev. A* 89 (5 2014), p. 053418. DOI: `10.1103/PhysRevA.89.053418`. URL: `https://link.aps.org/doi/10.1103/PhysRevA.89.053418`.

[81] Howard Carmichael. “An Open Systems Approach to Quantum Optics”. In: *Lecture Notes in Physics Monographs* 18 (Jan. 1993). DOI: `10.1007/978-3-540-47620-7`.

[82] R. Dum, P. Zoller, and H. Ritsch. “Monte Carlo simulation of the atomic master equation for spontaneous emission”. In: *Phys. Rev. A* 45 (7 1992), pp. 4879–4887. DOI: `10.1103/PhysRevA.45.4879`. URL: `https://link.aps.org/doi/10.1103/PhysRevA.45.4879`.

[83] Klaus Mølmer, Yvan Castin, and Jean Dalibard. “Monte Carlo wave-function method in quantum optics”. In: *J. Opt. Soc. Am. B* 10.3 (1993), pp. 524–538. DOI: `10.1364/JOSAB.10.000524`. URL: `http://josab.osa.org/abstract.cfm?URI=josab-10-3-524`.

[84] Andrew J. Daley. “Quantum trajectories and open many-body quantum systems”. In: *Advances in Physics* 63.2 (2014), 77–149. ISSN: 1460-6976. DOI: `10.1080/00018732.2014.933502`. URL: `http://dx.doi.org/10.1080/00018732.2014.933502`.

[85] G. Kordas et al. “The dissipative Bose-Hubbard model”. In: *The European Physical Journal Special Topics* 224.11 (2015), 2127–2171. ISSN: 1951-6401. DOI: `10.1140/epjst/e2015-02528-2`. URL: `http://dx.doi.org/10.1140/epjst/e2015-02528-2`.

Études des corrélations de spin dans un ensemble d'atomes dipolaires piégés dans un réseau optique

Dans ce manuscrit nous étudions le développement de corrélations de spin entre atomes de chrome piégés dans un réseau optique. Ce système se caractérise par le grand spin (S=3) des atomes utilisés ainsi que la grande portée et l'anisotropie des interactions interatomiques. Dans ce manuscrit sont décrites deux expériences dans lesquelles nous observons le développement de ces corrélations de spin. Ces deux expériences sont basées sur la mesure répétée des populations Zeeman globales et l'estimation de leurs second moments statistiques. Les valeurs expérimentales de ces propriétés statistiques ne sont pas uniquement dictées par la dynamique dipolaire, et elle sont en général impactées par de nombreux autres phénomènes aléatoires (les fluctuations du signal total, la fluorescence atomique etc...). Dans le deuxième chapitre de ce manuscrit, nous fournissons des méthodes de traitement statistique des données expérimentales qui permettent d'isoler la contribution du bruit de projection quantique. Dans le troisième chapitre de ce manuscrit, nous donnons la preuve expérimentale de la croissance de corrélations de spin dans notre système au fur et à mesure de sa thermalisation. Les résultats de ce chapitre mettent en évidence les possibilités nouvelles associées aux grands spins en termes de suivi des corrélations. Dans le quatrième chapitre nous décrivons la mise en oeuvre d'une nouvelle méthode de bipartition qui nous a permis d'examiner plus finement la structure des corrélations se développant dans notre système et d'en démontrer la relative complexité. La croissance de ces corrélations concorde avec les scénarios de thermalisation quantique communément acceptés selon lesquels la thermalisation des systèmes isolés est induite par l'intrication des différentes sous-parties du système.

Mots-clés : Corrélations, spin, réseau optique, interactions dipolaires, thermalisation quantique

Studies of spin correlations in an ensemble of lattice trapped dipolar atoms

In this manuscript we study the development of spin correlations in an ensemble of lattice trapped chromium atoms. This platform is characterized by the greater spin of its constituents S = 3 and its long range anisotropic interactions. We report on two complementary experiments in which the growth of these correlations is tracked without relying on state tomography like techniques. These experiments build on the repeated measurements of global Zeeman populations and the estimation of these observables' first and second statistical moments. As it turns out, these statistical moments are affected by many phenomena, some of which are of physical significance (dipolar dynamics), and some of which are mostly irrelevant (e.g. total signal fluctuations or fluorescence noise) to our experimental endeavor. In the second chapter of this manuscript, we show how to extract the sole contribution of the quantum projection noise from our data in a most rigorous way. In the third chapter of this manuscript, we prove - experimentally - that spin correlations do indeed develop in our system as it thermalizes through dipole dipole interactions. The results of this chapter illustrate the new possibilities offered by high spin particles $S > 1/2$ as far as correlations tracking is involved. In the fourth chapter we probe at these correlations using a novel bipartition method. We show that the correlations developing in our system are more finely structured than what might, a priori, be inferred from the results of the third chapter's experiment. The growth of these correlations is reminiscent of quantum thermalization scenarios, wherein isolated systems are predicted to thermalize through the development of entanglement.

Key words : Correlations, spins, optical lattice, dipolar interactions, thermalization